Doctoral Dissertation

Variety of nuclear structures in neutron-rich nuclei ^{30}Mg and ^{31}Mg investigated by spin-polarized Na beams

Hiroki NISHIBATA

Department of Physics,
Graduate School of Science,
Osaka University

February, 2016

ABSTRACT

The excited states of the neutron-rich nucleus ^{31}Mg were studied aiming at comprehensive understanding of the structure of the nucleus which is located in the region of the N=20 "island of inversion". This nucleus has been investigated in various types of experiments for a long time, but none of the spins and parities, the important key quantities to understand the nuclear structure, has been assigned experimentally until the ground state magnetic moment was determined and the spin-parity was assigned as $1/2^+$. Because of such a situation it has been difficult to systematically study how far the shell-model nature prevails and how the collective nature appears, when the neutron number N approaches to the magic number 20 around the region of island of inversion.

In the preset work the β decay of spin-polarized ^{31}Na to the excited states of ^{31}Mg were observed in coincidence with the γ-transitions in ^{31}Mg at TRIUMF, where highly polarized ^{31}Na beam is available. The spin values of all the observed positive-parity levels in ^{31}Mg were unambiguously determined from the β-decay asymmetry. Furthermore from the very detailed intensities of β-decays and γ-transitions, possible spin values for all the observed negative-parity levels in ^{31}Mg were restricted significantly.

The experimental results were compared with the theoretical predictions of collective rotational model and the AMD+GCM calculations. It was found that the levels in ^{31}Mg are categorized in four groups: (i) levels of the $K^\pi = 1/2^+$ and $1/2^-$ rotational band members [levels at 0.0 MeV ($1/2^+$), 0.050 MeV ($3/2^+$), 0.944 MeV ($5/2^+$), 0.221 MeV ($3/2^-$), 0.461 MeV ($7/2^-$), and 1.029 MeV ($1/2^-$)], (ii) a level of the $K^\pi = 3/2^-$ rotational band member [0.942 MeV ($3/2^-$)], (iii) levels with spherical nature [0.673 MeV ($3/2^+$), 2.015 MeV ($5/2^+$)], and (iv) a level which is not understood by theoretical models [2.244 MeV ($1/2^+$)].

In the present work the measurement was also performed with the spin-polarized ^{30}Na to obtain more detailed information on the ^{30}Mg structure than the preceding work. The experimental results were compared with the theoretical predictions of the AMD+GCM calculations and the shell-model calculations with the SDPF-M Hamiltonian. It was found that the levels in ^{30}Mg are categorized in five groups: (i) levels with spherical nature with 0p0h configurations [levels at 0.0 MeV (0^+), 1.483 MeV (2^+), and 3.381 MeV (4^+): assigned

in another work], (ii) levels of the largely deformed rotational band with 2p2h configurations [1.788 MeV (0^+)], (iii) a scissors mode state where protons and neutrons are moving in anti-phase like a scissors [4.967 MeV (1^+)], (iv) a band-head of the γ-vibrational band [2.468 MeV (2^+)], and (v) negative-parity states with 1p1h and 3p3h configurations in the excitation region of 3.3 - 4.8 MeV.

It is concluded that the present work successfully found a variety of structures in ^{30}Mg and ^{31}Mg as a result of competitions between the single particle nature and the collective nature.

TABLE OF CONTENTS

CHAPTER I

Introduction

1.1 Exotic structure of neutron-rich nuclei

Various phenomena of nuclei close to the β-stability line have been well explained by the shell model for nuclei with neutron and/or proton numbers close to the magic numbers, or by the collective model for nuclei far from the magic numbers. Typical examples are shown in Fig. 1.1 of the energy of the first 2^+ state of even-even Ca, Ar, S and Si isotopes [NNDC]. The highest energies of the 2_1^+ state at the neutron number $N = 20$ indicate the single-particle nature in these nuclei. Their energies rapidly decrease when the neutron numbers go apart from $N = 20$, showing rapid increase of the collective nature. However, that is not the case for nuclei far from the β stability line. The 2_1^+ energy for Mg and Ne isotopes do not show peaks at $N = 20$, indicating collective nature and disappearance of the magic number.

The ground state properties have been examined intensively for neutron-rich nuclei with the neutron number $N\sim20$ to investigate how the magic number prevails. Figure 1.2 shows a part of nuclear chart of neutron-rich nuclei with $N\sim20$. It was pointed out by the shell-model calculations that in nuclei within a red square the two-particle-two-hole (2p2h) configurations are dominant in the ground states and thus they are deformed, even though their neutron numbers are close to the magic number 20 [WAT81; POV87; WAR90]. This region of nuclear chart is symbolically called as "island of inversion" [WAR90]. Typical experimental evidences were such exotic features as anomalous binding energy in Ne [ORR91], Na [THI75], and Mg [DET83] isotopes, the low excitation energy of the 2_1^+ states of ^{32}Mg [DET79], ^{34}Mg [IWA01], ^{30}Ne [YAN03], and the significantly large $B(E2; \text{g.s.} \rightarrow 2_1^+)$ value in ^{32}Mg [MOT95] (the results of subsequent measurements are summarized in Ref. [CHU05]).

Large scaled shell-model calculations have been developed in order to understand the nuclear structures of nuclei located in the "island of inversion". Some of structures of nuclei in the "island of inversion" such as lowering of $E(2^+)$ were reproduced by the shell models

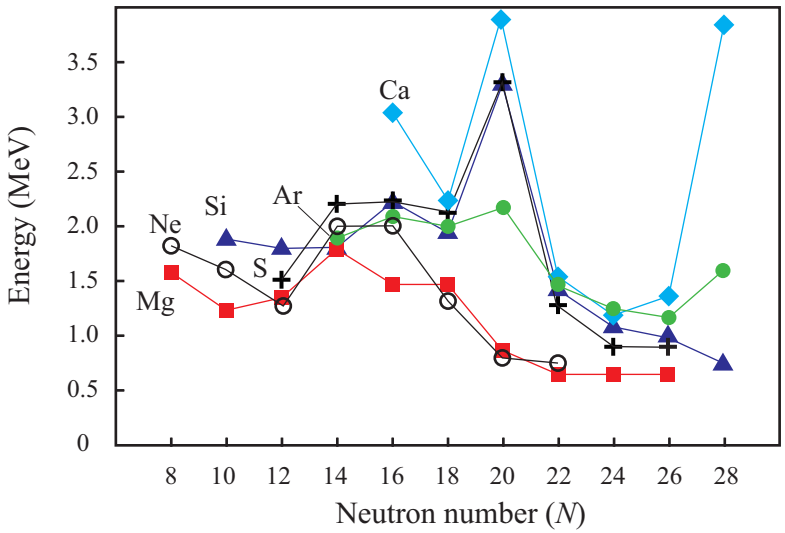

Figure 1.1: Systematics of first 2^+ energies in Ca, Ar, S, Si, Mg, and Ne isotopes [NNDC] for N = 8-28.

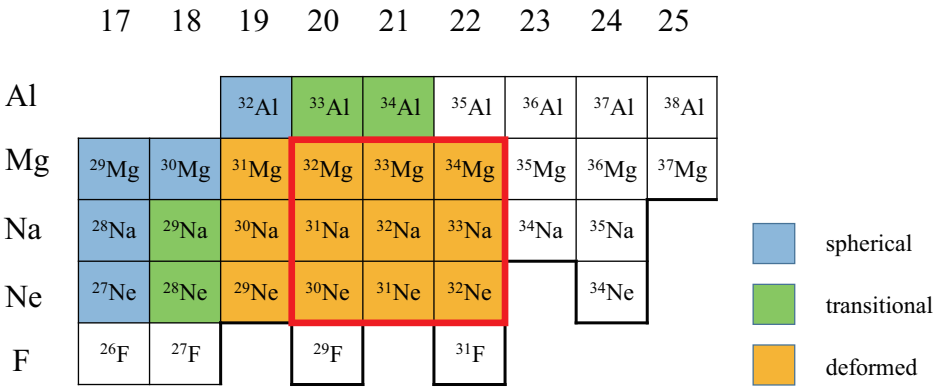

Figure 1.2: Part of nuclear chart of neutron-rich nuclei with N∼20.

which take into account 2p2h excitation from the *sd*-shell to the *pf*-shell across the $N = 20$ shell gap [WAT81; FUK92; WAR90; UTS04]. So far the gradual change of the ground state shape from spherical to deformed shapes are clarified with change of the proton or neutron number, as shown in Fig. 1.2.

As for the excited states, indications of shell evolution were observed such as the energies of the second 0^+ states in even-even Mg isotopes. Figure 1.3 shows the second 0^+ energies together with the shell-model calculations with a model space restricted in the *sd*-shell. It is seen that the experimental energy is much lower than the prediction at $N = 18$. This indicates that the second 0^+ state is spherical in ^{22}Mg, ^{24}Mg, ^{26}Mg and ^{28}Mg, however, it is rather deformed in ^{30}Mg. In the recent study of ^{32}Mg, the observation of the second 0^+ state has stimulated hot discussions about the structures of the excited states in the neutron-rich

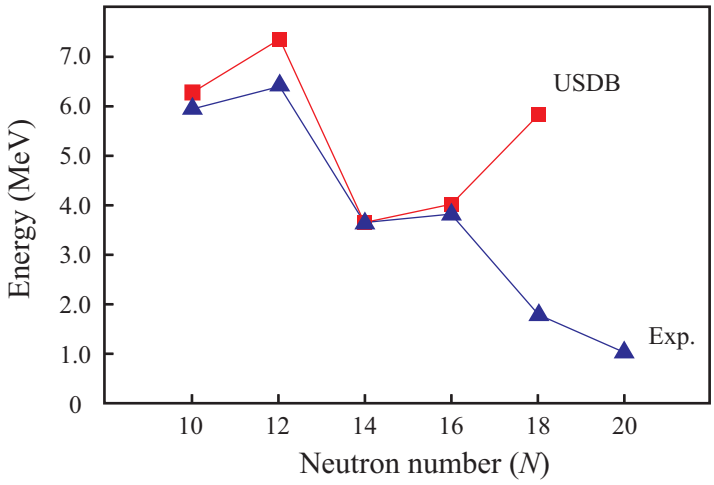

Figure 1.3: Comparison between the experimental energies of 0_2^+ in Mg isotopes for N = 10-20 (^{22}Mg [ALF86-1], ^{24}Mg [ZWI78], ^{26}Mg [ALF86-2], ^{28}Mg [MID64], ^{30}Mg [SCH09], and ^{32}Mg [WIM10]) and the shell-model calculations with USDB Hamiltonian [BRO06].

Mg isotopes [WIM10; FOR11; POV14]. In ^{30}Mg, the ground state have a spherical shape and the 0_2^+ state have been reported to have a deformed shape. On the other hand, it was suggested that the ground state in ^{32}Mg is deformed and the 0_2^+ state have a spherical shape. Such shape change may be due to the competition between the spherical nature and the collective nature.

The theoretical framework of antisymmetrized molecular dynamics (AMD) plus generator coordinate method (GCM), which demonstrates both the collective structures and single particle structures in the same framework, predicted various types of deformed states and spherical states at low excitation energy regions of neutron-rich Mg isotopes [KIM07; KIM11]. In the mean field theory, the calculations of constrained Hartree-Fock-Bogoliubov plus local quasiparticle random phase approximation method (CHFB + LQRPA) predicts the γ-vibrational motion and rotational motion at similar excitation energy in neutron-rich even-even Mg isotopes of ^{30}Mg, ^{32}Mg, and ^{34}Mg [HIN11].

Furthermore, another recent large-scale shell-model calculation [CAU14], predicted that shape coexistence – different shapes coexisting in a narrow low excitation energy region – appear in the excited states, as the result of the competition between the spherical mean field which favors the 0p0h configuration and the nuclear correlation which favors the deformed multi-particle-multi-hole ($np n$h) configurations. However, up to now, the experimental information on excited states has been very limited in most of the nuclei in the $N = 20$ island of inversion.

In neutron-rich ^{31}Mg ($N = 19$), the ground state was investigated by the recent measurement of a spin and magnetic moment in the ground state [NEY05]. It was suggested from these result that the ground state in ^{31}Mg is largely deformed [NEY05]. Excited states in ^{31}Mg have been investigated in various types of experiments, however, none of the spins and parities, which are the important key quantities to investigate the nuclear structures, has been assigned experimentally. In such situation, it has been rather difficult to discuss the nuclear structures in ^{31}Mg.

1.2 Purpose of the present work

The present work aims at comprehensive understanding of structures in neutron-rich nuclei ^{31}Mg and ^{30}Mg. The excited states in ^{31}Mg and ^{30}Mg were investigated in detail by the efficient method, which enables us to firmly assign spins and parities of the daughter states of the β decay of ^{31}Na and ^{30}Na, respectively. This method takes advantage of the anisotropic β decay of spin-polarized nucleus. We have been systematically studying the neutron-rich Mg isotopes ^{28}Mg [KUR12], ^{29}Mg [SHI14; TAJ12], and ^{30}Mg [SHI14; TAJ12] to investigate the excited states at TRIUMF, where highly spin-polarized alkali beam is available.

The present work has successfully shown evidence of the shape coexistence in ^{31}Mg and ^{30}Mg. This thesis is organized as follows. In Chapter II, historical reviews of the level structures in ^{31}Mg and ^{30}Mg are presented. In Chapter III, the principle of the spin-parity assignment and experimental procedures are shown. In Chapter IV, the analysis of the data is described. Chapters V and VI are devoted to the constructions of decay schemes of ^{31}Na and ^{30}Na, respectively. The structures of the excited states in ^{31}Mg and ^{30}Mg are discussed in Chapter VII. In Chapter VIII, we summarize the present work.

CHAPTER II

Up-to-date understanding of ^{31}Mg and ^{30}Mg structures

2.1 Level structures in ^{31}Mg

The level structures in ^{31}Mg have been investigated by various types of experimental experiments: the β decay of ^{31}Na [GUI84; KLO93], the β-delayed one neutron decay of ^{32}Na [KLO93; MAC05; MAT07], the laser spectroscopy of the ground state [NEY05], the one-neutron-removal reaction [TER08], the one-proton-removal reaction [MIL09], the Coulomb excitation [SEI11], and the proton resonant elastic scattering [IMA15], as summarized in Refs. [NEY11]. Figure 2.1 shows the ^{31}Mg levels proposed by various experiments [GUI84; KLO93; KLO93; MAC05; MAT07; TER08; MIL09; SEI11], together with the latest compilation [OUE13].

For the ground state of ^{31}Mg, the half-life [DET79] and the mass [DET83] were first measured in 1979 and 1983, respectively. However, its spin-party has not been assigned until the measurement of hyperfine structure and β-NMR in 2005 [NEY05]. The ground-state spin of 1/2 was assigned from the hyperfine structure and positive parity was proposed to reproduce the magnetic moment in the shell-model calculation [NEY05]. Once the ground state spin-parity was established as $1/2^+$, the $(3/2^+)$ assignment was proposed for the first excited state at 0.050 MeV [NEY05], based on the half-life $T_{1/2} = 16.0(28)$ ns of the 0.050-MeV level [KLO93].

It was suggested that the ground state is deformed to a large extent with a nearly pure 2p2h configuration [NEY05]. Note that the shell model at that time did not reproduce the spin-parity of $1/2^+$ as the ground state even with multi-particle-multi-hole excitation [NEY05], whereas theoretical calculations of the AMD+GCM reproduced the $1/2^+$ ground state and the magnetic moment ($\mu = -0.91\mu_{\rm N}$), and predicted a large deformation of the ground state [KIM07].

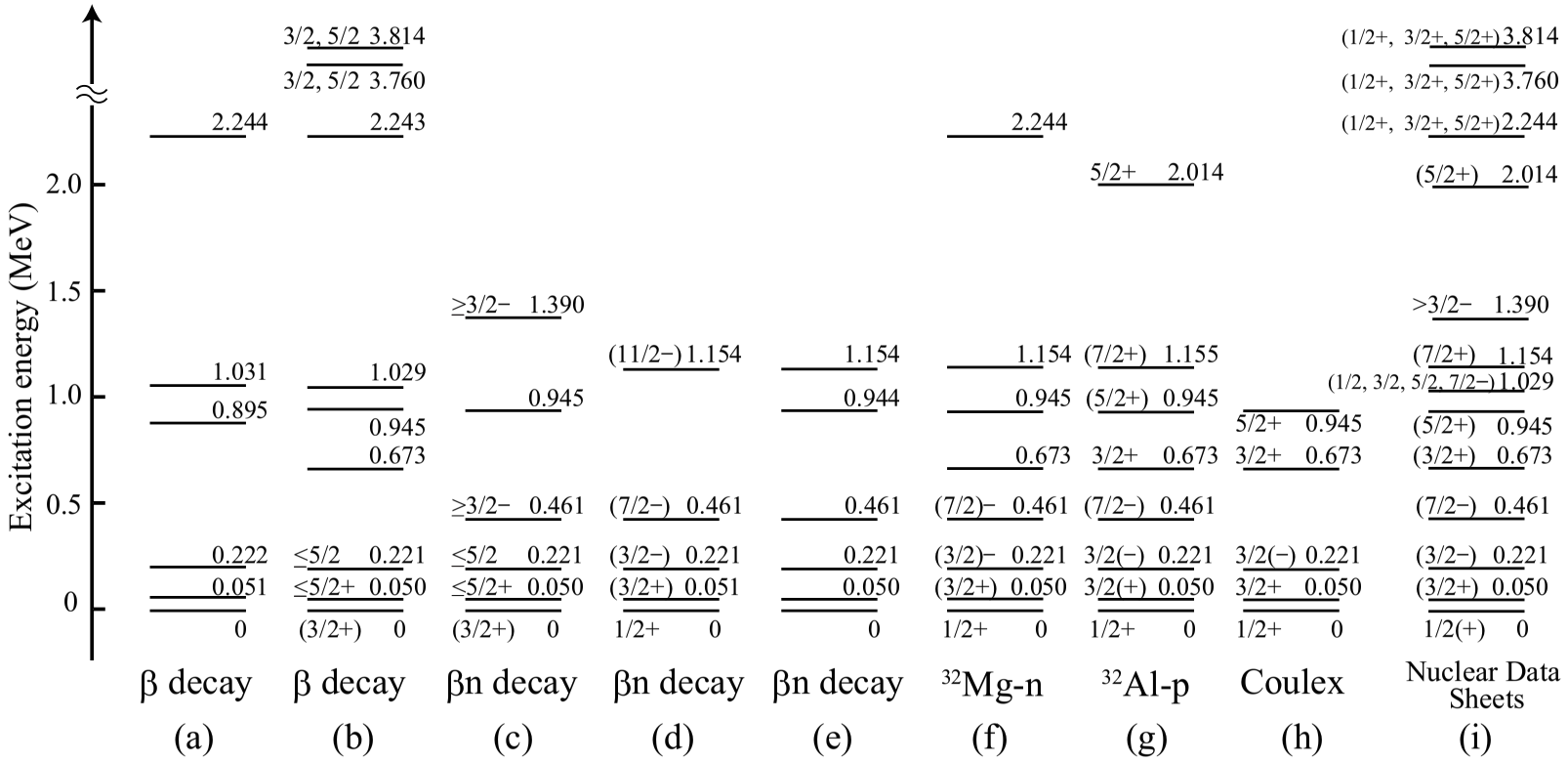

Figure 2.1: Experimental levels in ^{31}Mg, established in the β decay of ^{31}Na {(a) [GUI84] and (b) [KLO93]}, in the βn decay of ^{32}Na {(c) [KLO93], (d) [MAC05], and (e) [MAT07]}, in the one-neutron knockout reaction with ^{32}Mg beam {(f) [TER08]}, in the one-proton knockout reaction with ^{32}Al beam {(g) [MIL09]}, in the Coulomb excitation of ^{31}Mg {(h) [SEI11]}. The most recent data compilation is shown in (i) [OUE13].

Excited levels of ^{31}Mg were first studied in the β decay of ^{31}Na [GUI84]. Five excited levels at 0.051, 0.222, 0.895, 1.031, and 2.244 MeV were proposed in this experiments. Another β-decay experiment was performed by the group [KLO93], and they proposed another four levels at 0.673, 0.945, 3.760, and 3.814 MeV. The 0.895-MeV level, which was proposed in Ref. [GUI84], was removed in the level scheme in Ref. ^{31}Mg [KLO93]. In addition, they measured a half-life of $T_{1/2}$ = 16.0(28) ns for the first excited state at 0.050 MeV, which lead to assignment of a $M1$ transition of 50 keV (0.050 MeV $\rightarrow$ g.s.) [KLO93]. By the same group [KLO93], levels at 0.461 and 1.390 MeV were newly observed in the β-delayed one neutron (βn) decay of ^{32}Na. These two levels were assigned as negative-parity levels based on the large population by βn decay but no observation in the β decay of ^{31}Na.

In Ref. [MAC05], the half-lives of $T_{1/2}$ = 10.5(8) ns and 133(8) ps were determined for the 0.461- and 0.221-MeV levels, respectively. From the half-life of the 0.221-MeV level, the $E1$ assignment was proposed for the γ transitions of 221 [0.221 $\rightarrow$ g.s. $(1/2^+)$] and 171 keV [0.221 $\rightarrow$ 0.050 $(3/2^+)$], thus leading to the $(3/2^-)$ assignment for the 0.221-MeV level. The assignments of $(7/2^-)$ was also proposed for the 0.461-MeV level based on the $E2$ assignment for the 240-keV transition [0.461 $\rightarrow$ 0.221 $(3/2^-)$]. In the βn decay experiments [MAC05; MAT07], a level at 1.154 MeV was proposed

In the neutron knockout reaction with ^{32}Mg , whose ground state has a 2p2h configuration, the levels at 0.221 and 0.461 MeV were strongly populated, whereas the higher levels at 0.673, 0.945, 1.154, and 2.244 MeV were populated with small cross sections [TER08]. These results show a good correspondence with negative-parity 1p2h states for the 0.221- and 0.461-MeV levels. On the other hand, the 0.673-MeV level as well as the 2.015-MeV level were strongly populated in the one-proton knockout reaction using the ^{32}Al beam with a normal ground-state configuration, thus spin-parity assignments of $3/2^+$ for the 0.673-MeV level and $5/2^+$ for the 2.015-MeV level were proposed [MIL09]. In the recent Coulomb excitation experiment of ^{31}Mg [SEI11], it was found that the 0.945-MeV level was directly populated via an $E2$ transition from the $1/2^+$ ground state. Therefore a spin-parity of $5/2^+$ was proposed for the 0.945-MeV level.

So far, various types of experiments proposed spins and parities of various levels in ^{31}Mg. However, most of them are adopted with parentheses in the latest Nuclear Data Sheet [OUE13], except for the ground-state spin value, as shown in Fig. 2.1(i). In such a situation, it is difficult to discuss the structures in ^{31}Mg. Therefore, the experiments to determine the spins and parities of excited states in ^{31}Mg are strongly desired.

2.2 Level structures in ^{30}Mg

The level structure in ^{30}Mg has been studied by using the β decay of ^{30}Na [GUI84; BAU89; MAC05; SCH09; TAJ12], the βn decay of ^{31}Na [KLO93] the Coulomb excitation [PRI99; NIE05], the two-neutron-removal reaction [TAK09], and the fusion reaction of ^{14}C(^{18}O, 2p)^{30}Mg [DEA10]. Figure 2.2 shows the ^{30}Mg levels proposed by various experiments [GUI84; BAU89; KLO93; MAC05; SCH09; TAK09; DEA10; TAJ12; SHI14], together with the latest data compilation of ^{30}Mg [BAS10] updated in 2010. Note that the recent results of Refs. [TAJ12; SHI14] have not adopted in this data compilation [BAS10].

For the ground-state of ^{30}Mg, the half-life [DET79] and the mass [PAS78] were first measured in 1979 and 1978, respectively. Excited levels of ^{30}Mg were first observed in the β decay of ^{30}Na [GUI84], and this group reported 10 excited levels at 1.483, 1.788, 1.820, 2.468, 3.461, 3.542, 4.968, 5.022, 5.094, and 5.414 MeV. They assigned that the 1.483-MeV state was most likely the first 2^+ state. In another β-decay experiment [BAU89], a level at 4.414 MeV was proposed. They also measured neutrons associated with the βn decay of ^{30}Na and proposed many neutron unbound states in ^{30}Mg. The excited ^{30}Mg levels were also investigated in the βn decay of ^{31}Na [KLO93] and [GUI84]. In this experiment, the 1.483-, 1.788-, 1820-, 2.467-, and 3.460-MeV levels were observed. Note that they did not assigned spins and parities of the excited levels, except for the first excited 2^+ states.

For the first excited 2_1^+ state in ^{30}Mg, the $B(E2;0^+_{\rm g.s.} \rightarrow 2_1^+)$ value was measured in the Coulomb excitation experiment [PRI99] as $B(E2;0^+ \rightarrow 2_1^+) = 295(26)$ e^2fm^4. In another Coulomb excitation experiment [NIE05], a similar value of $B(E2;0^+ \rightarrow 2_1^+) = 241(31)$ e^2fm^4 was proposed. These values are consistent with the value predicted from a spherical configuration calculated by the shell-model calculations with a limited model space of only *sd*-shell. It was suggested from these results that the ^{30}Mg ground state has a spherical nature [PRI99].

For the 1.788-MeV level, the half-life was measured as $T_{1/2} = 3.9(4)$ ns [MAC05]. From the half-life, the $E2$ assignment for γ transition [1.788 MeV $\rightarrow$ 1.483 MeV (2^+)] was proposed, thus leading to a spin-parity assignment of 0^+ for the 1.788-MeV level. The conversion electron was measured for the transition [1.788 MeV (0^+) $\rightarrow$ g.s. (0^+)] and found a small transition strength of $\rho(E0,\ 0_2^+ \rightarrow 0_1^+) = (26.2\pm7.5)\times10^-3$, corresponding to a partial $E0$ lifetime of $T_{1/2} = 396(111)$ ns. This small transition strength indicates a small overlap of the wave function between the 0_2^+ state and the ground-state 0_1^+ state with spherical nature. It was proposed from these results that the 0_2^+ level is a deformed level. It is noted that the lowering of the second 0^+ in ^{30}Mg, comparing to the 0_2^+ state at 3.862 MeV in ^{28}Mg, is very interesting, and this fact shows shape coexistence in ^{30}Mg.

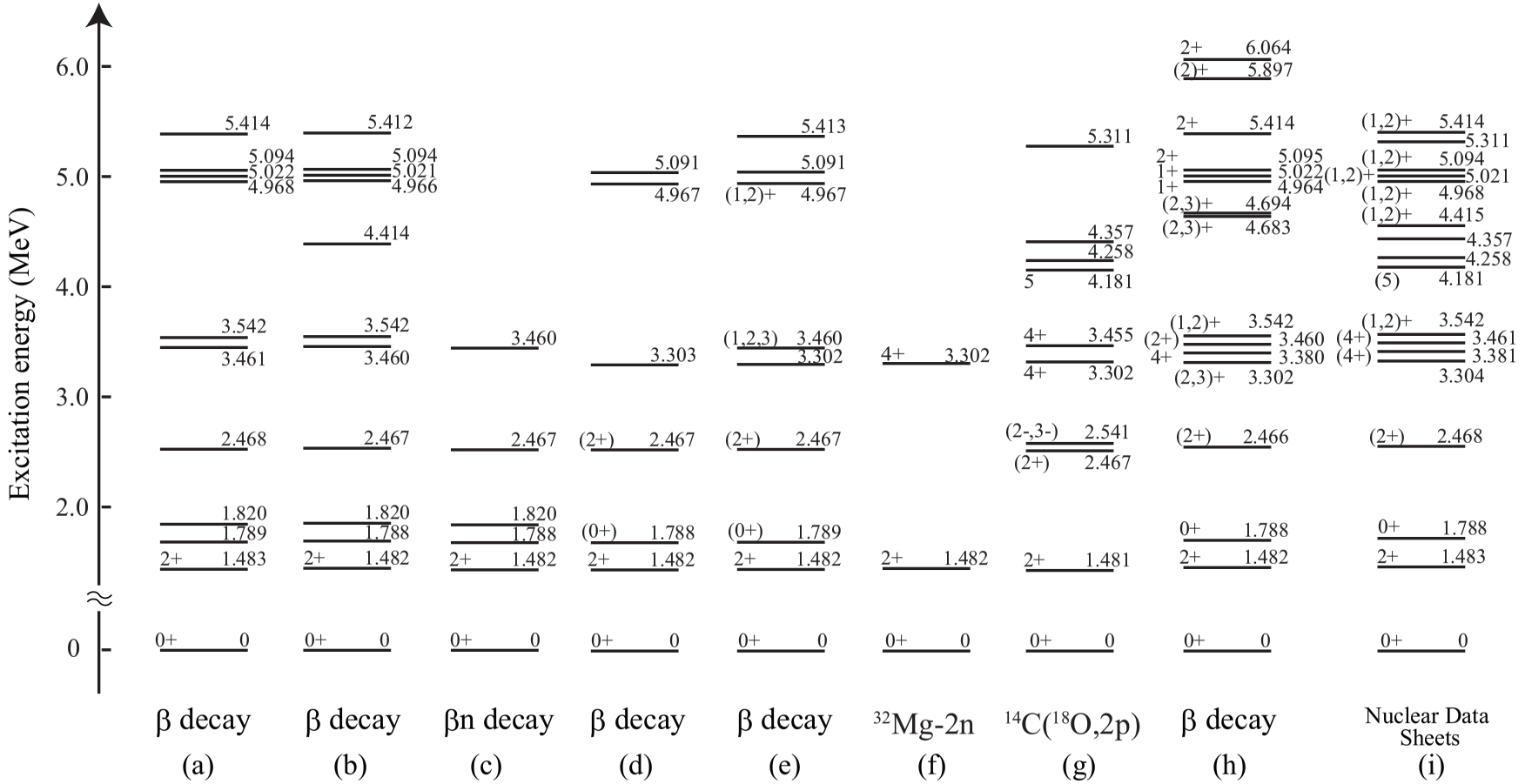

Figure 2.2: Experimental levels in ^{30}Mg, established in the β decay of ^{30}Na {(a) [GUI84], (b) [BAU89], (d) [MAC05], (e) [SCH09], and (h) [TAJ12; SHI14] }, in the βn decay of ^{31}Na {(c) [KLO93]}, in the one-neutron knockout reaction with ^{32}Mg beam {(f) [TER08]}, in two-neutron knockout reaction with ^{32}Mg {(f) [TAK09]}, and in the fusion-evarporation reaction of ^{14}C(^{18}O,2p) {(g) [DEA10]}. The most recent data compilation is shown in (i) [BAS10].

For the level at 2.467 MeV, the upper limit of the half-life of <5ps was measured [MAC05], therefore, it is tentatively assigned the 2.467-MeV level to (2^+) state. In the β decay measurements by H. Mach *et al.* [MAC05] and W. Schwerdfeger *et al.* [SCH09], coincidence between the transitions of 1820 keV, whose γ ray was placed at 1.820 MeV $\rightarrow$ g.s., and 1482 keV was observed, therefore, they put the 3.303-MeV level instead of the 1.820-MeV level.

By the two-neutron knockout reaction from ^{32}Mg [TAK09], the 1.482- and 3.302-MeV levels were observed and a spin-parity of 4^+ was proposed for this level. In another type of experiment using the fusion reaction of ^{14}C(^{18}O, 2p)^{30}Mg, six new levels at 2.541, 3.379, 4.181, 4.258, 4.357, and 5.311 MeV were observed. The spin-parity assignments of 4^+ and 4^+ for the 3.379 and 3.455 MeV levels were performed based on the γ-ray angular correlations.

In the recent β-decay experiment [TAJ12; SHI14], which is the preceding experiment of the present work, the spins and parities of the excited levels at 4.967, 5.022, 5.095, and 5.414 MeV were successfully determined to be 1^+, 1^+, 2^+, and 2^+, respectively, based on the β-ray asymmetry of the β decay of spin-polarized ^{30}Na. Four levels at 4.683, 4.694, 5.897, and 6.064 MeV were proposed. From the comparison with the theoretical models [TAJ12; SHI14], coexistence of various structure was proposed such as deformed levels (levels at 1.788, 3.460, 4.967, and 5.414 MeV) and γ-vibrational band (level at 2.466 MeV).

So far, some of experiments assigned the spins and parities of some excited levels in ^{30}Mg. However, spins and parities of many excited levels in ^{30}Mg have been still unknown, as shown Fig. 2.2.

CHAPTER III

Experiment

3.1 Principle of measurement

3.1.1 Spin-parity assignment

The spins and parities of nuclear levels are one of the most important physical quantities to discuss structures in nuclei and to compare the experimental results with theoretical calculations. However, there exist very few methods to experimentally measure the spins and parities. For example, in case of ^{31}Mg, no spin and parity has been given except for the ground state, although many experimental studies have been performed, as discussed in Sec. 2.1. Our unique feature is that spin-parity assignments can be experimentally performed by using the β decay of spin-polarized beam without dependence on nuclear models [MIY03; HIR05; KUR12; TAJ12]. The spin-parity assignments are performed as follows.

Figure 3.1(a) shows a schematic decay scheme of $^{\mathrm{X}}$Na to explain principle of the method of assigning the spin-parity of the daughter states. By the detailed γ-γ and β-γ coincidence measurements, the level energies can be determined. However, the spin-parity of the levels cannot be assigned. In the present work, we take advantage of the β-decay anisotropy of spin-polarized Na for an allowed transition, expressed as

$$W(\theta) = 1 + (v/c)AP\cos\theta, \tag{3.1}$$

where v, c, A, P and θ represent the velocity of β ray, the velocity of light, the asymmetry parameter, the polarization of parent nuclei, and β-ray emission angle to the polarization axis, respectively. In the case of the large Q value, v/c is approximately 1. The asymmetry parameter A takes three different values depending on the initial state spin I_i and the final

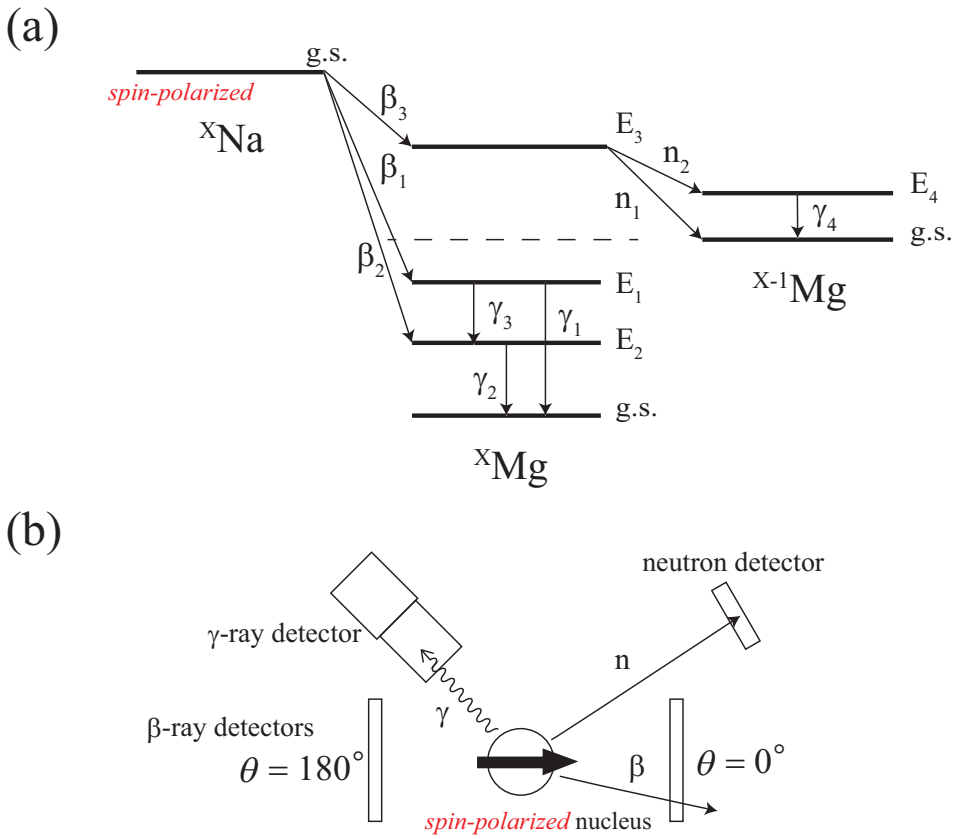

Figure 3.1: (a) Illustrative decay scheme of β decay and β-delayed one neutron decay of ^{X}Na and (b) schematic illustration of γ rays and neutrons detection coincident with β rays. The excited level of E_1, E_2, and E_3 in ^{X}Mg are populated by the β transitions of β_1, β_2, and β_3 in the β decay of the parent nucleus ^{X}Na. After the populations of E_1 and E_2, the γ rays of γ_1, γ_2, or γ_3 are emitted. When the E_3 level, which is located above one neutron separation energy (S_n), is populated, the neutron of n_1 or n_2 will be emitted. The neutrons n_1 and n_2 populate the g.s. and E_4 level, which is depopulated by the γ ray of γ_4, in $^{X-1}$Mg.

state spin I_f of the β transition, expressed as

$$A(I_i, I_f) = \begin{cases} \dfrac{I_i}{I_i + 1} & (\text{for } I_f = I_i + 1), \\ \dfrac{-1/(I_i+1) - \tau\sqrt{I_i/(I_i+1)}}{1+\tau^2} & (\text{for } I_f = I_i), \\ -1 & (\text{for } I_f = I_i - 1), \end{cases} \tag{3.2}$$

where τ is the mixing ratio of Fermi to Gamow-Teller transitions. The expected asymmetry

parameters for the β decays of ^{31}Na and ^{30}Na are listed in Table 3.1, assuming pure Gamow-Teller transitions. As shown in Table 3.1, in the case of the β decay of ^{31}Na ($I_i = 3/2$), the asymmetry parameter is either -1, -0.4, or $+0.6$, for a transition to the possible ^{31}Mg state with spin-parity of $I_f = 1/2^+$, $3/2^+$, and $5/2^+$, respectively. It should be noted that the A values show very discrete values depending on the final state spin (I_f), as seen in Table 3.1. If the A values are experimentally determined, we can assign the spins and parities of the excited states in daughter nuclei.

Table 3.1: Asymmetry parameters (A) depend on initial state spins (I_i) and the final state spins (I_f) for β decay of ^{31}Na and ^{30}Na, assuming pure Gamow-Teller transitions as $\tau = 0$.

	I_i^π	I_f^π	A
^{31}Na $\rightarrow$ ^{31}Mg	$3/2^+$	$5/2^+$	$+0.6$
		$3/2^+$	-0.4
		$1/2^+$	-1
^{30}Na $\rightarrow$ ^{30}Mg	2^+	3^+	$+0.67$
		2^+	-0.33
		1^+	-1

The asymmetry parameters are deduced from the β-ray counts measured by the β-ray detectors placed at right-hand ($\theta = 0^\circ$) and left-hand ($\theta = 180^\circ$) along the polarization axis as shown in Fig. 3.1 (b). The expected β-ray counts of the β-ray detectors placed on right- and left-hand side of the beam axis for the polarization direction "+" are given as

$$\begin{aligned} N_{R+} &= \varepsilon_R N(1 + AP), \\ N_{L+} &= \varepsilon_L N(1 - AP), \end{aligned} \tag{3.3}$$

where ε_R, and ε_L are efficiencies of the β-ray detectors placed on right- (R) and left-hand (L), respectively, and N, N_{R+}, and N_{L+} are total counts of the emitted β ray, and β-ray counts detected by the detectors placed at R and L, respectively. In order to cancel out the asymmetry of the β-ray detection efficiencies, the polarization direction is flipped by 180 degrees. The expected β-ray counts for the polarization direction "$-$" are expressed as

$$\begin{aligned} N_{R-} &= \varepsilon_R N(1 - AP). \\ N_{L-} &= \varepsilon_L N(1 + AP). \end{aligned} \tag{3.4}$$

By taking a double ratio of $R = (N_{R+}/N_{L+})(N_{R-}/N_{L-})$, the AP is deduced freely from β-ray detection efficiencies as

$$\begin{aligned} AP &= \frac{\sqrt{R}-1}{\sqrt{R}+1}. \\ R &= \frac{N_{R+}/N_{L+}}{N_{R-}/N_{L-}}. \end{aligned} \tag{3.5}$$

Note that the polarization P is common for all β transitions. Once P is known, A values for excited levels are obtained, thus the spin-parity assignments can be performed.

The AP value for the level E_1 in Fig. 3.1 (a) can be simply obtained from the β-ray counts in coincidence with the γ rays of γ_1 or γ_3. However, in many cases, the levels are not populated only by the β decay but also by the γ feeding from the higher levels, as the level E_2 in Fig. 3.1. In order to deduce the A value of the E_2 level, the contribution of the transition β_1-γ_3 must be eliminated. The A value of the β rays coincident with γ_2 $[A(\gamma_2)]$ is expressed as following;

$$A(\gamma_2) = \frac{I_{\gamma_2} - I_{\gamma_3}}{I_{\gamma_2}} \times A_{\beta_2} + \frac{I_{\gamma_3}}{I_{\gamma_2}} \times A_{\beta_1}, \tag{3.6}$$

where I_{γ_2}, I_{γ_3}, A_{β_1}, and A_{β_2} represent the γ-ray intensities of γ_2 and γ_3, and A value of β_1 and β_2 transitions, respectively. Thus A_{β_2} is obtained from

$$A_{\beta_2} = \frac{I_{\gamma_2}}{I_{\gamma_2} - I_{\gamma_3}} \times A(\gamma_2) - \frac{I_{\gamma_3}}{I_{\gamma_2} - I_{\gamma_3}} \times A_{\beta_1}. \tag{3.7}$$

A more general form of Eq. (3.7) is expressed as

$$A = \frac{\sum_n I_{\gamma_n} \cdot \sum_n A_{\gamma_n}}{\sum_n I_{\gamma_n} - \sum_k I_{\gamma'_k}} - \frac{\sum_k I_{\gamma'_k} A_{\gamma'_k}}{\sum_n I_{\gamma_n} - \sum_k I_{\gamma'_k}}, \tag{3.8}$$

where γ_n and γ'_k indicate γ rays which depopulate and populate the level, respectively.

The relative error of AP value is given as

$$\left| \frac{\Delta(AP)}{AP} \right| \sim \left| \frac{1}{AP\sqrt{N}} \right|, \tag{3.9}$$

where N is total β-ray counts (see Appendix A). It is seen that the high polarizations of Na nuclei contribute to reducing the error of the β-ray asymmetry to a large extent. For example, in case of $P = 3$ %, which is typical polarization obtained by using nuclear reaction

process, 3×10^4 counts for N is required to distinguish between $A = -0.4$ and -1, with 3σ accuracy. Whereas, in case of a high polarization of $P = 30\%$ in the present work, only 3×10^2 counts is required. Therefore, such a highly polarization enables us to apply our method to very neutron-rich Na isotopes with low production yield.

3.1.2 Production of polarization

Before going to the principle of our optical pumping, the description of the hyperfine structure will be shown as follows. Due to the hyperfine interactions caused by the interaction between the nucleus and electrons, atomic levels are split for each total angular momentum ($\boldsymbol{F}$). The total angular momentum ($\boldsymbol{F}$) is given as

$$\boldsymbol{F} = \boldsymbol{I} + \boldsymbol{J}, \tag{3.10}$$

where $\boldsymbol{J}$ and $\boldsymbol{I}$ are the electronic angular momentum and the nuclear spin, respectively. The energy shifts of hyperfine splitting (ΔE_F) in weak external magnetic field B_0 is given as

$$\Delta E_F = \frac{AK}{2} + B\Big(\frac{3/2K(K+1) - 2I(I+1)J(J+1)}{2I(2I-1)2J(2J-1)}\Big) - \boldsymbol{\mu_F} \cdot \boldsymbol{B_0}, \tag{3.11}$$

where $K = F(F+1)$-$I(I+1)$-$J(J+1)$. The A constant is characterized by the strength of the magnetic-dipole interaction and is expressed as

$$A = \frac{g_I \mu_N B_J}{\sqrt{J(J+1)}}, \tag{3.12}$$

where g_I, μ_N, and B_J represent that g-factor of the nucleus, nuclear magneton, and the strength of magnetic field by the electron, respectively. The B constant is electric quadrupole coupling constant which is characterized by the strength of the electric quadrupole interaction, given as

$$B = eQ_0\phi, \tag{3.13}$$

where e, Q_0, and ϕ are electron charge, the quadrupole moment of the nucleus, and the gradient of the electronic field by the surrounding electrons at the nucleus position, respectively. The second item of Eq. (3.11) which relates with the quadrupole interaction is zero in case

of either I or J is 1/2 or 0. The $\boldsymbol{\mu_F}$ is given as

$$\boldsymbol{\mu_F} = \frac{g_F \mu_B \boldsymbol{F}}{\hbar}, \tag{3.14}$$

with

$$\begin{aligned} g_F = g_J \frac{F(F+1) + J(J+1) - I(I+1)}{2F(F+1)} \\ + g_I \frac{\mu_F}{\mu_B} \frac{F(F+1) + I(I+1) - J(J+1)}{2F(F+1)}, \end{aligned} \tag{3.15}$$

where g_J and μ_B represent the electron g-factor and Bohr magnetron, respectively. The electron g-factor is given by the Lande's formula as

$$\begin{aligned} g_J = g_L \frac{J(J+1) + L(L+1) - S(S+1)}{2J(J+1)} \\ + g_S \frac{J(J+1) + S(S+1) - L(L+1)}{2J(J+1)}, \end{aligned} \tag{3.16}$$

where L and S are electron orbital angular momentum and electron spin, respectively. The electron g-factor g_L and g_S are approximately -1 and -2, respectively.

Figure 3.2 shows the atomic levels of ^{31}Na ($I = 3/2$ [HUB78]) to explain our unique optical pumping method. The hyperfine structures of the ^{31}Na levels are well-studied by the laser spectroscopy [HUB78]. The A constant of ^{31}Na is 912(15) MHz for $^3S_{1/2}$ [HUB78], which leads to the hyperfine splitting of 1368 MHz between $F = 1$ and 2 states. The A of $^2P_{1/2}$ have not been measured, and the splitting is much less than that of $^2S_{1/2}$ state. Both the ground $^2S_{1/2}$ and excited $^2P_{1/2}$ split into two levels with the total angular momentum $F = 1$ and 2. In our experiment, a 10 Gauss magnetic field is applied parallel to the beam line to define the polarization axis, so that the sub-levels with M_F, where is z component of F, split due to the third term of Eq. (3.11). Note that in case of $^2S_{1/2}$ and $^2P_{1/2}$ states, the second term of Eq. (3.11) does not contribute to the splitting because the electronic angular momentums of $^2S_{1/2}$ and $^2P_{1/2}$ are 1/2.

At first, the sub-levels with M_F in the atomic ground $^2S_{1/2}$ are equally populated. In a typical optical pumping method, a circularly polarized laser with a frequency ν_1 and helicity "+", for example, excites the ground-state $^2S_{1/2}$ with $F = 2$ an $M_F = 0$ (hereafter $|F, M_F\rangle = |2, 0\rangle$) to the $^2P_{1/2}$ sub-levels with $|2, +1\rangle$ ($\Delta M_F = +1$), as shown by the red upward arrows. The excited sub-levels deexcite in due course back to the $^2S_{1/2}$ sub-levels with either $|1, -1\rangle$, $|1, 0\rangle$, $|1, +1\rangle$, $|2, -1\rangle$, $|2, 0\rangle$, or $|2, +1\rangle$ according the selection rule of $\Delta F = 0, \pm 1$ $\Delta M_F =$

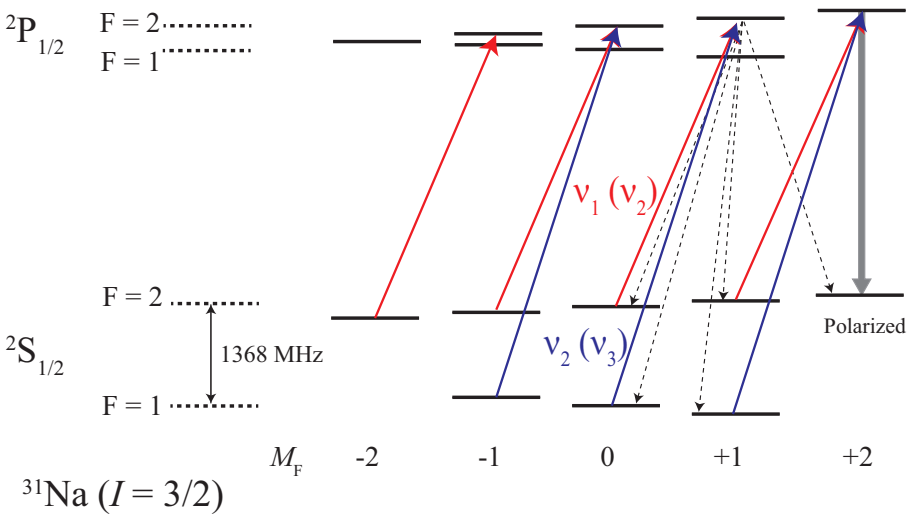

Figure 3.2: Atomic levels of ^{31}Na with the hyperfine interaction.

0, ± 1, as show by the downward arrows in blue. The excitation and deexcitation process is repeated many time. Because the ground-state sub-levels with $|2, +2\rangle$ does not absorb the laser light, its population becomes larger gradually. Namely, the atomic polarization is produced. The nuclear polarization is also produced because the atomic and nuclear spins are parallel in the sub-level with $|2, +2\rangle$. However, the ground $F = 1$ states, including those populated by the deexcitation process with ν_1 laser, are not pumped. As a result, the polarization becomes rather low. In the present work, we use laser with two different frequencies (ν_1 and ν_2) to pump the both atomic ground $^2S_{1/2}$ with $F = 1$ and 2 to achieve a high polarization.

Note that by using the pumping laser with helicity "$-$", the population of the sub-level with $|2, -2\rangle$ becomes large, namely the spin-polarization with the opposite direction can be produced. The "$-$" helicity laser is easily obtained by using a $\lambda/2$ plate.

3.2 Production of radioactive ^{31}Na and ^{30}Na at TRIUMF

The experiment in the present work was performed at the TRIUMF Isotope Separator and Accelerator (ISAC) facility, where the isotope separation on-line (ISOL) technique is used to produce the radioactive rare-isotopes. The system consists of a high resolution mass separator to select beams and a beam transport system for a variety of experiments. The radioactive isotopes are produced by a target-fragmentation reaction induced by a 500-MeV proton beam, which is accelerated by the TRIUMF cyclotron. Diffused isotopes from the target pass through the heated tube and are ionized. The isotopes are accelerated off the high-voltage up to 60 keV and sent through a mass separator in order to select the isotope. Then, they are delivered to the experimental hall (ISAC-I), as shown in Fig. 3.3.

The ^{31}Na and ^{30}Na beams are provided by bombarding an uranium carbide (UC_x) target with the 500-MeV proton beam with 10 μA. The beam was transported to the OSAKA beam line, where β-ray, γ-ray, and neutron measurement was performed, through the polarized beam line. The beam intensities of spin-polarized ^{31}Na and ^{30}Na beams are typically 2.1×10^2 and 2.4×10^3 pps at the Osaka beam line, respectively.

3.3 Production of spin-polarized Na beams

In order to polarized the nuclear spins of alkali metal atoms, ^{31}Na and ^{30}Na, we take advantage of the collinear optical pumping technique. In order to produce highly spin-polarized Na beams, the laser with two different frequencies pumping both atomic ground states are used. The principle of our optical pumping technique is described in Sec. 3.1.2, and the polarizer in ISAC-I is shown in Sec. 3.3.1.

3.3.1 Polarizer at ISAC-I

Figure 3.4 show a schematic illustration of the polarized beam line, consisting of a Na vapor neutralizer, a He gas re-ionizer, and an optical pumping region in between [LEV04] The spin-polarized beam is obtained in the following three steps:

1) The $^{31}Na^+$ ions from the left-side of Fig. 3.4 are neutralized in collisions with the Na vapor in the neutralizer. This process is necessary to apply the optical pumping to Na atoms because we take advantage of the atomic process of the last electron which occupies outermost electron shell. The neutralization efficiency is approximately 50%. The unneutralized $^{31}Na^+$ ions are kicked out by electrostatic deflection plates.

(a)

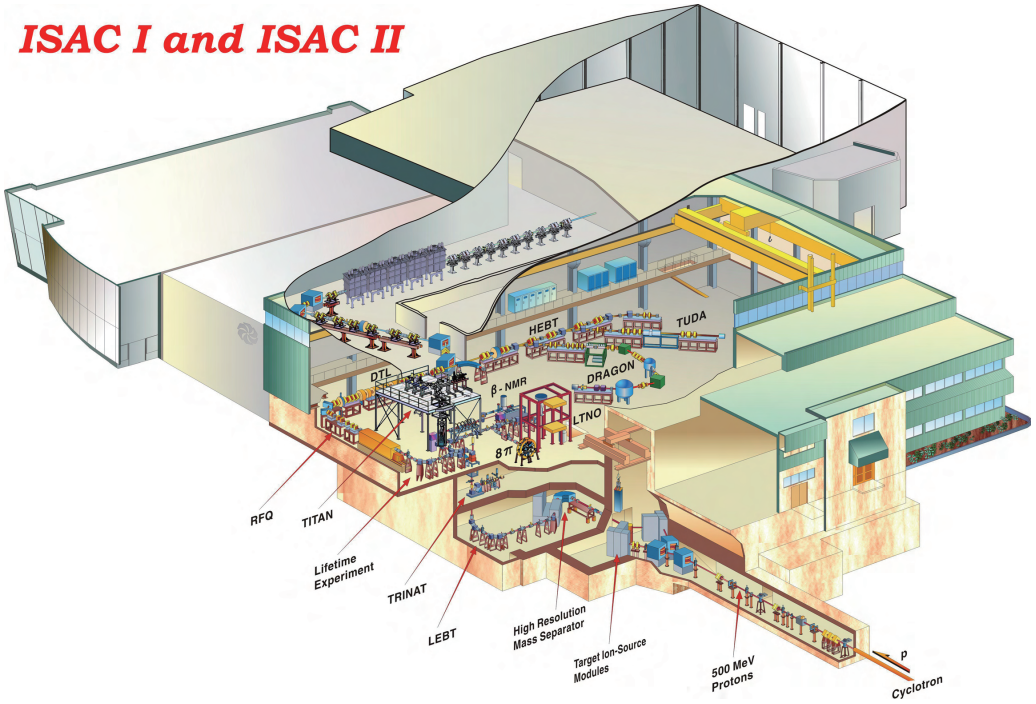

(b)

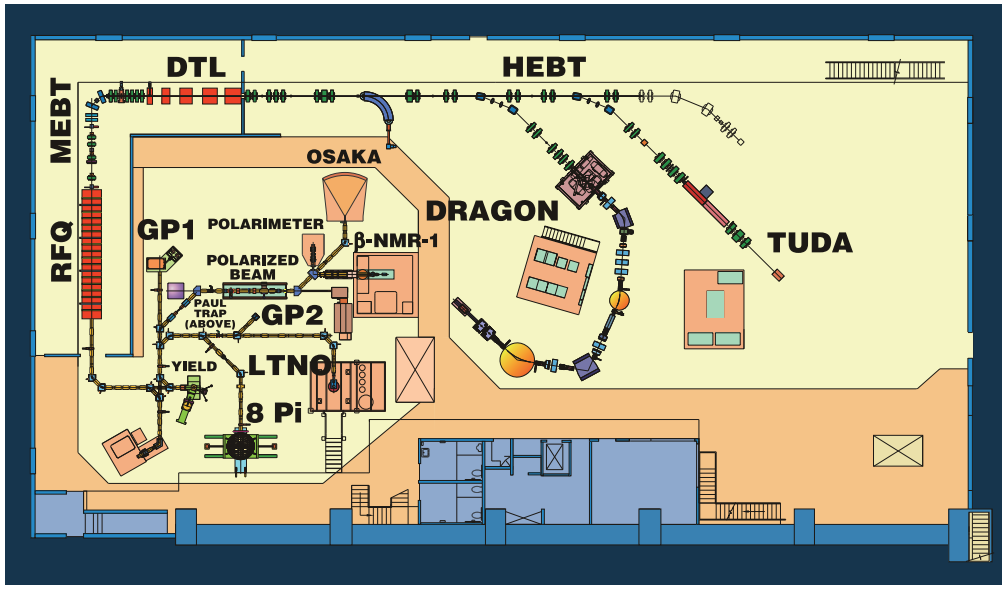

Figure 3.3: (a) Schematic drawing of the ISAC facilities and (b) ISAC-I experimental hall.

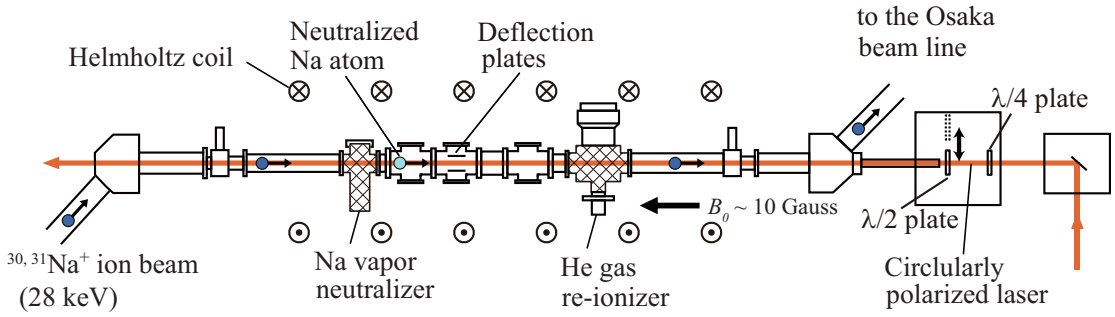

Figure 3.4: Schematic layout of the polarized beam line at ISAC-I.

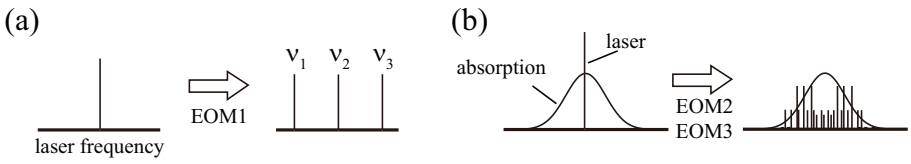

Figure 3.5: Schematic illustrations of (a) splitting and (b) broadening of the laser frequencies by the EOMs.

2) The neutralized ^{31}Na atoms are optically pumped by the collinear laser beam with a wavelength of 590 nm, which corresponds to D_1 transition (between the $^3S_{1/2}$ and the $^3P_{1/2}$), from the right-side of Fig. 3.4(a). The laser frequency is modulated, before injecting into the beam line, with three EOM's in cascade arrangement, as shown in Figs. 3.5(a) and (b). The first EOM splits the laser frequency into three with an equal interval which exactly corresponds to the hyperfine splitting energy (1368 MHz for ^{31}Na and 1560 MHz for ^{30}Na), and the second and third EOM's broaden the laser line width to meet the Doppler-broadened absorption line width In order to precisely adjust the resonance frequency, the beam energy is fine-tuned by applying high voltage to the neutralizer, which will be shown in following section. The polarization direction is longitudinal as defined by a static magnetic field of ∼1 mT applied along the beam axis. The polarization direction is alternated by inserting or removing the $\lambda/2$ plate.

3) The polarized ^{31}Na and ^{30}Na neutral beam is ionized at the He gas re-ionizer which contains cooled He gas (∼20 K). Then the beam is delivered to the Osaka beam line, where the experimental apparatus for β-γ spectroscopy is placed. The re-ionization efficiency is also approximately 50%. Since the atomic magnetic moment of the $^{31}Na^+$

ion is very small, the nuclear spin orientation is not significantly affected even without the guiding magnetic field during the transport.

3.3.2 Optimization of bias voltage to the neutralizer

The laser frequency relative to the Na beam was shifted by the Doppler shift. By changing the velocity of the Na atoms, we could precisely adjust the resonance frequency. The bias voltage of the neutralizer was optimized as follows. Figures 3.6 (a) and (b) show the AP values as a function of the voltage, obtained from the $0°/180°$ asymmetry for all the β transitions from ^{30}Na and ^{31}Na, respectively. The optimum high voltage of 83 and 92 V was determined to obtain the maximum absolute AP value for ^{30}Na and ^{31}Na, respectively. Note that when the laser is off, the AP value of $AP = -0.004(5)$ is consistent with zero, showing clear evidence for polarization.

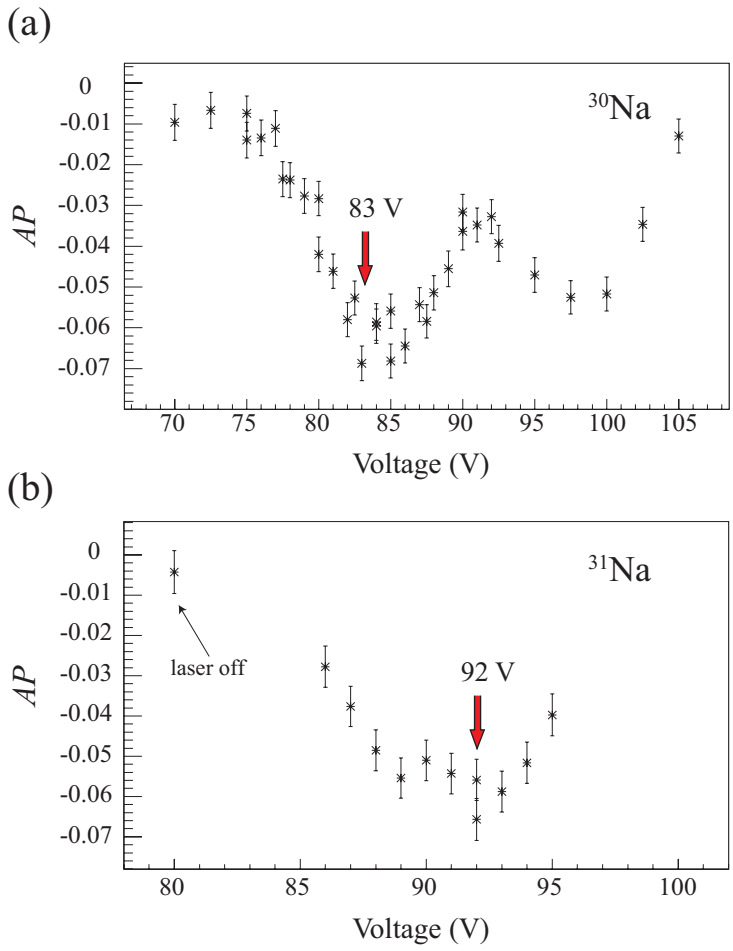

Figure 3.6: Asymmetry of the β rays from (a) ^{30}Na and (b) ^{31}Na as a function of the voltage of the Na cell.

3.4 Detector setup and devices surrounding the beam stopper

Figures 3.7 and 3.8 show a schematic view of experimental setups and a picture of the setups surrounding the beam stopper, respectively. The Na beams come from the left- to right-side of Fig. 3.7 along the z-axis and stop in a 20 μm-thick Pt foil in vacuum. The Pt stopper is surrounded by a vacuum chamber made from a fiber-reinforced plastic (FRP). A magnetic field of 0.53 T is applied to the Pt foil along the polarization axis by a Nd permanent magnet in order to preserve the polarization. The polarization direction is perpendicular to the beam axis in the horizontal plane, as shown by the thick arrow along the x axis in Fig 3.7.

The β rays and γ rays associated with the β decays of ^{31}Na and ^{30}Na beams are detected through the FRP vacuum chamber wall (1 mm in thickness) by 8 telescopes surrounding the Pt foil. Each telescope consists of a high-purity germanium (Ge) detector and a plastic scintillator(s). The β-ray asymmetry is measured by the telescopes placed at right- and left-hand side along the polarization direction. The β-delayed neutron is also measured by 3 thick and large plastic scintillators, as shown on the right-side of the figure.

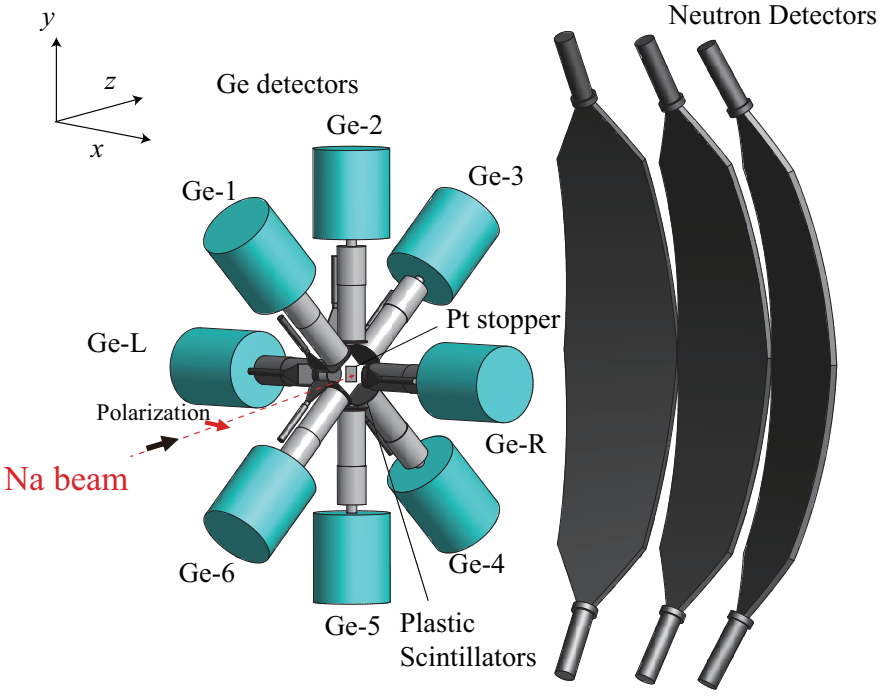

Figure 3.7: Schematic illustration of detector setups consists of eight Ge detectors, 10 plastic scintillators, and three neutron detectors.

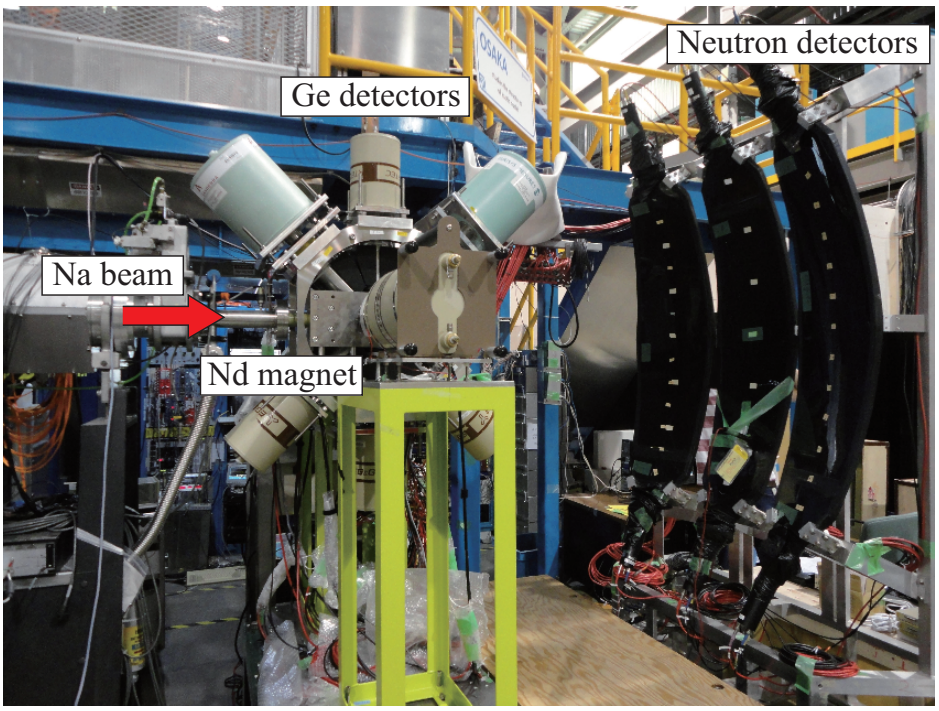

Figure 3.8: Picture of the detector system, the support frame, and devices surrounding the Pt stopper.

3.4.1 Pt stopper, FRP chamber, Nd permanent magnet, and Pb Compton shield

The layout of the surrounding devices around the Pt stopper in shown in Figs. 3.9 (z-y plane) and 3.10 (z-x plane). In the present experiment, a well-annealed Pt foil was used as the beam stopper because polarized Na nuclei in Pt is expected to have the longitudinal relaxation times of $T_1 = 0.7$ s for ^{30}Na and $T_1 = 0.3$ s for ^{31}Na (see Appendix B). These relaxation times are much longer than the half-lives of ^{30}Na ($T_{1/2} = 48(2)$ ms) and ^{31}Na ($T_{1/2} = 17.4(4)$ ms). The size of the Pt stopper is 24 mm $\times$ 24 mm $\times$ 20μm. The Pt stopper was tilted at a 45° in order not to prevent the β-ray ways to the β-ray telescopes. The Pt stopper was well-annealed in order to avoid the relaxation of the spin-polarization of Na beam due to a magnetic field caused by lattice defects in the Pt foil. The procedure annealing of the Pt stopper is shown in Appendix C.

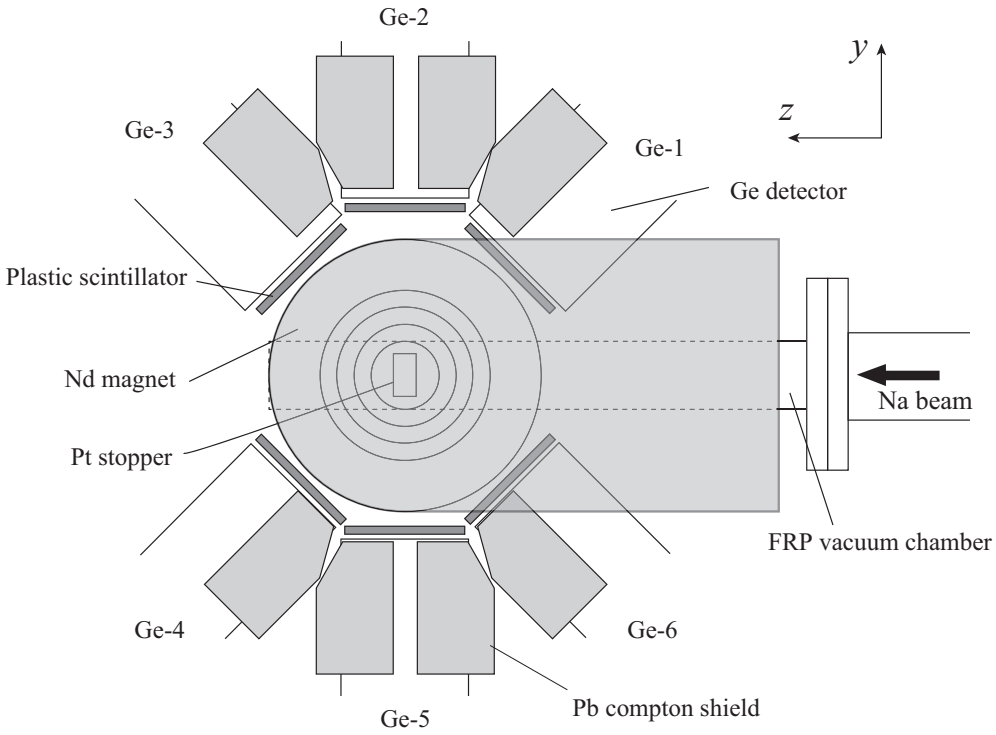

Figure 3.9: Arrangement of the detectors and the experimental devices around the Pt stopper on the y-z plane.

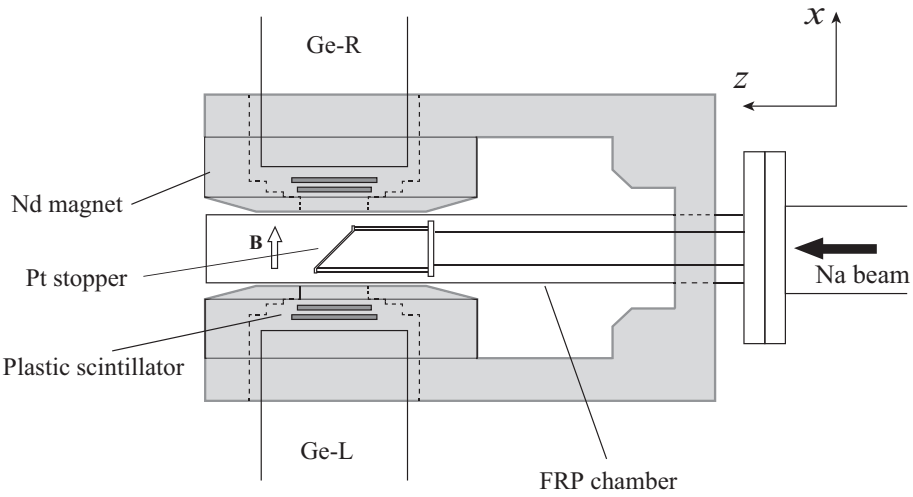

Figure 3.10: Arrangement of the detectors and the experimental devices around the Pt stopper on the z-x plane.

The Nd permanent magnet applies a static magnetic field of 0.53 T to the Pt stopper to preserve the polarization. The gap of the magnet is 40 mm, the hole of ϕ40 mm was opened for the β-ray and γ-ray detection of telescopes at right- and left-hand in Fig. 3.10. The return yoke to enforce the magnetic field with the hole of ϕ50 mm for the FRP chamber was attached. The drawing is shown in Fig. 3.11 (a).

The FRP chamber is located between the gap of the magnet and was surrounding the Pt stopper, as shown in Fig. 3.11 (b). The diameter of the FRP chamber is ϕ38 mm, and thickness of the FRP chamber wall is 1 mm. This is designed to minimize the energy losses of β rays.

Eight of lead shields are placed between Ge detectors, as shown in Fig. 3.9. Gamma rays scattered in a Ge detector by Compton scattering may hit another Ge detector. It is called a Compton cross-talk event. This causes dummy γ-γ coincidence events, and sometimes γ-ray peaks by Compton cross-talk events overlap with real γ-ray peaks. The Pb Compton shield reduces such cross-talk event as shown Fig. 3.12.

3.4.2 Detector telescope consisting of Ge detectors and plastic scintillators

In the present experiment, 8 telescopes were used for the β- and γ-ray detection. Six of telescopes are placed in a plane defined by the beam axis and the vertical axis, each consisting of a Ge detector (named as Ge-1, Ge-2, Ge-3, Ge-4, Ge-5, or Ge-6) and a 1.5-mm-thick (or 2-mm-thick) plastic scintillator. The right- and left-side telescopes of Fig. 3.7 along the polarization axis measure the β-ray asymmetry, each consisting a Ge detector (Ge-R or Ge-L) and two 1.5-mm-thick plastic scintillators. Such telescope enables us to distinguish between the β and γ rays with low background, as shown in Fig. 3.7

All of the Ge detectors are n-type co-axial Ge detectors to measure γ rays with wide energy range of 40 to 6000 keV. The relative efficiencies of Ge detectors are 60 % (Ge-R and Ge-L), 50 % (Ge-3), 45 % (Ge-1), and 30 % (Ge-2 , Ge-4, Ge-5, and Ge-6). A detector windows are 0.5-mm-thick Be + 1-mm-thick plastic cap for Ge-5, 0.5-mm-thick Be + 0.3-mm-thick Al for Ge-R and Ge-L, and 0.5-mm-thick Al for the other Ge detectors.

The attenuations of γ rays in the plastic scintillators are negligible because estimated attenuations in 2 mm plastic scintillators is less than 10 % for 50-keV γ rays. The photomultiplier tubes (PMT) connected plastic scintillators are covered with the cylindrical magnetic shield of steel and permalloy sheet in order to shield the PMTs from stray magnetic field of the Nd permanent magnet. Table 3.2 and Fig. 3.13 shows the specifications of Ge detectors and the plastic scintillators.

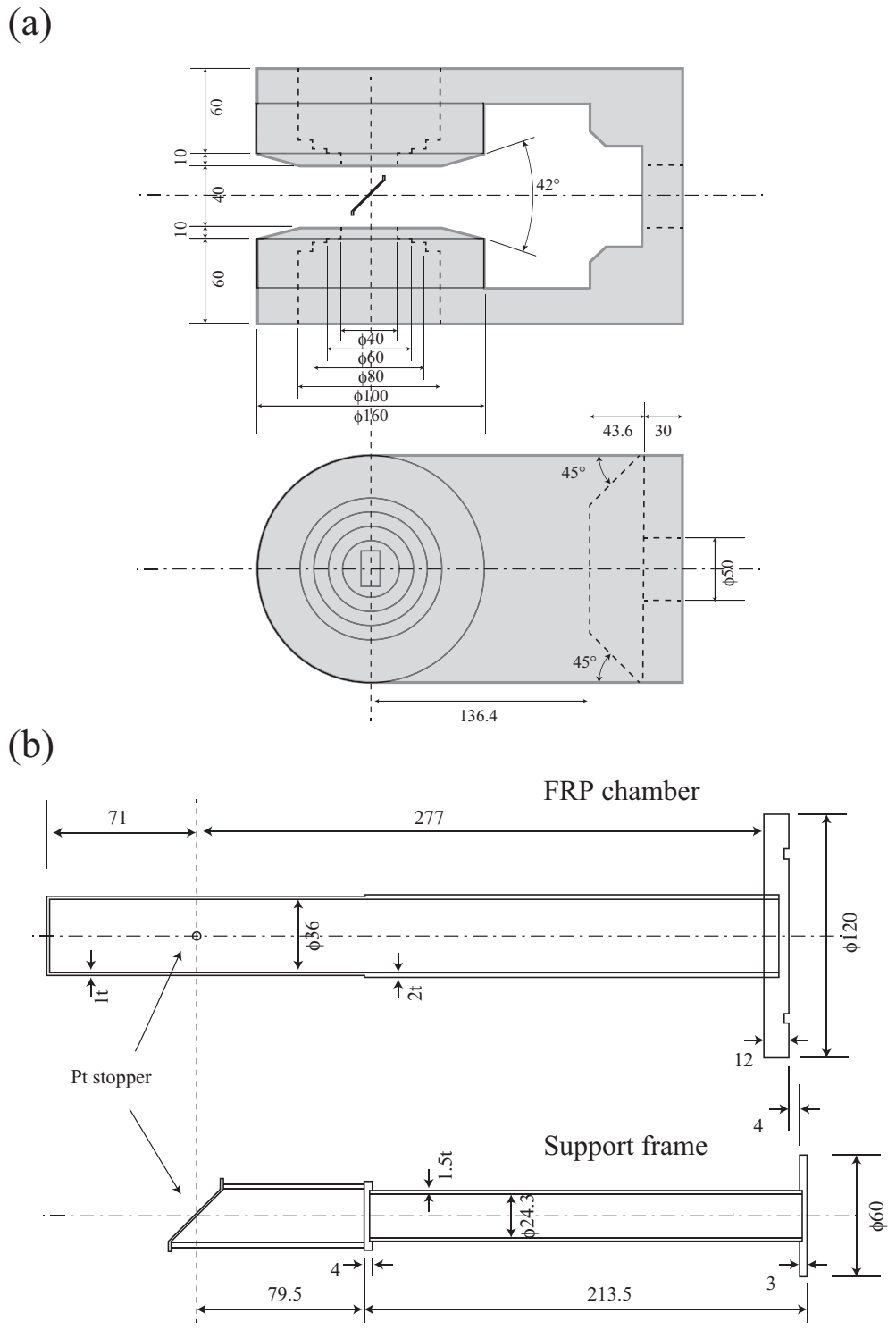

Figure 3.11: Drawing of (a) the Nd permanent magnet and (b) FRP vacuum chamber and support frame of the Pt stopper.

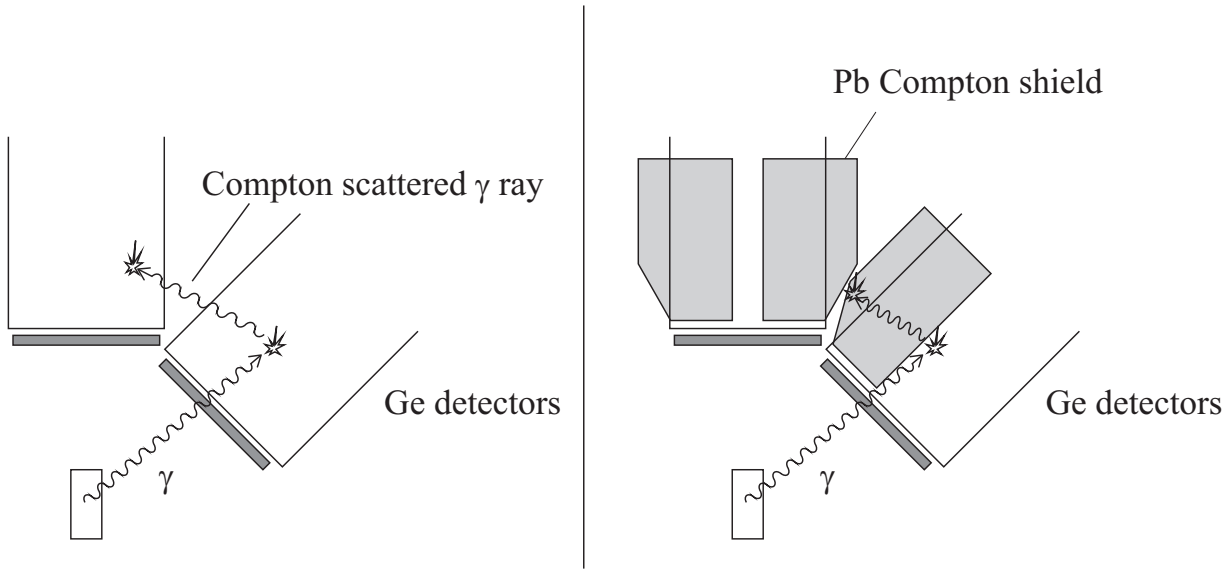

Figure 3.12: Schematic illustration of Compton cross-talk event with and without the Pb Compton shield.

The total absolute efficiency of γ rays is 16% for 50 keV and 2.9% for 1332 keV. The β-detection efficiency is $\sim$16% in total for $\theta = 0^\circ$ and 180° and $\sim$32% for all 8 telescopes. Note that due to the finite solid angles of the telescopes, the AP values are attenuated by 92%.

Table 3.2: List of Ge detectors and the scintillators in front of each Ge detectors. The scintillators types of (a)-(f) are shown in Fig. 3.13.

	Name	relative efficiency(%)	Energy resolution(keV)	Pair β counter type
Ge-1	HANDAI45%	45	2.7	(d)
Ge-2	CINDY	30	2.0	(c)
Ge-3	HANDAI50%	50	2.4	(c)
Ge-4	CAROL	30	2.5	(c)
Ge-5	ALICE	30	2.1	(e)
Ge-6	PETER	30	2.3	(d)
Ge-R	HANDAI60%A	60	2.8	(a) and (b)
Ge-L	HANDAI60%B	60	2.5	(a) and (b)

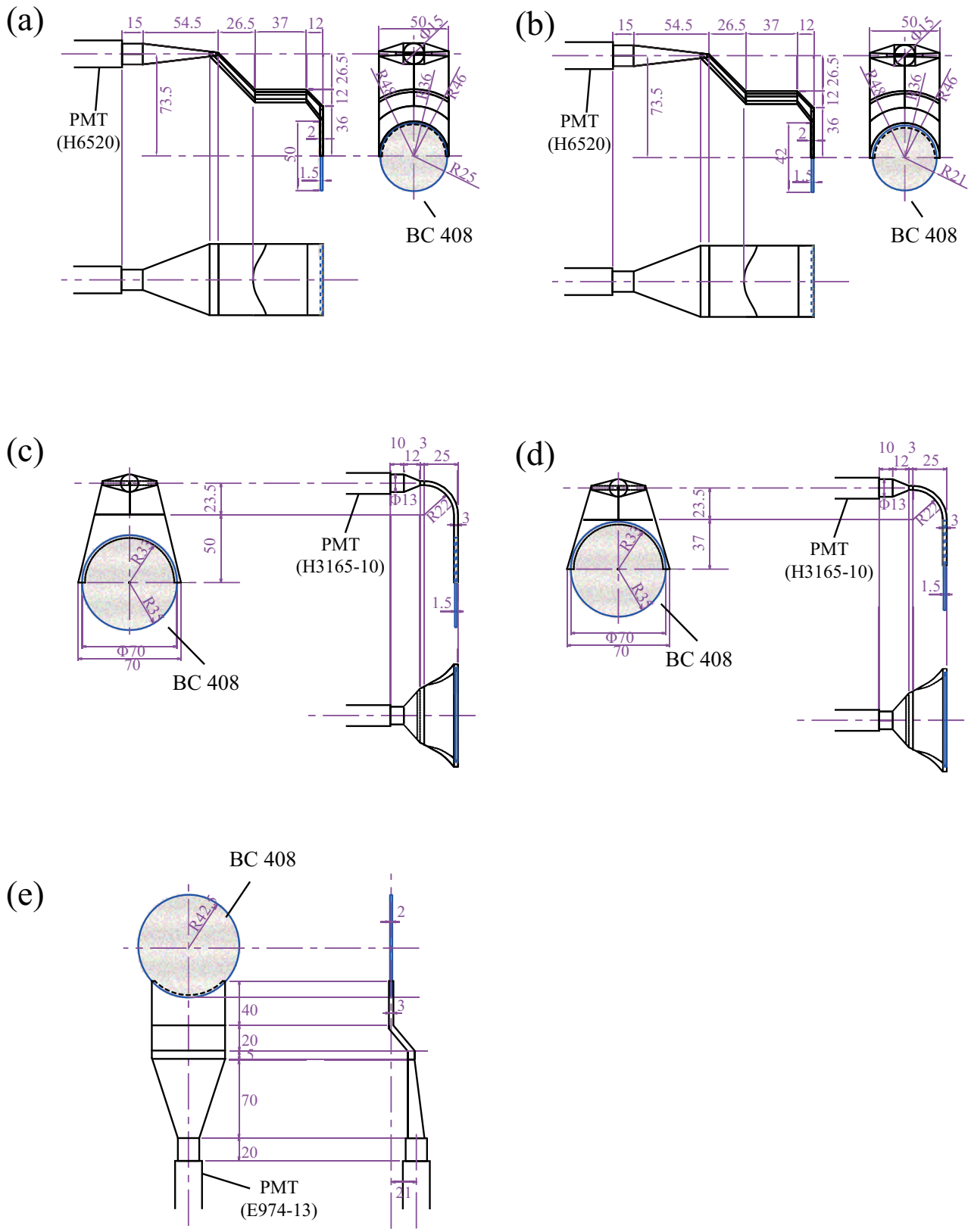

Figure 3.13: Drawing of the plastic scintillators.

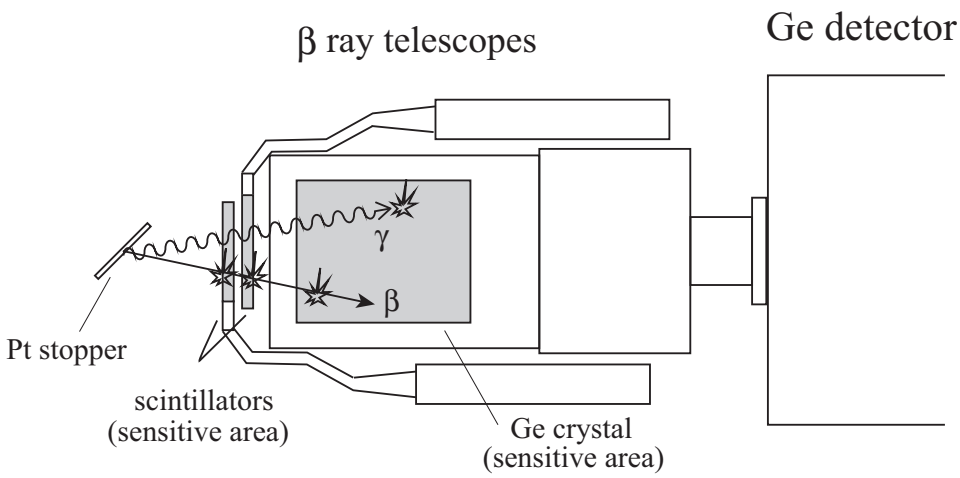

Figure 3.14: Schematic view of the β-ray telescopes consist of two thin plastic scintillators and one Ge detector for β-ray asymmetry measurement.

3.4.3 Neutron detectors

The β-delayed neutrons associated with the β-delayed neutron decay of ^{30}Na and ^{31}Na are measured by three large plastic scintillators using the time of flight (TOF) method. Fig. 3.15 (a) and (b) show a neutron detector and the arrangement of the neutron detectors, respectively. The detectors are placed 1.5 m downstream of the Pt stopper, as shown in Fig. 3.15 (b). Each neutron detector is curved with a 1.5 m radius which eliminated position correlations of the neutron flight length, and has a 1.6 m arclength. The thickness of the scintillators is 20 mm. The longitudinal width is 40 cm in the median z-x plane and become narrow to the connection of PMT, which is designed to maximize the light correction of PMTs. Two PMTs are each connected to end of the scintillator of the up- and down-side. Taking an average of these two PMT timing, the time fluctuations come from the neutron hit positions can be reduced. Also, the coincidence between two PMTs reduces the background. The scintillators is made from BC408, which has a larger light attenuation length of 210 cm and has a approximately 2 ns decay time.

The energy of neutron is measured by taking the time difference between the promptly emitted β rays detected by the telescopes and the neutrons. This time difference corresponds to the neutron energy. The energy resolution of neutron detectors comes from the time resolution of the neutron detectors (FWHM 4 ns in this work) and uncertainty of the flight length (2cm/150cm = 1.3 %). The total solid angle of the neutron detectors was approximately 4 %, which was limited to the support flames and Ge detectors. The intrinsic efficiency of the neutron detectors are approximately 20 % for 2-MeV neutrons. In the present thesis, only

neutron TOF spectrum and the A values for the β decay of ^{31}Na are shown. The detailed results of the neutron detection will be discussed elsewhere [KAN16].

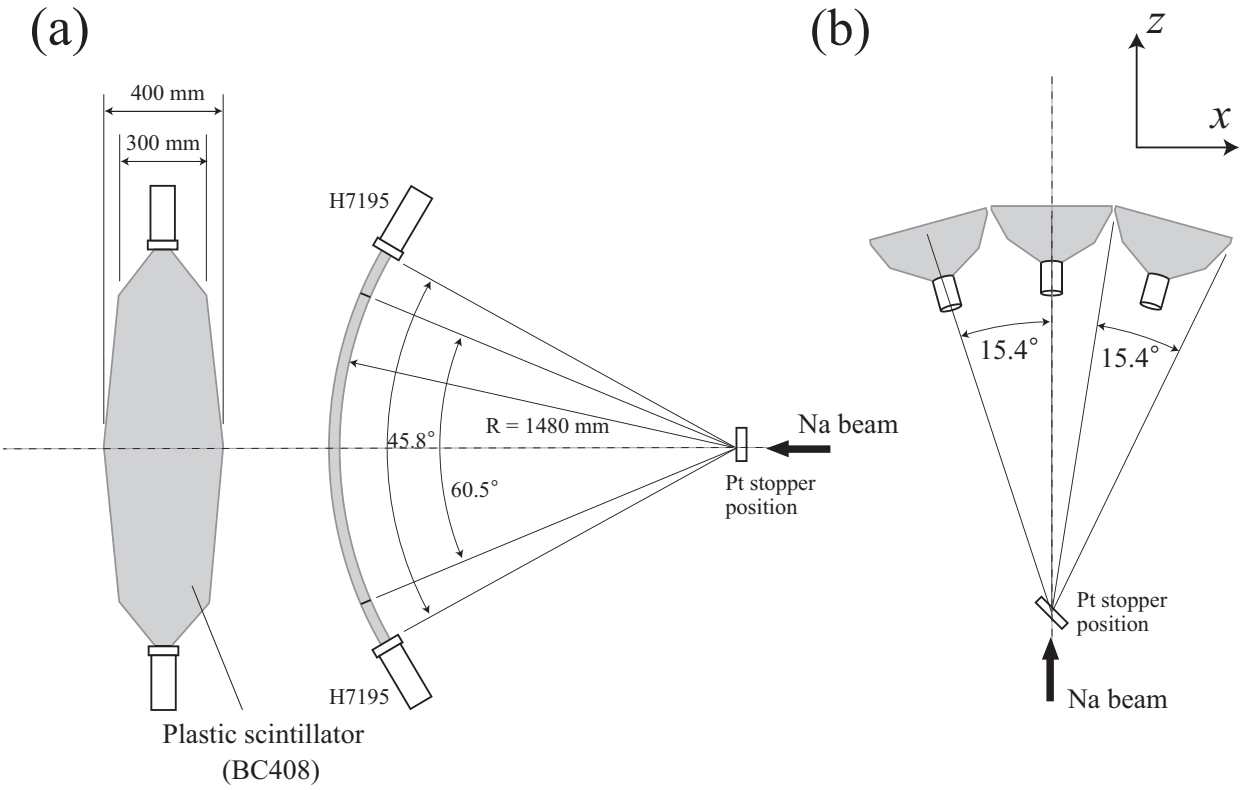

Figure 3.15: Schematic drawing of the neutron detectors and its arrangement.

3.5 Data acquisition system

The energies and timing information of the plastic scintillators, the Ge detectors, and the neutron detectors were accumulated by using analog-to-digital converters (ADC), charge-to-digital converters (QDC) and time-to-digital converter (TDC), based on a CAMAC system. CAMAC The accumulating event data were stored in the PC and were analyzed.

3.5.1 CAMAC systems

Fig. 3.16 schematically shows conception of our data acquisition system consists of main and sub CAMAC crates. In the preset work, the two CAMAC systems work in parallel in order to reduce a dead time of the data acquisition. By using single CAMAC system, the dead time is typically more than 60% for 4 kHz trigger rates. On the other hand, in our acquisition system, the dead time was improved to be approximately 40%.

For the data acquisition and accumulation from the modules, a CAMAC crate controller of CC/NET, which has a stand-alone board computer, was used. In the CC/NET, a data acquisition system of NBBQ developed in RIKEN [BAB16] was installed. ADCs, TDCs, and charge-to-digital converters (QDC), were mounted in main CAMAC create to get the information on the energies of β and γ rays detected by the telescopes and on the neutron TOF. In the sub CAMAC crate, ADCs and TDCs were used for energy and timing information of Ge detectors and plastic scintillators. The analog signals of Ge detectors are fed to the ADC inputs, and the ADCs analyzed the pulse height of the signals which corresponds to the γ ray energies. The energy information of the plastic scintillators and neutron detectors were accumulated by the QDCs, and these energy information was not equal to the incident β-ray and neutron energy.

Scalars, a coincidence register, and an output register were also installed. A measurement time and count rates of the detectors were measured by the scaler with the 1-kHz clock pulses. The output register generated the signals of the spin flip operations, explained in Sec. 3.5.3). The coincidence register monitors the direction of the polarization.

3.5.2 Electronic circuit

Figure 3.17 shows an electronic circuit in the present experiment. Ge-detector signals are divided into two (three for Ge-R and Ge-L) for the energy (with low and high gain for Ge-R and Ge-L) and timing. For the energy information on Ge detectors, the signals were shaped by shaping amplifiers (S-Amp: ORTEC 570, 572, 672, or 673) with shaping time of 6 μs, and

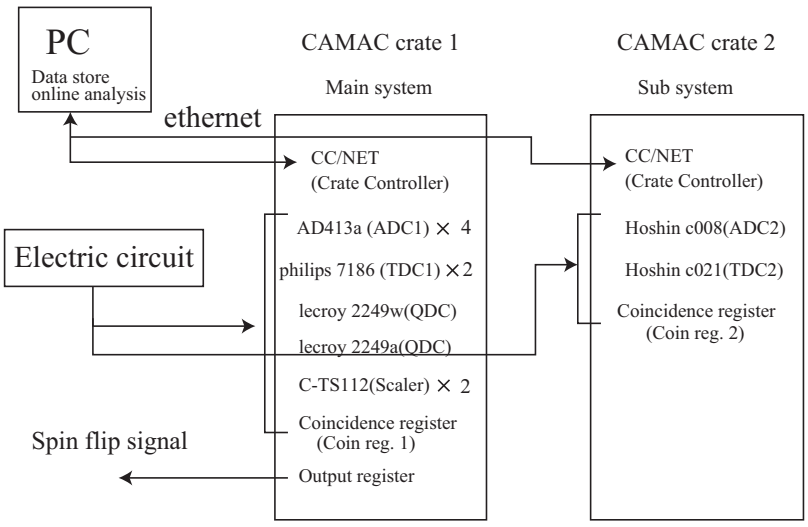

Figure 3.16: Diagram of the data acquisition system consists of two CAMAC systems.

the shaped signals were sent to ADCs. The dynamic range of Ge-detector energy was set to be from 40 keV to 6000 keV. For Ge-R and Ge-L, analog signals with the different gain were prepared and the dynamic ranges were set to be 18 MeV in order to cover all the β rays: $Q_\beta(^{31}\mathrm{Na}) = 15.38$ MeV [OUE13] and $Q_\beta(^{30}\mathrm{Na}) = 17.27$ MeV [BAS10]. The analog signals for the timing were formed by the timing filter amplifiers (TFA: ORTEC 474) with shorter time constant of 50 ns. The analog signals were converted to the digital signals by constant fraction discriminators (CFD: ORTEC 935), which minimize time deviations depend on the pulse height. The external delays of 30 ns (Ge-2, Ge-4, Ge-5, and Ge-6) or 40 ns (Ge-1, Ge-3, Ge-R, Ge-L) were applied to the CFDs. Their digital signals were sent to the TDC stop inputs.

Similarly, the plastic scintillators and neutron detectors were prepared for the energy and timing signal. For the plastic scintillators, the signals were amplified in order to get enough pulse height by amplifiers (Philips 778). The one of the outputs were sent to the QDCs. The leading edge discriminators converted the other analog signals from the amplifiers to the digital signal and thresholds were adjusted to cut the noise. The example of QDC spectrum is shown in Appendix D. For the neutron detectors, the signals from PMTs were directly delivered to the QDC. The timing signals were created by the leading edge discriminators, whose thresholds were set to be as low as possible to maximize the efficiency of neutron detectors , as mentioned in Sec. 3.4.3. In timing signals of the neutron detectors, the only signals from the up (down) PMT which were coincident with the down(up) PMT with in $\pm$ 20 ns were sent to TDCs, thus the noise from each PMT was reduced a lot.

The selectable triggers of [all plastic scintillators or all Ge detectors] (β or γ trigger) and

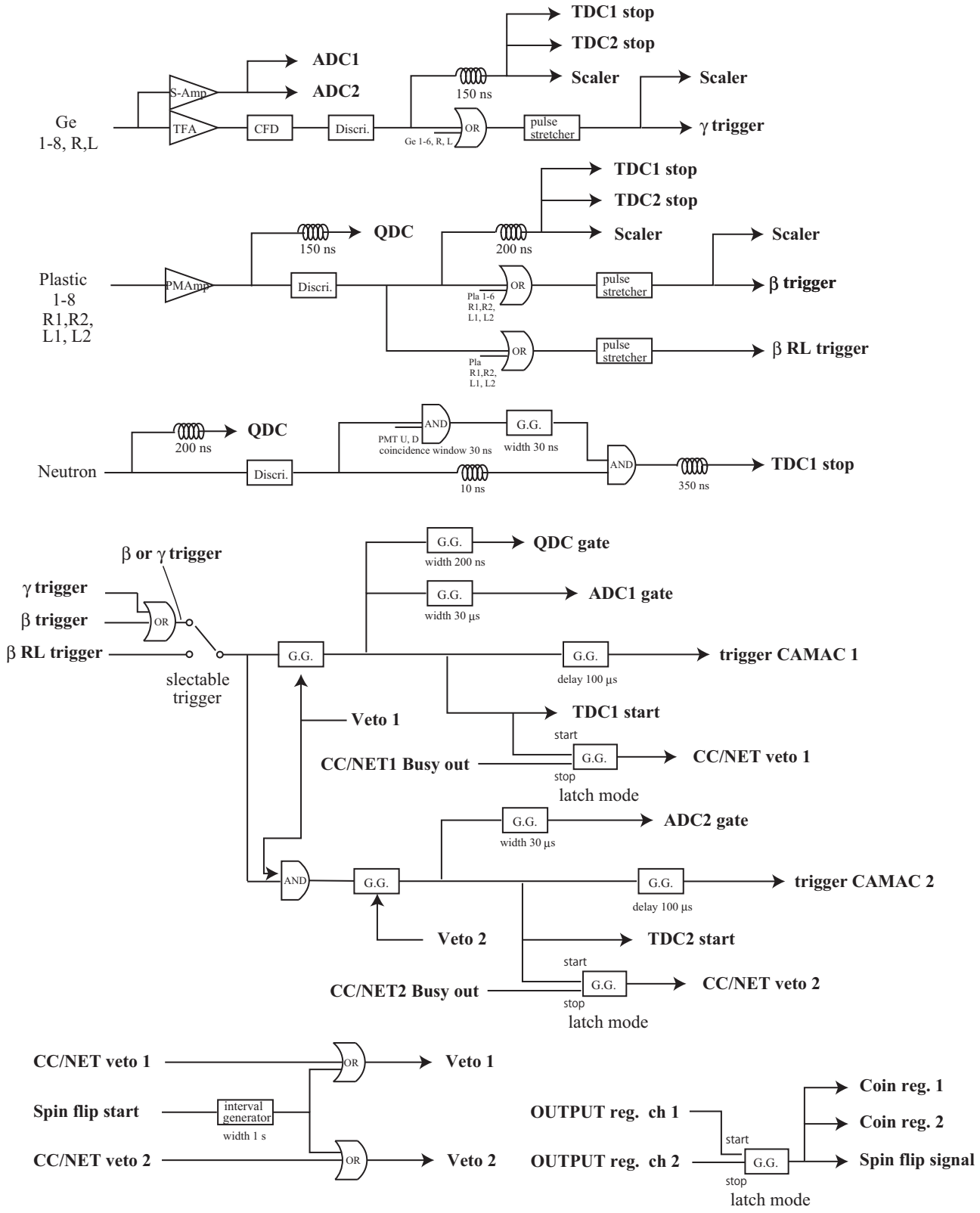

Figure 3.17: Diagram of the electronic circuits.

[the plastic scintillators located at R and L] (β RL trigger) were prepared. The β or γ trigger was used for the measurement of β-ray asymmetry. For the beam tuning, the β RL trigger was used.

3.5.3 Time sequence of the data taking

Figure 3.18 shows the time sequence of the data taking and the spin flip operations. The spin flip was controlled by the output register in the main CAMAC crate. The pulse was generated from channel 1 and 2 of the output register every 200 s, and the phase of the pulses are shifted 100 s, so that the polarization directions are switched for every 100 s. The spin flip was achieved by mechanically putting on and off the $\lambda/2$ plate on the pumping laser way. The data taking started 1 s after sending the spin-flip operation, because it takes a few hundreds ms to finish putting on or off the $\lambda/2$ plate.

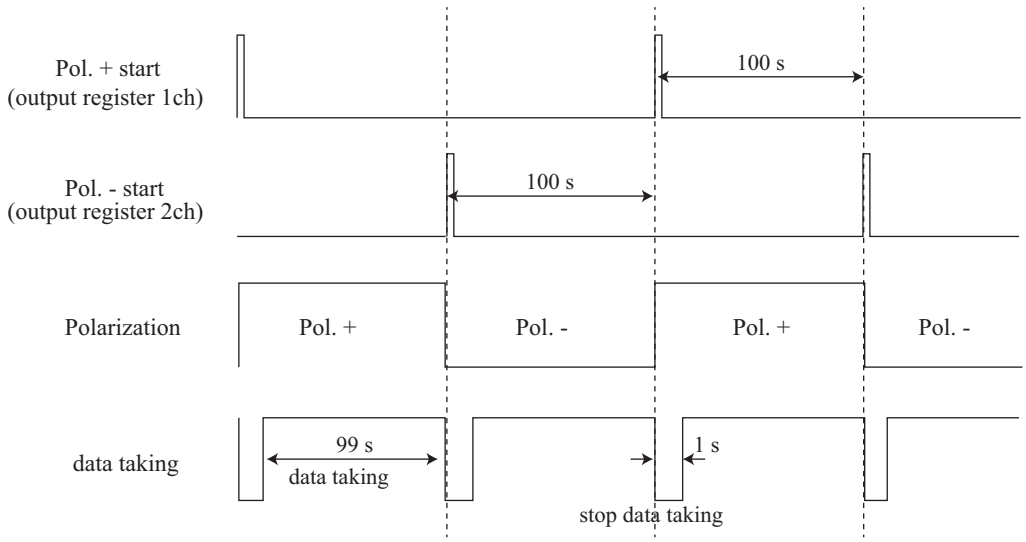

Figure 3.18: Time chart of spin flip and data taking.

CHAPTER IV

Data Analysis

4.1 Presorting

In order to analyze energy and timing information of the detectors accumulated by the ADCs and TDCs in the CAMAC systems, presorting of the event data is required at first. As a presorting, the energy calibration (Sec. 4.1.1) and gain-shift correction of the energy (Sec. 4.1.2) were performed, and slew correction (Sec. 4.1.3) was carried out for the timing information.

4.1.1 Energy Calibration of Ge detectors

All the Ge detectors' energy data accumulated by CAMAC ADC were calibrated by using the standard sources of ^{152}Eu and ^{56}Co. The ^{152}Eu source was used for energy calibration of γ-ray detectors because of emitted γ rays with various energies (100 - 1500 keV). However, some of energies of reported and expected γ-rays emitted from ^{30}Mg and ^{31}Mg were more than 3000 keV. To reduce the error of energy calibration for high-energy γ rays, the ^{56}Co source, which emits γ-rays with higher energies ($\sim$ 3500 keV), was used. The energy calibration for Ge detectors was performed as follows.

(1) The γ-rays peaks from the calibration sources were fitted by RADWARE package software [RAD11] to obtain the accurate peak positions.

(2) The least-square fitting was performed in the plot of the peak position (ch) vs. γ-ray energy with linear expression as

$$E = p0 + p1 \times ch. \tag{4.1}$$

Table 4.1: Energy resolutions of each Ge detector for the 2235 keV γ ray before and after the gain shift correction.

Ge ID	energy resolution for the 2235 keV γ ray (keV)	
	before correction	after correction
Ge-1 (HANDAI45%)	3.2	3.2
Ge-2 (CINDY)	2.6	2.5
Ge-3 (HANDAI50%)	3.0	2.8
Ge-4 (CAROL)	3.1	3.0
Ge-5 (ALICE)	2.7	2.5
Ge-6 (PETER)	3.1	2.9
Ge-R (HANDAI60%A)	3.4	3.3
Ge-L (HANDAI60%B)	3.3	3.3

The fitting area was divide into two regions for high ($E > 1000$ keV) and low energy ($E < 1000$ keV) to reduce the error of energy calibration.

Examples (Ge-L) of difference between γ-ray energy from the Table of Isotopes ($E_{\rm ref}$) [TOI96] and from fitting functions ($E_{\rm fit}$) using one line and two lines are shown in Fig. 4.1 (a) and (b), respectively. Non-linearity is observed around 1000 keV and the difference between $E_{\rm ref}$ and $E_{\rm fit}$ was more than 1 keV for $E > 3000$ keV , as shown in Fig. 4.1 (a). On the other hand, two line fitting shows much better results than one line fitting as in Fig. 4.1 (b); energy difference within 0.2 keV for wide energy range from 100 keV to 3000 keV The other Ge detectors except for Ge-R(handai 60%A) show similar trend. The non-linearity was much more in Ge-R at low energy region around 50-100 keV, therefore three line fitting was performed for the calibraition of Ge-R. These non-linearity of energy calibration possibly comes from the non-linear amplification of the pre-amplifier and/or the shaping amplifier.

4.1.2 Gain shift correction

As the next step of the data analysis, gain shift correction for Ge detectors was performed. Ge detectors are very sensitive to fluctuation of the gains of the pre-amplifier or the shaping amplifier because of its good energy resolution (typically less than 0.3% for 1.3MeV). Continuous and non-continuous gain shifts are often caused by the consenescence of internal electric circuits in the modules and by the change of the temperature. As the results, energy

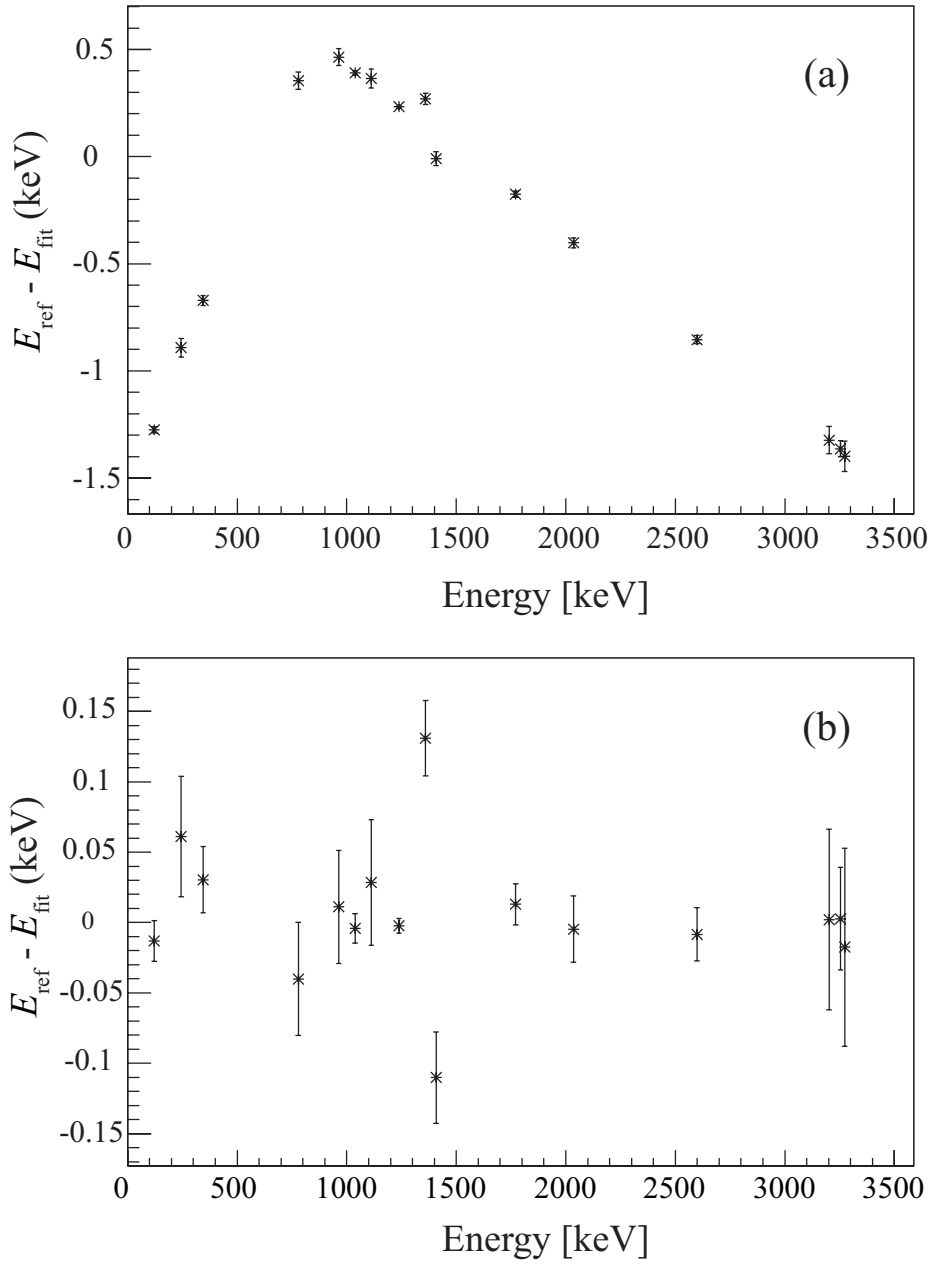

Figure 4.1: Energy difference between E_{ref} and E_{fit} fitted with one line (a) and two lines (b).

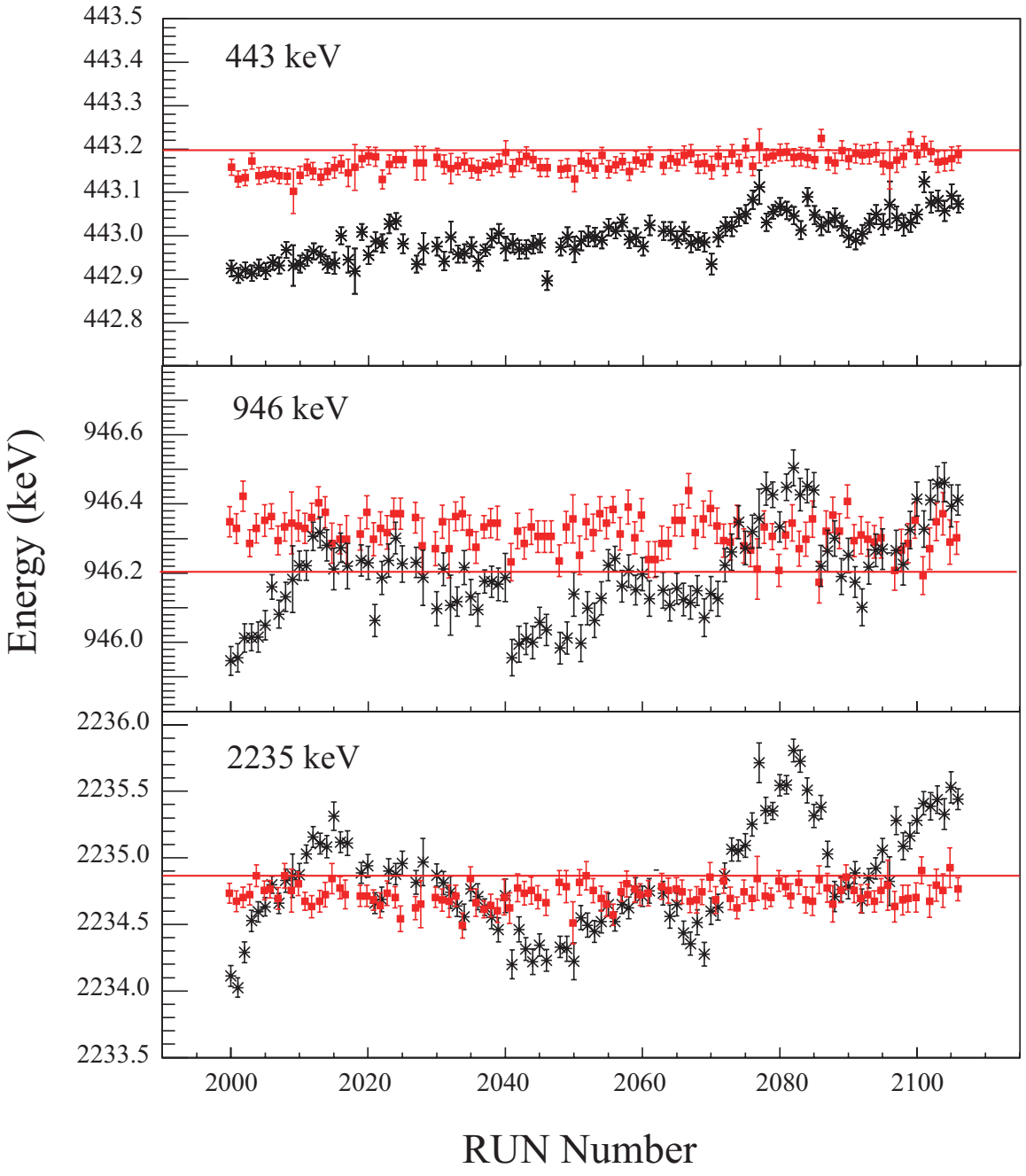

Figure 4.2: Peak positions of the 443-, 946-, and 2235-keV γ rays before and after gain shift correction, indicated by astarisks in black and closed squares in red, respectively. The solid lines are the reference energies for these γ rays.

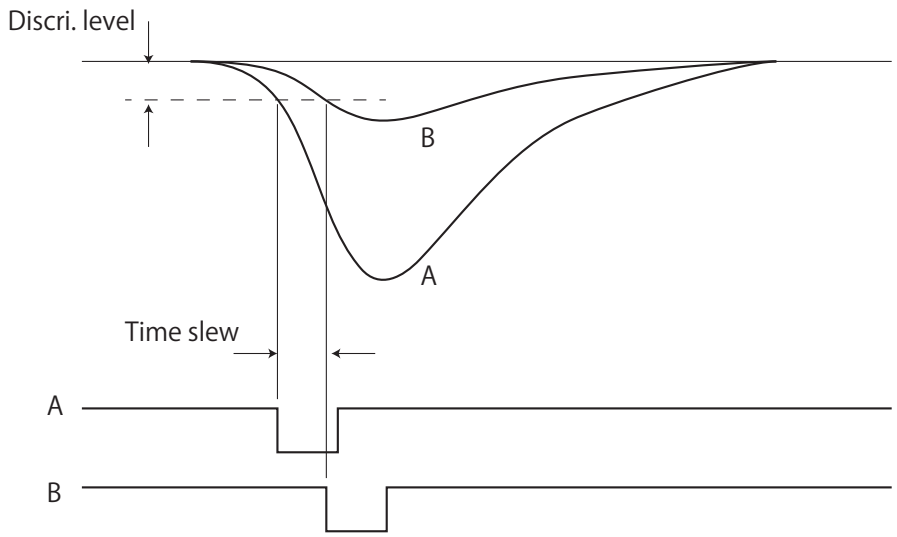

Figure 4.3: Principle of the time slewing. Assuming two pulses with different pulse height as identified by A and B, their outputs are shown on the down-side.

resolutions of γ-ray energies go worse, and sometimes ghost peaks appear. Therefore, gain shift correction was indispensable.

The calibration parameters of ADC channel was corrected for each RUN (typical data accumulation time: 1 hour for one RUN data) by using well-known intense γ-ray peaks from the β decay of the daughter and ground-daughter nuclei: 443 keV (^{30}Mg $\rightarrow$ ^{30}Al) [BAS10], 946 keV (^{31}Mg $\rightarrow$ ^{31}Al) [OUE13], and 2235 keV (^{30}Al $\rightarrow$ ^{30}Si) [BAS10].

For example, Fig. 4.2 (a) and (b) show peak position for Ge detector (Ge-3; handai 50%) for 443-, 946-, and 2235-keV γ-rays before and after the gain shift correction, respectively. In Fig. 4.2 (a), it is clearly found that the peak positions deviate from the reference values , which are indicated in red line, as a function of RUN number. The referece values of 443.2 keV, 946.2 keV, and 2234.8 keV are determined by using the nearest six RUNs 2035-2040 from the energy calibration RUN 2034. As the results of the gain shift correction, the deviation of the peak positions is much less, shown in Fig. 4.2 (b). The energy resolutions in sum of all the RUN data also became better, and the improvements of energy resolutions for each Ge detector are listed in Table. 4.1.

4.1.3 Slew Correction

Time information of γ rays as well as energy information is one of the most important data to reveal the detailed level structure. The most important factor in measurement of timing is the time resolution. The better time resolution enables a more accurate measurement of

life time of the excited states.

The time information, which was accumulated by using electronic modules such as discriminators, time to digital convertor, and so on, shows correlation with its energy. It is so-called "time slewing". Sometimes, such correlation causes bad time resolution or makes analysis of life time measurement more complicated. Fig. 4.3 graphically demonstrates the principles of the time slewing in case of leading edge discrimination. Two pulses shown are completely coincident, whereas the logic output signals are not identical, and the signal with lower amplitude is delayed. In order to reduce the effect of the time slewing, constant fraction discriminators were used for Ge detectors' timing in our experiment. However, our timing system was not completely free from the time slewing.

The two-dimensional plot of [energy detected by the Ge detector (Ge-3; ALICE)] vs. [time difference between plastic scintillator and the Ge detector (Ge-3; ALICE)] is presented in Fig. 4.4 (a). It is found that the prompt position curves as a function of energy and this effect is more serious at lower energy. In order to correct this, the chi-square fitting was performed in [energy detected by the Ge detector] ($E_{\rm Ge}$) vs. [prompt position in a time difference spectrum between plastic scintillator and Ge detector] ($T_{\rm Pla-Ge}$) plot by following functions;

$$T_{Pla-Ge} = \begin{cases} p_0 + p_1/E + p_2/E^2 & (E \leq E_{\rm c}) \\ \\ p_3 + p_4/E + p_5/E^2 & (E > E_{\rm c}) \end{cases} \tag{4.2}$$

The p_{0-5} and $E_{\rm c}$ are parameters for fitting. The p_{0-5} are limited to satisfy the smoothly connection of two functions at $E_{\rm c}$ as follows;

$$\begin{aligned} p_0 + \frac{p_1}{E_c} + \frac{p_2}{E_c^2} &= p_3 + \frac{p_4}{E_c} + \frac{p_5}{E_c^2} \\ \frac{d}{dE}(p_0 + \frac{p_1}{E} + \frac{p_2}{E^2})|_{E=E_c} &= \frac{d}{dE}(p_3 + \frac{p_4}{E} + \frac{p_5}{E^2})|_{E=E_c} \end{aligned} \tag{4.3}$$

The time slewing was canceled out by subtracting a shift of timing on the event-by-event analysis. Fig. 4.4 (b) shows the two-dimensional plot of $E_{\rm Ge}$ vs. $T_{\rm Pla-Ge}$ with slew correction.

4.2 Efficiency of γ rays

The determination of γ-ray efficiency was necessary to determine the intensities of the γ rays. The γ-ray intensity is also one of the key quantities to study the level structures. The γ-ray absolute efficiency was deduced by using the standard sources of ^{152}Eu, ^{60}Co ^{56}Co, and

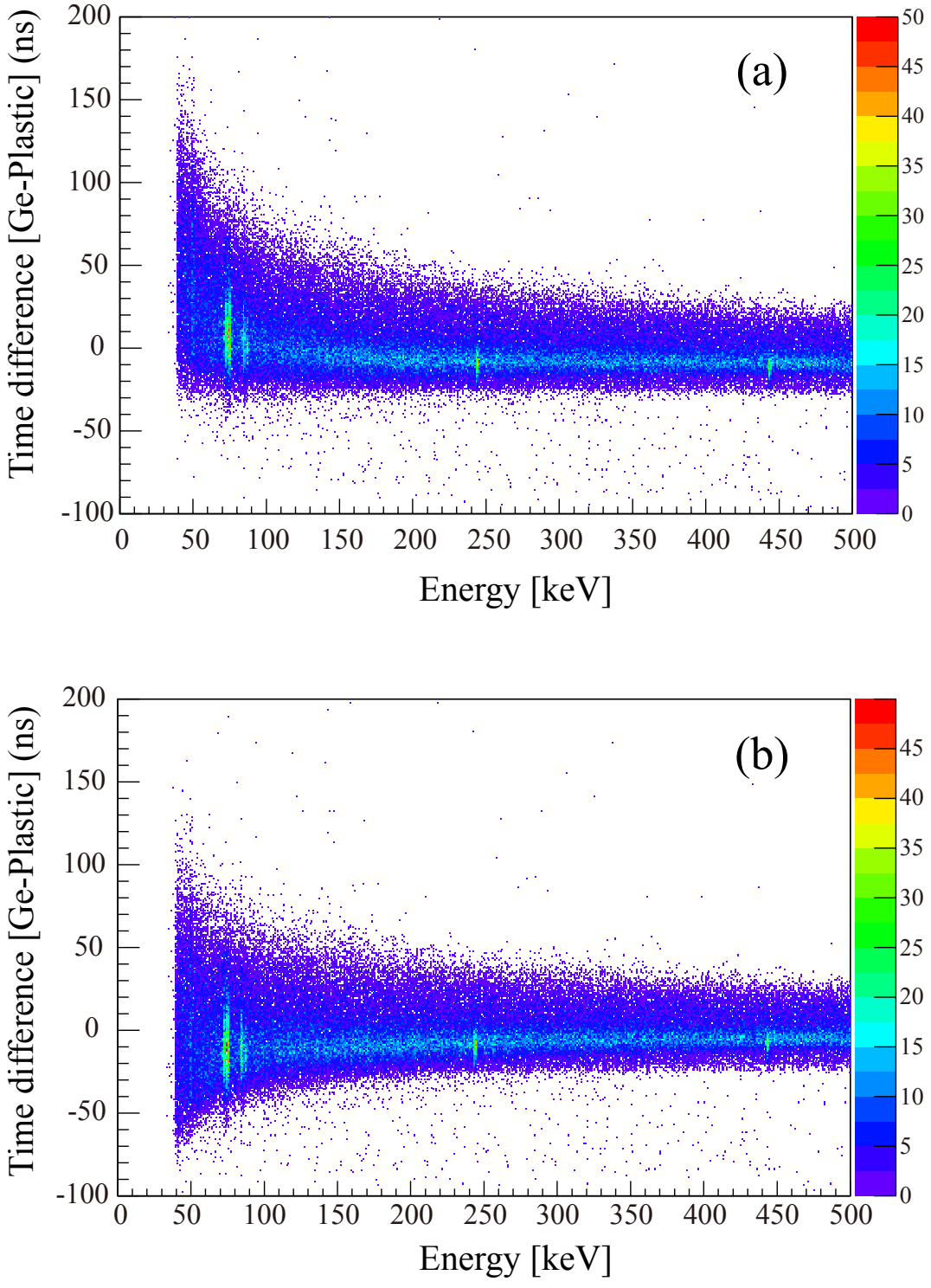

Figure 4.4: Two dimensional histograms of [energy of Ge detectors] vs. [timing of Ge detectors] with (a) and without (b) the slew correction.

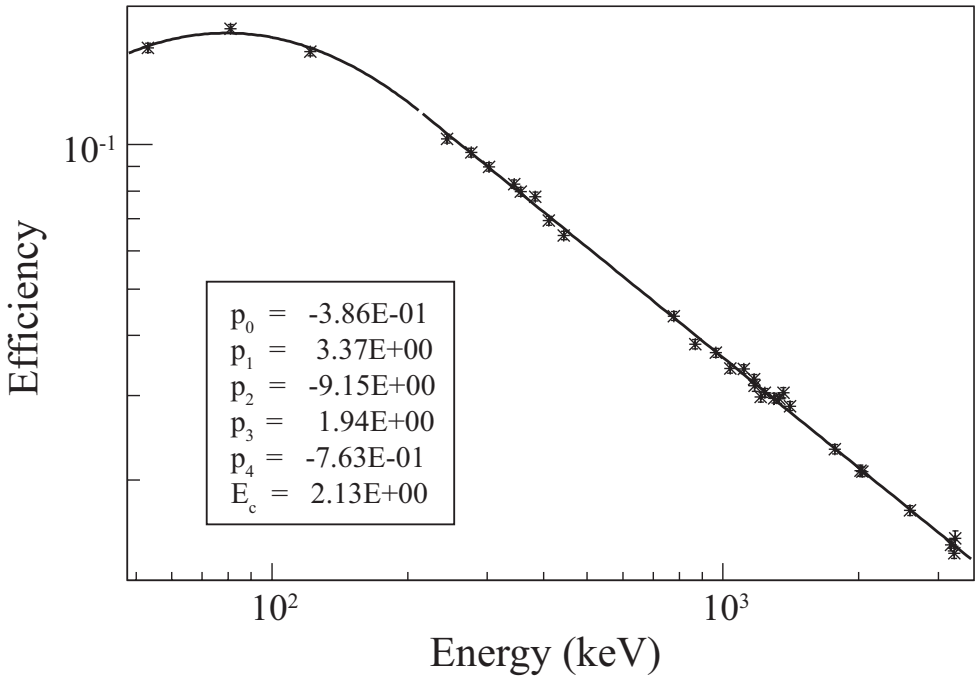

Figure 4.5: Total absolute efficiency of Ge detectors. The solid line indicates the fitting result, and the parameters are given in the inset.

^{133}Ba. The total efficiency summed up those of the all eight Ge detectors is shown in Fig. 4.5. It shows a linear function at $E \geq 200$ keV in the logarithmic scale. The efficiency at ≤ 200 keV is lower than what is expected from the extrapolation from that at ≥ 200 keV because of the absorption by the dead layer of Ge detectors, the Al windows at the entrance of the detectors, etc. Therefore, the efficiency ε_γ was fitted as the following function divided into two energy regions.

$$log(\varepsilon_\gamma) = \begin{cases} p_0 + p_1 \times log(E) + p_2 \times log(E)^2 & (E \leq Ec) \\ \\ p_3 + p_4 \times log(E) & (E \geq Ec) \end{cases} \tag{4.4}$$

The parameters p_{0-4} and $E_{\rm c}$ were determined to minimize the chi square. The parameters p_{0-4} are also given with a limit to the smoothly connection of two equations at $E = E_{\rm c}$. In our γ-rays detection system, highly efficiencies for widely energy region (16% at $E = 0.05$ MeV, 2.9% at $E = 1.3$ MeV, and 1.5% at $E = 3.0$ MeV) were archived.

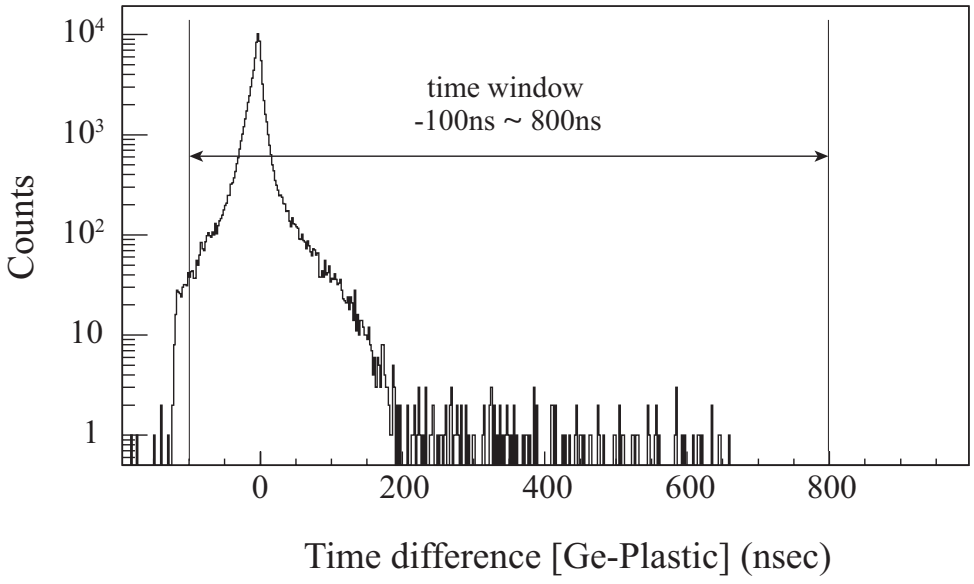

Figure 4.6: Time difference spectrum between the Ge detector and the plastic scintillator. The horizontal lines indicates the range of the coincidence window.

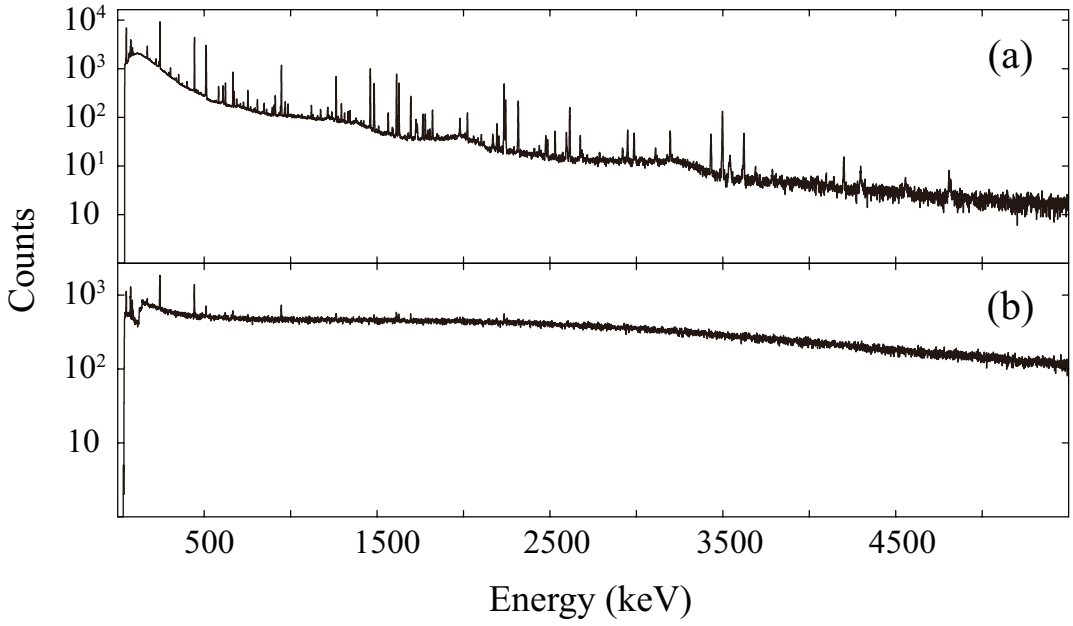

Figure 4.7: The energy spectra of the Ge detectors anti-gated (a) and gated (b) by the plastic scintillator.

4.3 Analysis of γ ray

4.3.1 Distinction between γ rays and β rays

The γ rays and β rays were measured by eight telescopes consisting of the Ge detectors and one or two (for Ge-R and Ge-L) thin plastic scintillators placed in front of them. The telescopes enable us low-background and high-S/N β-ray detection. The energies are measured by the Ge detectors which have much better energy resolution than the plastic scintillators, and the plastic scintillators were used in order to distinguish between γ rays and β rays and measure the timing because of their good time resolution.

In the analysis, a detected particle by the Ge detector in a time window of -100−800 ns with respect to the plastic scintillator was concluded to be a β ray. In case only the Ge detectors are hit in the time window, this is analyzed as a γ ray. Fig. 4.6 shows the time difference spectrum and its time gate condition. The chance coincidence events could be reduced by the time gate. The coincidence window of $\pm$800 ns was set in order to cover all γ rays associated with levels which have long half-lives with $\sim \mu s$. The energy spectra of the Ge detectors with different gate conditions for γ ray and β rays are shown in Fig. 4.7 (a) and (b), respectively. It is clearly seen that the γ peaks observed in the Fig. 4.7 (a) disappear and/or are suppressed a lot in the Fig. 4.7 (b). The continuum β-ray spectrum is seen in Fig. 4.7 (b), whereas γ rays and β rays could not be completely separated. Some of γ peaks remains in Fig. 4.7 (b). It is difficult to eliminate this events caused by the difference between the solid angles of the plastic scintillator and the Ge crystal. However, they did not cause any significant effect to the analysis because the ratio of these events are estimated to be less than 5% of the entire β hit events.

4.3.2 γ-γ coincidence analysis

The γ-γ coincidence analysis is a very effective tool to construct the level scheme. For this analysis, the matrix which consists of the two dimensional 5500 $\times$ 5500 histogram was made in this work as follows. Assuming that the two γ rays with energies of $E_{\gamma a}$ and $E_{\gamma b}$ are detected in the coincidence time window, the histogram is filled in the bins of ($E_{\gamma a}$, $E_{\gamma a}$) and ($E_{\gamma b}$, $E_{\gamma a}$). In case that three γ rays are hit in the time window, the histogram is filled by the six combinations of events. The coincidence time windows was $\pm$ 800 ns to cover all γ rays associated with isomers, as shown in Fig. 4.8. The chance coincidence events, which appear as a flat component in the time spectrum, are much less than the prompt component in Fig. 4.8. Therefore it enables a high-S/N γ-ray coincidence measurement. The coincidence data

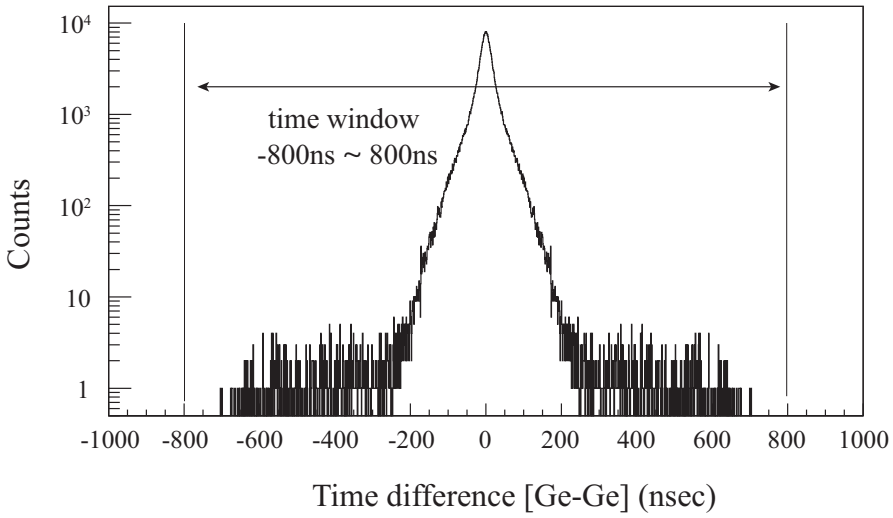

Figure 4.8: Time difference spectrum between the γ rays. The horizontal lines indicates the range of the coincidence window.

was analyzed by RADWARE package software [RAD11].

Figure 4.9 schematically shows the essence of the γ-γ analysis using the two-dimensional matrix of [the energy of the γ] vs. [energy of the γ], which is called (E_γ-E_γ matrix). The example of a level scheme with four of the γ transitions is displayed on the right-hand of Fig. 4.9. Since the γ rays of γ_1, the γ_2, and γ_3 have the cascade relation with each other and the γ_4 which parallels the γ_1 and the γ_2, a lot of events should be observed as shown the closed circles in the matrix on the center in Fig. 4.9. The spectrum gating on the peak of γ_2 is displayed on the left-hand in the figure. The peaks of the cascade γ rays of γ_1 and γ_3 should be emphasized in the gate spectrum, and the γ_4 peak is not in the spectrum. The level scheme will be constructed by using the coincidence relation of each γ ray from the gate spectrum as well as the intensity balance.

When the gate spectrum is created, the subtraction of background from Compton-scattered γ-ray, and natural radiation is needed, otherwise the γ-ray coincidence relation may be misassigned. The background subtraction was performed as following steps in this analysis. Firstly, the background spectrum was made from the spectrum gated by the continuum background region beside the objective peak. The background spectrum normalized by the gate width was subtracted from the spectrum gating on the peak position. This background subtraction method can be applied to not only the analysis of the E_γ - E_γ matrix but also the E_γ - T_γ matrix analysis which was used for the measurement of half-lives of isomers.

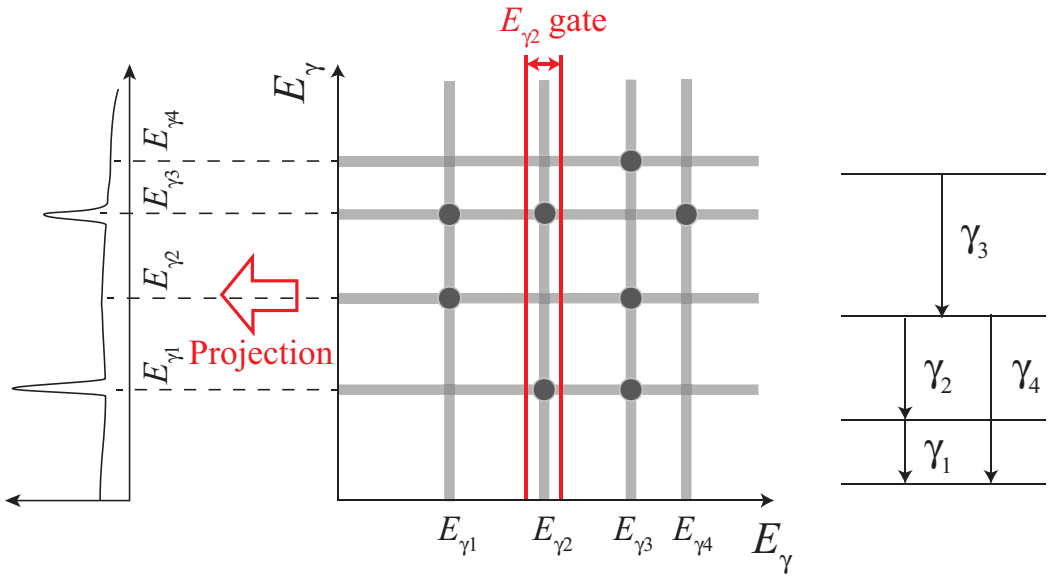

Figure 4.9: Schematic two dimensional matrix of (the energy of the γ rays) vs. (the energy of the γ rays), assuming an illustrative level scheme on the right-hand, and the projection spectrum gated by the peak of γ_2.

CHAPTER V

Results -^{31}Mg-

5.1 Gamma rays in ^{31}Mg

The total projection spectrum of γ-γ coincidence data for ^{31}Na beam in a time window of $\pm$ 800 ns is shown in Fig. 5.1. The most of observed peaks are due to known γ rays from the β decay of ^{31}Na (asterisks) [KLO93; GUI84], ^{31}Mg (closed squares) [MAR05], ^{31}Al (closed triangles) [DET79], ^{30}Mg (open squares) [HIN08], and ^{30}Al (open triangles) [ALB74] and the β-delayed neutron decay of ^{31}Na (crosses) [KLO93] in Fig. 5.1. In the γ-γ coincidence spectrum, γ rays from natural radiation are suppressed, and γ rays which has cascade relation with other γ rays are emphasized. Fig. 5.2 shows a γ-ray spectrum gated by the β rays with higher than 8 MeV in order to reject γ rays from the beta decay with low Q value. The Q value of ^{31}Na (Q_β = 15.4 MeV [OUE13]) is highest in the decay chain, and the nucleus which has the second highest Q value with Q_β = 11.8 MeV [OUE13] is ^{31}Mg. Since the other nuclei have lower than 8-MeV Q values, all of the γ rays except for those from the β decays of ^{31}Na and ^{31}Mg are completely eliminated and the γ rays from ^{31}Mg are suppressed a lot in the spectrum Fig. 5.2. The γ-ray peaks of 50, 171, 221, 452, 623, 673, 808, 894, 1215, 2023, 2194, 2244 keV previously reported in Refs. [KLO93] and [GUI84] are clearly observed in Fig. 5.2. Some of weak peaks which have not been assigned are also found, and these unknown peaks are candidates for unobserved transitions from the known levels or unknown levels in ^{31}Mg.

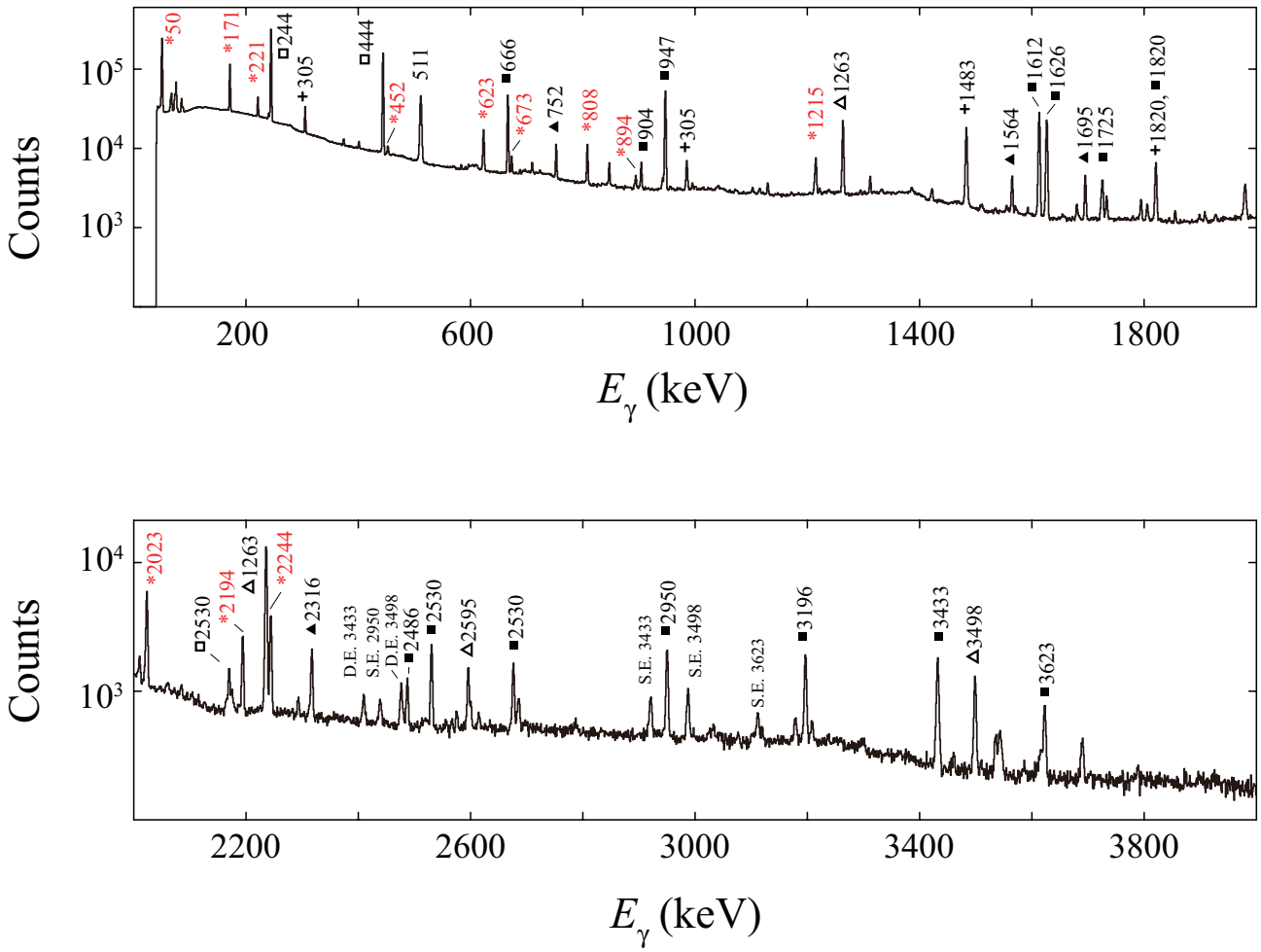

Figure 5.1: Total γ-γ projection spectrum in a time window of $\pm$ 800 ns for ^{31}Mg. The γ-ray peaks labeled with asterisks, crosses, closed square, closed triangles, open square and open triangles are originated from the γ rays in ^{31}Mg, ^{30}Mg, ^{31}Al, ^{31}Si, ^{30}Al, and ^{30}Si, respectively. The numbers are the γ-ray energies in keV. The γ-ray peaks originated from single or double escape of 511-keV γ rays from the pair creation were labeled as S.E. and D.E., respectively.

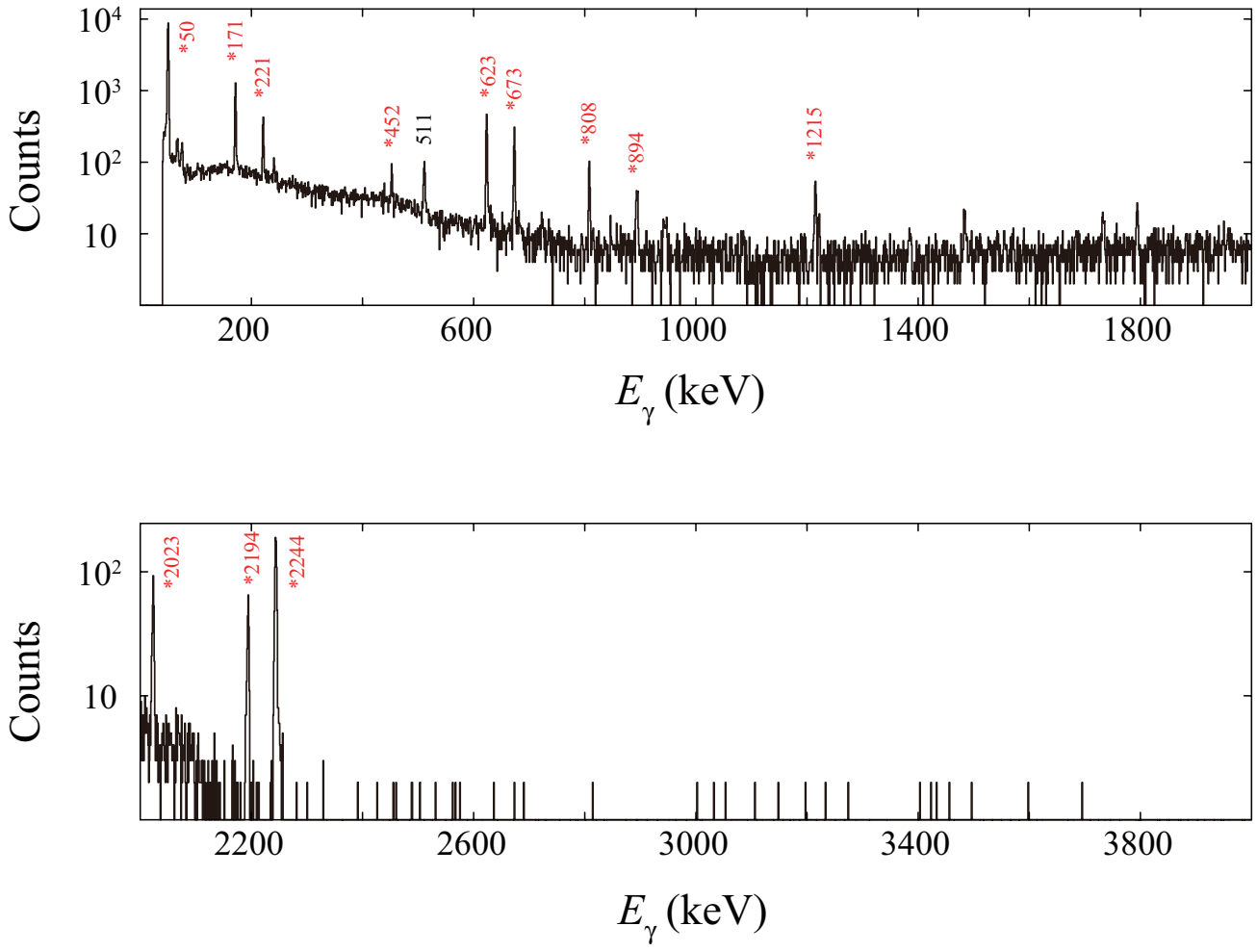

Figure 5.2: Beta-γ coincidence spectrum for ^{31}Mg gated by the β rays with higher than 8 MeV. The peaks labeled with asterisks are known γ rays in ^{31}Mg [KLO93; GUI84]. The energies are indicated in keV.

5.2 Confirmation of previous decay scheme of ^{31}Na $\rightarrow$ ^{31}Mg

The previously reported γ rays of 50, 171, 221, 452, 623, 673, 808, 894, 1215, 2023, 2194, and 2244 keV in ^{31}Mg [KLO93] were confirmed in the γ-γ projection spectrum in Fig. 5.1 and also in the β-γ coincidence spectrum in Fig. 5.2. Firstly, coincidence relations of these γ rays and reported excited levels were confirmed in the coincidence spectra by the analysis using the E_γ-E_γ matrix.

5.2.1 0.050-, 0.221-, and 0.673-MeV levels

The levels at 0.050 MeV and 0.221 MeV were well established by the β decay of ^{31}Na [KLO93] [GUI84], the β-delayed neutron (β-n) decay of ^{32}Na [KLO93; GUI84], and the β-delayed two neutron (β-2n) decay of ^{33}Na [MAT07], the one-neutron-removal reaction from ^{32}Mg [TER08], the one-proton-removal reaction from ^{32}Al [MIL09], and coulomb excitation [SEI11]. The 0.673-MeV level was reported by the β decay, one-neutron-removal reaction from ^{32}Mg [TER08], the one-proton-removal reaction from ^{32}Al [MIL09], and coulomb excitation. The γ transitions de-populating these levels and the placements of these transitions in the level scheme are consistent with each level scheme reported in the previous works.

Firstly, the γ-ray coincidence spectra gated by the peaks of 50-, 171-, 221-, 452-, and 623-keV γ rays were made in order to confirm the coincidence relations between the γ transitions in ^{31}Mg, as shown in Fig. 5.3. The cascade relation between 50 keV and 171 keV is confirmed and the 221-keV γ ray is not coincident with the 50-keV and 171 -keV γ rays in the Fig. 5.3. The cascade relations and energy consistency between the γ-ray energy of 220.8(1) keV and energy sum of 49.9(1) + 170.9(1) = 220.8(1) keV support the existence of the 0.050-MeV level depopulated by the 50-keV γ ray and the 0.221-MeV level depopulated by 171- and 221-keV γ rays, as shown in Fig. 5.4.

Similarly, the cascade relations of the 452-keV γ ray with the 50-, 171-, and 221-keV γ rays were confirmed in the energy spectrum gated by the 452-keV peak, and the coincidence relation between 623- and 50-keV γ rays was observed in the Fig. 5.4. The energy consistency between the γ-ray energy of 673.1(1) keV, 673.2(2) [452.4(2) + 220.8(1)] keV, and 673.0(1) [623.1(1) + 49.9(1)] keV also supports the existence of the 0.673-MeV level.

5.2.2 0.944-, 1.029-, and 2.244-MeV levels

The 0.944-MeV level was proposed by the β decay [KLO93], the β-n decay from ^{32}Na [KLO93; MAC05], one-neutron-removal reaction from ^{32}Mg [TER08], one-proton-removal

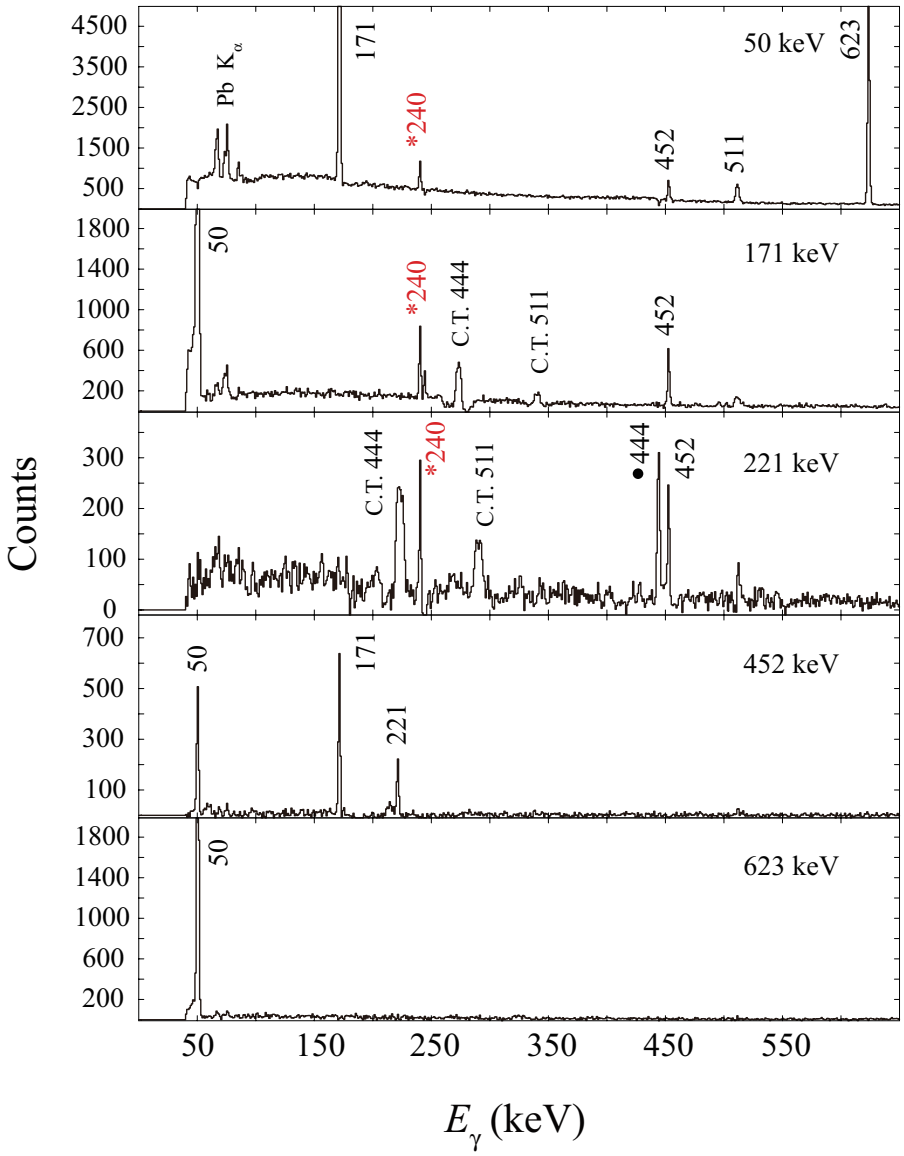

Figure 5.3: γ-γ coincidence spectra gating on the 50-, 171-, 221-, 452-, and 623-keV γ rays. The energy labels are shown in keV. The cross-talk peaks are indicated as C.T. and the original γ-ray energy. The γ-ray peak labeled with a closed circle is a contaminant originated from the β decay of ^{30}Mg. The γ rays with asterisks were newly proposed in this work.

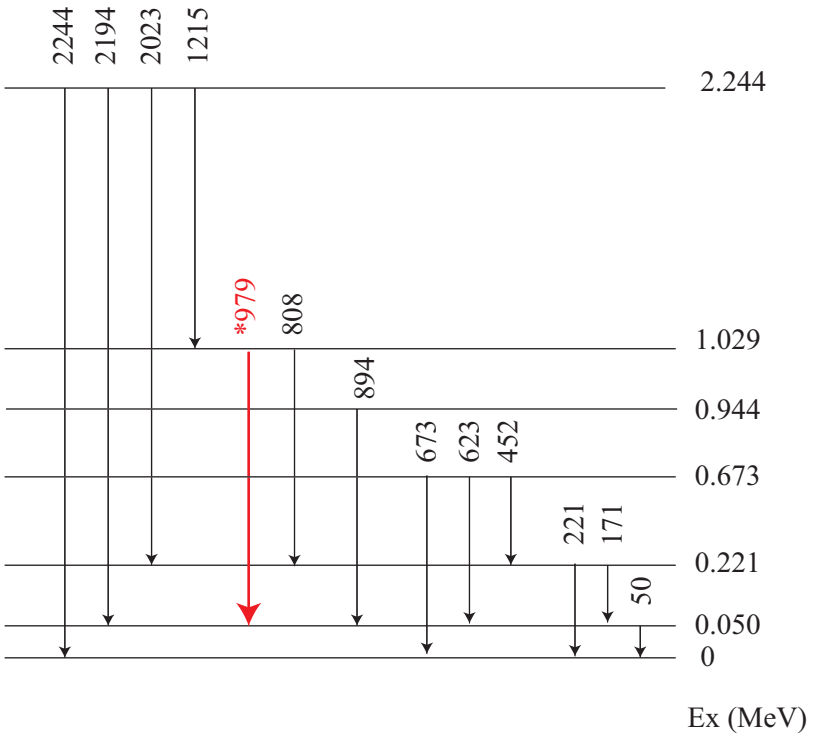

Figure 5.4: Partial level scheme of ^{31}Mg. The transition with an asterisk is newly proposed in this work.

reaction from ^{32}Al [MIL09], and coulomb excitation [SEI11]. The 1.029-MeV level was reported only by the β decay [KLO93; GUI84]. The 2.244-MeV level was largely populated by the the β decay [KLO93; GUI84] and weakly populated by one-neutron-removal reaction from ^{32}Mg [TER08].

The γ rays of 2023, 2194, and 2244 keV were reported as γ rays depopulating the 2.244-MeV level [KLO93; GUI84]. These γ rays were observed in the γ-γ and β-γ projection spectra in Fig. 5.1 and Fig. 5.2, respectively. The 2023- and 2194-keV γ ray peaks were observed in the γ-γ coincidence spectra, as shown in Fig. 5.5. Therefore, the 2.244-MeV level was confirmed based on the coincidence relation and energy consistency between the γ-ray energy of 2243.6(1) keV, 2243.5(1) [2193.6(1) + 49.9(1)] keV, and 2243.6(1) [2022.8(1) + 220.8(1)] keV. The partial level scheme of ^{31}Mg is shown in Fig. 5.4.

In the previous work, the 1.029-MeV level has been established only by the coincidence relation between the 808-keV and 1215-keV depopulating and populating the 1.029-MeV level, respectively [KLO93]. The reported relative intensities for 100 decays of ^{31}Na are 1.2(4) in Ref. [GUI84] and 1.6(3) in Ref. [KLO93] for the 1215-keV γ ray and 1.6(5) in Ref. [GUI84] and 1.5(3) in Ref. [KLO93] for the 808-keV γ ray. The reversed γ-ray placement as the transitions of 808 (2.244 MeV $\rightarrow$ 1.436 MeV) and 1215 (1.436 MeV $\rightarrow$ 0.221 MeV) keV

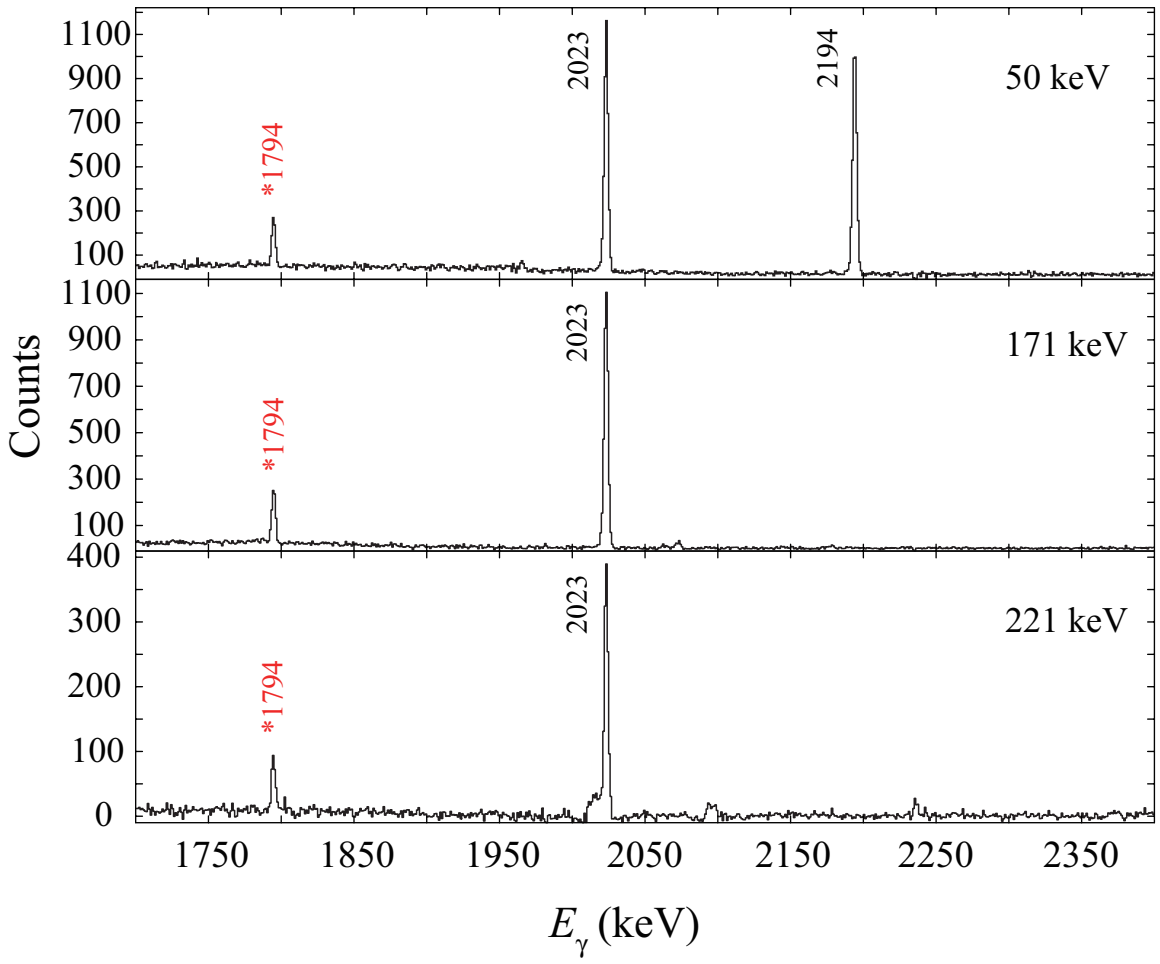

Figure 5.5: γ-γ coincidence spectra gating on the 50-, 171-, 221- γ rays. The γ rays with asterisks are newly observed in the β decay from ^{31}Na.

was also possible from the previous reported data, although previous works [KLO93; GUI84] placed a level at 1.029 MeV. In this work, the 808-keV peak was found in the coincidence spectra gated by the peaks of 50, 171, 221, and 1215 keV, and the 1215-keV peak was found in the spectra gated by the 50-, 171-, 221-, and 808-keV peak. The coincidence spectra gated by the 50-, 171-, 808-, and 1215-keV peaks are shown in Fig. 5.6. In addition to these γ-ray peaks, a weak 979-keV peak was newly found in the spectra gated by the 50-keV and 1215-keV γ rays in this work. The energy difference between the γ-rays of 978.6(3) and 807.8(1) keV was 170.8(3), this energy corresponds with the energy difference between the levels at 0.2208(1) and 0.0499(1) MeV within the error range. The 979-keV transition was most likely the transition (1.029 MeV $\rightarrow$ 0.050 MeV). Therefore, the 1.029-MeV level was confirmed by the energy consistency between the 1028.5(3) [978.6(3) + 49.9(1)] keV, 1028.6(1) [807.8(1) + 220.8(1)] keV, and 1028.5(1) [2243.5(1)- 1215.0(1)] keV and the coincidence relations.

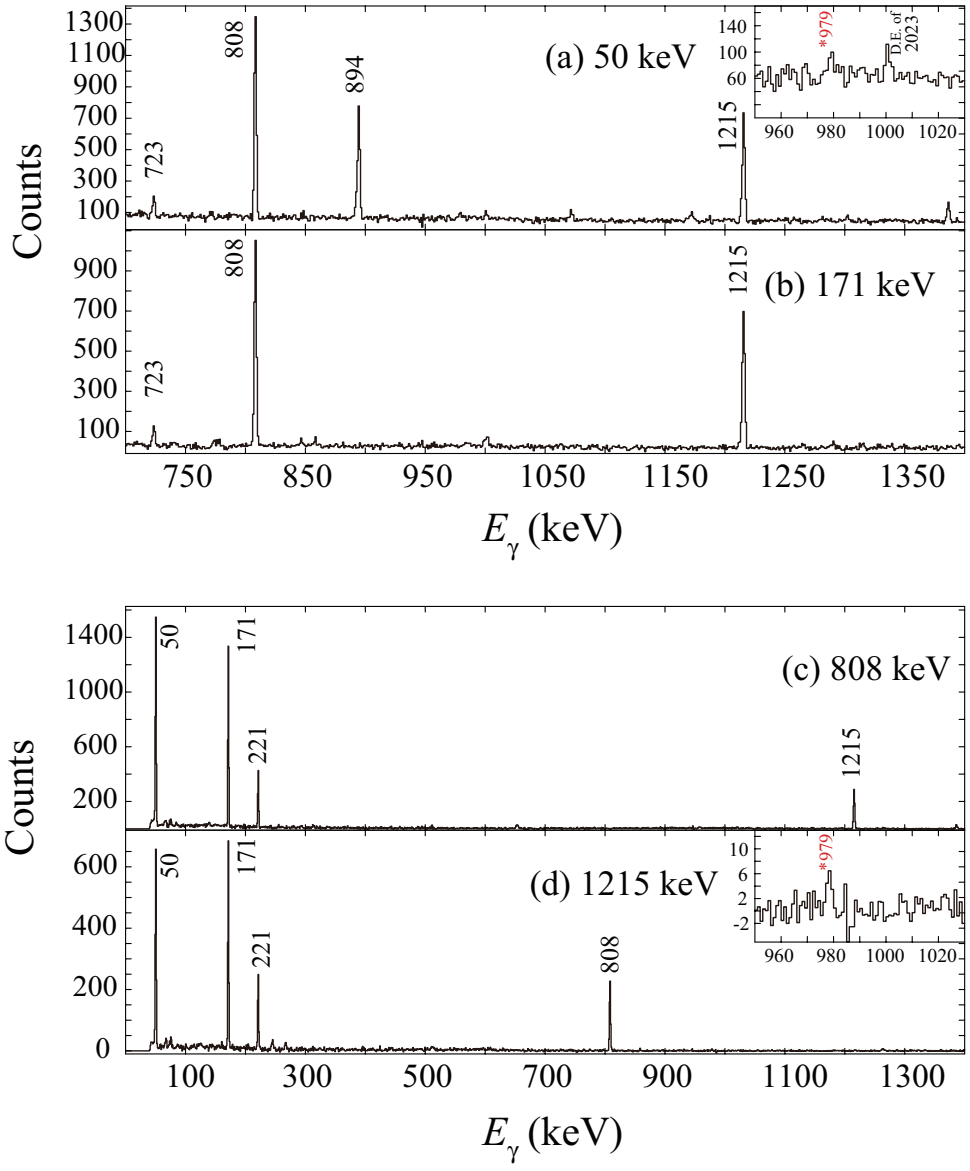

Figure 5.6: γ-γ coincidence spectra gating on the (a) 50-, (b) 171-, (c) 808- , and (d) 1215-keV γ rays. The enlarged spectra from 950 keV to 1030 keV are displayed in the insets in (a) and (d). The γ rays with asterisks are newly observed in the β decay from ^{31}Na. The peak at 1001 keV in the inset of (a) is the double escape peak the 2023-keV γ ray.

The 0.944-MeV level was well-established by various experimental studies [KLO93; MAC05; MIL09; SEI11]. In the previous β-decay experiment [KLO93], the 0.944-MeV level was reported as a level populated by the 894-keV γ ray. In one of previous works using the β decay of ^{31}Na [GUI84], the 894-keV γ ray was assigned to the different placement, and they proposed the 0.894-MeV level depopulated by the 894-keV γ ray. Figures 5.7 and 5.6 (a) show the γ-ray energy spectra gated by the 50- and 894-keV γ rays, respectively. It is clearly found that the 50-keV γ ray was coincident with the 894-keV γ ray in Fig. 5.7 and 5.6 (a). The γ ray of 723 keV was previously reported as a transition of (0.944 MeV $\rightarrow$ 0.221 MeV) in Ref. [SEI11]. The 723-keV γ-ray peak was observed in the γ-ray energy spectra gated by the 50-, and 171-keV γ rays, as shown in the Fig. 5.6 (a) and (b). This results strongly support the placement of the 0.944-MeV level unlike the placement in Ref. [GUI84].

5.2.3 3.760-MeV and 3.814-MeV levels

In Ref. [KLO93], γ rays of 3539, 3710, and 3760 keV depopulating the 3.760-MeV level, which is located above one neutron separation energy at 2.310 MeV [OUE13], were reported in the level scheme. The 3538-keV γ ray was also reported in Ref. [GUI84], although this transition was not placed in the level scheme. However, in the present work, the γ-ray peaks of 3539, 3710, and 3760 keV were not found in the γ-ray energy spectrum, as shown in Fig. 5.8. In the figure, the solid line shows the β-γ coincidence spectrum focused on the energy range around 3539, 3710, and 3760 keV, and the dashed line indicates the γ-ray counts expected from the γ-ray intensities in the level scheme of Ref. [KLO93]. It is concluded that these γ rays are not due to the β decay of ^{31}Na, thefore the 3760-MeV level was removed from the level scheme in the present work.

The 3.814-MeV level was reported as a level depopulated by the 1571-keV γ ray (3.814 MeV $\rightarrow$ 2.244 MeV) in Ref. [KLO93]. This level was also located above the neutron separation energy of 2.310 MeV. In this work, the 1571-keV γ-ray peak was found in the coincidence spectra gated by the 50-, 623-, and 673-keV, as shown in Fig. 5.9 (a). Also, the 50-, 623-, and 673-keV peaks were found in the 1571-keV gate spectrum in Fig. 5.9 (b). However, there are no coincidence peaks in the 2244 keV gate spectrum, as shown in Fig. 5.10. The fluctuation of counts due to background γ rays around 1500 - 1600 keV in the spectrum gated by 2244 keV is approximately $\pm$ 2 counts/channel, therefore a limit of observable peak counts is about 20 counts, which corresponds to a branching ratio of 0.06% for the 3.814-MeV level. Therefore, the different placement of 1571-keV γ ray from that in Ref. [KLO93] was proposed in this work. The 1571-keV γ ray was assigned as a transition

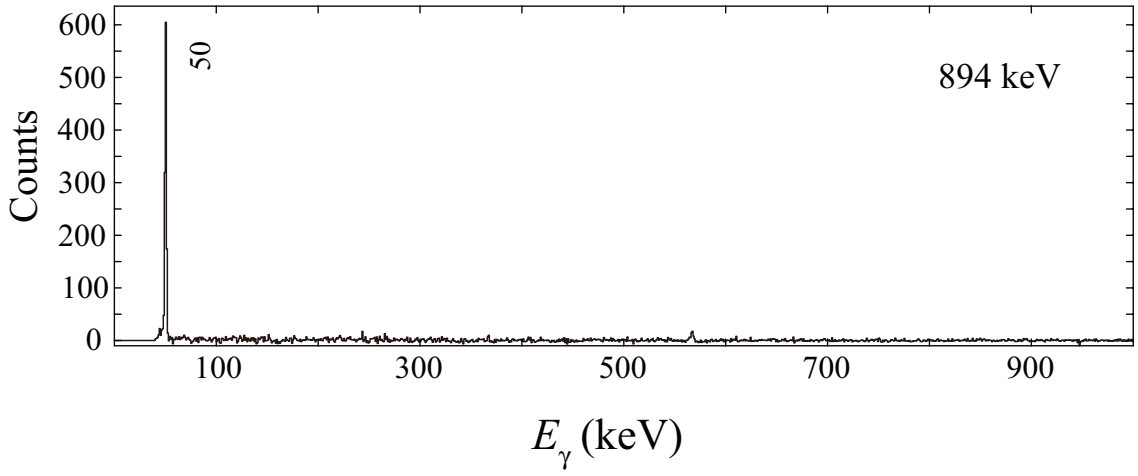

Figure 5.7: γ-γ coincidence spectra gated by the 894-keV γ ray.

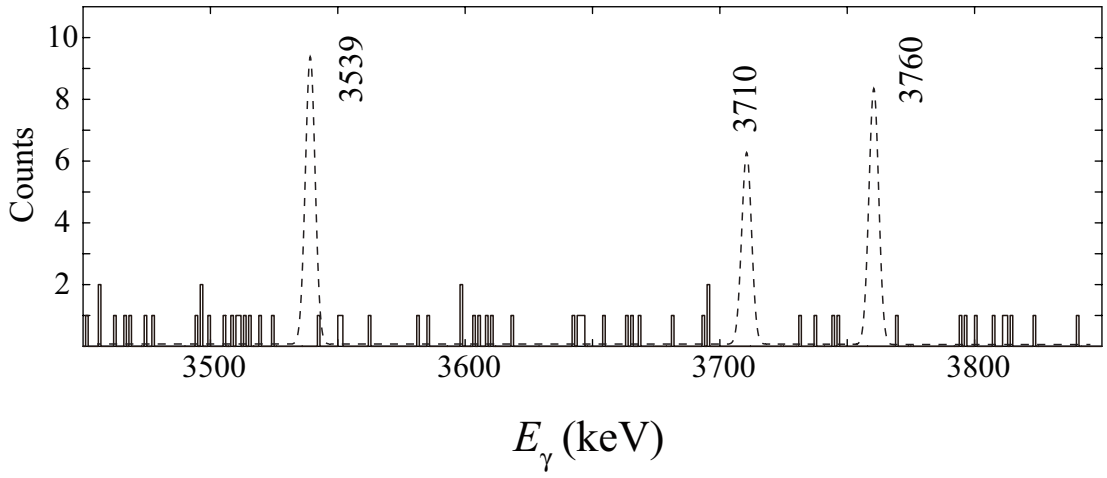

Figure 5.8: Enlarged β-γ coincidence spectrum for ^{31}Mg gated by β rays with more than 8 MeV indicated by solid line and the expected spectrum from the level scheme of Ref. [KLO93] shown in the dashed line.

of (2.244 MeV $\rightarrow$ 0.673 MeV) based on the strong coincidence relation between 1571-keV γ ray and the γ rays depopulating the 0.673-MeV level and the energy consistency between 1570.6(2) keV and 1570.4(1) [2243.5(1) - 673.1(1)] keV.

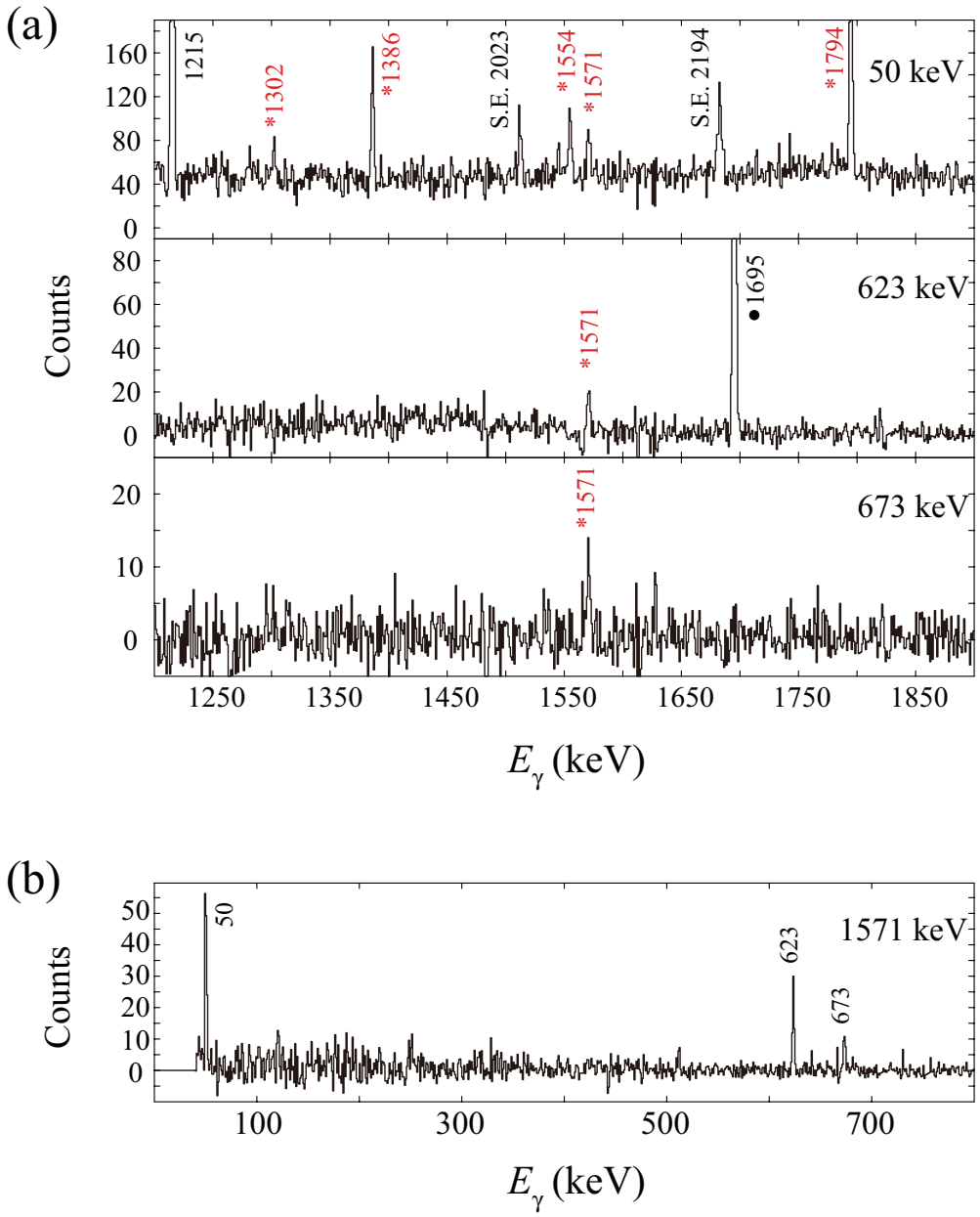

Figure 5.9: γ-γ coincidence spectra gated by the (a) 50-, 623-, 673-, and (b) 1571-keV γ rays. The peaks labeled with asterisks are newly observed in the present work. The 1695-keV peak labeled with a closed circle in the 623-keV gate spectrum was a contaminant associated with the β decay of ^{31}Al. Single escape peaks are indicated as S.E. and the original energy.

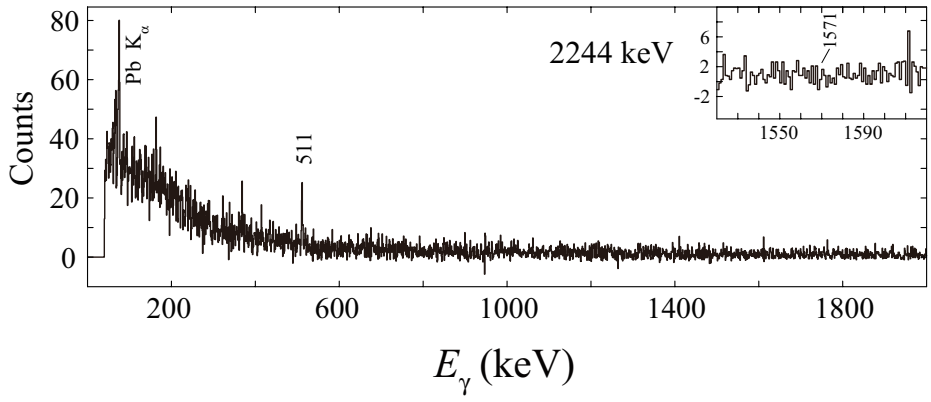

Figure 5.10: Gamma-ray coincidence spectrum gated by the 2244-keV γ ray. The enlarged spectrum around 1571 keV is shown in the inset.

5.3 Construction of levels newly found in the present work

New levels in ^{31}Mg were searched for by referring to the coincidence spectra gated by known γ rays based on the well-established level scheme discussed in Sec. 5.2 The 0.461-MeV and 2.015-MeV levels are newly observed in the β decay of ^{31}Na, and the 0.942-MeV and 1.436-MeV level are newly proposed, as discussed following sections.

5.3.1 0.461- and 2.015-MeV levels observed for the first time by the β decay of ^{31}Na

The 0.461-MeV level is one of key levels in the ^{31}Mg, because this level is most likely a level with negative parity of $7/2^-$ and the low-lying negative-parity state was essential to discuss the systematics of level energies of negative-parity states. The 0.461-MeV level has not been observed by the β decay of ^{31}Na in the previous works [KLO93; GUI84] and has been largely populated in the reaction of neutron knockout from ^{32}Mg [TER08] and the β-n decay of ^{32}Na [KLO93; MAC05]. The 240-keV γ ray depopulating the 0.461-MeV level was reported in Refs. [TER08; KLO93; MAC05]. In the present work, the 240-keV peak was observed in the γ-ray energy spectra gated by 50-, 171-, and 221-keV γ-ray peaks, as shown in Fig. 5.3. This result was consistent with the results in Refs. [TER08; KLO93; MAC05]. Therefore, the 0.461-MeV level was placed for the first time in the decay scheme of ^{31}Na in this work.

The 2.015-MeV level was reported only by the proton knockout reaction from ^{32}Al [MIL09] and was reported to be depopulated by the 1794-keV γ ray. In the present work, this γ-ray peak of 1794 keV was clearly seen in the γ-ray coincidence spectra gated by the

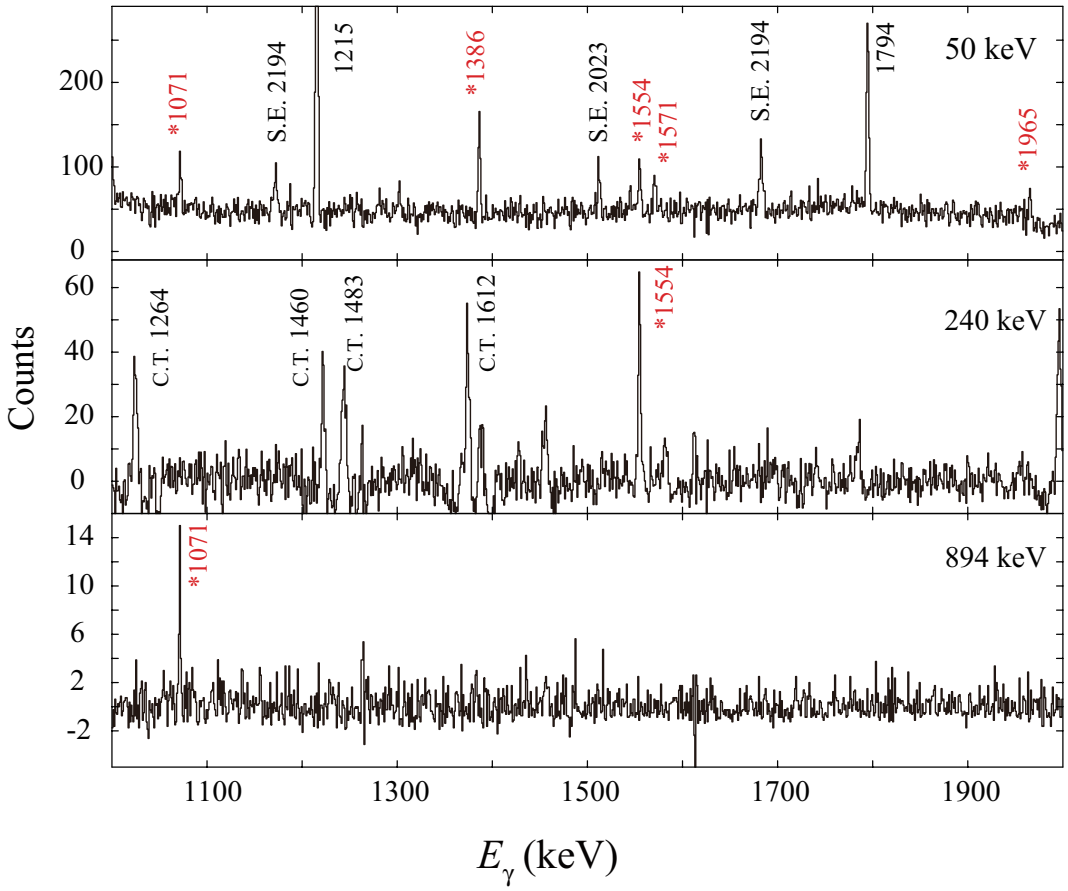

Figure 5.11: Gamma-ray energy spectra gated by the 50-, 240-, and 894-keV γ rays. The numbers are energies of the γ rays in keV. The γ rays originated from single escape of annihilation γ rays and cross talk of Compton scattering were indicated as S.E. and C.T., respectively. The γ rays with asterisks are newly observed in the present work.

50-, 171-, and 221-keV γ rays. These coincidence relations were consistent with the level scheme in Ref. [MIL09]. From these results, it was newly found that the 2.015-MeV level is also weakly populated in the β decay of ^{31}Na. In the present work, another three transitions from the 2.015-MeV level were found. The 1965- (2.015 MeV $\rightarrow$ 0.050 MeV), 1554- (2.015 MeV $\rightarrow$ 0.461 MeV), and 1071-keV (2.015 MeV $\rightarrow$ 0.944 MeV) γ transitions were newly proposed based on the coincidence relations observed in the γ-ray spectrum gated by the γ rays of 50, 239, and 894 keV, as shown in Fig. 5.11. The energy consistency between 2014.9(2) [1965.0(2) + 49.9(1)] keV, 2015.1(1) [1794.3(1) + 220.8(1)], 2015.0(2) [1554.3(1) + 239.9(1) + 220.8(1)] keV, and 2014.9(2) [1070.9(2) + 894.1(1) + 49.9(1)] keV also supports the existence of the 2.015-MeV level.

5.3.2 Newly proposed 0.942-MeV level

In this work, a new level at 0.942 MeV is proposed based on the cascade relations between the 892-, 942-, and 1302-keV γ rays. The 892-keV peak is a doublet of the 894-keV γ ray which depopulating the 0.944-MeV level. The energy difference between the 892- the 894-keV γ rays is just 2 keV, and it is difficult to separate these doublet peaks by Ge detectors. The 892-keV γ ray is firstly found in the γ-γ projection spectrum. The width of peak appears around 892-894 keV (2.7 keV) was larger than what is expected from the intrinsic energy resolution of Ge detectors (2.2 keV for 900-keV γ ray), so that it is concluded that the peak at 894 keV was originated from two different γ rays, as shown in the Fig. 5.12 (a). In order to confirm the existence of 892-keV γ ray, the γ-ray energy spectra with two different gate conditions was made. Fig. 5.12 (b-1) and (b-2) show the γ-ray energy spectra gated by two different energy regions of the peak shown in Fig. 5.12 (a). In the gate spectra, the different coincidence relations are observed. In Fig. 5.12 (b-1), there is a γ-ray peak at 1302 keV, whereas, in Fig. 5.12 (b-2), the 1071-keV peak appears instead of the 1302-keV peak. The 892-keV γ ray could not be assigned to a transition in the known level scheme, therefore, the 892-keV γ ray is considered to depopulate and/or populate unknown levels in ^{31}Mg. Fig. 5.13 shows the γ-ray coincidence spectrum gating on the 1302-keV peak. The γ-ray peaks of 50, 892, 942 keV were seen in the figure. Therefore, the 0.942-MeV level is newly proposed based on the cascade relations of 50-892-1302 and 942-1302 and energy consistency between 941.9(2) [892.0(2) + 49.9(1)], 941.8(2), and 941.8(2) [2243.5(1) - 1301.7(2)] keV.

5.3.3 Newly proposed 1.436-MeV level

The 1.436-MeV level with small branching ratio is newly proposed in this work as follows. The 1386-keV γ ray peak was found in the γ-ray spectrum gated by the 50- and 808-keV γ rays, as shown in Figs. 5.9(a) and 5.14, whereas there is no peak at 1386 keV in γ-ray energy spectra gated by the 171- and 221-keV γ-ray which have cascade relation with 808-keV γ ray. If the 1386-keV transition was placed above the 1.029-MeV level in the level scheme, observed coincidence relation of 1386 keV conflicts with the previous level and γ-ray placement discussed in Sec. 5.2. In order to avoid such a contradiction, another 808-keV transition is proposed in the level scheme of ^{31}Mg in the present work. In the γ-ray energy coincidence spectrum gated by the 808-keV γ ray, shown in Fig. 5.14, not only the 1386-keV peak but also the weak 1436-keV peak are newly observed. The energies of 1435.8(2), 1435.8(1) [1385.9(1) + 49.9(1)], and 1435.9(1) [2243.5(1) - 807.6(1)] are consistent with each other. Therefore we reasonably proposed the new level at 1.436 MeV depopulated by the

transitions of 1386 keV (1.436 MeV → 0.050 MeV) and 1436 keV (1.436 MeV → g.s.).

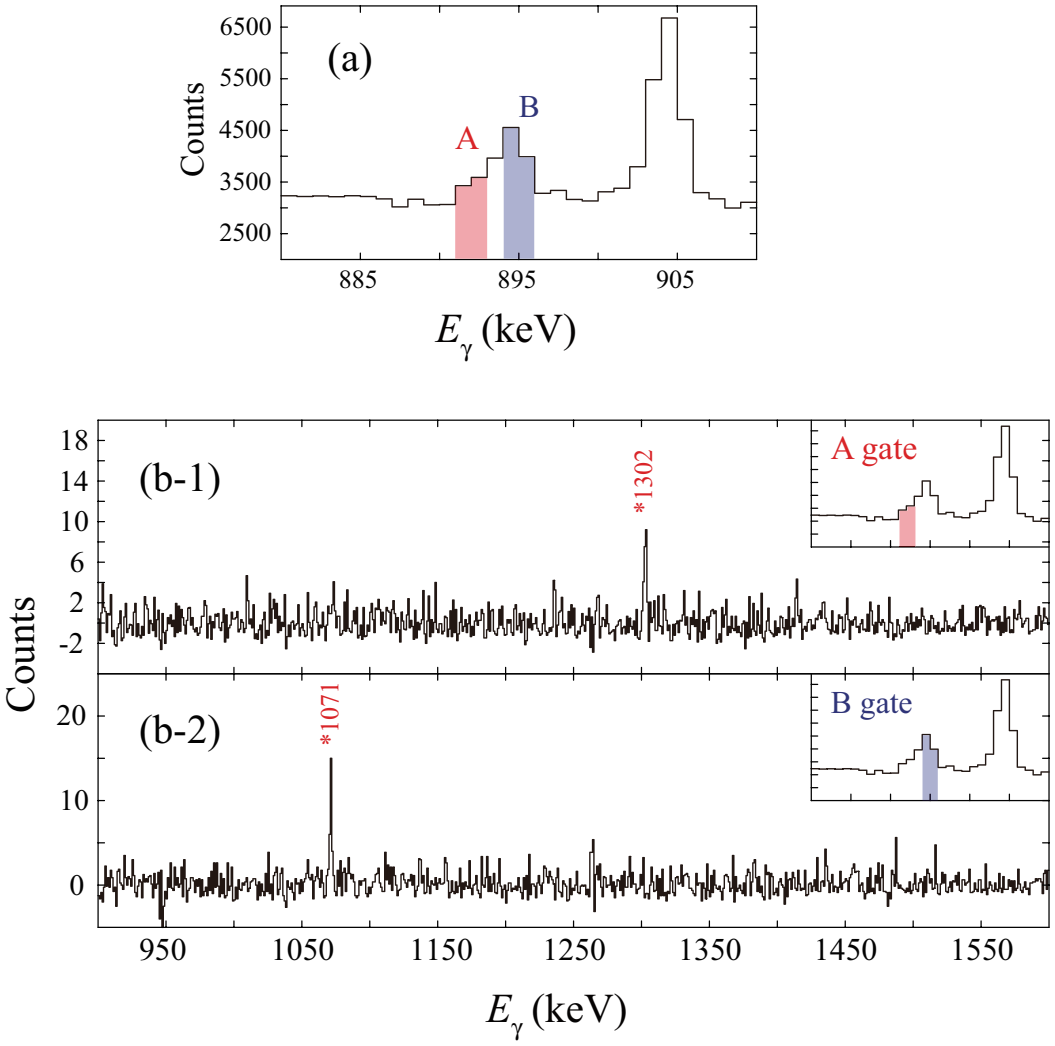

Figure 5.12: (a) γ-γ projection spectrum and γ-ray energy spectra gated by (b-1) lower and (b-2) higher energy regions of the doublet peaks of 892 and 894 keV. The gate areas are displayed in each inset. The blue region (A) and the red region (B) represent the γ ray energy gate for 894- and 892-keV γ rays.

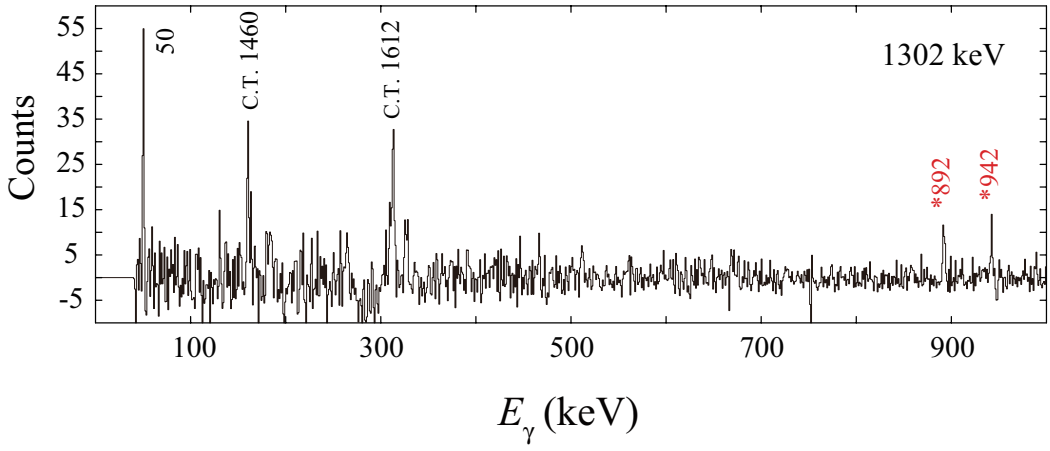

Figure 5.13: Gamma-ray coincidence spectrum gated by the 1302-keV peak. The numbers are energies of the γ-ray peaks in keV. The newly observed peaks in the present work are labeled with asterisks. The γ-ray peaks with C.T. are cross-talk peaks.

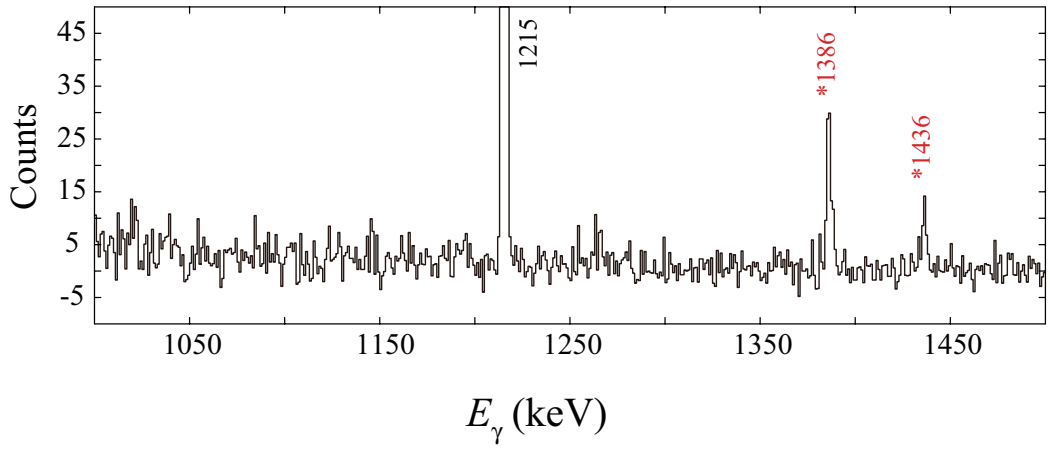

Figure 5.14: Gamma-ray coincidence spectrum gated by the 808-keV peak. The numbers are energies of the γ-ray peaks in keV. The newly observed peaks in the present work are labeled with asterisks.

5.4 Summary of the γ-γ coincidence relation and γ-ray intensities

The summary of the γ-γ coincidence measurement in the present work is listed in the Table. 5.1. This table shows whether the γ-ray peaks listed on the upper-side were observed in the γ-ray energy spectrum gated by the γ ray on the left-side. The circles (crosses) indicate that the coincidence relation was observed (not observed) in the energy spectrum. The triangles mean that the coincidence relation could not be confirmed due to low statistics or doublet peaks from the cross talk peaks, although the coincidence relations should be observed according to the constructed level scheme in the present work.

The summary of the γ-ray transition energies and intensities are listed in the Table. 5.2. The relative intensities of γ rays which were evaluated by using a γ-ray singles spectrum for intense γ rays and/or an efficiency weighted γ-γ matrix for the weak γ rays or the γ rays which cannot be eliminated from the contaminations, for example the doublet peaks come from the other neuclei. The relative intensities are shown relative to that of the 50-keV γ ray. The absolute γ-ray intensities was deduced by using absolute intensity of 19.5(39) per 100 decay for 50-keV γ rays which de-excites the 0.050-MeV level in the previous report [KLO93]. The absolute intensities in the present work compared with the previous reports in Refs. [KLO93; GUI84]. All of the γ-ray intensities except for 1571-keV γ ray are consistent with each other. It is noted that the placement of 1571-keV transition in this work is different from that in Ref. [KLO93] (in Sec. 5.2.3). Thus, there may be contaminates around a 1571 keV peak in the spectrum of the previous report [KLO93].

In this work, we should take into account the effect of the anisotropy of γ-ray emission due to the residual polarization,as described in Appendix E, when we evaluate the γ-ray intensities. The detected asymmetry between Ge detectors placed at 0° and 90° from the polarization direction for the transition of $2^+ \rightarrow 0^+$ (5095 keV; 5.095-MeV $\rightarrow$ g.s.), which is expected to be the most asymmetric transition, was 13% in this work. The intensities of the γ rays were evaluated by using all of detectors placed at 0°, 90°, and 180°. Therefore, the anisotropy should be suppressed, and estimated ambiguity of the γ-ray intensities caused by the residual polarization was less than 2 %. This ambiguity was taken into account in Table 5.2.

Table 5.1: Summary of observed coincidence relations of the γ rays in ^{31}Mg. The open circles (crosses) indicate that the γ-ray peak displayed in upper-side is observed (not observed) in the energy spectrum gated by the γ-ray energy in the left-side. The triangles mean that the coincidence relations could not be confirmed.

	50	171	221	240	452	623	673	723	808	892	894	942	979	1071	1215	1302	1386	1436	1554	1571	1794	1965	2023	2194	2244
50	−	○	×	○	○	○	×	○	○	○	○	×	○	○	○	○	○	×	○	○	○	○	○	○	×
171	○	−	×	○	○	×	×	○	○	×	×	×	×	×	○	×	×	×	○	×	○	×	○	×	×
221	×	×	−	○	○	×	×	△	○	×	×	×	×	×	○	×	×	×	○	×	○	×	○	×	×
240	○	○	○	−	×	×	×	×	×	×	×	×	×	×	×	×	×	×	○	×	×	×	×	×	×
452	○	○	○	×	−	×	×	×	×	×	×	×	×	×	×	×	×	×	×	△	×	×	×	×	×
623	○	×	×	×	×	−	×	×	×	×	×	×	×	×	×	×	×	×	×	○	×	×	×	×	×
673	×	×	×	×	×	×	−	×	×	×	×	×	×	×	×	×	×	×	×	○	×	×	×	×	×
723	○	○	△	×	×	×	×	−	×	×	×	×	×	△	×	×	×	×	×	×	×	×	×	×	×
808	○	○	○	×	×	×	×	×	−	×	×	×	×	×	○	×	○	○	×	×	×	×	×	×	×
892	○	×	×	×	×	×	×	×	×	−	×	×	×	×	×	○	×	×	×	×	×	×	×	×	×
894	○	×	×	×	×	×	×	×	×	×	−	×	×	○	×	×	×	×	×	×	×	×	×	×	×
942	×	×	×	×	×	×	×	×	×	×	×	−	×	×	×	△	×	×	×	×	×	×	×	×	×
979	○	×	×	×	×	×	×	×	×	×	×	×	−	×	○	×	×	×	×	×	×	×	×	×	×
1071	○	×	×	×	×	×	×	△	×	○	×	×	×	−	×	×	×	×	×	×	×	×	×	×	×
1215	○	○	○	×	×	×	×	×	○	×	×	×	○	×	−	×	×	×	×	×	×	×	×	×	×
1302	○	×	×	×	×	×	×	×	×	○	×	○	×	×	×	−	×	×	×	×	×	×	×	×	×
1386	○	×	×	×	×	×	×	×	○	×	×	×	×	×	×	×	−	×	×	×	×	×	×	×	×
1436	×	×	×	×	×	×	×	×	○	×	×	×	×	×	×	×	×	−	×	×	×	×	×	×	×
1554	○	○	○	○	×	×	×	×	×	×	×	×	×	×	×	×	×	×	−	×	×	×	×	×	×
1571	○	×	×	×	×	○	○	×	×	×	×	×	×	×	×	×	×	×	×	−	×	×	×	×	×
1794	○	○	○	×	×	×	×	×	×	×	×	×	×	×	×	×	×	×	×	×	−	×	×	×	×
1965	○	×	×	×	×	×	×	×	×	×	×	×	×	×	×	×	×	×	×	×	×	−	×	×	×
2023	○	○	○	×	×	×	×	×	×	×	×	×	×	×	×	×	×	×	×	×	×	×	−	×	×
2194	○	×	×	×	×	×	×	×	×	×	×	×	×	×	×	×	×	×	×	×	×	×	×	−	×
2244	×	×	×	×	×	×	×	×	×	×	×	×	×	×	×	×	×	×	×	×	×	×	×	×	−

Table 5.2: γ rays observed in the β decay of ^{31}Na $\rightarrow$ ^{31}Mg in the present work. The relative γ-ray intensities are shown relative to the 50-keV γ ray. The absolute γ-ray intensities for 100 decays from the present are compared with the previous reports in Refs. [KLO93] and [GUI84].

E_γ (keV)	$E_i \rightarrow E_f$ (MeV)	I_γ (relative)	I_γ (per 100 decays)		
			Present work	Ref. [KLO93]	Ref. [GUI84]
49.9(1)	0.050→ 0	100	20(4)	19.5(39)	-
170.9(1)	0.221→ 0.050	24(2)	5(1)	5.4(9)	4.9(15)
220.8(1)	0.221→ 0	8.9(6)	1.8(4)	2.2(4)	2.1(7)
239.9(1)	0.461→ 0.221	1.2(1)	0.24(5)	-	-
452.4(2)	0.673→ 0.221	1.7(2)	0.34(8)	0.4(1)	-
623.1(1)	0.673→ 0.050	16(2)	3.2(7)	3.6(6)	3.3(10)
673.1(1)	0.673→ 0	10.2(8)	2.0(4)	1.8(3)	1.4(4)
723.1(1)	0.944→ 0.221	0.51(7)	0.10(2)	-	-
807.6(1)	2.244→ 1.436	1.6(7)	0.3(1)	-	-
807.8(1)	1.029→ 0.221	5.7(7)	1.1(3)	1.5(3)	1.6(5)
892.0(2)	0.942→ 0.050	0.68(9)	0.14(3)	-	-
894.1(1)	0.944→ 0.050	3(2)	0.6(1)	0.9(2)	0.8(3)
941.8(2)	0.942→ 0	0.6(2)	0.12(4)	-	-
978.6(3)	1.029→ 0.050	0.15(4)	0.03(1)	-	-
1070.9(2)	2.015→ 0.944	0.6(1)	0.12(3)	-	-
1215.0(1)	2.244→ 1.029	6.8(5)	1.4(3)	1.6(3)	1.2(4)
1301.7(2)	2.244→ 0.942	0.37(8)	0.07(2)	-	-
1385.9(1)	1.436→ 0.050	0.9(1)	0.17(4)	-	-
1435.8(2)	1.436→ 0	0.31(7)	0.06(2)	-	-
1554.3(1)	2.015→ 0.461	0.7(1)	0.14(4)	-	-
1570.6(2)	2.244→ 0.673	1.1(2)	0.21(5)	2.6(5)	-
1794.3(1)	2.015→ 0.221	3.4(4)	0.7(2)	-	-
1965.0(2)	2.015→ 0.050	0.29(6)	0.06(2)	-	-
2022.8(1)	2.244→ 0.221	18(1)	3.6(8)	4.5(9)	3.9(13)
2193.6(1)	2.244→ 0.050	14(1)	2.8(6)	4.0(8)	3.1(10)
2243.6(1)	2.244→ 0	54(4)	11(2)	13.3(23)	10.6(33)
(3538)	3.760→ 0.221	-	-	1.2(3)	0.8(4)
(3710)	3.760→ 0.050	-	-	0.6(4)	-
(3760)	3.760→ 0	-	-	0.9(4)	-

5.5 Half-life of the 0.050-MeV level

In the previous work [KLO93], a half-life of 0.050-MeV level has been measured in the time difference spectrum between β rays and the 50-keV γ ray by using the NE102 plastic scintillator and the BaF_2 scintillator. The reported half-life is 16.0(28) ns [KLO93].

In the present work, the half-life of 0.050-MeV level was measured by using the thin plastic scintillators in front of Ge detectors for β ray counting and the Ge detector (Ge-5; ALICE) which shows the best time resolution in our Ge detectors. Typically, the time response of the Ge detector is much worse than that of the BaF_2 scintillator. On the other hand, the Ge detector has better energy resolution and enable the precise γ-ray energy selection, therefore the life-time measurement is free from the contaminants from other γ rays. The time resolution of Ge detector(Ge-5; ALICE) was 100 ns (FWHM) for 50-keV γ ray. It is much larger than the reported half-life of 0.050-MeV level, so that it is difficult to fit a slop of the decay curve. In order to measure the shorter half-life than time resolution, the centroid shift method was used [WEA60]. In this method, the centroid position of the time distribution of delayed γ rays is compared with that of prompt γ rays, and a half-life is obtained from the difference between the centroid positions.

Fig. 5.15 shows the time difference spectrum between β rays and prompt γ rays (black), β rays and the 50-keV γ rays depopulating 0.050-MeV level (red). It is clearly found that the time distribution of the 50-keV γ ray deviate from the prompt position. From the spectrum, the difference of the centroid position is determined to be 16.5(6) ns. The relation between the half-life and difference of the peak positions was shown in the Fig. 5.16. The half-life of 0.050-MeV level was extracted by using the plot in Fig. 5.16 and was determined to be 11.8(4) ns. We successfully improve the accuracy of the life-time measurement for 0.050-MeV level. The measured life-time of 11.8(4) ns was consistent with the values of 16.0(28) ns in the previous report within the 2σ confidence level.

5.6 Spin-parity assignments of Levels in ^{31}Mg

As explained in Sec. 3.1, spin-parity assignments of the levels in ^{31}Mg were performed through the measurement of the β-ray asymmetry from the β decay of spin-polarized ^{31}Na in the present work.

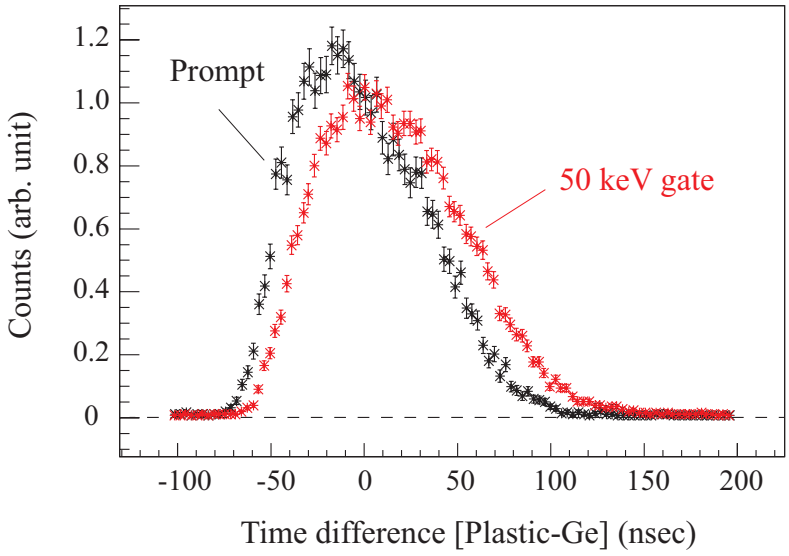

Figure 5.15: Time difference spectrum between β rays and prompt γ rays (black), β rays and the 50-keV γ rays depopulating 0.050-MeV level (red).

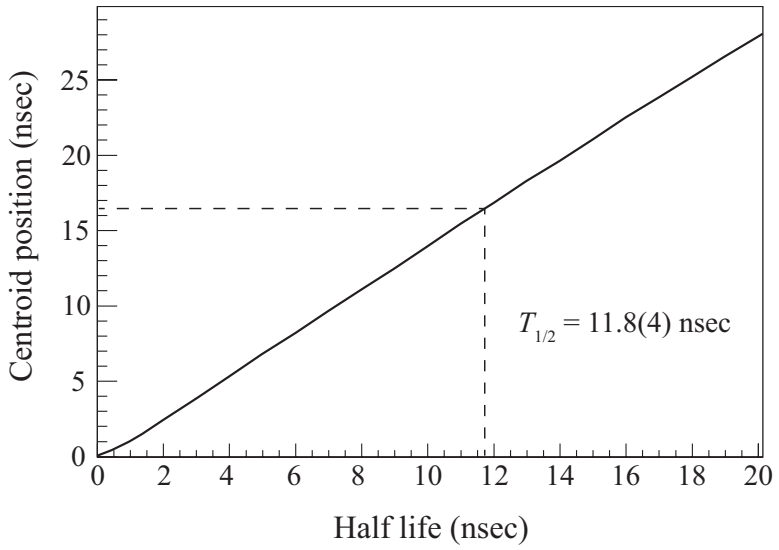

Figure 5.16: Plot of the half-life vs. the time difference between the centroid positions. The dashed line indicates the experimental value for 0.050-MeV level.

5.6.1 Polarization of ^{31}Na beam and spin-parity of the 0.673- and 2.244-MeV levels

As a first step, the polarization (P) should be determined in order to deduce the asymmetry parameter (A) for each level. If there were levels with known spins and parities, the polarization of Na beam could be determined by a reference to the levels. In ^{31}Mg, there are no excited levels whose spins and parities are experimentally assigned, so that we could not obtain the polarization from the known spin-parity levels. In order to determine the polarization of Na beam, spin-parity of one excited level in ^{31}Mg at least must be assign.

At first, the AP values of the 0.673- and 2.244-MeV levels, which have large β-decay branch, were deduced from the γ-ray counts coincident with the β-ray detectors placed at right(R)- and left(L)-hand toward the downstream of beam line for each polarization direction. For example, Fig. 5.17 shows the γ-ray spectra focused on the peak of 2244-keV γ ray, which depopulates the 2.244-MeV level, in the four combinations of the β-ray detectors (R or L) and the polarization direction ("+" or "−"). It is found that the ratio of the γ-ray counts of 2244 keV gated by β-ray detectors R and L in the polarization direction of "+" are clearly different from that in case of "−". From the double ratio of the counts of the γ rays de-exciting the 2.244-MeV level (2023, 2194, and 2244 keV) in the for patterns of N_{R+}, N_{L+}, N_{R-}, and N_{L-} expressed in Eq. (3.5), the AP value of the 2.244-MeV level was calculated to be $-0.33(1)$. On the other hand, the 2235-keV peak which comes from the β decay of ^{30}Al shows a similar ratio for the polarization direction of "+" or "−" in Fig. 5.17. The AP value deduced by the counts of 2235-keV γ-ray peak was 0.002(6). This nearly zero value is consistent with the naive idea that the polarization of ^{30}Al should be attenuated in the decay process.

Similarly, the AP value of the 0.673-MeV level was determined to be $-0.11(1)$. In case of the 0.673-MeV level, this level was not directly populated only by the β decay, but also by the γ transition from the 2.244-MeV level. The population from the 2.244-MeV level was much less than the β decay, so that it could be ignored. By taking the ratio of the AP values of the 0.673- and 2.244-MeV levels, the ratio of the A values of these levels were calculated as following.

$$A_{2.244}P/A_{0.673}P = A_{2.244}/A_{0.673} = 3.0(3). \tag{5.1}$$

Figure 5.18 shows the experimental ratio of the A values of 0.673- and 2.244-MeV levels.

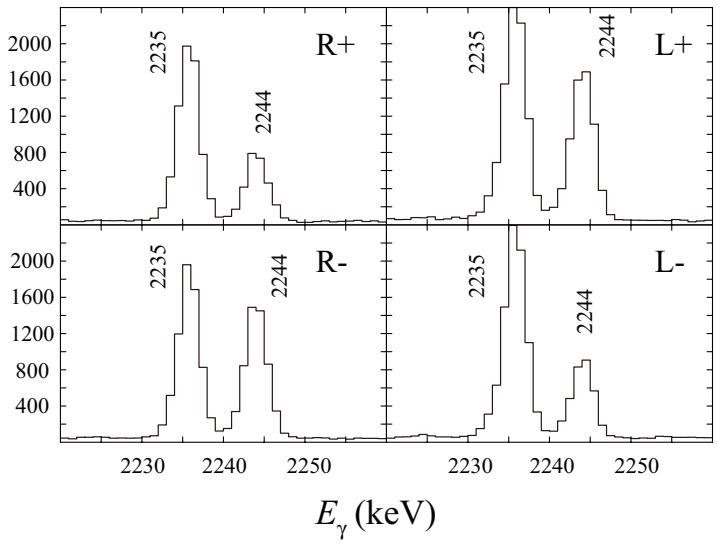

Figure 5.17: γ-ray energy spectra gated by the right (R) and left (L) β-ray detectors for each polarization direction defined as "+" or "-". The 2235-keV γ-ray peak comes from γ rays assosiated with β decay of ^{30}Al.

In the Figure, the lines show the ratio of the A values expected from the possible 9 combinations of spins and parities of 0.673- ($1/2^+$, $3/2^+$, and $5/2^+$) and 2.244-MeV ($1/2^+$, $3/2^+$, and $5/2^+$) levels. The experimental result is consistent with the line for ($I^\pi_{2.244}$, $I^\pi_{0.673}$) = ($1/2^+$, $3/2^+$). Therefore, we reasonably assigned the spins-parity of the 0.673- and 2.244-MeV levels to $3/2^+$ and $1/2^+$, respectively. The spin-parity of the 2.244-MeV level is completely newly established in this work for the first time, and the $3/2^+$ assignment for the 0.673-MeV level is consistent with that in the proton knockout reaction from ^{32}Al [MIL09]. It is noted that the assignment of $1/2^+$ for the 2.244-MeV level is unexpected and very interesting, because there are no $1/2^+$ states at such low excitation energy in the theoretical calculation of AMD+GCM framework except for the ground state [KIM07]. The details are discussed in Sec. 7.1.

The polarization of 28(3)% and 33(1)%was obtained from the A values of -0.4 and -1.0 for the 0.673- and 2.244-MeV levels, respectively. The polarization was determined to be 32(1)% from a weighted average of 33(1)% and 28(3)%, and A values of other excited levels in ^{31}Mg are deduced from this value.

5.6.2 Spin-parity of the 2.015-MeV level

In order to achieve the highly-S/N β-ray asymmetry measurement, the β rays with more than 5 MeV was selected. In this way, $A_{2.015} = 0.33(21)$ was deduced from the counts of the

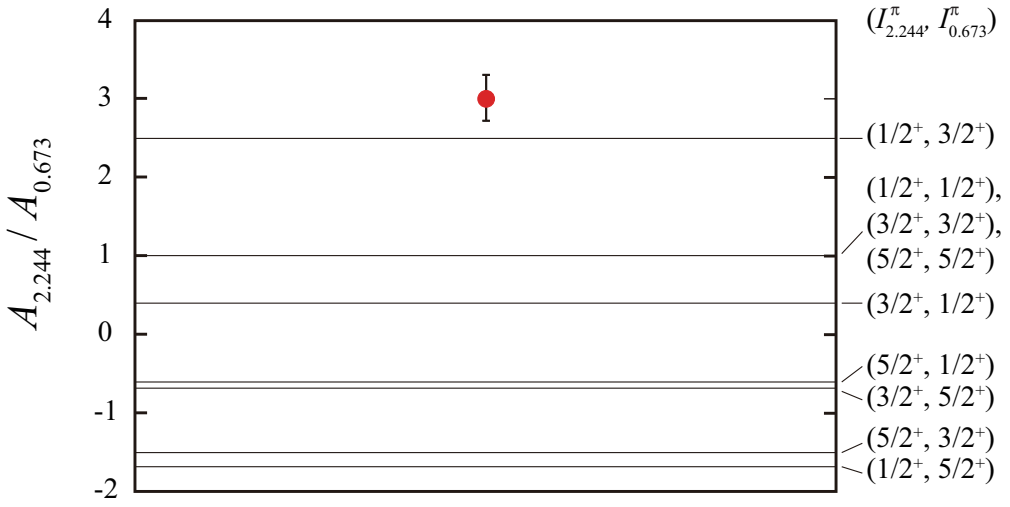

Figure 5.18: Ratio of the asymmetry parameters of 2.244- and 0.673-MeV levels. The lines show expected values from each combination of the spin-parity.

1794-keV γ rays gated by more than 5-MeV β rays. This A value of 0.33(21) is close to the A value of 0.6 for a $5/2^+$ level. Even the error of A value is considered, it is consistent with the A value of 0.6 within the 3σ. Therefore, the spin and parity of the 2.015-MeV level is firmly assigned to $5/2^+$ in the present work.

5.6.3 Spin-parity of the 0.050- and 0.944-MeV level

The determination of the β-ray asymmetry in 0.050- and 0.944-MeV levels is rather complex than that in other levels, because these levels are not directly populated only by the β decay, but also by the γ transition from other levels. These effects are not negligible for the 0.050- and 0.944-MeV levels due to large feeding from γ transitions, unlike the 0.673-MeV level case. Therefore, the contribution of this effect to the β-ray asymmetry should be eliminated. By using Eq. (3.7), the A value of the 0.944 ($A_{0.944}$) was obtained from an equation of

$$A_{0.944} = \frac{I_{894} + I_{723}}{I_{894} + I_{723} - I_{1070}} \times A(\gamma_{894}) - \frac{I_{1070}}{I_{894} + I_{723} - I_{1070}} \times A_{2.015}. \tag{5.2}$$

The I_{723}, I_{894}, and I_{1070} are relative γ ray intensities of 723, 894, and 1070 keV, respectively. The $A_{0.944}$ and $A_{2.015}$ are asymmetry parameters of the 0.944- and 2.015-MeV levels, respectively. The A value of 0.7(2) is determined for 0.944-MeV level. This value was nicely consistent with the A value for $5/2^+$. Therefore we reasonably assigned the spin-parity of $5/2^+$ for the 0.944-MeV level.

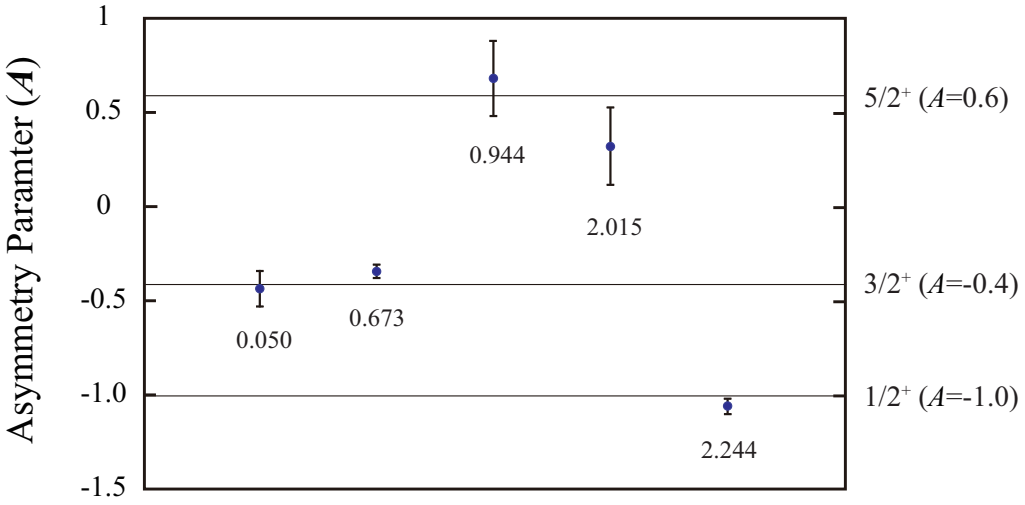

Figure 5.19: Summary of the experimental asymmetry paramters (A) for each excited state in ^{31}Mg. The lines indicate the expected A values for the spin-parity shown on right-hand.

The similar examination was performed for the first excited state of 0.050-MeV level. The A values of 0.050-MeV level was determined to be -0.43(9). This value leads to the $3/2^+$ assignment for the 0.050-MeV level.

5.6.4 Summary of the spin-parity assignment in ^{31}Mg by β-ray asymmetry

The summary of the spin-parity assignment by β-ray asymmetry measurement is shown in the Fig. 5.19. The plots show the experimental A values for each level in ^{31}Mg. The lines indicate A values expected from each spin-parity of level in ^{31}Mg. Spins and parities of five excited levels are newly assigned in the present work.

5.6.5 Spin-parity assignment for other levels at 0.942 and 1.436 MeV

The 0.942- and 1.436-MeV levels are newly proposed in this work, as mentioned in Sec. 5.3. These 0.942- and 1.436-MeV levels show very small β decay branch of $I_\beta = 0.2(1)$ and $I_\beta < 0.06$, respectively. These values lead to the large logft values of 6.9 and >7.4. From such large logft values, the ^{31}Na (g.s.) $\rightarrow$ ^{31}Mg (0.942 or 1.436 MeV) β transitions are most likely first-forbidden transitions. Thus the possible spins and parities are $1/2^-$, $3/2^-$, $5/2^-$, and $7/2^-$ for 0.942- and 1.436-MeV levels. In order to narrow down the candidates, the γ-ray transition intensities were compared with those calculated from the Weisskopf estimate.

Table 5.3 shows the comparison between the experimental γ-ray intensity of 808 keV [2.244 MeV $(1/2^+) \rightarrow$ 1.436 MeV] relative to 2244 keV [2.244 MeV $(1/2^+) \rightarrow$ g.s. $(1/2^+)$].

The calculations by Weisskopf estimate were performed for the three expected multipolarities of transitions: $E1$, $M2$, and $E3$. It is noted that the $E1$ transition is typically hindered with a factor of 10^{-2} - 10^{-7}, in the ^{31}Mg case, the hindrance was estimated to be approximately a factor of 10^{-2} from the comparison between the intensities of transitions of 2244 [2.244 MeV $(1/2^+) \rightarrow$ g.s. $(1/2^+)$] and 2023 keV [2.244 MeV $(1/2^+) \rightarrow$ 0.221 MeV $(3/2^-)$]. Taking into acount the hindrance, the relative intensity calculated as the $E1$ transition is close to the experimental value, thus the multipolarity of 808-keV transition is most likely $E1$. The fact leads to the spin-parity assignment of $1/2^-$ or $3/2^-$ for 1.436-MeV level.

A similar examination was applied for the 0.942-MeV level. Table 5.4 shows the comparison between the relative intensities of the 892 keV [0.942 MeV $\rightarrow$ 0.050 MeV $(3/2^+)$] and 942 keV [0.942 MeV $\rightarrow$ g.s. $(1/2^+)$] from the experiment and Weisskopf estimate. Assuming the spin-parity of the 0.942-MeV level is $1/2^-$ or $3/2^-$, the γ-ray intensities are well reproduced. Therefore, we narrow down the candidates of the spin-parity of the 0.942-MeV level to $1/2^-$ or $3/2^-$.

Table 5.3: Comparison of the relative γ-ray transition intensities between the experimental results (I_{exp}) and Weisskopf estimate ($I_{W.e.}$). relative to the 2244-keV transition (2.244 MeV $\rightarrow$ g.s.). $T_{W.e.}$ $(\sigma\lambda)$ is calculated half-life for each possible multipolarity of the transition $(\sigma\lambda)$.

E_γ (keV)	$E_i \rightarrow E_f$ (MeV)	$I_{\rm exp}$ (relative)	I^π(1.436 MeV)	$\sigma\lambda$	$T_{\rm W.e.}$ $(\sigma\lambda)$ (s)	$I_{\rm W.e.}$ (relative)
2244	2.244 $\rightarrow$ g.s.	1		$M1$	2.0×10^{-15}	1
808	2.244 $\rightarrow$ 1.436	0.03(2)	$7/2^-$	$E3$	9.4×10^{-5}	2.1×10^{-11}
			$5/2^-$	$M2$	9.1×10^{-9}	2.1×10^{-7}
			$1/2^-$, $3/2^-$	$E1$	1.3×10^{-15}	1.5×10^{0}

5.7 Newly proposed decay scheme of ^{31}Na $\rightarrow$ ^{31}Mg

.

The constructed level in this work is shown in Fig. 5.20. The numbers placed above arrows mean the γ-ray energies and absolute intensities per 100 decays. The newly proposed levels and γ transitions are indicated in red. The blue lines and arrows show the levels and transitions found for the first time in the β decay of ^{31}Na, respectively. The number in red on the right-hand of the level energies is the revised half-life in the present work, and the other half-life in black is taken from Ref. [MAC05]. The Q value of ^{31}Na β decay and neutron

Table 5.4: Comparison of the relative γ-ray transition intensities between the experimental results ($I_{\rm exp}$) and Weisskopf estimate ($I_{\rm W.e.}$. relative to the 892-keV transition (0.942 MeV $\rightarrow$ 0.050 MeV). $T_{\rm W.e.}$ ($\sigma\lambda$) is calculated half-life for each possible multipolarity of the transition ($\sigma\lambda$).

E_γ (keV)	$E_i \rightarrow E_f$ (MeV)	$I_{\rm exp}$ (relative)	I^π(0.942 MeV)	$\sigma\lambda$	$T_{\rm W.e.}$ ($\sigma\lambda$) (s)	$I_{\rm W.e.}$ (relative)
892	0.942 $\rightarrow$ 0.50	1	$7/2^-$	$M2$	5.6×10^{-9}	1
942	0.942 $\rightarrow$ g.s.	0.8(3)	$7/2^-$	$E3$	3.2×10^{-5}	1.9×10^{-4}
892	0.942 $\rightarrow$ 0.50	1	$1/2^-$,$3/2^-$, $5/2^-$	$E1$	9.7×10^{-16}	1
942	0.942 $\rightarrow$ g.s.	0.8(3)	$5/2^-$	$M2$	3.4×10^{-6}	2.9×10^{-10}
			$1/2^-$, $3/2^-$	$E1$	8.2×10^{-16}	1.2×10^{0}

separation energy (S_n) are taken from Ref. [OUE13]. The branching ratio of β-delayed one neutron decay (P_{1n}) and two neutron decay (P_{2n}) are from Ref. [GUI84].

The levels observed in the β decay of ^{31}Na is listed in Table 5.5. The absolute β-decay branches for levels in ^{31}Mg are calculated from the difference between the γ-ray intensities populate and depopulate the levels. The logft values are compared with the previous works [KLO93; GUI84]. All of logft values except for levels newly found in this work for the first time are consistent with Ref. [KLO93].

Table 5.5: Observed levels in ^{31}Mg by the β decay of ^{31}Na. The logft values in the present work are compared with the previous reports [KLO93; GUI84].

E_x (MeV)	I^π	A	I_β (%)	logft		
				Present work	Ref. [KLO93]	Ref. [GUI84]
0	$1/2^+$	-	27(8)	4.9(1)	4.9	4.8
0.0499(1)	$3/2^+$	$-0.43(9)$	8(5)	5.4(3)	5.6	-
0.22079(8)	$(3/2^-)$	-	<2.2	>6.0	>6.0	5.1
0.4607(1)	$(7/2^-)$	-	0.09(7)	10(1)	-	-
0.67306(8)	$3/2^+$	$-0.33(3)$	5(1)	5.55(9)	5.5	-
0.9418(2)	$(1/2^-, 3/2^-)$	-	0.2(1)	6.9(2)	-	-
0.9439(1)	$5/2^+$	0.7(2)	0.6(2)	6.4(2)	6.2	-
1.0286(1)	$(1/2^-, 3/2^-)$	-	<0.2	>6.9	>6.1	6.6
1.4357(1)	$(1/2^-, 3/2^-)$	-	<0.07	>7.4	-	-
2.01501(9)	$5/2^+$	0.3(2)	1.0(2)	6.05(9)	-	-
2.24354(7)	$1/2^+$	$-1.05(4)$	19(4)	4.7(1)	4.7	4.7
(3.760)	-	-	-	-	5.3	-
(3.814)	-	-	-	-	5.3	-

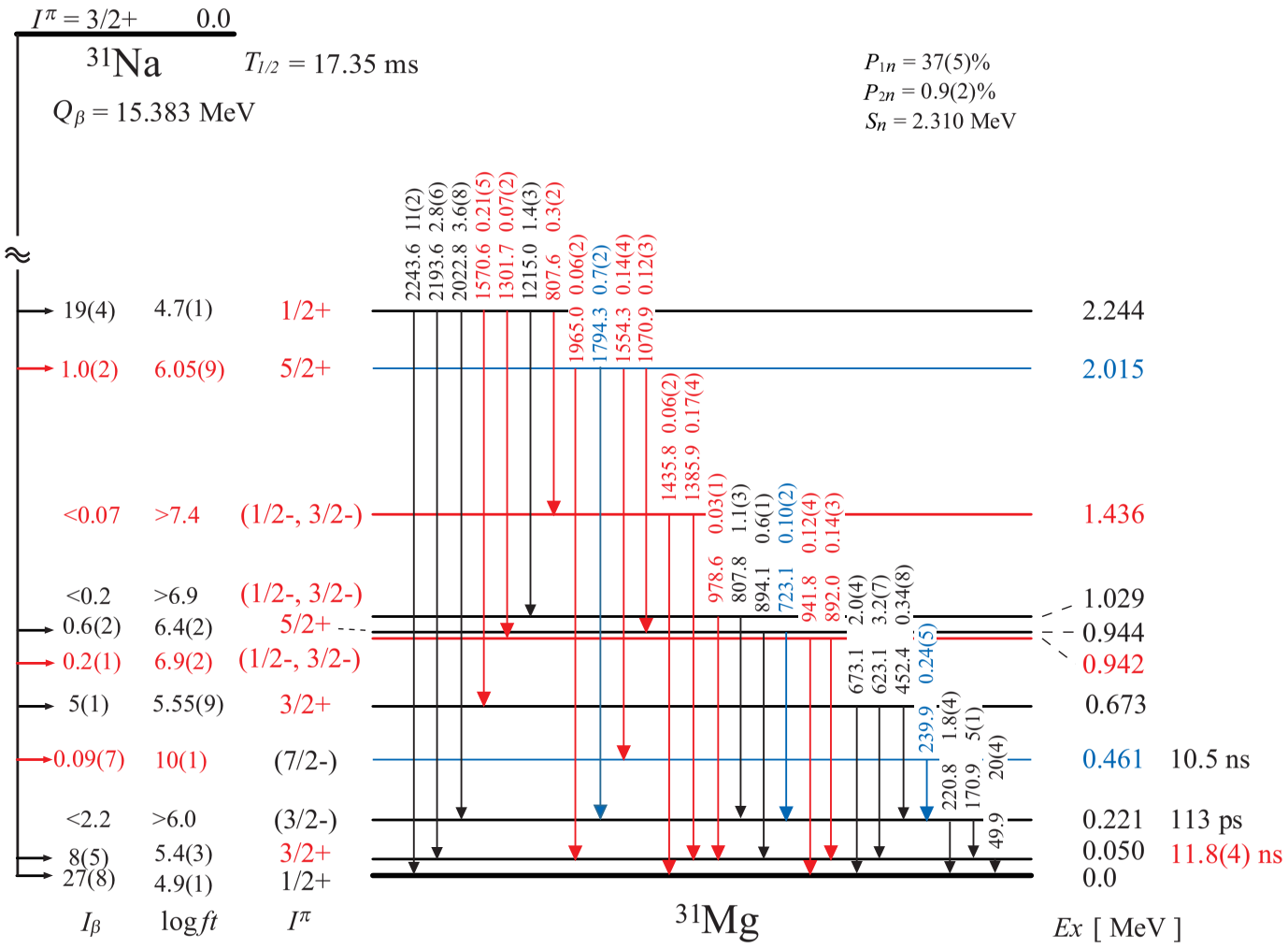

Figure 5.20: Decay scheme of ^{31}Na $\rightarrow$ ^{31}Mg. The transitions and levels indicated in red were observed and are newly proposed, respectively, for the first time. The transitions and levels in blue were observed for the first time in the β decay of ^{31}Na.

5.8 Neutron TOF spectrum

So far, the levels below the neutron separation energy (S_n; 2.3 MeV for ^{31}Mg) are discussed. In this work, in order to construct the level scheme above S_n the β-delayed neutrons were detected by the thick and large plastic scintillators placed at 1.5 m downstream of the Pt stopper, as shown in Sec. 3.4.3.

Figure 5.21 shows the time difference spectrum between β rays detected by the thin plastic scintillators and neutrons detected by neutron detectors. This spectrum was constructed by using summing up the data of three neutron detectors. By the previous work [BAU87], neutron peaks at 1.6-, 1.0-, 0.7-, and 0.5-MeV were reported, although the levels above neutron separation energy were not given. In the present work, there are clear peaks around 90, 110, 130, and 160 ns, which correspond to 1.6-, 1.0-, 0.7-, and 0.5-MeV neutrons, and the statistics and S/N of the neutron spectrum are improved much. The γ rays were also measured by Ge detectors with high energy resolution and efficiency in this work, and the coincidence measurement of β-γ-neutron enables us to construct the level scheme above the neutron separation energy.

In addition to this, the β-ray asymmetry was measured, as shown in Fig. 5.22. The anisotropy of β rays coincident with the neutron enable us to assign the spin-parity of the levels above S_n. The detailed results are discussed in the other thesis [KAN16].

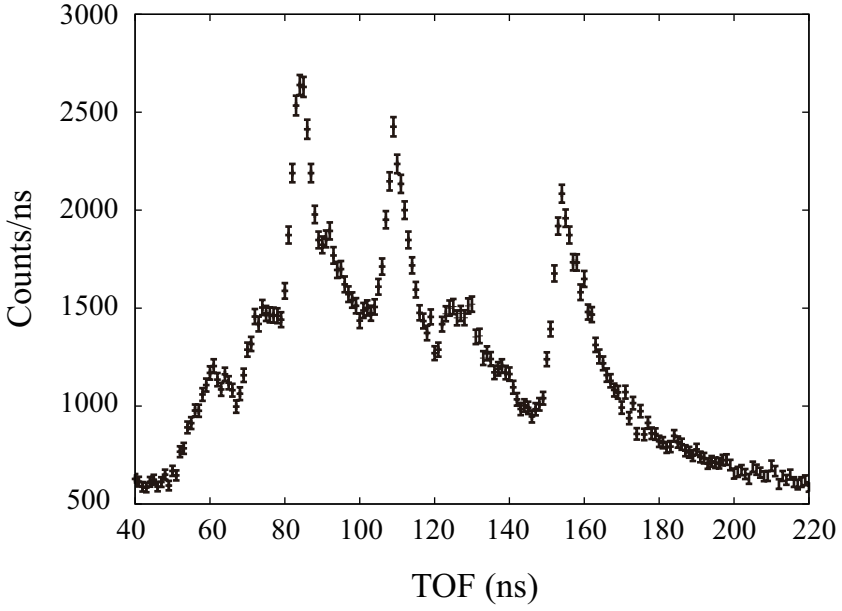

Figure 5.21: Neutron TOF spectrum (time difference between β rays and neutron).

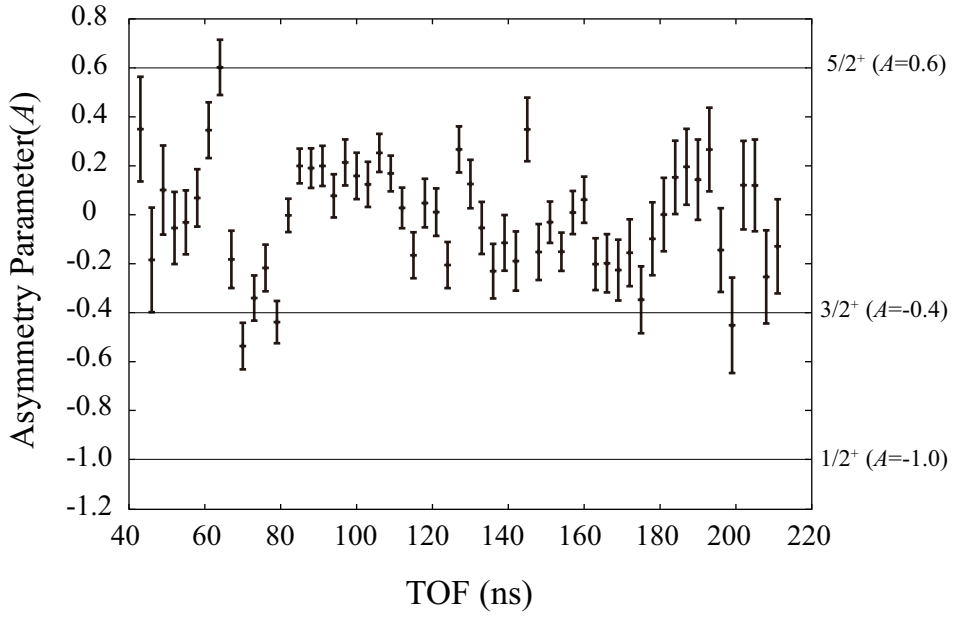

Figure 5.22: Beta ray asymmetry spectrum. Each point is plotted at 3 ns intervals. The lines indicate the expected A values for the spin-parity shown on right-hand.

CHAPTER VI

Results -^{30}Mg-

6.1 Gamma rays in ^{30}Mg

Figure 6.1 shows the total γ-γ projection spectrum of the β decay of ^{30}Na $\rightarrow$ ^{30}Mg. In the figure, most of the peaks are associated with the β decays of ^{30}Na (asterisks) [TAJ12], ^{30}Mg (closed squares) [HIN08], ^{30}Al (closed triangle) [ALB74], ^{29}Mg (open squares) [GUI84], and ^{29}Al (open triangles) [ALB82] and with the β-delayed one neutron decay of ^{30}Na (crosses) [BAU89]. Figure 6.2 shows the γ-ray energy spectrum gated by higher than 5-MeV β rays. The γ rays emitted from the β decay and the β-delayed one neutron decay of ^{30}Na are labeled with asterisks and crosses, respectively. It is clearly found that the γ-ray peaks from the β decay and β-delayed one neutron decay of ^{30}Na with large Q-values of 17.270 MeV [BAS10] are only observed in the spectrum. The peaks of γ rays emitted from the daughter and granddaughter nuclei with relatively small Q-values are suppressed in the spectrum.

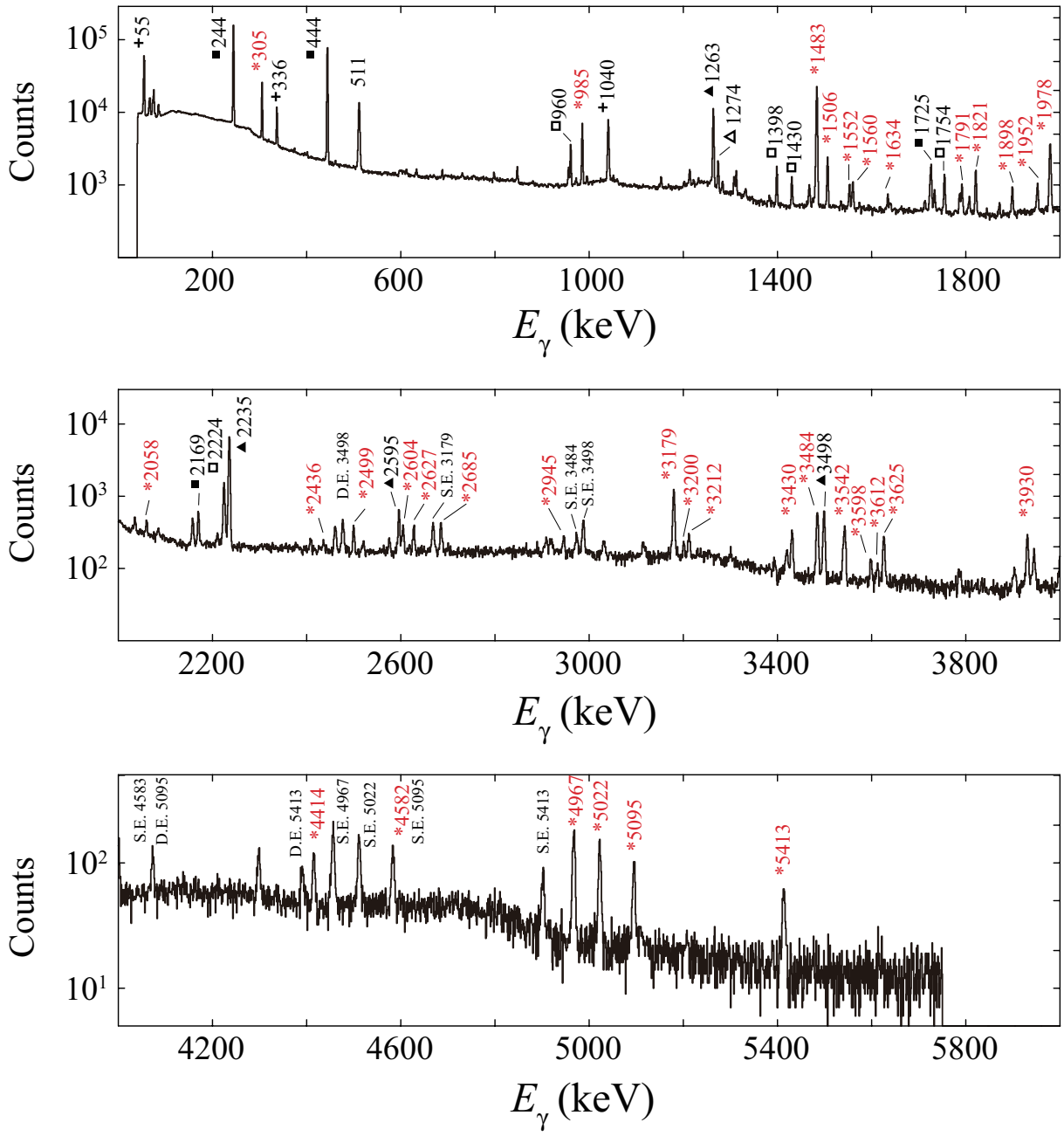

Figure 6.1: Total γ-γ projection spectrum in a time window of $\pm$ 800 ns for ^{30}Mg. The γ-ray peaks are associated with β decays of ^{30}Na (asterisks) [TAJ12], ^{30}Mg (closed squares) [TAJ12], ^{30}Al (closed triangles) [ALB74], ^{29}Mg (open squares) [GUI84], ^{29}Al (open tringles) [ALB82], and β-delayed one neutron decay of ^{30}Na (crosses) [BAU89]. The numbers are the γ-ray energies in keV. The single and double escape peaks are labeled with S.E. and D.E., respectively.

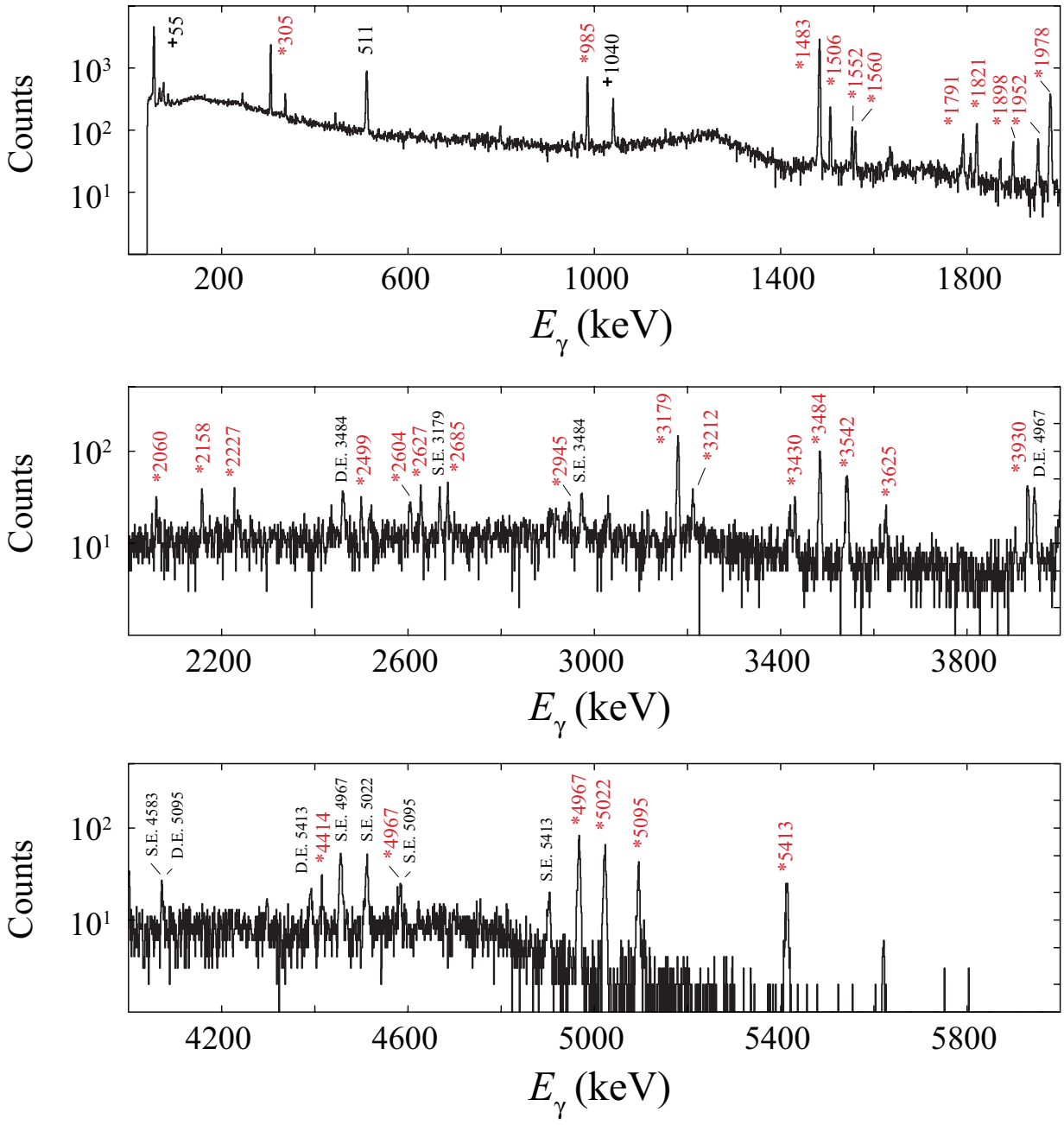

Figure 6.2: β-γ coincidence spectrum gated by higher than 5-MeV β rays. The peaks labeled with asterisks and crosses are known γ rays from the β decay [TAJ12] and the β-delayed neutron decay of ^{30}Na [BAU89], respectively. The numbers are γ-ray energies in keV. The single and double escape peaks are labeled with S.E. and D.E. ,respectively.

6.2 Construction of the decay scheme of ^{30}Na $\rightarrow$ ^{30}Mg

The level scheme construction for ^{30}Mg was performed by using the γ-γ coincidence data in the same manner of level scheme construction of ^{31}Mg, as discussed in Chapter V.

6.2.1 Previously reported 1.483-, 1.788-, 2.468-, 3.304-, 3.543-, 4.967-, 5.022-, 5.095-, 5.413-MeV levels

The energy levels at 1.483, 1.788, 2.468, 3.304, 3.543, 4.967, 5.022, 5.095, and 5.413 MeV have been well-studied and established by the β decay of ^{30}Na [TAJ12; BAU89; MAC05; SCH09; GUI84], β-delayed neutron decay of ^{31}Na [KLO93; GUI84], and fusion-evaporation reaction of ^{14}C(^{18}O, 2p) [DEA10].

The 1.483-MeV level is the first excited level in ^{30}Mg which is populated by the 1483-keV γ ray. This γ ray was also observed as the most intense γ-ray peak in this work, so that the 1483-keV γ ray is most likely the first $2^+ \rightarrow 0^+$ (1.483 MeV $\rightarrow$ g.s.) transition. The second excited state at 1.788-MeV level is a candidate for the second 0^+ state [SCH09]. In the γ-ray energy spectrum gated by the 1483 keV peak, the intense 305-keV γ-ray peak was observed, as shown in Fig. 6.3. The cascade relations between 1483- and 305-keV γ rays lead to the existence of the 1.788-MeV level.

The γ-ray peak of 985 keV was also clearly observed in the 1483-keV γ-ray gate spectrum in Fig. 6.3. On the other hand, the coincidence relation between the γ rays of 985 and 305 keV is not found in the energy spectrum gated by 985- or 305-keV γ rays. Therefore, the 2.468-MeV level was reasonably placed based on the cascade relation of the 985- and 1483-keV γ rays.

The 3.304-MeV level has been reported in the previous reports [TAJ12; MAC05; SCH09; TAK09]. This level is considered to be depopulated by the 1821-keV transition to the 1.483-MeV level. In Ref. [BAU89; KLO93; GUI84], the 1821-keV γ ray was assigned to different placement as a transition of 1.821 MeV $\rightarrow$ g.s.. In this work, the 1821-keV γ ray peak is observed in the coincidence spectrum gated by 1483 keV, as shown in Fig. 6.3, therefore the 1821-keV transition which depopulates the 3.304-MeV level was placed above the 1.483-MeV level.

The 3.543-MeV level was depopulated by the 3542- and 2060-keV γ rays. The 3542- and 2060-keV γ ray was clearly observed in the β-γ coincidence spectrum gated by higher than 5-MeV β rays in Fig. 6.2. The 2060-keV γ-ray peak was also clearly observed in the 1483-keV gate spectrum in Fig. 6.3. The energy consistency between the 3542-keV γ-ray energy

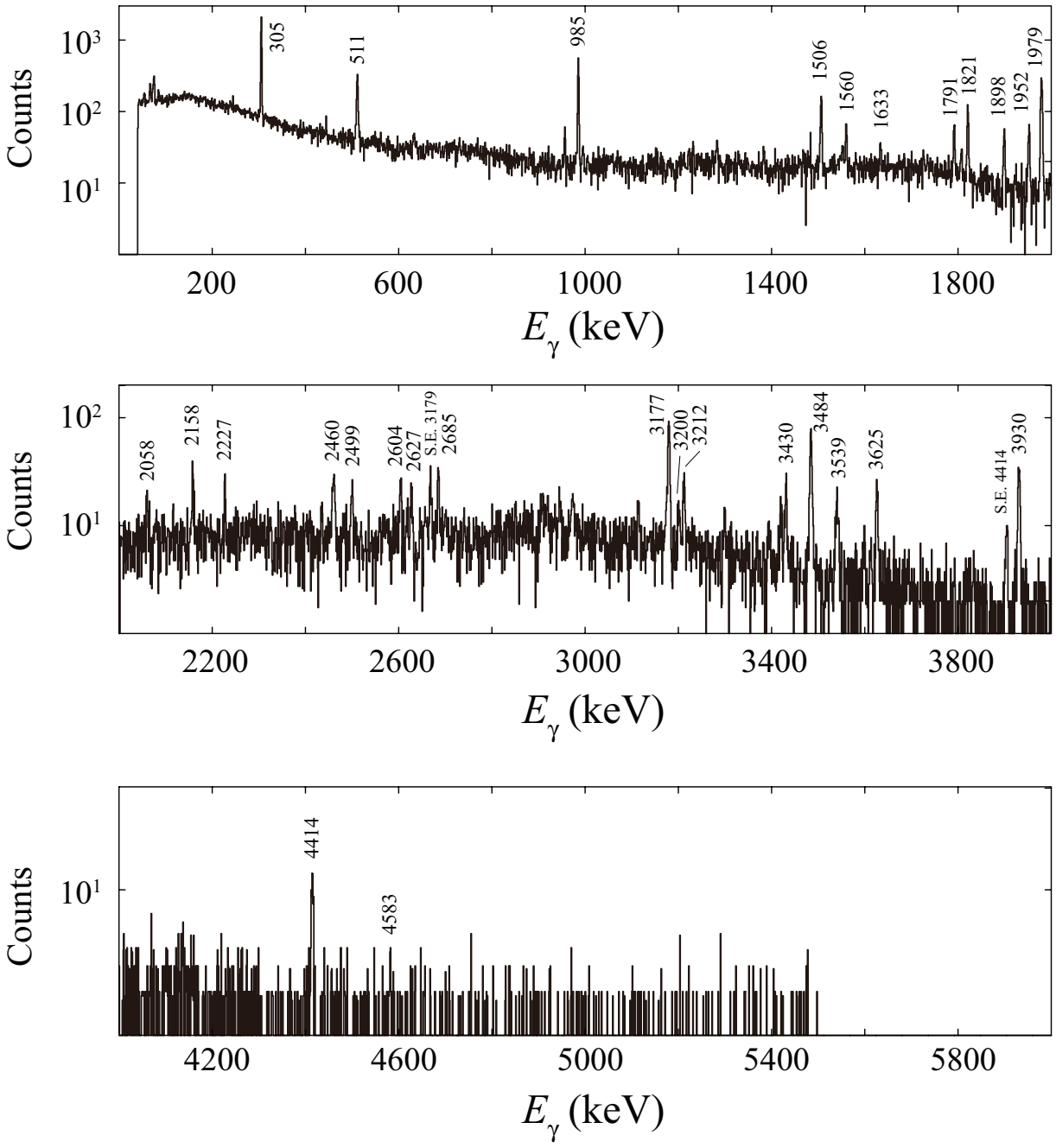

Figure 6.3: Gamma-ray energy spectrum gated by the 1483-keV γ ray. The numbers are γ-ray energies in keV. The γ rays labeled with S.E. are single escape peaks.

[3542.4(1)] and 3542.6(1) [1483.1(1) + 2059.5(1)] supports the existence of the 3543-MeV level.

The 4.967-MeV level has been observed only in the β decay of ^{30}Na [TAJ12; BAU89; MAC05; SCH09; GUI84]. They have reported the γ rays of 4967 (4.967 MeV $\rightarrow$ g.s.), 3484 (4.967 MeV $\rightarrow$ 1.483 MeV), 3179 (4.967 MeV $\rightarrow$ 1.788 MeV), and 2499 keV (4.967 MeV $\rightarrow$ 2.468 MeV) depopulating the 4.967-MeV level. These γ rays were observed in this work and the coincidence relations are also consistent with the previous reports.

The 5.022-MeV level was depopulated by the γ rays of the 5022 (5.022 MeV $\rightarrow$ g.s.), 3539 keV (5.022 MeV $\rightarrow$ 1.483 MeV) [TAJ12; BAU89; GUI84], and 2554 keV (5.022 MeV $\rightarrow$ 2.468 MeV) only reported in Ref. [TAJ12]. In the present work, the 5022- and 3539-keV transitions were confirmed in the β-γ coincidence spectrum in Fig. 6.2 and γ-γ coincidence spectrum gated by 1483 keV, respectively. However, the 2554-keV transition was not found in γ-ray energy spectrum gated by the 985-keV γ ray and also in the β-γ coincidence spectrum. The 5.095-MeV level was depopulated by the 5095- (5.095 MeV $\rightarrow$ g.s.), 3612- (5.095 MeV $\rightarrow$ 1.483 MeV), 2627- (5.095 MeV $\rightarrow$ 2.468 MeV), 1791- (5.095 MeV $\rightarrow$ 3.304), 1552-keV (5.095 MeV $\rightarrow$ 3.543 MeV) γ rays [TAJ12; BAU89; MAC05; SCH09; GUI84]. All the γ rays observed in β-γ coincidence spectrum shown in Fig. 6.2. The coincidence relations between these γ rays are consistent with those in previous works. The energy consistency between energy sums of 5094.9(1) [3542.5(1) + 1552.4(1)], 5095.0(3) [3304.7(2) + 1791.3(1)], 5095.1(1) [2468.0(1) + 2627.1(1)], 5095.1(3) [1483.1(1) + 3612.0(3)], and γ ray energy of 5094.7(1) also supports the placement of the 5.095-MeV level.

The 5.413-MeV level has been established by the γ rays of 5413 (5.413 MeV $\rightarrow$ g.s.), 3930 (5.413 MeV $\rightarrow$ 1.483 MeV), 3625 (5.413 MeV $\rightarrow$ 1.788 MeV), and 1871 (5.413 MeV $\rightarrow$ 3.543 MeV) which depopulates this level [TAJ12; BAU89; SCH09; GUI84], and the transition of 2945 keV (5.413 MeV $\rightarrow$ 2.468 MeV) was reported only in the Ref. [TAJ12]. These γ rays including the 2945-keV γ ray are also confirmed in this work, and the coincidence relations are consistent with the previous work. The energy sums of 5413.5(2) [3542.5(1) + 1871.0(1)], 5413.3(2) [2468.0(1) + 2945.3(1)], 5413.3(1) [1483.1(1) + 3930.2(1)] and 5.413.0(2), and γ-ray energy of 5.413.0(1) show very close energies, therefore these γ rays are most likely γ rays depopulating the 5.413-MeV level.

6.2.2 Previously reported 3.461-MeV level and newly proposed 3.463-MeV level

The 3.461-MeV was reported in the β decay of ^{30}Na [TAJ12; BAU89; MAC05; SCH09; GUI84] and the β-delayed neutron decay of ^{31}Na [KLO93]. In the level scheme of previous

work [TAJ12; BAU89; MAC05; SCH09; GUI84; KLO93], this level was depopulated by the 1978-keV transition (3.461 MeV $\rightarrow$ 1.483 MeV), and was mainly populated by the 1506-, 1560-, and 1952-keV γ rays. In this work, in addition to the 3.461-MeV level, a new level at 3.463 MeV, which is depopulated by 1980-keV transition is proposed. There are two reasons for placing the new 3.643-MeV level in the level scheme.

(1) Width of the peak at 1978-1980 keV (FWHM 3.7 keV) is wider than that expected from energy resolution of Ge detectors (FWHM 3.1 keV).

(2) The peak positions of 1978-1980 keV are different between the energy spectra gated by the 1560- and 1506-keV γ rays, as shown in Fig. 6.4 (a).

These facts strongly suggest the existence of another unsolved 1980-keV peak, and it leads to placing a new level at 3.463 MeV in the level scheme of ^{30}Mg.

These peak positions of the 1978.1(1) and 1979.6(1) were determined in the peak fitting in the spectra gated by the 1506- and 1560-keV γ rays, respectively. A level at 3.463 MeV which is populated by the 1980-keV transition was newly proposed in this work based on the evidences mentioned above. The placement of the γ ray of 1560 keV, which was above the 3.461-MeV level in previous works [TAJ12; BAU89; GUI84; KLO93], was changed and the 1560-keV is placed as a transition of (5.022 MeV $\rightarrow$ 3.463 MeV). The energy consistency between 3462.7(1) [1483.1(1) + 1979.6(1)] and 3462.6(1) [5022.2(1) - 1559.6(1)] also supports this assignment. The same examination was performed for the cascade γ rays of 1506 and 1978 keV. The energy sums of 3461.1(1) [4967.0(1) - 1505.9(1)] and 3461.2(1) [1483.1(1) + 1978.1(1)] are consistent with each other.

In order to make sure of these very close energy-level assignments, level energies of 3.461 and 3.463 MeV were calculated from various transition passes, as shown in Fig. 6.5. The each data point shows calculated level energies of 3.461 or 3.463 MeV by using γ-ray energies of 1505.9(1), 1559.6(1), 1952.0(2), 1221.9(2), 2157.6(1), 2458.9(3), 2605.1(2), and 1633.2(3) keV. The γ rays of 1221.9(2), 2157.6(1), 2458.9(3), 2605.1(2), and 1633.2(3) keV are discussed following sections. The lines indicate the level energies calculated from the γ rays of 1979.6(1) and 1978.1(1) keV, each width corresponds to the errors for 1 σ. It is clearly found that two data points from 1560- and 2459-keV γ-rays are consistent with the line of 3462.7(1) keV within error bars, the others are consistent with that of 3461.2(1) keV. Therefore, it is confirmed that the transitions of 1560 and 2459 keV populate 3.463-MeV level, and the others populate 3.461-MeV level.

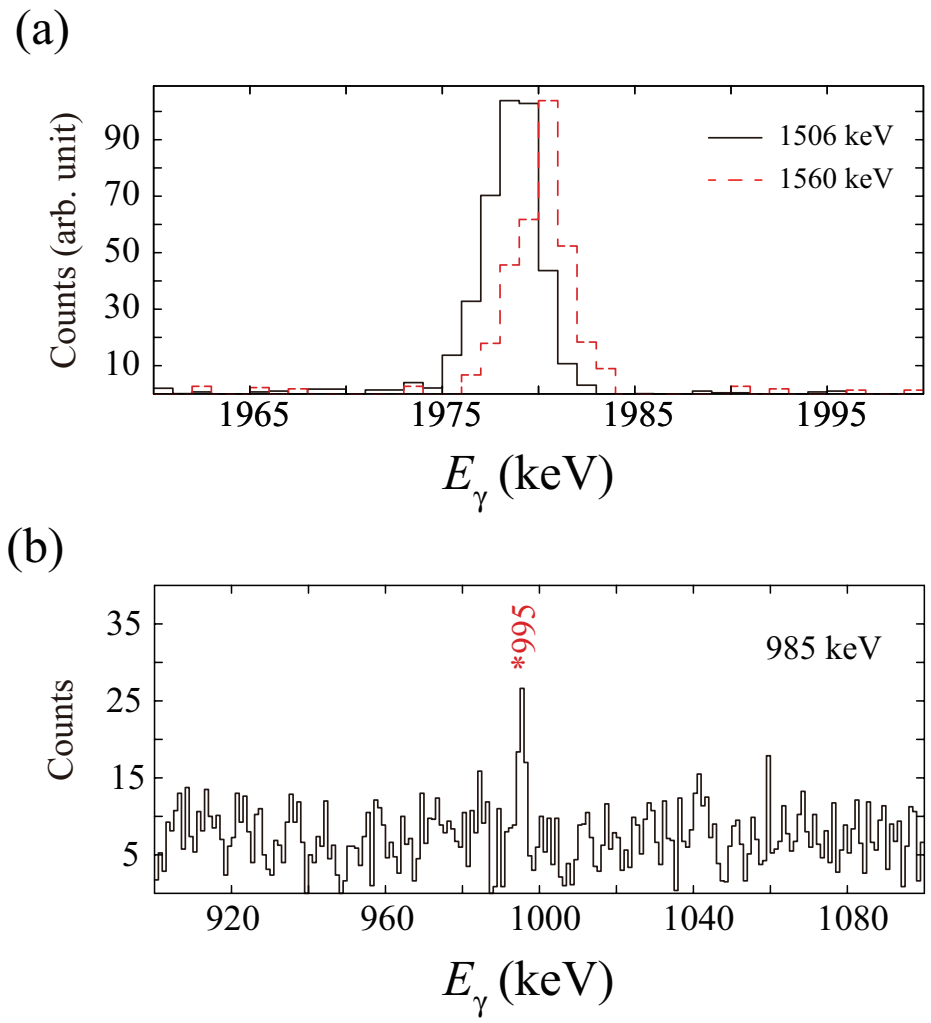

Figure 6.4: (a) Peaks at 1978-1980 keV in energy spectra gated by the 1506- (solid line) and 1560-keV (dashed line) and (b) γ-ray energy spectrum gated by the 985-keV γ ray. The numbers are γ-ray energies in keV.

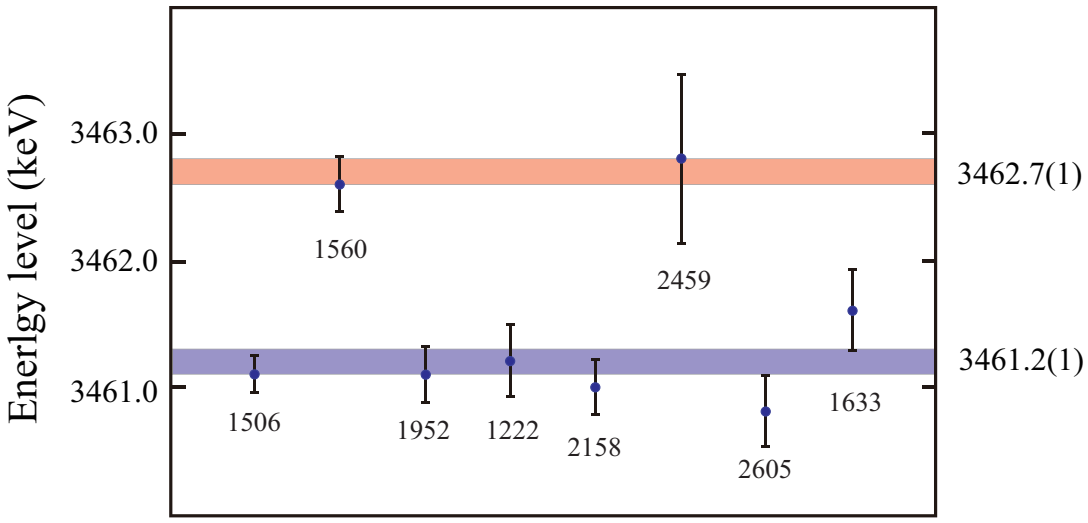

Figure 6.5: Level energies of 3.461 and 3.463 MeV calculated by the γ-ray energies of 1505.9(1), 1559.6(1), 1952.0(2), 1222(2), 2157.6(1), 2458.9(3), 2605.1(2), and 1633.2(3) keV. The lines shows the level energies calculated from the γ rays of 1979.6(1) and 1978.1(1) keV, and each width corresponds to the errors for 1 σ.

A new 995-keV γ-ray peak was observed in γ-ray energy spectrum gated by the 985-keV γ ray, as shown in Fig. 6.4. The energy sum of 3462.7(2) [2468.0(1) + 994.7(2)] lead to assignment of 995-keV transition to 3.463 MeV $\rightarrow$ 2.468 MeV.

6.2.3 Previously reported 3.381-, 4.259-, 4.683-, 4.695-, 5.898-, 6.066-MeV levels

The 3.381- and 4.259-MeV levels were established by the fusion evaporation reaction of ^{14}C(^{18}O, 2p) [DEA10]. The 3.381-MeV level was largely populated by fusion reaction and was strongly connected to the first 2^+ state, thus this level was considered to be the 4^+ state of the ground band. The γ-ray angular distribution coefficients for the 1898-keV transition (3.381 MeV $\rightarrow$ 1.483 MeV) reported in Ref. [DEA10] also support this assignment. In Ref. [TAJ12], the 1898-keV transition was observed in the β decay of ^{30}Na for the first time. In the present work, the 1898-keV γ-ray peak was also found in β-γ coincidence spectrum and in the γ-ray energy spectrum gated by the 1483-keV γ ray, as shown in Figs. 6.2 and 6.3, respectively.

The 4.259-MeV level was depopulated by 880-keV γ ray in Ref. [DEA10]. This γ-ray peak could not be confirmed in the γ-ray energy spectrum gated by 1898 keV, in this work. It is noted that there is something like a peak around 880 keV, however, this peak is very small and the peak height is as same as background level. On the other hand, the 956-keV

γ ray peak was observed in the energy spectrum gated by the 1821-keV γ ray. The energy sum of 4.259.4(2) [3303.7(1) + 955.7(2)] is very close to the level energy of reported 4.259 MeV.

The level at 4.683-MeV was observed only in the β decay of ^{30}Na in Ref. [TAJ12]. The two transitions of 3200 (4.683 MeV $\rightarrow$ 1.483 MeV) and 2216 keV (4.683 MeV $\rightarrow$ 2.468 MeV) which depopulate the 4.683-MeV level was reported. The 3200-keV γ-ray peak was found in the energy spectrum gated by the 1483-keV γ ray, however, the 2216-keV γ-ray peak could not be found in any spectra. Instead of 2216-keV peak, a 1222-keV γ ray was observed in the enegy spectrum gated by 1483 keV. Figure 6.6 shows the γ-ray energy spectra gated by the 1222- and 3200-keV γ rays. The 1483-keV peak was clearly found in both of the gate spectra in Fig. 6.6, and the 1978-keV peak was observed in the 1222-keV gate spectrum. The energy sum of 4683.0(2) [3461.1(1) + 1221.9(2)] was consistent with that of 4683.1(2) [1483.1(1) + 3200.0(2)], thus the 4.683-MeV level was reasonably placed in the level scheme.

The level at 4.695 MeV was proposed only in Ref. [TAJ12], and the 3212- and 2227-keV γ rays which depopulate the 4.695-MeV level were reported. In this work, these two γ rays were also observed in the energy spectra gated by the 1483 keV, as shown in Fig. 6.3. In addition, a 1152-keV γ-ray peak was newly observed in the energy spectrum gated by the 3542-keV γ ray, as shown in Fig. 6.7. The energy consistency between 4694.6 (2) [1483.1(1) + 3211.5(2)], 4694.6(2) [2468.0(1) + 2226.6(2)], and 4694.5(3) [3542.5(1) + 1152.0(3)] strongly supports the placement of the 4.695-MeV level.

The 5.898-MeV level was proposed by the coincidence relation between 1483- and 4415-keV γ rays in Ref. [TAJ12]. In Ref. [BAU89], they also found the 4415-keV γ ray and assigned this γ transition to 4.415 MeV $\rightarrow$ g.s.. In Ref [TAJ12], two additional γ rays of 3430 keV (5.898 MeV $\rightarrow$ 2.468 MeV) and 2437 keV (5.898 MeV $\rightarrow$ 3.461 MeV) were proposed. In this work, the coincidence relation between 1483- and 4415-keV γ rays were confirmed in Fig. 6.3. The placement of 3430-keV γ ray in Ref. [TAJ12] was also consistent with coincidence relation by our data. These facts support the level placement in Ref. [TAJ12] Although the 2437-keV γ-ray peak could not be confirmed in the present work, this does not affect the placement of 5.898-MeV level.

The 6.066-MeV level was reported only by Ref. [TAJ12] in β decay of ^{30}Na. The 6.066-MeV level was established based on finding γ rays of 4583 (6.066 MeV $\rightarrow$ 1.483 MeV), 3598 (6.066 MeV $\rightarrow$ 2.468 MeV), 2685 (6.066 MeV $\rightarrow$ 3.381 MeV), and 2604 keV (6.066 MeV $\rightarrow$ 3.461 MeV) [TAJ12]. In the present work, these four γ rays were also confirmed, and another two γ rays were newly found in the present work. A 1807-keV γ ray was newly observed in

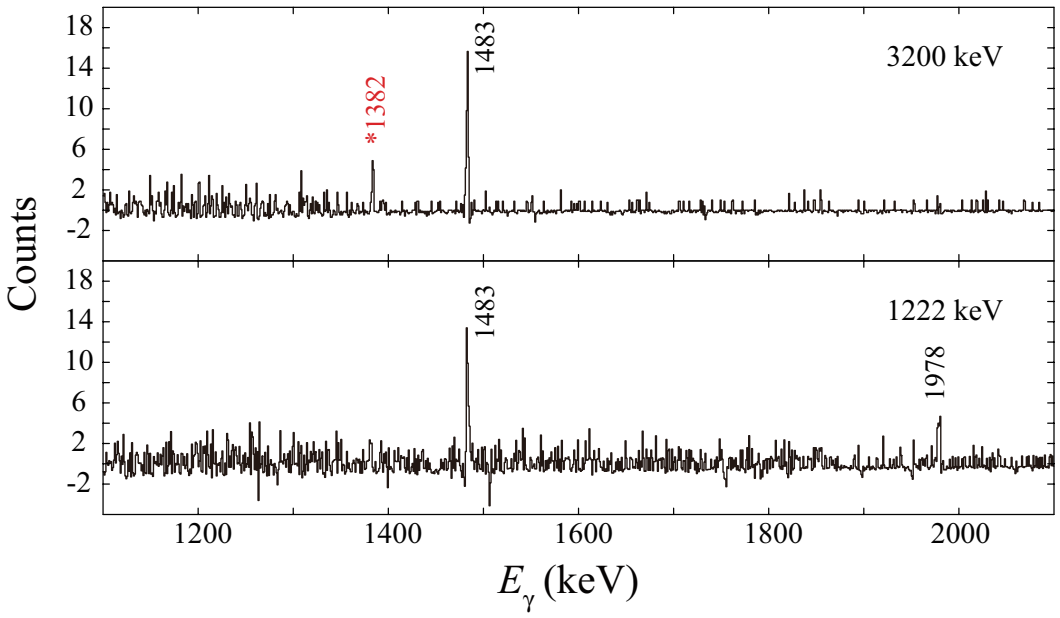

Figure 6.6: Gamma-ray energy spectrum gated by the 3200- and 1222-keV γ rays. The γ-ray energy are labeled in keV. The peaks with asterisks are newly found in this work.

coincidence spectrum gated by 956-keV γ ray, thus this γ ray corresponds to a transition of 6.066 MeV $\rightarrow$ 4.259 MeV. In 3200- and 1483-keV gate spectra, a new 1382-keV γ-ray peak was observed,as shown in Fig. 6.6, thus we reasonably assigned this γ ray to a transition of 6.066 $\rightarrow$ 4.683 MeV.

6.2.4 Newly proposed 4.297-MeV level

A 4.297-MeV level was newly proposed in this work, as folloing. First of all, a γ-ray peak at 4297 keV was found in β-γ coincidence spectrum gated by higher than 5-MeV β rays, as shown in Fig. 6.8 (a). Although the 4297 keV peak possibly is due to single escape of 4810-keV γ ray associated with β decay of ^{30}Al with Q-value of 8.6 MeV, there still found this peak in β-γ coincidence spectrum gated by higher than 5-MeV β rays, thus there is a 4297 keV peak associated with β decay with at least 9.3 MeV [5 + 4.3] Q-value. Only β decay of ^{30}Na satisfies this requirement, therefore, we conclude that the 4297-keV γ ray was associated with ^{30}Mg.

For the next step, energy spectrum gated by the 4297-keV γ ray was made, as shown in Fig. 6.8 (b). In the spectrum, we could not found known γ-ray peak from β decay of ^{30}Na, however new three peaks of 670, 724, and 797 keV which are coincident with 4297-keV γ ray were observed. It is found that the energy sums of 5094.6(4) [797(2) + 4297.2(3)], 5021.6(5) [724.4(4) + 4297.2(3)], and 4966.7(4) [669.5(3) + 4297.2(3)] were consistent with the known

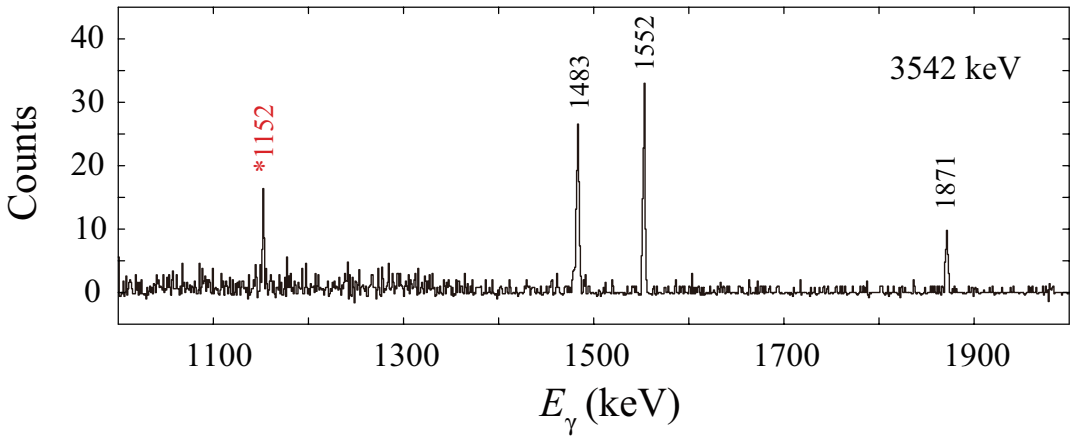

Figure 6.7: Gamma-ray energy spectrum gated by 3542-keV γ ray. The numbers are γ-ray energies in keV. Newly found γ rays in this work is labeled with asterisks.

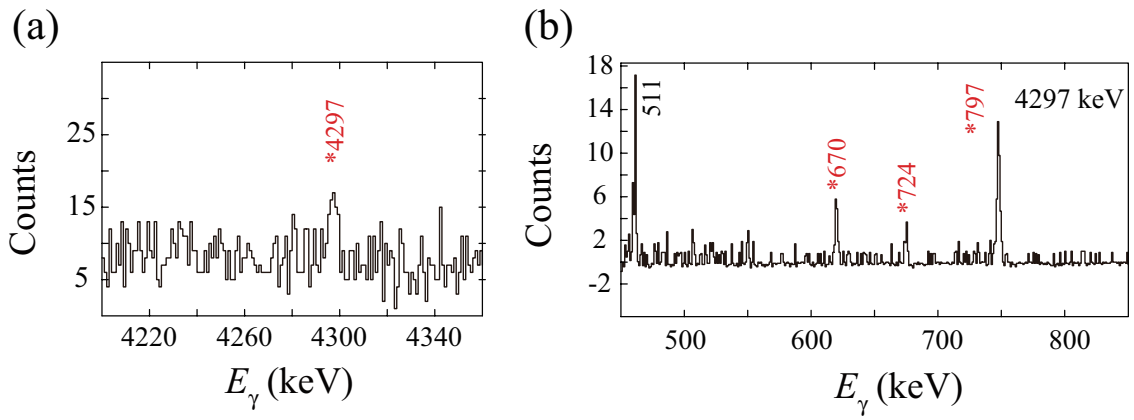

Figure 6.8: (a) β-γ coincidence spectrum gated by higher than 5-MeV β ray and (b) γ-γ coincidence spectrum gated by 4297-keV γ ray. The γ-ray peaks labeled with asterisks are newly observed in this work. The numbers are γ-ray energies in keV.

5.095-, 5022-, and 4967-MeV levels in ^{30}Mg, respectively. Therefore, we assigned these three γ rays to those of ^{30}Mg and proposed a new level at 4.297 MeV which is populated by the 670, 724, and 797-keV transitions and is depopulated by the 4297-keV transition.

6.2.5 Newly proposed 4.783-MeV level

A new level at 4.783 MeV was proposed based on the γ-γ coincidence analysis. In this work, new γ rays of 3300, 1283, and 1480 keV were proposed. Figure 6.9 shows the γ-γ coincidence spectra gated by the 1483-, and 3300-keV γ rays. The 3300- and 1283-keV γ-ray peaks are clearly observed in energy spectra gated by the 1483-keV γ ray, and the 1283- and 1483-keV γ-ray peaks are found in the 3300-keV gate spectrum in Fig. 6.9. These facts

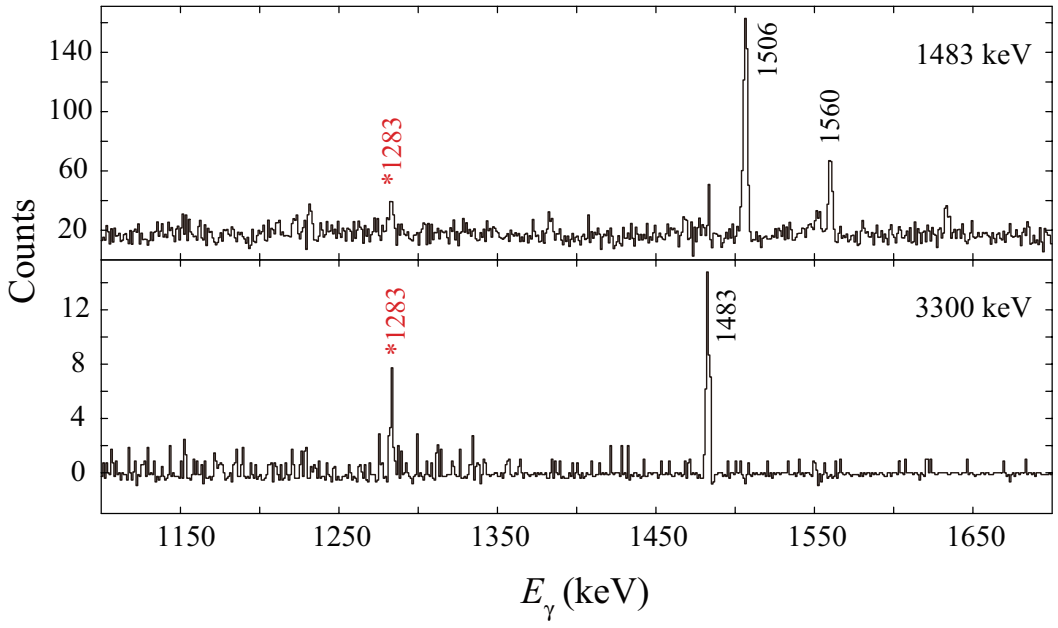

Figure 6.9: Gamma-ray coincidence spectra gated by 1483 and 3300 keV γ rays. The numbers are γ-ray energies in keV. The γ-ray peaks with asterisks are newly observed in this work.

indicate the cascade relation between 1483-, 3300-, and 1283-keV γ rays. The energy sum of these three γ rays was 6066.2(3) [1483.1(1) + 3300(3) + 1283.0(1)] keV, which is consistent with level energy of 6.066 MeV [6065.9(2)]. Therefore, possible placements of these 3300- and 1283-keV transitions are 6.066 MeV $\rightarrow$ 4.783 MeV $\rightarrow$ 1.483 MeV or 6.066 MeV $\rightarrow$ 2.766 MeV $\rightarrow$ 1.483 MeV. Taking a careful looking at the energy spectrum gated by 1821 keV, a small tail of 1483-keV γ-ray peak at a lower energy part, which is not observed in other gate spectra, was found, as shown in Fig. 6.10 (a). Figure 6.10 (b-1) and (b-2) show the γ ray energy spectrum gated by the peak and tail regions of 1483-keV peak, respectively. In the comparison between Fig. 6.10 (b-1) and (b-2), the 1483-keV γ ray peak is clearly observed in Fig. 6.10 (b-1). The γ-ray peak of 1821 keV in Fig. 6.10 (b-1) was emphasized relative to other γ-ray peaks observed in Fig. 6.10 (b-2). From these evidences, a new 1480-keV γ ray, which have a cascade relation with 1821 and 1483 keV, was proposed. The energy sum of 1480-, 1821-, and 1483-keV γ rays is 4783.2(5) [1479.5(5) + 1820.6(2) + 1483.1(1)], this value is consistent with the energy sum of 4783.2(1) [3300.1(1) + 1483.1(1)]. Therefore, we reasonably proposed a new level at 4.783 MeV which was depopulated by 3300- and 1480-keV γ rays and populated by 1283-keV γ ray.

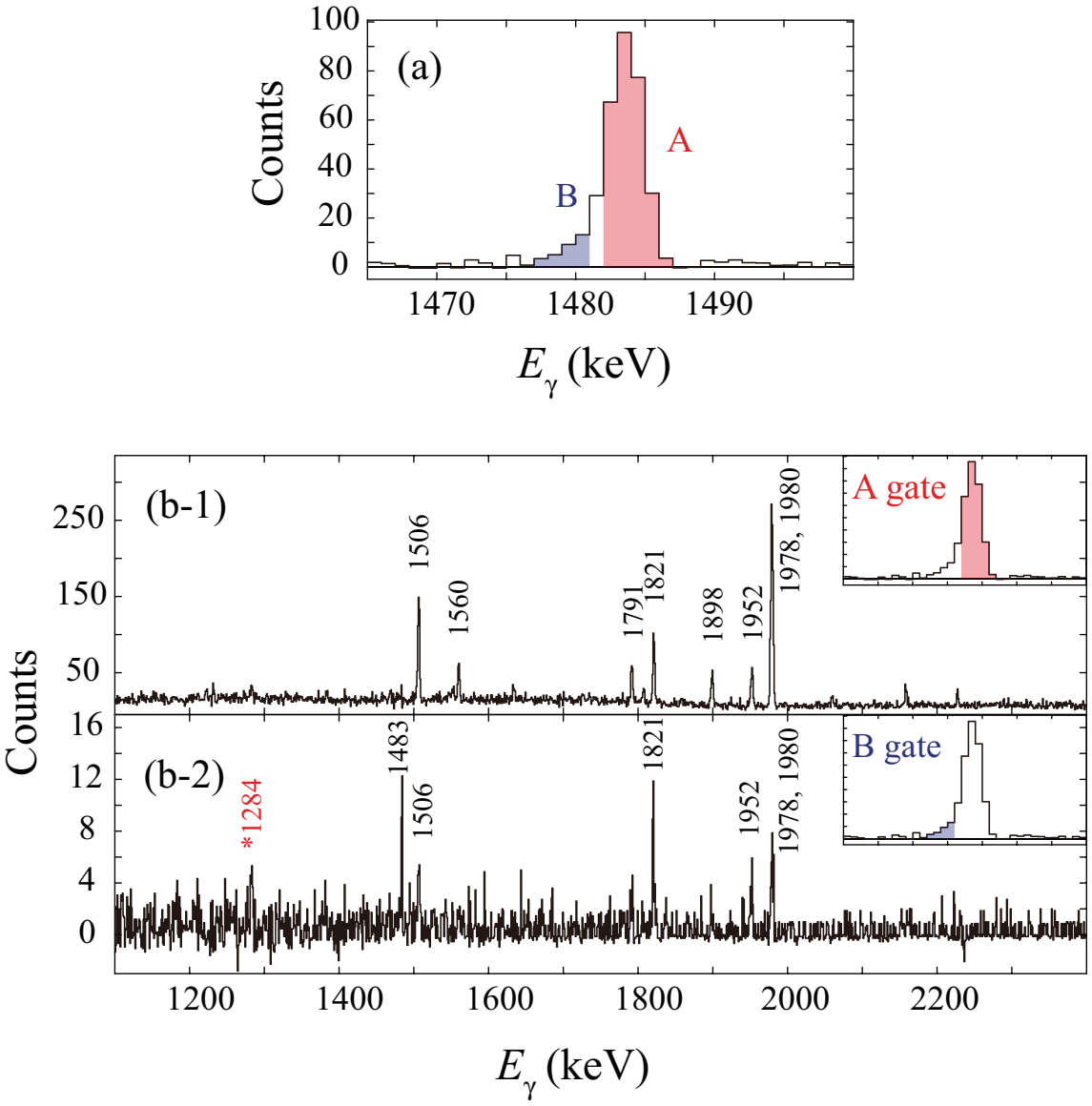

Figure 6.10: (a) Peak at 1483 keV in γ-ray energy spectrum gated by 1821 keV and γ-γ coincidence spectra gated by the energy regions of (b-1) peak and (b-2) tail parts of the 1483-keV peak, respectively. The gate region of peak and tail parts are shown as "A" in red and "B" in blue, respectively. The numbers are γ-ray energies in keV.

6.2.6 Newly proposed 5.619- and 5.922-MeV level

The 5.619- and 5.922-MeV levels were newly proposed in this work. The 5.619-MeV level was established based on observation of new γ rays of 5619 and 2158 keV. Figure 6.11 (a) shows the γ-ray energy spectrum gated by the 1978-keV peak which depopulate the 3.461-MeV level. In the figure, there found a new 2158-keV peak and this γ-ray peak was observed also in the energy spectrum gated by 1483 keV. In the β-γ coincidence spectrum, a γ-ray peak of 5619-keV was newly observed, as shown in Fig. 6.11 (b). A new level at 5.619 MeV was reasonably proposed in this work based on the energy consistency between γ-ray energy of 5618.6(2) and energy sum of 5618.7(1) [2157.6(1) + 3461.1(1)].

A new level at 5.922 MeV was proposed based on newly found 2618- and 2459-keV γ rays. The γ rays of 1821 and 1980 keV were found in the γ-ray energy spectra gated by 2618 and 2459 keV, respectively, as shown in Fig. 6.12. From the energy consistency between energy sums of 5921.6(3) [2458.9(3) + 3462.7(1)] and 5921.7(5) [2618.0(5) + 3303.7(2)], the new 5.922-MeV level was reasonably proposed in this work.

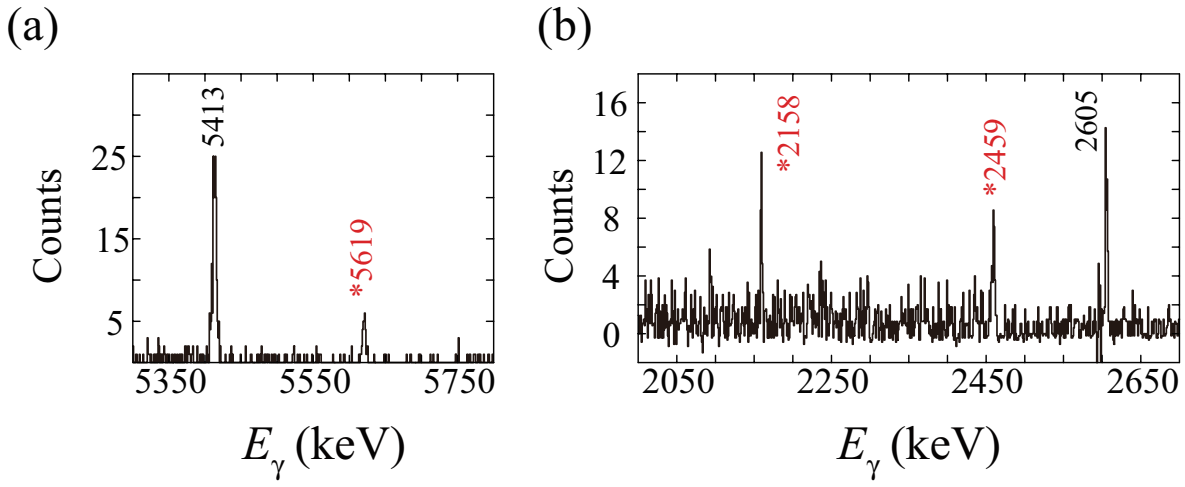

Figure 6.11: (a) Gamma-ray coincidence spectrum gated by higher than 5-MeV β rays and (b) γ-γ coincidence spectrum gated by the 1978-keV γ ray. The peaks labeled with asterisks are newly observed γ-ray peaks in this work. The numbers are γ-ray energies in keV.

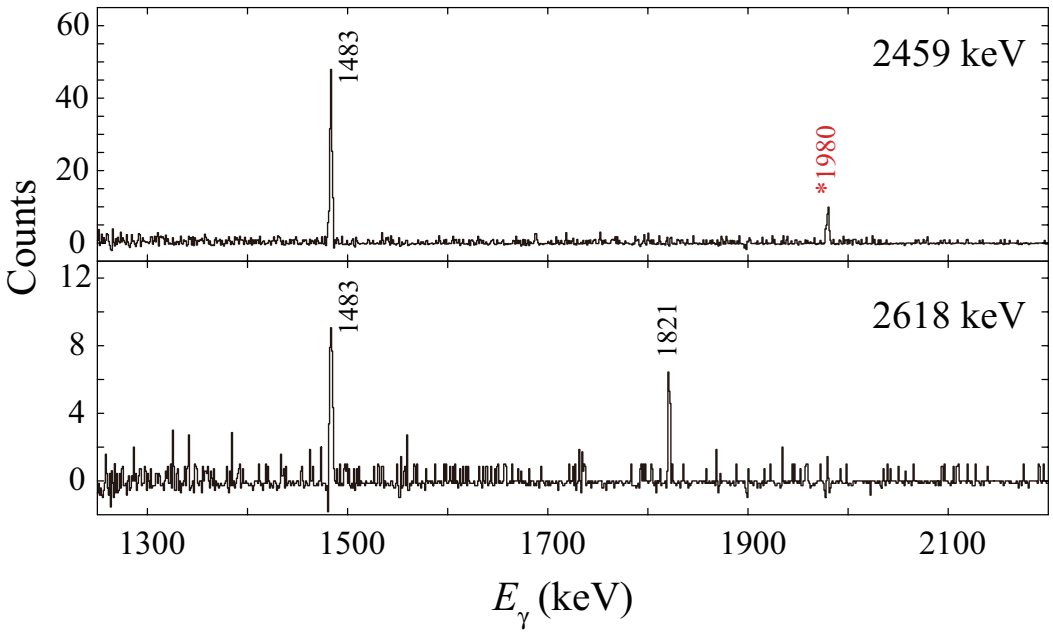

Figure 6.12: Gamma-ray coincidence spectra gated by the 2459- and 2618-keV γ rays. The γ-ray energies are indicated in keV. The newly found γ rays are labeled with asterisks.

6.3 Summary of the γ-γ coincidence relation and γ-ray intensities

The summary of the γ-γ coincidence measurements in ^{30}Na $\rightarrow$ ^{30}Mg data is shown in Table. 6.1. The table shows whether the γ-ray peaks on the first line were observed in the energy spectra gated by the γ rays on the first row. The circles and crosses mean that the coincidence relations were observed and not observed in the coincidence spectrum. The triangles indicate that the coincidence relations should be observed according to the level scheme, however, these were not confirmed because of small statistics or doublet peaks.

The γ-ray energies and intensities in β decay of ^{30}Na $\rightarrow$ ^{30}Mg are listed in Table 6.2. The relative intensities of γ rays are evaluated by the γ ray singles spectrum and efficiency weighted γ-γ matrix. The absolute intensities were deduced by using β decay branch of 69(4)% calculated from the ratios of β-delayed one neutron decay P_{1n} = 30(4)% and two neutron decay P_{2n} = 1.15(25)% [BAS10].

Table 6.1: Summary of observed coincidence relations of the γ rays in ^{30}Mg.

	305	670	724	797	956	985	995	1153	1222	1283	1382	1480	1483	1506	1552	1560	1633	1791	1807	1821	1871	1898	1952	1978	1980	2060	2158	2227	2459	2499	2605	2618	2627	2685	2945	3179	3200	3212
305	-	×	×	×	×	×	×	×	×	×	×	×	○	×	×	×	×	×	×	×	×	×	×	×	×	×	×	×	×	×	×	×	×	×	×	○	×	×
670	×	-	×	×	×	×	×	×	×	×	×	×	×	×	×	×	×	×	×	×	×	×	×	×	×	×	×	×	×	×	×	×	×	×	×	×	×	×	×
724	×	×	-	×	×	×	×	×	×	×	×	×	×	×	×	×	×	×	×	×	×	×	×	×	×	×	×	×	×	×	×	×	×	×	×	×	×	×	×
797	×	×	×	-	×	×	×	×	×	×	×	×	×	×	×	×	×	×	×	×	×	×	×	×	×	×	×	×	×	×	×	×	×	×	×	×	×	×	×
956	×	×	×	×	-	×	×	×	×	×	×	×	○	×	×	×	×	×	○	○	×	×	×	×	×	×	×	×	×	×	×	×	×	×	×	×	×	×	×
985	×	×	×	×	×	-	○	×	×	×	×	×	○	×	×	△	×	×	×	×	×	×	×	×	×	×	×	○	△	○	×	×	○	×	○	×	×	×
995	×	×	×	×	×	○	-	×	×	×	×	×	○	×	×	△	×	×	×	×	×	×	×	×	×	×	×	×	△	×	×	×	×	×	×	×	×	×
1153	×	×	×	×	×	×	×	-	×	×	×	×	○	×	×	×	×	×	×	×	×	×	×	×	×	△	×	×	×	×	×	×	×	×	×	×	×	×
1222	×	×	×	×	×	×	×	×	-	×	△	×	○	×	×	×	×	×	×	×	×	×	×	×	○	×	×	×	×	×	×	×	×	×	×	×	×	×
1283	×	×	×	×	×	×	×	×	×	-	×	△	○	×	×	×	×	×	×	○	×	×	×	×	×	×	×	×	×	×	×	×	×	×	×	×	×	×
1382	×	×	×	×	×	×	×	×	△	×	-	×	○	×	×	×	×	×	×	×	×	×	×	×	×	×	×	×	×	×	×	×	×	×	×	×	○	×
1480	×	×	×	×	×	×	×	×	×	○	×	-	○	×	×	×	×	×	×	○	×	×	×	×	×	×	×	×	×	×	×	×	×	×	×	×	×	×
1483	○	×	×	×	○	○	○	△	○	○	○	○	-	○	○	○	○	○	○	○	△	○	○	○	○	○	○	○	○	○	○	○	△	○	○	○	○	○
1506	×	×	×	×	×	×	×	×	×	×	×	×	○	-	×	×	×	×	×	×	×	×	×	×	○	×	×	×	×	×	×	×	×	×	×	×	×	×	×
1552	×	×	×	×	×	×	×	×	×	×	×	×	○	×	-	×	×	×	×	×	×	×	×	×	×	×	○	×	×	×	×	×	×	×	×	×	×	×	×
1560	×	×	×	×	×	×	△	×	×	×	×	×	○	×	×	-	×	×	×	×	×	×	×	×	×	○	×	×	×	×	×	×	×	×	×	×	×	×	×
1633	×	×	×	×	×	×	×	×	×	×	×	×	○	×	×	×	-	×	×	×	×	×	×	×	○	×	×	×	×	×	×	×	×	×	×	×	×	×	×
1791	×	×	×	×	×	×	×	×	×	×	×	×	○	×	×	×	×	-	×	○	×	×	×	×	×	×	×	×	×	×	×	×	×	×	×	×	×	×	×
1807	×	×	×	×	○	×	×	×	×	×	×	×	○	×	×	×	×	×	-	○	×	×	×	×	×	×	×	×	×	×	×	×	×	×	×	×	×	×	×
1821	×	×	×	×	○	×	×	×	×	×	×	○	○	×	×	×	×	○	○	-	×	×	×	×	×	×	×	×	×	×	×	×	×	○	×	×	×	×	×
1871	×	×	×	×	×	×	×	×	×	×	×	×	△	×	×	×	×	×	×	×	-	×	×	×	×	×	△	×	×	×	×	×	×	×	×	×	×	×	×
1898	×	×	×	×	×	×	×	×	×	×	×	×	○	×	×	×	×	×	×	×	×	-	×	×	×	×	×	×	×	×	×	×	×	×	○	×	×	×	×
1952	×	×	×	×	×	×	×	×	×	×	×	×	○	×	×	×	×	×	×	×	×	×	-	×	○	×	×	×	×	×	×	×	×	×	×	×	×	×	×
1978	×	×	×	×	×	×	×	×	△	×	×	×	○	×	○	○	○	×	×	×	×	×	×	-	×	×	○	×	○	×	○	×	×	×	×	×	×	×	×
1980	×	×	×	×	×	×	×	×	△	×	×	×	○	×	○	○	○	×	×	×	×	×	○	×	-	×	○	×	○	×	○	×	×	×	×	×	×	×	×
2060	×	×	×	×	×	×	×	×	×	×	×	×	○	×	○	×	×	×	×	×	△	×	×	×	×	-	×	×	×	×	×	×	×	×	×	×	×	×	×
2158	×	×	×	×	×	×	×	×	×	×	×	×	○	×	×	×	×	×	×	×	×	×	×	×	○	×	-	×	×	×	×	×	×	×	×	×	×	×	×
2227	×	×	×	×	×	○	×	×	×	×	×	×	○	×	×	×	×	×	×	×	×	×	×	×	×	×	×	-	×	×	×	×	×	×	×	×	×	×	×
2459	×	×	×	×	×	×	×	×	×	×	×	×	○	×	×	×	×	×	×	×	×	×	×	×	×	○	×	×	-	×	×	×	×	×	×	×	×	×	×
2499	×	×	×	×	×	○	×	×	×	×	×	×	○	×	×	×	×	×	×	×	×	×	×	×	×	×	×	×	×	-	×	×	×	×	×	×	×	×	×
2605	×	×	×	×	×	×	×	×	×	×	×	×	○	×	×	×	×	×	×	×	×	×	×	×	○	×	×	×	×	×	-	×	×	×	×	×	×	×	×
2618	×	×	×	×	×	×	×	×	×	×	×	×	○	×	×	×	×	×	×	○	×	×	×	×	×	×	×	×	×	×	×	-	×	×	×	×	×	×	×
2627	×	×	×	×	×	○	×	×	×	×	×	×	○	×	×	×	×	×	×	×	×	×	×	×	×	×	×	×	×	×	×	×	-	×	×	×	×	×	×
2685	×	×	×	×	×	×	×	×	×	×	×	×	○	×	×	×	×	×	×	×	×	×	○	×	×	×	×	×	×	×	×	×	×	×	-	×	×	×	×
2945	×	×	×	×	×	○	×	×	×	×	×	×	○	×	×	×	×	×	×	×	×	×	×	×	×	×	×	×	×	×	×	×	×	×	×	-	×	×	×
3179	○	×	×	×	×	×	×	×	×	×	×	×	○	×	×	×	×	×	×	×	×	×	×	×	×	×	×	×	×	×	×	×	×	×	×	×	-	×	×
3200	×	×	×	×	×	×	×	×	×	×	○	×	○	×	×	×	×	×	×	×	×	×	×	×	×	×	×	×	×	×	×	×	×	×	×	×	×	-	×
3212	×	×	×	×	×	×	×	×	×	×	×	×	○	×	×	×	×	×	×	×	×	×	×	×	×	×	×	×	×	×	×	×	×	×	×	×	×	×	-
3300	×	×	×	×	×	×	×	×	×	○	×	×	○	×	×	×	×	×	×	×	×	×	×	×	×	×	×	×	×	×	×	×	×	×	×	×	×	×	×
3430	×	×	×	×	×	○	×	×	×	×	×	×	○	×	×	×	×	×	×	×	×	×	×	×	×	×	×	×	×	×	×	×	×	×	×	×	×	×	×
3484	×	×	×	×	×	×	×	×	×	×	×	×	○	×	×	×	×	×	×	×	×	×	×	×	×	×	×	×	×	×	×	×	×	×	×	×	×	×	×
3539	×	×	×	×	×	×	×	×	×	×	×	×	○	×	×	×	×	×	×	×	×	×	×	×	×	×	×	×	×	×	×	×	×	×	×	×	×	×	×
3542	×	×	×	×	×	×	×	○	×	×	×	×	×	×	○	×	×	×	×	×	○	×	×	×	×	×	×	×	×	×	×	×	×	×	×	×	×	×	×
3598	×	×	×	×	×	○	×	×	×	×	×	×	○	×	×	×	×	×	×	×	×	×	×	×	×	×	×	×	×	×	×	×	×	×	×	×	×	×	×
3612	×	×	×	×	×	×	×	×	×	×	×	×	○	×	×	×	×	×	×	×	×	×	×	×	×	×	×	×	×	×	×	×	×	×	×	×	×	×	×
3625	○	×	×	×	×	×	×	×	×	×	×	×	○	×	×	×	×	×	×	×	×	×	×	×	×	×	×	×	×	×	×	×	×	×	×	×	×	×	×
3930	×	×	×	×	×	×	×	×	×	×	×	×	○	×	×	×	×	×	×	×	×	×	×	×	×	×	×	×	×	×	×	×	×	×	×	×	×	×	×
4297	×	○	○	○	×	×	×	×	×	×	×	×	×	×	×	×	×	×	×	×	×	×	×	×	×	×	×	×	×	×	×	×	×	×	×	×	×	×	×
4415	×	×	×	×	×	×	×	×	×	×	×	×	○	×	×	×	×	×	×	×	×	×	×	×	×	×	×	×	×	×	×	×	×	×	×	×	×	×	×
4583	×	×	×	×	×	×	×	×	×	×	×	×	○	×	×	×	×	×	×	×	×	×	×	×	×	×	×	×	×	×	×	×	×	×	×	×	×	×	×
4967	×	×	×	×	×	×	×	×	×	×	×	×	×	×	×	×	×	×	×	×	×	×	×	×	×	×	×	×	×	×	×	×	×	×	×	×	×	×	×
5022	×	×	×	×	×	×	×	×	×	×	×	×	×	×	×	×	×	×	×	×	×	×	×	×	×	×	×	×	×	×	×	×	×	×	×	×	×	×	×
5095	×	×	×	×	×	×	×	×	×	×	×	×	×	×	×	×	×	×	×	×	×	×	×	×	×	×	×	×	×	×	×	×	×	×	×	×	×	×	×
5413	×	×	×	×	×	×	×	×	×	×	×	×	×	×	×	×	×	×	×	×	×	×	×	×	×	×	×	×	×	×	×	×	×	×	×	×	×	×	×
5619	×	×	×	×	×	×	×	×	×	×	×	×	×	×	×	×	×	×	×	×	×	×	×	×	×	×	×	×	×	×	×	×	×	×	×	×	×	×	×

Table 6.1: Continued.

	3300	3430	3484	3539	3542	3598	3612	3625	3930	4297	4415	4583	4967	5022	5095	5413	5619
305	×	×	×	×	×	×	×	○	×	×	×	×	×	×	×	×	×
670	×	×	×	×	×	×	×	×	×	○	×	×	×	×	×	×	×
724	×	×	×	×	×	×	×	×	×	○	×	×	×	×	×	×	×
797	×	×	×	×	×	×	×	×	×	○	×	×	×	×	×	×	×
956	×	×	×	×	×	×	×	×	×	×	×	×	×	×	×	×	×
985	×	○	×	×	×	○	×	×	×	×	×	×	×	×	×	×	×
995	×	×	×	×	×	×	×	×	×	×	×	×	×	×	×	×	×
1153	×	×	×	×	○	×	×	×	×	×	×	×	×	×	×	×	×
1222	×	×	×	×	×	×	×	×	×	×	×	×	×	×	×	×	×
1283	○	×	×	×	×	×	×	×	×	×	×	×	×	×	×	×	×
1382	×	×	×	×	×	×	×	×	×	×	×	×	×	×	×	×	×
1480	×	×	×	×	×	×	×	×	×	×	×	×	×	×	×	×	×
1483	○	○	○	○	×	○	△	○	○	×	○	○	×	×	×	×	×
1506	×	×	×	×	×	×	×	×	×	×	×	×	×	×	×	×	×
1552	×	×	×	×	○	×	×	×	×	×	×	×	×	×	×	×	×
1560	×	×	×	×	×	×	×	×	×	×	×	×	×	×	×	×	×
1633	×	×	×	×	×	×	×	×	×	×	×	×	×	×	×	×	×
1791	×	×	×	×	×	×	×	×	×	×	×	×	×	×	×	×	×
1807	×	×	×	×	×	×	×	×	×	×	×	×	×	×	×	×	×
1821	×	×	×	×	×	×	×	×	×	×	×	×	×	×	×	×	×
1871	×	×	×	×	○	×	×	×	×	×	×	×	×	×	×	×	×
1898	×	×	×	×	×	×	×	×	×	×	×	×	×	×	×	×	×
1952	×	×	×	×	×	×	×	×	×	×	×	×	×	×	×	×	×
1978	×	×	×	×	×	×	×	×	×	×	×	×	×	×	×	×	×
1980	×	×	×	×	×	×	×	×	×	×	×	×	×	×	×	×	×
2060	×	×	×	×	×	×	×	×	×	×	×	×	×	×	×	×	×
2158	×	×	×	×	×	×	×	×	×	×	×	×	×	×	×	×	×
2227	×	×	×	×	×	×	×	×	×	×	×	×	×	×	×	×	×
2459	×	×	×	×	×	×	×	×	×	×	×	×	×	×	×	×	×
2499	×	×	×	×	×	×	×	×	×	×	×	×	×	×	×	×	×
2605	×	×	×	×	×	×	×	×	×	×	×	×	×	×	×	×	×
2618	×	×	×	×	×	×	×	×	×	×	×	×	×	×	×	×	×
2627	×	×	×	×	×	×	×	×	×	×	×	×	×	×	×	×	×
2685	×	×	×	×	×	×	×	×	×	×	×	×	×	×	×	×	×
2945	×	×	×	×	×	×	×	×	×	×	×	×	×	×	×	×	×
3179	×	×	×	×	×	×	×	×	×	×	×	×	×	×	×	×	×
3200	×	×	×	×	×	×	×	×	×	×	×	×	×	×	×	×	×
3212	×	×	×	×	×	×	×	×	×	×	×	×	×	×	×	×	×
3300	-	×	×	×	×	×	×	×	×	×	×	×	×	×	×	×	×
3430	×	-	×	×	×	×	×	×	×	×	×	×	×	×	×	×	×
3484	×	×	-	×	×	×	×	×	×	×	×	×	×	×	×	×	×
3539	×	×	×	-	×	×	×	×	×	×	×	×	×	×	×	×	×
3542	×	×	×	×	-	×	×	×	×	×	×	×	×	×	×	×	×
3598	×	×	×	×	×	-	×	×	×	×	×	×	×	×	×	×	×
3612	×	×	×	×	×	×	-	×	×	×	×	×	×	×	×	×	×
3625	×	×	×	×	×	×	×	-	×	×	×	×	×	×	×	×	×
3930	×	×	×	×	×	×	×	×	-	×	×	×	×	×	×	×	×
4297	×	×	×	×	×	×	×	×	×	-	×	×	×	×	×	×	×
4415	×	×	×	×	×	×	×	×	×	×	-	×	×	×	×	×	×
4583	×	×	×	×	×	×	×	×	×	×	×	-	×	×	×	×	×
4967	×	×	×	×	×	×	×	×	×	×	×	×	-	×	×	×	×
5022	×	×	×	×	×	×	×	×	×	×	×	×	×	-	×	×	×
5095	×	×	×	×	×	×	×	×	×	×	×	×	×	×	-	×	×
5413	×	×	×	×	×	×	×	×	×	×	×	×	×	×	×	-	×
5619	×	×	×	×	×	×	×	×	×	×	×	×	×	×	×	×	-

Table 6.2: γ rays observed in the β decay of ^{30}Na $\rightarrow$ ^{30}Mg in the present work. The relative γ-ray intensities are shown relative to the 1483-keV γ ray. The absolute γ-ray intensities for 100 decays from the present are compared with the previous reports in Refs. [TAJ12] and [BAU89].

E_γ (keV)	$E_i \rightarrow E_f$ (MeV)	I_γ (relative)	I_γ (per 100 decays)		
			Present work	Ref. [TAJ12]	Ref. [BAU89]
304.8(1)	1.788→ 1.483	16(1)	7.6(8)	7.7(5)	4.8(5)
669.5(3)	4.967→ 4.297	0.3(1)	0.16(6)	-	-
724.4(4)	5.022→ 4.297	0.22(8)	0.10(4)	-	-
797.4(2)	5.095→ 4.297	0.95(9)	0.45(5)	-	-
955.7(1)	4.259→ 3.304	1.3(1)	0.63(7)	-	-
984.9(1)	2.468→ 1.483	15(1)	7.1(7)	6.9(4)	6.2(7)
994.7(2)	3.463→ 2.468	0.41(8)	0.19(4)	-	-
1152.0(3)	4.695→ 3.543	1.9(2)	0.9(1)	-	-
1221.9(2)	4.683→ 3.461	0.47(9)	0.22(5)	-	-
1283.0(1)	6.066→ 4.783	1.0(1)	0.45(6)	-	-
1382.3(1)	6.066→ 4.683	0.38(6)	0.18(3)	-	-
1479.5(5)	4.783→ 3.304	0.3(2)	0.14(8)	-	-
1483.1(1)	1.483→ 0	100	47(3)	49(3)	42(3)
1505.9(1)	4.967→ 3.461	7.8(6)	3.7(4)	3.9(3)	3.6(5)
1552.4(1)	5.095→ 3.543	3.4(3)	1.6(2)	1.8(1)	2.0(3)
1559.6(1)	5.022→ 3.463	2.8(2)	1.3(1)	1.3(1)	1.5(2)
1633.2(3)	5.095→ 3.461	1.5(1)	0.69(8)	0.9(1)	-
1791.3(1)	5.095→ 3.304	3.2(3)	1.5(2)	1.5(1)	1.7(4)
1806.6(2)	6.066→ 4.259	0.8(1)	0.36(6)	-	-
1820.6(2)	3.304→ 1.483	5.8(5)	2.8(3)	3.0(2)	2.3(3)
1871.0(1)	5.413→ 3.543	1.2(1)	0.58(7)	0.5(1)	0.6(1)
1898.3(1)	3.381→ 1.483	2.8(2)	1.3(1)	1.4(1)	-
1952.0(2)	5.413→ 3.461	3.3(4)	1.6(2)	2.0(1)	2.0(2)
1978.1(1)	3.461→ 1.483	16(2)	8(1)	11.0(7)	10.5(11)
1979.6(1)	3.463→ 1.483	7(1)	3.3(5)	-	-
2059.5(1)	3.543→ 1.483	1.0(1)	0.47(6)	0.6(1)	0.8(1)
2157.6(1)	5.619→ 3.461	0.9(3)	0.4(2)	-	-
2226.6(2)	4.695→ 2.468	1.1(3)	0.5(2)	0.7(1)	-
2458.9(3)	5.922→ 3.463	0.9(3)	0.4(2)	-	-
2499.3(1)	4.967→ 2.468	1.6(2)	0.76(9)	1.1(1)	0.8(1)
2605.1(2)	6.066→ 3.461	1.7(1)	0.82(9)	0.9(1)	-
2618.0(5)	5.922→ 3.304	0.21(6)	0.10(3)	-	-
2627.1(1)	5.095→ 2468	1.8(2)	0.9(1)	1.0(1)	1.0(1)
2684.5(1)	6.066→ 3.381	2.7(2)	1.3(1)	1.5(1)	-

Table 6.2: Continued.

E_γ (keV)	$E_i \rightarrow E_f$ (MeV)	I_γ (relative)	I_γ (per 100 decays)		
			the present work	Ref. [TAJ12]	Ref. [BAU89]
2945.3(1)	5.413→ 2.468	1.2(1)	0.57(7)	0.9(2)	-
3179.3(1)	4.967→ 1.788	11(1)	5.4(6)	5.6(2)	5.4(7)
3200.0(2)	4.683→ 1.483	1.0(1)	0.46(8)	0.5(1)	-
3211.5(2)	4.695→ 1.483	2.3(3)	1.1(2)	1.0(1)	-
3300.1(3)	4.783→ 1.483	0.61(8)	0.29(4)	-	-
3430.2(1)	5.898→ 2.468	3.7(9)	1.8(4)	1.6(1)	-
3484.1(1)	4.967→ 1.483	9.6(8)	4.5(5)	4.7(3)	5.1(5)
3539.3(2)	5.022→ 1.483	1.8(3)	0.9(2)	0.9(6)	0.7(5)
3542.4(2)	3543→ 0	5.5(6)	2.6(3)	2.7(6)	2.8(5)
3597.9(2)	6.066→ 2.468	0.9(1)	0.42(5)	0.4(1)	-
3612.0(3)	5.095→ 1.483	0.7(3)	0.4(2)	0.4(1)	0.3(1)
3625.2(2)	5.413→ 1.788	2.9(3)	1.4(2)	1.3(1)	1.3(2)
3930.2(1)	5.413→ 1.483	5.6(5)	2.6(3)	2.6(2)	2.8(3)
4297.2(3)	4297→ 0	1.3(4)	0.6(2)	-	-
4414.9(1)	5.898→ 1.483	2.5(2)	1.2(1)	1.7(2)	1.1(2)
4583.0(1)	6.066→ 1.483	0.4(3)	0.2(1)	0.8(3)	-
4966.8(1)	4.967→ 0	14(1)	6.7(7)	7.1(5)	6.9(7)
5022.1(1)	5.022→ 0	11(1)	5.4(6)	5.4(4)	5.4(6)
5094.7(1)	5.095→ 0	6.6(6)	3.1(3)	3.1(3)	3.1(4)
5413.0(1)	5.413→ 0	5.8(5)	2.8(3)	3.0(3)	2.7(3)
5618.6(2)	5.618→ 0	1.2(1)	0.57(7)	-	-
(1947)	4.415→ 2.468	-	-	-	0.7(1)
(2216)	4.683→ 2.468	-	-	0.7(1)	-
(2437)	5.898→ 3.461	-	-	0.3(2)	-
(2554)	5.022→ 2.468	-	-	0.4(1)	-

6.4 Half-life of the 1.788-MeV level

A half-life of 1.788-MeV level has been measured by using thin plastic scintillator as a β-ray detector and BaF_2 detectors as a γ-ray detectors in Ref. [MAC05]. They fitted the time spectrum between β rays and the 305-keV γ ray and determined a half-life of 3.9(4) ns. In the present work, the half-life of the 1.788-MeV level was measured by using the centroid shift method [WEA60] (see Sec. 5.5), because the reported half-life was too short to fit the slope of the time spectrum by using Ge detectors, whose time resolution is 11 ns (FWHM) for the 305-keV γ ray.

Figure 6.13 shows the time difference spectrum between the β rays and prompt γ rays (black) and 305-keV γ rays (red). It is clearly found the time distribution of the 305-keV gated spectrum was different from that of the prompt γ rays. The difference of the centroid position between these two spectra was 5.0(4) ns. From this value, the half-life of 1.788-MeV level was determined to be 3.6(4) ns in this work. Although the accuracy of the half-life could not be improved much, we re-confirmed nano-second order half-life of the 1.788-MeV level.

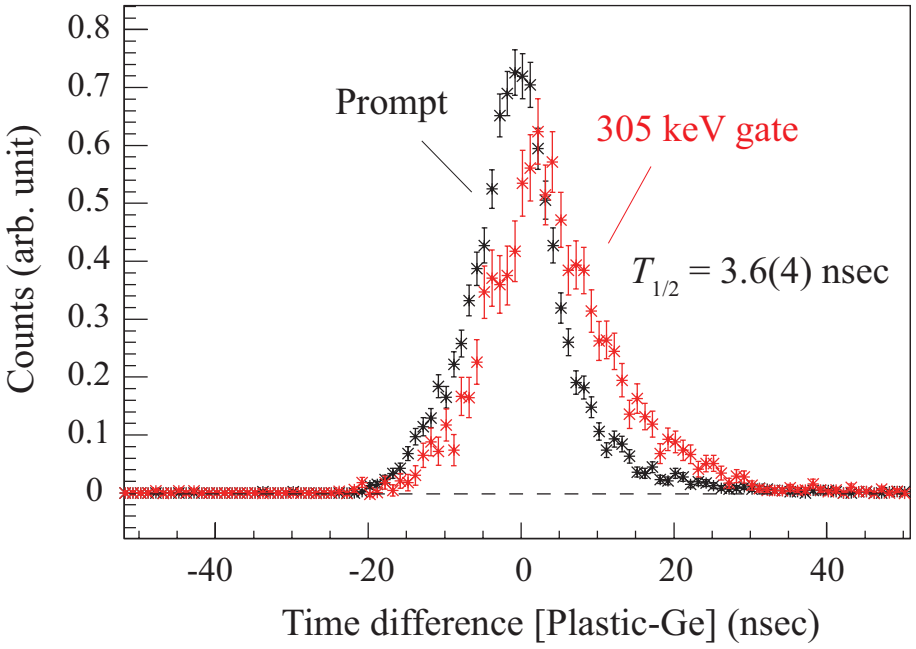

Figure 6.13: Time difference spectra gated by the prompt γ rays (black) and 305-keV γ ray. The half-life of the 1.788-MeV level was calculated by the difference between the centroid positions of the spectra of the prompt and the 305-keV γ rays.

6.5 Spin-parity assignments of levels in ^{30}Mg

Firmly spin-parity assignments were performed by taking advantage of the β-ray asymmetry from the β decay of polarized ^{30}Na.

6.5.1 Polarization of ^{30}Na beam and spin-parity assignment of the 4.967- and 5.095-MeV levels

The polarization of ^{30}Na was deduced by the same way in Sec. 5.6.1. At first, the AP ratios of 4.967- and 5.095-MeV levels are determined by using the γ-ray counts in the four combinations of the γ-ray energy spectra. Figure 6.14 shows the γ-ray energy spectra gated by the four combinations of the β-ray detectors (R or L) and the polarization direction ("+" or "-"). In Fig. 6.14, the counts of 4967-keV γ ray, which depopulates the 4.967-MeV level, are clearly different for each polarization direction. The counts of 4967-keV γ-ray peak in L^+ and R^- are larger than those in R^+ and L^-. The AP value of $-0.31(1)$ was obtained from sum of γ ray counts of 4967, 3484, 3179, and 1506 keV for each polarization direction. The same examination was performed for the 5.095-MeV level, and the AP value of 5.095-MeV level was determined to be $-0.085(26)$ using the γ rays of 5095, 3612, 2627, and 1791 keV which depopulate the 5.095-MeV level.

The ratio of the A values of levels at 4.967 and 5.095 MeV was calculated to be

$$A_{4.967}P/A_{5.095}P = A_{4.967}/A_{5.095} = 3.6(10). \tag{6.1}$$

This ratio is compared with the values expected from the possible 9 combinations of the spin-parity of 4.967- (1^+, 2^+, 3^+) and 5.095-MeV (1^+, 2^+, 3^+) levels, as shown in Fig. 6.15. The experimental value of 3.6(10) is uniquely consistent with the ratio of ($I^\pi_{4.967}$, $I^\pi_{5.095}$) = (1^+, 2^+), therefore, we reasonably assigned the spins and parities of 4.967- and 5.095-MeV levels to 1^+ and 2^+, respectively. This spin-parity assignments agree with the previous reports by Ref. [TAJ12].

The polarization of 31(1) and 26(8) % was calculated from the AP values of 4.967- and 5.095-MeV levels, respectively. From a weighted average of these values, the polarization of ^{30}Na beam was estimated to be 31(1) %.

6.5.2 Spin-parity assignments of 5.022- , 5413-, 5.898-, and 6.066-MeV levels

These 5.022- and 5413-MeV levels show large β-decay branching ratios around 10 %, and β transitions to these levels are most likely allowed transitions. Therefore our methods

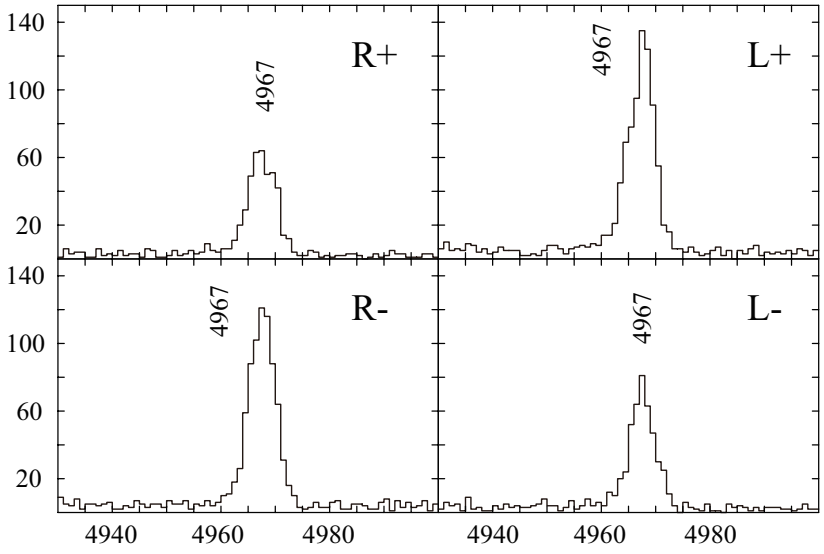

Figure 6.14: Gamma-ray counts of the 4967-keV γ ray gated by the β-ray detectors (R or L) for each polarization direction ("+" or "−").

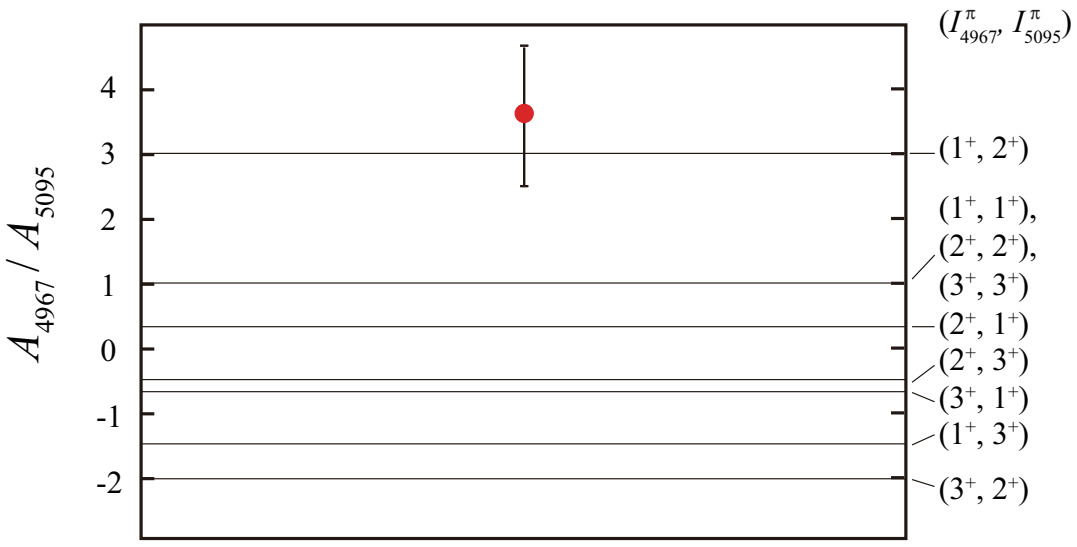

Figure 6.15: Ratio of the asymmetry parameters (A) of 4.967- and 5.095-MeV levels. The lines show expected values from combinations of spin-parity for each levels.

could be applied to these two levels, and their spins and parities are given the limitations to 1^+, 2^+, or 3^+ due to the natures of allowed transitions. The AP value of $-0.29(2)$ for the 5.022-MeV level was determined by the counts of 5022- and 1560-keV γ rays which depopulate the 5.022-MeV level . The A value of $-0.94(9)$ for this level was calculated by the AP value of $-0.29(2)$ divided by the polarization of 31(1)%. In the β decay of ^{30}Na $\rightarrow$ ^{30}Mg, expected A values for spins and parities of 1^+, 2^+, and 3^+ are -1, -0.33, and 0.67, respectively. The A value of the 5.022-MeV level shows very good agreement with the A value for 1^+ state, therefore we reasonably assigned spin-parity of 5.022-MeV level to 1^+. The same examination was performed for the 5.413-MeV level. The AP value of $-0.10(2)$ was determined by the counts of 5413-, 3930-, and 3627-keVγ rays which depopulate the 5.413-MeV level, and the A value is $-0.34(8)$. This A value leads to 2^+ assignment for the 5.413-MeV. These spin-parity assignments are consistent with the previous assignments by Ref. [TAJ12]

The spin-parity assignments of 2^+ and (2^+) for the 5.898-, and 6.066-MeV levels were performed based on the β-ray asymmetry and γ-ray transition strength in Ref. [TAJ12], respectively. The reported A values of the 5.898- and 6.066-MeV levels are $-0.7(6)$ and 0.07(55), respectively [TAJ12]. The errors of A values for these levels in Ref. [TAJ12] were so large that different spin-parity assignments are also possible within 2σ confidence level. In our work, the A values of the 5.898- and 6.066-MeV levels were determined to be $-0.9(2)$ and 0.8(2), respectively. We successfully improved the accuracy of these A values and revised spin-parity assignments of 1^+ and 3^+ for these levels with more than 2σ confidence levels.

6.5.3 Spin-parity assignments of 4.695- and 5.619-MeV levels

The β-decay branching ratio of 4.695- and 5.619-MeV levels are 2.5(3) and 1.0(2) for 100 decays, and their logft values are 6.0(1) and 6.2(1), respectively. The β transitions are considered to be allowed transitions, thus their spins and parities are limited to 1^+, 2^+, or 3^+.

The A value of $-0.9(4)$ for 5.619-MeV level was deduced by using the counts of 5619-keV γ rays gated by the β-ray counters on left- and right-hand for each polarization direction. This A value has large uncertainty because of small γ-ray detection efficiency due to high energy γ ray of 5619 keV, so that both of 1^+ and 2^+ spin-parity assignments are possible for this level. The positive A value of 0.4(3) was observed for the 4.695-MeV by using the counts of the 3212-keV γ ray. Only a 3^+ level shows positive A value, therefore the spin-parity of 4.695-MeV level was assigned to be 3^+.

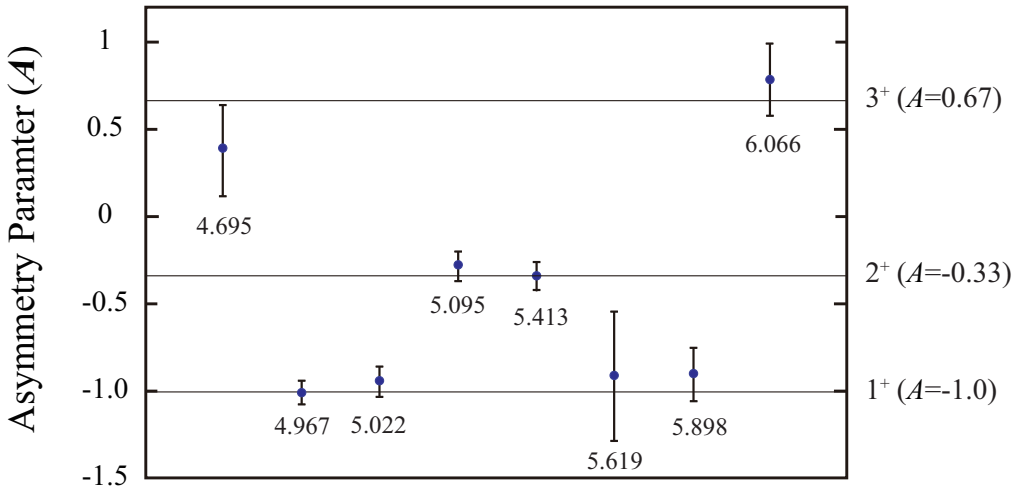

Figure 6.16: Summary of the experimental asymmetry parameter (A) of exited states in ^{30}Mg. The lines indicate the expected A values of -1.0, -0.33, and $+0.67$ for 1^+, 2^+, and 3^+ level, respectively.

6.5.4 Summary of the spin-parity assignment in ^{30}Mg by β-ray asymmetry

Figure 6.16 shows summary of the asymmetry parameter A of the levels at 4.695, 4.967, 5.022, 5.095, 5.413, 5.898, and 6.066 MeV in ^{30}Mg obtained in this work. It is clearly found that the experimental A values of these levels are classified three groups: 1^+ (4.967, 5.022, 5.619 and 5.898 MeV), 2^+ (5.095, 5.413, and 5.619 MeV), and 3^+ (4.695 and 6.066 MeV). Spins and parities of 7 levels in ^{30}Mg were assigned by the β-ray asymmetry, and those of levels at 4.695, 5.898, and 6.066 MeV were proposed for the first time in this work.

6.5.5 Spin-parity assignment of the 1.788-MeV level

The 1.788-MeV level have been good candidate for the excited 0^+ state. The measurement of the half-life of the 1.788-MeV level [MAC05] and the observation of internal conversion electron [1.788 MeV $\rightarrow$ g.s. (0^+)] [SCH09]. The reported half-life of 3.9(4) ns for the 1.788-MeV level was also confirmed in this work, and our value was 3.6(4) ns (see Sec. 6.4). Table 6.3 show the comparison between experimental half-life of this level and Weisskopf estimate of 305-keV γ ray populating the first 2^+ state at 1.483 MeV. In the table, the assignment of $E2$ transition to 305-keV transition is the most probable, thus the spin-gap between the 1.789- and 1.483-MeV level was two. The experimental γ-ray transition intensities of 3179 and 3484 keV to 1.788- and 1.483-MeV levels, respectively, depopulating the 4.967-MeV (1^+) level are compared with the Weisskopf estimate, as shown in Table 6.4. From the comparison, the spin-parity assignment of 0^+ is reasonable for the 1.788-MeV level.

Table 6.3: Comparison between the experimental half-life of 1.788-MeV level and Weisskopf estimate. $T_{W.e.}$ $(\sigma\lambda)$ is calculated half-life for each possible multipolarity of the transition $(\sigma\lambda)$.

$T_{\rm exp}$ (ns)	I^{π}(1.788 MeV)	$\sigma\lambda$	$T_{\rm W.e.}$ $(\sigma\lambda)$ (ns)	$T_{\rm W.e.}/T_{\rm exp}$
3.6(4)	0^-, 4^-	$M2$	2.2×10^{3}	6.1×10^{2}
	0^+, 4^+	$E2$	1.3×10^{2}	3.6×10^{1}
	1^-, 2^-, 3^-	$M1$	7.8×10^{-4}	2.2×10^{-4}
	1^-, 2^-, 3^-	$E1$	4.6×10^{5}	1.2×10^{-5}

Table 6.4: Comparison of the relative γ-ray transition intensities between the experimental results (I_{exp}) and Weisskopf estimate ($I_{W.e.}$. relative to the 3484-keV transition (4.967 MeV $\rightarrow$ 1.483 MeV) for possible spin parities of 1.788-MeV level. $T_{W.e.}$ $(\sigma\lambda)$ is calculated half-life for each possible multipolarity of the transition $(\sigma\lambda)$.

E_γ (keV)	$E_i \rightarrow E_f$ (MeV)	$I_{\rm exp}$ (relative)	I^{π}(1.788 MeV)	$\sigma\lambda$	$T_{W.e.}$ $(\sigma\lambda)$ (s)	$I_{\rm W.e.}$ (relative)
3484	4.967 $\rightarrow$ 1.483	1		$M1$	5.2×10^{-16}	1
3179	4.967 $\rightarrow$ 1.788	1.2(1)	0^+	$M1$	6.9×10^{-16}	7.5×10^{-1}
3484	4.967 $\rightarrow$ 1.483	1		$M1$	5.2×10^{-16}	1
3179	4.967 $\rightarrow$ 1.788	1.2(1)	4^+	$M3$	1.0×10^{-10}	5.2×10^{-6}

In order to make sure the 0^+ assignment for the 1.788 MeV level, γ-γ angular correlation of the two cascade γ rays of 305 [1.788 MeV $\rightarrow$ 1.483 MeV (2^+)] and 1.483 keV [1.483 MeV (2^+) $\rightarrow$ g.s. (0^+)] was performed in this work. Figure 6.17 shows the γ-ray angular correlation between 305 and 1483 keV γ rays as a function of the difference between the azimuthal angles. The experimental data was taken for possible angles of $\theta = 45°$, $90°$, $135°$, and $180°$ by using all Ge detectors except for Ge-R and Ge-L which have the larger crystal volumes and are closer to the Pt stopper than the other Ge detectors. In Fig 6.17, expected angular correlations are also illustrated for the five cases of spin values for the 1.788-MeV level [0, 1, 2, 3, and 4; $0 \rightarrow 2 \rightarrow 0$ (solid line in red), $1 \rightarrow 2 \rightarrow 0$ (dashed line in green), $2 \rightarrow 2 \rightarrow 0$ (dashed-dotted line in black), $3 \rightarrow 2 \rightarrow 0$ (dashed-two dotted line in purple), and $4 \rightarrow 2 \rightarrow 0$ (dotted line in blue)], where only the lowest multipolarity is considered for the γ-ray transitions. The experimental angular resolutions of Ge detectors (typically $\sim30°$) are folded in the theoretical values. The theoretical and experimental values are displayed relative to that of $\theta = 45°$. In the comparison of γ-ray angular correlation between the experimental and theoretical values in Fig. 6.17, the experimental values are in excellent agreement with

the $0 \rightarrow 2 \rightarrow 0$ line. The 1.788-MeV level was firmly assigned to be the second 0^+ state.

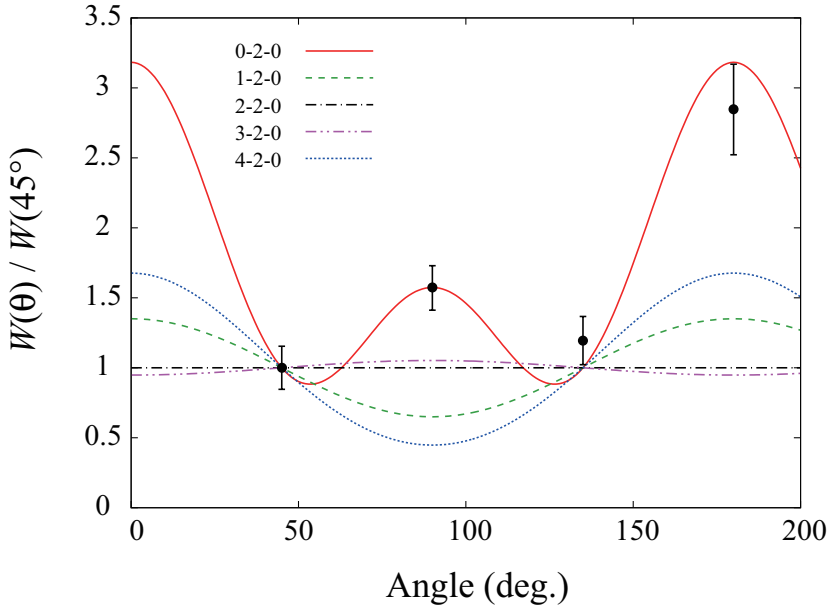

Figure 6.17: Gamma-ray angular correlation for 305 and 1483-keV γ rays. Solid line (red), dashed line (green), dashed-dotted line (black), dashed-two dotted line (purple), and dotted line (blue) show the theoretical predictions assuming five cases of spin values of 0 ($0 \rightarrow 2 \rightarrow 0$), 1 ($1 \rightarrow 2 \rightarrow 0$), 2 ($2 \rightarrow 2 \rightarrow 0$), 3 ($3 \rightarrow 2 \rightarrow 0$), and 4 ($4 \rightarrow 2 \rightarrow 0$) for the 1.788-MeV level, respectively.

6.5.6 Spin-parity of 2.468-MeV levels

The spin-parity of the 2.468-MeV level was tentatively assigned to 2^+ based on measurement of the upper limit of the half-life by the previous work [MAC05]. The upper-limit of half-life of the 2.468-MeV level was 5 ps, thus the 985-keV transition may have a dominant $M1$ component [MAC05]. In Ref. [DEA10], they measured the angular distribution of 985-keV γ ray, and this results agree with the 2^+ assignment. However, they could not make a robust assignment because of large uncertainty of the measurement. Taking into account the discussions mentioned above, 2^+ and 3^+ spin-parity assignment for this level is still possible. In this work, the strong transitions of 3430 keV from 5.898-MeV (1^+) state to this 2.468-MeV level was confirmed through the firmly spin-parity assignments. From this fact, possibility of 3^+ state is eliminated because $1^+ \rightarrow 3^+$ transition have mainly $E2$ component and the $E2$-transition strength should be much small, taking into account enhancement of $E2$ transitions. Therefore, the (2^+) assignment for the 2.468-MeV level is the most reliable.

6.5.7 Spin-parity of 3.304-, 3.381-, 3.543-, and 3.461-MeV levels

In Ref. [TAJ12], the spin-parity of the 3.304-MeV level was assigned to 2^+ or 3^+ based on the observed β-decay branching ratio of 1.4(2) for 100 decays, which results in the allowed transition. However, β-transition intensity of 3.304-MeV level in this work is updated to be 0.4(3) with $\log ft$ of 7.0(4) due to the new finding γ rays of 956, 1480, and 2618 keV. Such a large $\log ft$ value with larger than 7 indicates that possibility of a forbidden β transition should be considered. Therefore, negative-parity assignment is also possible for this level. Table 6.5 shows the comparison between γ-ray intensity ratios of 1791 and 3612 keV by the experimental values and those estimated by Weisskopf estimate. In the comparison, the relative γ-ray intensity estimated for $E1$ and $M1$ transition reproduce the experimental value. Taking into account hindrance due to l-forbidden $M1$ transition and possible mixing of $E2$ transition, difference of a factor of 10^{-2} is also possible [MOR76]. From the $E1$ or $M1$ transition of 1791 keV, possible spin-parity of the 3.304 MeV is 1^+, 2^+, 3^+, 1^-, 2^-, and 3^-.

The spin-parity assignment was performed under the assumption that this is allowed transition, in Ref. [TAJ12]. The β-decay branching ratio of this level was reported to be 1.0(7) [TAJ12], whereas the 1152-keV γ ray which populates the 3.543-MeV level is newly observed in this work, and the β-decay branching ratio of this level is recalculated to be $I_\beta <$ 0.3. Speculated from this small β-transition rate, the β transition to this level is most likely a forbidden transition, therefore the spin-parity assignment for the 3.543-MeV level should be reconsidered. Table 6.6 shows the relative intensities of the γ rays of 3212 and 1152 keV which depopulate the 4.695-MeV (3^+) level and of 2060 and 3542 keV which depopulate the 3.543-MeV level calculated by experimental values and by Weisskopf estimate. From the comparison between 3212- and 1152-keV γ-ray intensities, the 1152 keV is thought to be $M1$ or $E1$ transition. From the $M1$ or $E1$ nature of this transition, the spin-gap of one or zero between levels of 4.695 and 3.543 are allowed. This $M1$ or $E1$ transition to the 3.543-MeV level gives the limitation of the spin to 2, 3, or 4. Similarly, the $M1$ and $E2$ transitions of 2060- and 3542-keV γ rays are plausible, respectively. The spin-parity of 2^+ only satisfies this requirements, therefore the spin-parity of (2^+) assignment for the 3.543-MeV level is proposed in this work.

The spin-parity of 3.381-MeV level was reported to be 4^+ by the γ-ray angular distribution [DEA10]. In this work, the $\log ft$ value of this level is below a limit of measurement (>7.3). This result agrees with the $2^+ \rightarrow 4^+$ second forbidden transition.

The 3.461-MeV level has the β-decay branching ratio of 1(1), and the $\log ft$ value is 6.4(4). Table 6.7 shows the comparisons between the experimental γ-ray transition intensities and

Weisskopf estimate of 4583 and 2605 keV depopulating the 6.066-MeV (3^+) level and of 3484 and 1506 keV depopulating the 4.967 MeV (1^+) level. From the comparison, the 2605 and 1506 keV are most likely $M1$ or $E1$ transitions, therefore the spin-parity of 3.461-MeV is assigned to 2^+ or 2^-.

Table 6.5: Comparison between the relative γ-ray transition intensities (I_{exp}) and Weisskopf estimate ($I_{W.e.}$), relative to the 3612-keV transition (5.095 MeV $\rightarrow$ 1.483 MeV). $T_{W.e.}$ ($\sigma\lambda$) is calculated half-life for each possible multipolarity of the transition ($\sigma\lambda$).

E_γ (keV)	$E_i \rightarrow E_f$ (MeV)	I_{exp} (relative)	I^π(3.304 MeV)	$\sigma\lambda$	$T_{W.e.}$ ($\sigma\lambda$) (s)	$I_{\text{W.e.}}$ (relative)
3612	5.095 $\rightarrow$ 1.483	1		$M1$	5.6×10^{-9}	1
1791	5.095 $\rightarrow$ 3.304	3.8(19)	0^-, 4^-	$M2$	3.2×10^{-10}	1.5×10^{-6}
			0^+, 4^+	$E2$	1.9×10^{-11}	2.5×10^{-5}
			1^+, 2^+, 3^+	$M1$	3.8×10^{-15}	1.2×10^{-1}
			1^-, 2^- ,3^-	$E1$	2.2×10^{-16}	2.1×10^{0}

Table 6.6: Comparison between the relative γ-ray transition intensities (I_{exp}) and Weisskopf estimate ($I_{W.e.}$). $T_{W.e.}$ ($\sigma\lambda$) is calculated half-life for each possible multipolarity of the transition ($\sigma\lambda$).

E_γ (keV)	$E_i \rightarrow E_f$ (MeV)	I_{exp} (relative)	I^π(3.543 MeV)	$\sigma\lambda$	$T_{W.e.}$ ($\sigma\lambda$) (s)	$I_{\text{W.e.}}$ (relative)
3212	4.695 $\rightarrow$ 1.483	1		$M1$	6.6×10^{-16}	1
1152	4.695 $\rightarrow$ 3.543	0.81(17)	1^-, 5^-	$M2$	2.9×10^{-9}	2.3×10^{-7}
			1^+, 5^+	$E2$	1.7×10^{-10}	3.9×10^{-6}
			2^+, 3^+, 4^+	$M1$	1.4×10^{-14}	4.6×10^{-2}
			2^-, 3^-, 4^-	$E1$	8.4×10^{-16}	7.9×10^{-1}
2060	3.543 $\rightarrow$ 1.483	1	1^+, 2^+, 3^+	$M1$	2.5×10^{-15}	1
3.542	3.543 $\rightarrow$ 0	5.5(9)	3^+	$M3$	4.9×10^{-7}	5.2×10^{-9}
			2^+	$E2$	6.2×10^{-13}	4.1×10^{-3}
2060	3.543 $\rightarrow$ 1.483	1	1^-, 2^-, 3^-	$E1$	1.5×10^{-16}	1
3.542	3.543 $\rightarrow$ 0	5.5(9)	3^-	$E3$	2.0×10^{-9}	7.5×10^{-9}
			2^-	$M2$	1.1×10^{-11}	1.4×10^{-5}

Table 6.7: Comparison between the relative γ-ray transition intensities (I_{exp}) and Weisskopf estimate ($I_{W.e.}$). $T_{W.e.}$ ($\sigma\lambda$) is calculated half-life for each possible multipolarity of the transition ($\sigma\lambda$).

E_γ (keV)	$E_i \rightarrow E_f$ (MeV)	$I_{\rm exp}$ (relative)	I^π(3.461 MeV)	$\sigma\lambda$	$T_{W.e.}$ ($\sigma\lambda$) (s)	$I_{\rm W.e.}$ (relative)
4583	6.066 $\rightarrow$ 1.483	1		$M1$	2.3×10^{-16}	1
2605	6.066 $\rightarrow$ 3.461	4(2)	1^-, 5^-	$M2$	4.9×10^{-11}	4.8×10^{-6}
			1^+, 5^+	$E2$	2.9×10^{-12}	7.9×10^{-5}
			2^+, 3^+, 4^+	$M1$	1.2×10^{-15}	1.9×10^{-1}
			2^-, 3^-, 4^-	$E1$	7.3×10^{-17}	3.1×10^{0}
3484	4.967 $\rightarrow$ 1.483	1		$M1$	5.6×10^{-16}	1
1506	4.967 $\rightarrow$ 3.461	0.82(9)	3^-	$M2$	7.6×10^{-10}	6.8×10^{-7}
			3^+	$E2$	4.5×10^{-11}	1.2×10^{-5}
			0^+, 1^+, 2^+	$M1$	6.4×10^{-15}	8.1×10^{-2}
			0^-, 1^-, 2^-	$E1$	3.8×10^{-17}	1.4×10^{0}

6.5.8 Spin-parity of 3.463-, 4.259-, 4.683-, 4.783-, and 5.922-MeV levels

The β-decay branching ratio of 3.463-, 4.259-, 4.683-, 4.783-, and 5.922-MeV levels are enough small that these transitions may not be allowed transitions. The both of negative and positive parity assignments are possible for these states. From the observation of strong 1560-keV transition [5.022 MeV (1^+) $\rightarrow$ 3.463 MeV], the spin of the 3.463-MeV level is limited to 1 or 2. The transitions of 6.066 MeV (3^+) $\rightarrow$ 4.259 MeV, $\rightarrow$ 4.683 MeV, and $\rightarrow$ 4.783 MeV give the limitation of the spin to 2, 3, or 4 for 4.259-, 4.683-, and 4.783-MeV levels, respectively. Since the 4.297-MeV level was populated by the 797- and 724-keV transitions from the 5.095- (2^+) and 5.022-MeV (1^+), respectively, the spin of 1 or 2 is plausible.

6.6 Newly proposed decay scheme of ^{30}Na $\rightarrow$ ^{30}Mg

The newly revised level scheme of ^{30}Na $\rightarrow$ ^{30}Mg is show in Fig. 6.18. Newly proposed levels and observed transitions are indicated in red lines and arrows, respectively. The logft and I_β in red were newly obtained in this work. The logft values, the I_β, and γ-ray energy labeled in blue numbers are revised values or are changed placements in the level scheme. The Q value and branching ratios of β-delayed one neutron (P_n) and two neutron decay (P_{2n}) are taken from Ref. [BAS10]. The levels of ^{30}Mg observed in the β decay of ^{30}Na are listed in Table 6.8.

Table 6.8: Proposed levels in ^{30}Mg by the β decay of ^{30}Na. The level energies (E_x) are shown in keV. A is asymmetry parameter for each level. The I_β indicates the absolute β branching ratios for 100 decays. The logft values in the present work are compared with the previous reports [TAJ12; BAU89]

E_x (MeV)	I^π	A	I_β (%)	logft		
				Present work	Ref. [TAJ12]	Ref. [BAU89]
0	0^+	-	-	-	-	
1.4831(1)	2^+	-	6(1)	6.1(1)	6.2(3)	5.8
1.7879(1)	(0^+)	-	0.9(7)	6.8(4)	7.1(4)	>7.0
2.4680(1)	(2^+)	-	1.7(7)	6.5(2)	>7.0	6.1
3.3037(2)	(1, 2, 3)	-	0.4(3)	7.0(4)	6.5(1)	-
3.3814(1)	4^+	-	<0.19	>7.3	-	-
3.4612(2)	(2)	-	1(1)	6.4(4)	6.4(4)	6.0
3.4627(2)	(1, 2)	-	1.8(5)	6.3(1)	-	-
3.5425(1)	(2^+)	-	<0.30	>7.1	6.7(4)	6.5
4.2593(3)	(2, 3, 4)	-	0.27(7)	7.0(1)	-	-
4.2972(3)	(1, 2)	-	<0.02	>8.1	-	-
4.6831(2)	(2, 3, 4)	-	0.50(9)	6.7(1)	6.4(1)	-
4.6947(2)	3^+	0.4(3)	2.5(3)	6.0(1)	6.2(1)	-
4.7831(3)	(2, 3, 4)	-	<0.09	>7.4	-	-
4.9670(1)	1^+	−1.01(7)	21(2)	5.0(1)	5.0(1)	5.0
5.0222(1)	1^+	−0.94(9)	7.6(7)	5.4(1)	5.4(1)	5.5
5.0948(1)	2^+	−0.28(9)	8.1(7)	5.4(1)	5.4(1)	5.5
5.4131(1)	2^+	−0.34(8)	9.4(8)	5.3(1)	5.3(1)	5.3
5.6187(1)	$(1^+, 2^+)$	−0.9(4)	1.0(2)	6.2(1)	-	-
5.8981(1)	1^+	−0.9(2)	2.9(5)	5.7(1)	5.6(1)	-
5.9216(2)	-	-	0.5(2)	6.5(2)	-	-
6.0659(1)	3^+	0.8(2)	3.7(3)	5.6(1)	5.6(1)	-

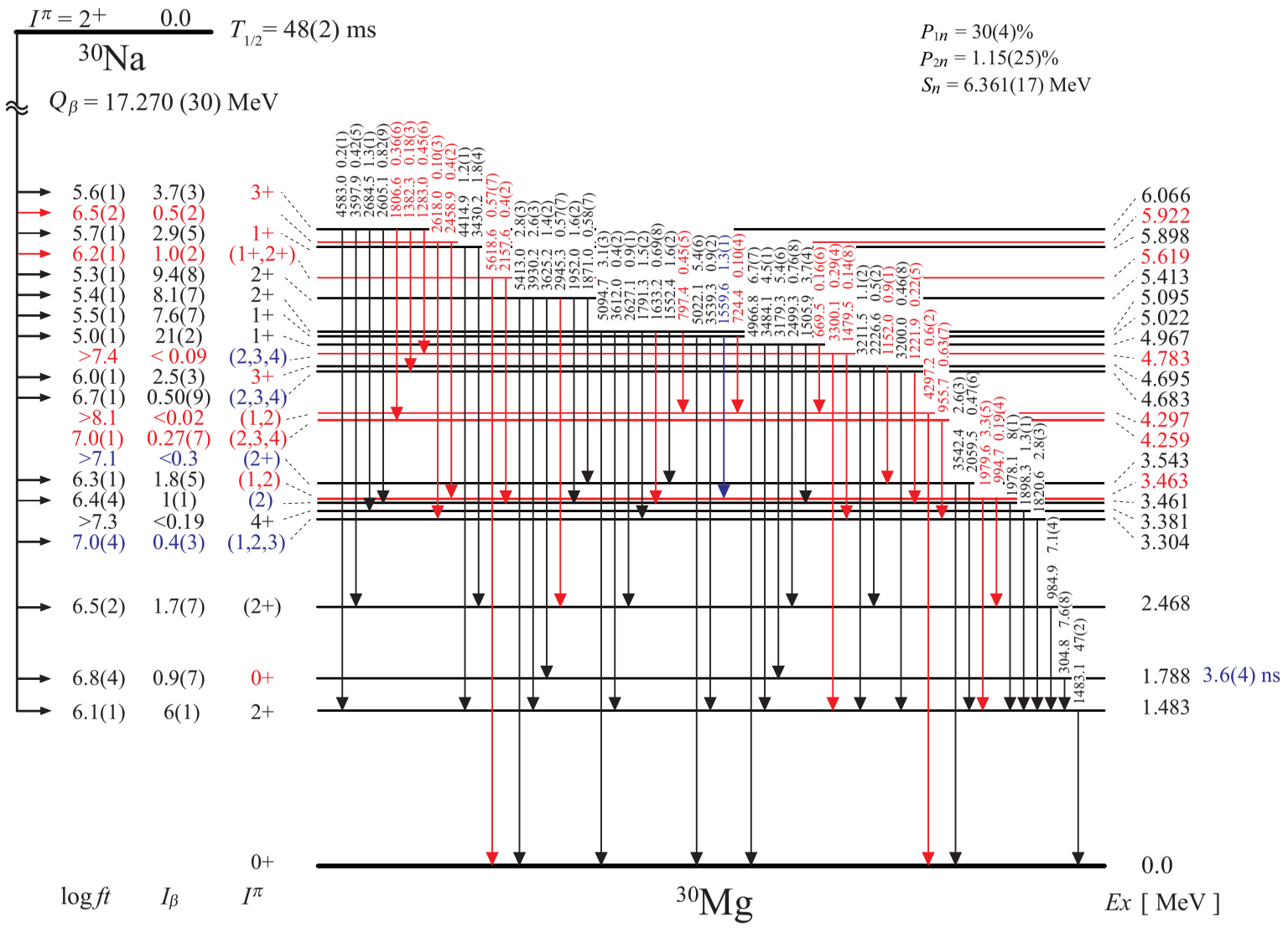

Figure 6.18: Decay scheme of ^{30}Na $\rightarrow$ ^{30}Mg. The transitions and levels indicated in red were observed and are proposed for the first time. The spins and parities in red and blue are newly assigned and revised in this work, respectively.

CHAPTER VII

Discussion

7.1 Structure of states in ^{31}Mg

In the present work, a very detailed decay scheme of ^{31}Na $\xrightarrow{\beta}$ ^{31}Mg has been established as shown in Fig. 5.20 of Chapter V. It should be noted that all the spins of the positive-parity excited states below the neutron separation energy were firmly assigned based solely on the experimental results, and furthermore the detailed β- and γ-transition information enabled us to propose spin assignments also for all the negative-parity levels. The present spin-parity assignments of the known levels were consistent with the previous proposals [$(3/2^+_1)$ [NEY05], $(3/2^-_1)$ [MAC05], $(7/2^-_1)$ [MAC05], $(3/2^-_2)$ [MIL09], and $(5/2^+_1)$ [SEI11]]. The present work found new 11 γ transitions and as a result placed 2 new levels at 0.942 MeV [$(1/2^-, 3/2^-)$] and 1.436 MeV [$(1/2^-, 3/2^-)$]. Now it becomes possible to discuss the structure of each level by comparing the data with theoretical predictions.

As explained in Chapter II, it has been found by the measurements of magnetic moment ($\mu = -0.88355\mu_N$) and spin-parity ($1/2^+$) that the ground state of ^{31}Mg is largely deformed ($\beta \sim +0.4$)[NEY05]. The magnetic moment was explained by the shell model calculations assuming the 2p-2h intruder configurations, however, the $1/2^+$ level could not be reproduced as the ground state even with the np-nh configurations [NEY05]. Another theoretical calculations in a framework of antisymmetrized molecular dynamics plus generator coordinate method (AMD+GCM) [KIM07], which assumes neither quadrupole deformation nor mean fields, successfully predicted a $1/2^+$ ground state as a band head of $K^\pi = 1/2^+$ rotational band. The magnetic moment was predicted also successfully as $\mu = -0.91\mu_N$, which is close to the experimental value. Recently, a Coulomb excitation experiment of ^{31}Mg beam has been performed [SEI11] and a positive-parity rotational band ($1/2^+_1$; g.s., $3/2^+_1$ at 0.050 MeV, $5/2^+_1$ at 0.945 MeV) was proposed. This result is consistent with the AMD+GCM prediction. The AMD+GCM calculations predicted also negative-parity rotational bands

with $K^\pi = 1/2^-$ and $3/2^-$ [KIM07].

In the following sections the ^{31}Mg levels in terms of the rotational band scheme are discussed in Sec. 7.1.1 and in terms of the AMD+GCM framework are discussed in Sec. 7.1.2. The levels which are explained neither by the rotational band scheme nor by the AMD+GCM framework will be discussed in Sec. 7.1.3. Various structures in ^{31}Mg are summarized in Sec. 7.1.4.

7.1.1 Levels understood in terms of collective rotational motion

7.1.1.1 assignments of $K^\pi = 1/2^+$ and $1/2^-$ bands members

Figure 7.1 (a) shows the experimental partial level schemes with selected levels of ^{31}Mg, separately displayed according to the parity. The levels with dashed lines were not observed in the present work but observed in other experiments [MAT07; KLO93; MAC05; TER08; MIL09]. The level sequence is in good accord with that in typical rotational bands with $K^\pi = 1/2^+$ and $1/2^-$ in odd nuclei, as shown in Fig 7.2 for the case of ^{25}Mg, which is taken from the text book by Bohr and Mottelson (p.284 of [BOH75]). Before discussing the rotational band structure in ^{31}Mg, the idea of the rotational band is briefly described below.

The rotational band structure is explained in a model where an unpaired nucleon occupies a single-particle orbit in a deformed potential and when a rotational angular momentum is given, the whole system (the deformed core plus the unpaired nucleon) rotates and is excited. A series of excited states associated with the same single-particle orbit is called a "rotational band" built on the band head formed by the rigid core plus the single particle. In order to assign the single-particle orbit, useful are the projection K of the total angular momentum I (nuclear spin) of the band head (with the rotational angular momentum $R = 0$) to the symmetry axis of the core and the parity of the single-particle orbit, as schematically shown in Fig 7.3.

In the case of $K = 1/2$ band, the level energies are expressed as

$$E(I) = \frac{\hbar^2}{2\mathcal{J}}\big[I(I+1) + a(-1)^{I+1/2}(I+1/2)\big], \tag{7.1}$$

where $\mathcal{J}$ and a are the moment of inertial of the core and the decoupling parameter, respectively (see Appendix F) [BOH75; CAS05]. The second term in the right side is due to the effect of the Coriolis forces in a rotating coordinate system and may cause a seemingly irregular level sequence.

Figure 7.1 (b) shows the level energies as a function of the decoupling parameter a. Note

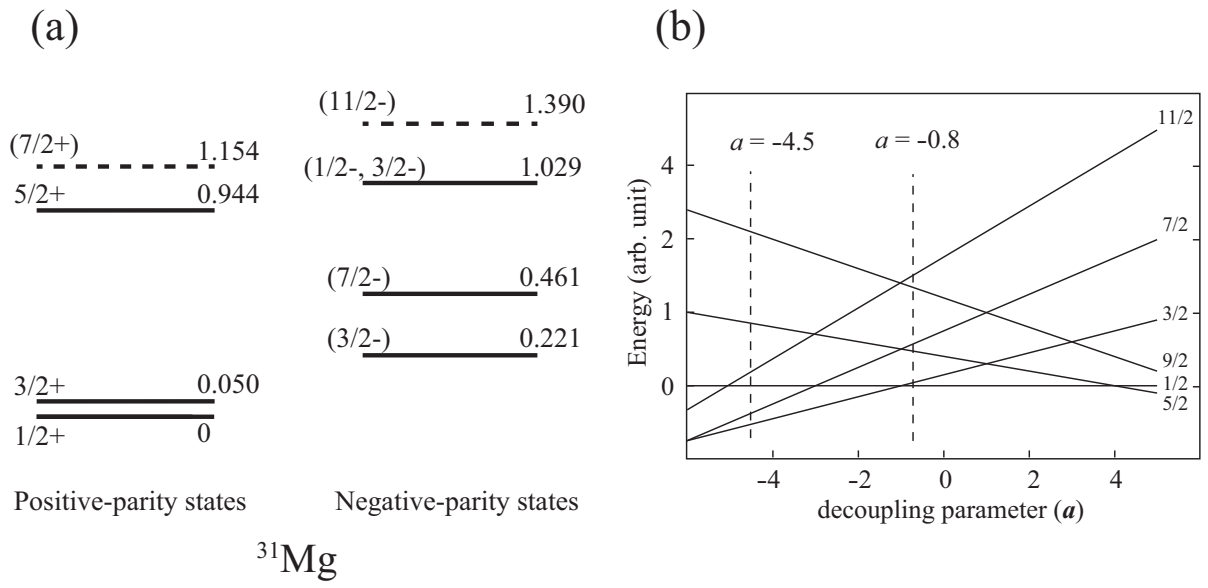

Figure 7.1: (a) Partial level scheme of ^{31}Mg with selected levels. The levels with dashed lines were not observed in the present work but observed in other experiments [KLO93; MAC05; MAT07; TER08; MIL09]. Their spins and parities are proposed in the present work for the first time. (b) Level energies of the $K = 1/2$ rotational bands as a function of the decoupling parameter a based on Eq. (1.3). Note that the energies are shown relative to the 1/2 level in arbitrary unit.

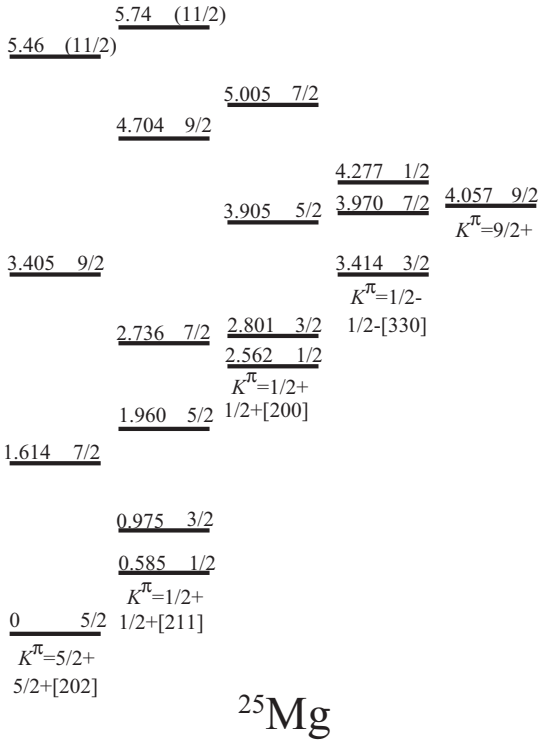

Figure 7.2: Rotational band in ^{25}Mg (based on the figure in p.284 of Ref. [BOH75].)

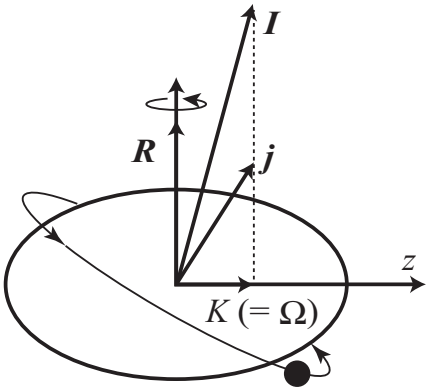

Figure 7.3: Schematic explanation of quantum numbers in collective rotational motion in an odd-mass nucleus. The single particle is in a deformed potential with axial symmetry and occupies the orbit with total angular momentum $\boldsymbol{j}$. The nuclear spin $\boldsymbol{I}$ is given as a vector sum of $\boldsymbol{j}$ and the rotational angular momentum $\boldsymbol{R}$. The projection of $\boldsymbol{I}$ on the symmetry axis z is defined as K. In the case of prolate deformation K equals to Ω, which is defined as the projection of $\boldsymbol{j}$.

the arbitrary unit in energy. For the positive-parity states in Fig. 7.1 (a), the level energy differences between the g.s., $3/2^+$ and $5/2^+$ levels are best explained with a decoupling parameter of $a = -0.8$. This value predicts the $7/2^+$ level at 1.1 MeV, whose energy is close to that of the experimental level at 1.154 MeV. This level has been populated in the β-delayed one neutron decay of ^{32}Na [MAC05; MAT07], one-neutron-removal reaction [TER08], and one-proton-removal reaction [MIL09]. None of the previous works assigned its spin and parity. In the present work, it is proposed that the 1.154-MeV level is the $7/2^+$ member of the $K^\pi = 1/2^+$ rotational band.

For the negative-parity states in Fig. 7.1 (a), the level energy differences between the lower three levels are best explained with a decoupling parameter of $a = -4.5$, assuming $1/2^-$ spin-parity for the 1.029-MeV level. This decoupling parameter predicts the $11/2^-$ level at 1.3 MeV, whose energy is close to that of the experimental level at 1.390 MeV. This level has been populated also in the β-delayed one neutron decay of ^{32}Na [KLO93]. However, they did not assign its spin and parity. In the present work, it is proposed that the 1.390-MeV level is the $11/2^-$ member of the $K^\pi = 1/2^-$ rotational band. It is also proposed that the 1.029-MeV level is the $1/2^-$ member of the same band.

It is very interesting to note that the decoupling parameters -0.8 and -4.5 of the $K^\pi = 1/2^+$ and $1/2^-$ bands in ^{31}Mg, respectively, are rather close to those in ^{25}Mg; -0.5 and -3.5, respectively [BOH75]. These facts suggest that the last neutron occupies the same single-particle orbit both in ^{25}Mg and ^{31}Mg for the respective bands. The single-particle

orbits in ^{25}Mg are assigned as $1/2^+[200]$ and $1/2^-[330]$ for the $K^\pi = 1/2^+$ and $1/2^-$ bands, respectively [BOH75]. Here, the orbits are denoted by a set of quantum numbers $K^\pi[Nn_z\Lambda]$, where N, n_z, and Λ are the principal quantum number, the oscillation quantum number in the direction of symmetry axis, and the orbital angular momentum projected on the symmetry axis, respectively.

From the experimental decoupling parameter a and the experimental level energies, it is possible to estimate the moment of inertia $\mathcal{J}$ in Eq. (7.1) for both the $K^\pi = 1/2^+$ and $1/2^-$ bands in ^{25}Mg and ^{31}Mg, according to the following equation.

$$\mathcal{J} = \frac{\hbar^2}{2} \cdot \frac{4I + 6 + 2a(-1)^{I+1/2}}{E(I+2) - E(I)}. \tag{7.2}$$

In order to compare the moment of inertia between the isotopes, the effect of mass difference has to be taken into account. A naive method is to take a ratio of $\mathcal{J}/\mathcal{J}_{\rm sphere}$, where $\mathcal{J}_{\rm sphere}$ is the moment of inertia of a rigid sphere, defined as

$$\mathcal{J}_{\rm sphere} = \frac{2}{5} M R_0^2, \tag{7.3}$$

where M and R_0 are the mass and the nuclear radius, respectively. The results are listed in Table 7.1. It is found that the ratios are close to each other; for the positive-parity band 1.37 (^{25}Mg) and 1.28 (^{31}Mg), and for the negative-parity band 1.52 (^{25}Mg) and 1.58 (^{31}Mg). These results suggest similar structures in the K=1/2 rotational bands between isotopes. Although the above discussion may be rather crude because the effect of pairing interactions

Table 7.1: Moment of inertia of rotational band $\mathcal{J}$ [Eq. (7.2)], of rigid sphere $\mathcal{J}_{\rm sphere}$ [Eq. (7.3)], and ratio of $\mathcal{J}/\mathcal{J}_{\rm sphere}$ for rotational band in ^{25}Mg and ^{31}Mg. The nuclear radius R_0 in Eq. (7.3) is evaluated according to $R_0 = 1.2A^{1/3}$.

	$\mathcal{J}$ [$\hbar^2$/MeV]	$\mathcal{J}_{\rm sphere}$ [$\hbar^2$/MeV]	$\mathcal{J}/\mathcal{J}_{sphere}$
^{25}Mg($1/2^+[200]$)	4.04	2.95	1.37
^{25}Mg($1/2^-[330]$)	4.50	2.95	1.52
^{31}Mg(positive)	5.08	4.22	1.20
^{31}Mg(negative)	6.25	4.22	1.48

is not considered, the configurations of $1/2^+[200]$ and $1/2^-[330]$ for the $K^\pi = 1/2^+$ and $1/2^-$ band are proposed, respectively, also in ^{31}Mg. As will be discussed in the following sections, the experimental results of the positive- and negative-parity bands support the $1/2^+[200]$

and $1/2^-[330]$ configuration, respectively.

It should be emphasized that the $K^\pi = 1/2^+$ and $1/2^-$ bands, which have been found many years ago in ^{25}Mg in the high excitation energy region, appear in ^{31}Mg as the ground-state band or very low-lying band. In the conventional shell model, when going through Mg isotopes from ^{25}Mg ($N = 13$) to ^{31}Mg ($N = 19$), the collective nature should disappear and in turn the single-particle nature should be dominant. However, the present work clarifies that it is not the case in ^{31}Mg. The development of deformation will be discussed in Sec. 7.1.1.3.

7.1.1.2 deformation of band head in rotational band

In order to investigate deformation of the band head based on the configurations of $1/2^+[200]$ and $1/2^-[330]$, the energies of neutron single-particle orbits in ^{31}Mg were calculated as a function of deformation parameter β (see Appendix G) in axially deformed Woods-Saxon potential [YAM16]. Figure 7.4 shows the results. Note that the lower orbits of $p_{3/2}$ and $s_{1/2}$ are not displayed. Since each $K^\pi[Nn_z\Lambda]$ orbit can accept two neutrons, the last neutron is in the $3/2^+[202]$ orbit for the deformation parameter β from 0 up to $\sim$+0.27. However, with increasing β, it is found from the neutron filling rule that the neutron in the $3/2^+[202]$ orbit hops into the $1/2^-[330]$ orbit after the intersection of the two orbits. As a result the last neutron is in the $1/2^-[330]$ orbit. In such a way the red thick line is drawn for the single-particle orbit of the last neutron in the ground state of ^{31}Mg.

In order to realize the $1/2^+[200]$ configuration for the $K^\pi = 1/2^+$ band proposed in the previous section, the deformation parameter β must be in a range of $+0.40 < \beta < +0.58$. As explained in Chapter 2.1, the experimental ground-state spin-parity $1/2^+$ has clearly rejected the $1/2^-[330]$ configuration. A more elaborated calculation of single-particle orbits and by I. Hamamoto [HAM10] showed the most plausible deformation parameter of $\beta \sim +0.45$ and the $1/2^+[200]$ configuration to reproduce $\mu = -1.00\mu_\mathrm{N}$. In order to realize the $1/2^-[330]$ configuration for the $K^\pi = 1/2^-$ band proposed in the previous section, it is found from the above discussion that the deformation parameter β must be in a range of $+0.27 < \beta < +0.40$.

In conclusion, based on the single-particle orbit calculation, the band heads of the $K^\pi = 1/2^+$ and $1/2^-$ rotational bands are largely deformed with $+0.40 < \beta < +0.58$ and $+0.27 < \beta < +0.40$, respectively.

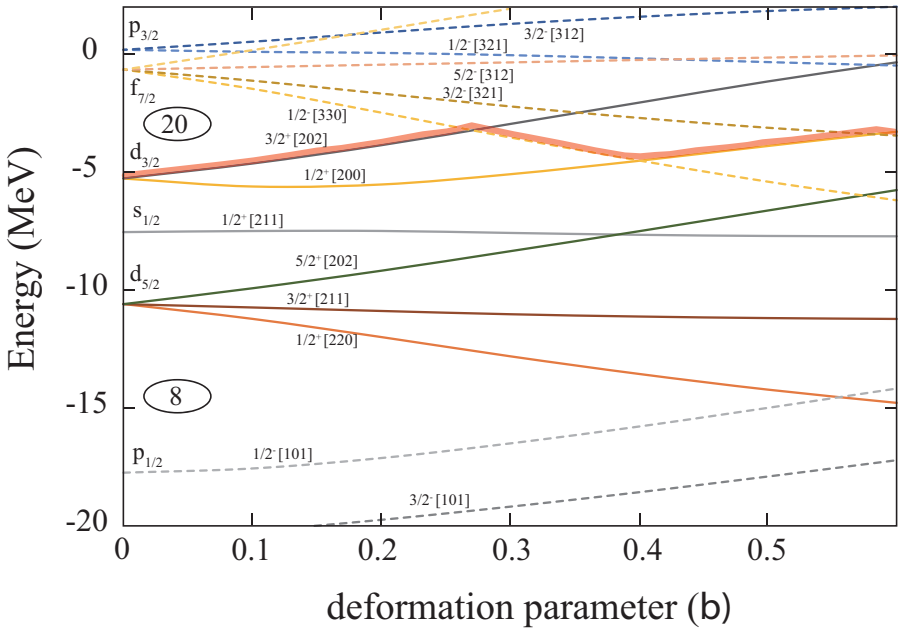

Figure 7.4: Single-particle orbits in prolate-deformed potential for ^{31}Mg. Thick red line indicates the orbits occupied by the last neutron.

7.1.1.3 systematics in $N = 19$ isotones: development of deformation with decreasing proton number

In order to see how such a large deformation develops, the two lowest negative-parity observed levels are compared in Fig. 7.5 for the N=19 isotones. With decreasing proton number from ^{39}Ca down to ^{33}Si, a gradual lowering of the $7/2^-$ and $3/2^-$ levels are observed. However, a very rapid drop is seen at ^{31}Mg and the level inversion between the $7/2^-$ and $3/2^-$ levels is observed.

The level ordering in ^{39}Ca, which is located near the doubly magic nucleus ^{40}Ca, is reasonably understood by the single-particle orbits of $f_{7/2}$ and $p_{3/2}$ with $\beta \sim 0$ in Fig. 7.5. The level inversion and rapid level lowering indicate abrupt increase of collectivity and deformation in ^{31}Mg. It is interesting to see the situation in ^{33}Mg, but not detailed data is available. The present work should be extended to ^{33}Mg in near future.

7.1.2 Levels understood in a framework of AMD+GCM

Figure 7.6 compares the experimental level scheme and the AMD+GCM calculations [KIM07]. The experimental levels assigned in the previous section as the rotational band members are shown separately. It is seen that all the $K^\pi = 1/2^+$ and $1/2^-$ rotational band levels are predicted in the AMD+GCM calculations, except for the 1.390-MeV $(11/2^-)$ level,

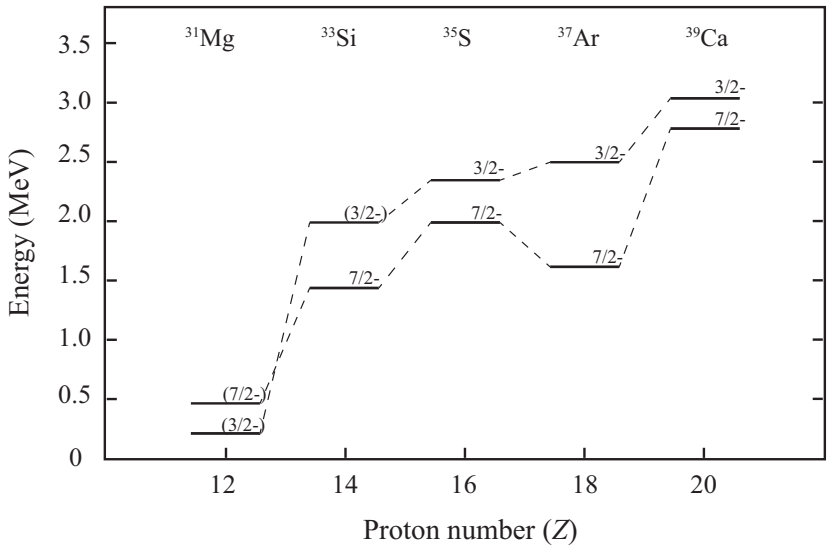

Figure 7.5: Systematics of energies of $7/2^-$ and $3/2^-$ levels for $N = 19$ isotones of ^{33}Si [WAN10], ^{35}S [WAR86], ^{37}Ar [HAG97], and ^{39}Ca [MAT93]. The same spin-parity levels are connected with the dashed lines.

which is not observed in the present work. The single-particle configurations of $1/2^+[200]$ and $1/2^-[330]$ proposed by the AMD+GCM calculations for the $K^\pi = 1/2^+$ and $1/2^-$ bands, respectively, and the estimated deformation parameter β are very consistent with our conclusion presented in the previous section. However, as shown in Fig. 7.7, the theoretical $\log ft$ value of the β decay $^{31}\mathrm{Na}_{\mathrm{g.s.}} \rightarrow {}^{31}$Mg ($5/2^+_1$, 0.944 MeV) of 5.3 [KIM07] is much smaller than the experimental one of 6.4(2) , whereas the $\log ft$ values for the $1/2^+$ and $3/2^+$ levels of the $K^\pi = 1/2^+$ band are reasonably reproduced. Note that the AMD+GCM calculations take into account the large deformation in the parent nucleus of $^{31}\mathrm{Na}_{\mathrm{g.s.}}$ [HUB78].

Since the $\log ft$ values are the clues to the overlap of wave functions between the ground state of ^{31}Na and the respective ^{31}Mg states, the small $\log ft$ value for the $1/2^+_1$ level indicates that the core of the rotational band is well deformed, as has been discussed so far. The extraordinarily large $\log ft$ value for the $5/2^+$ level at 0.944 MeV may suggest structure change of the core.

The AMD+GCM calculations also predict a $K^\pi = 3/2^-$ rotational band with larger deformation (see the second column from right in Fig. 7.6). The experimental 0.942-MeV level assigned as ($1/2^-$, $3/2^-$) most likely corresponds to the lowest $3/2^-$ level predicted by the calculation. The levels of $5/2^-$ and $7/2^-$ in this band are out of sensitivity of the present β-decay experiment.

In the very right of Fig. 7.6, the predicted levels with spherical configurations are shown. It seems that the $3/2^+$ and $5/2^+$ levels at 0.673 MeV and 2.015 MeV are well corresponding

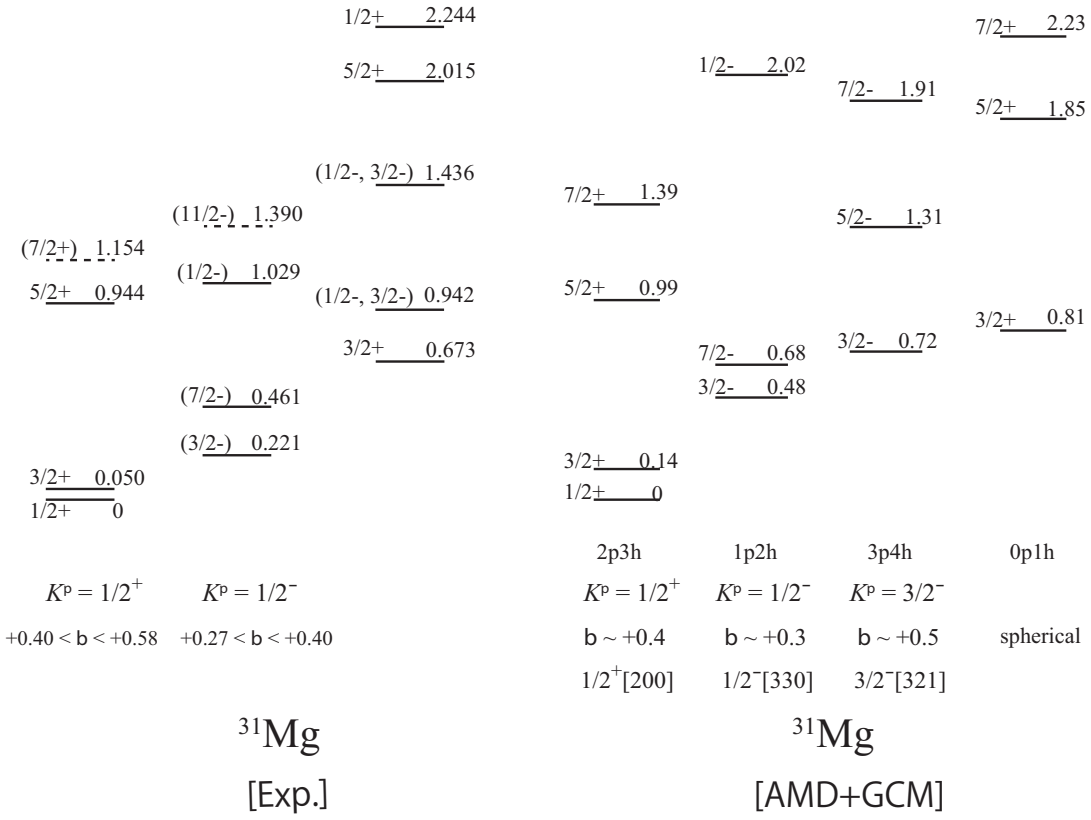

Figure 7.6: Comparison between the level energies of the experimental results and AMD+GCM calculations.

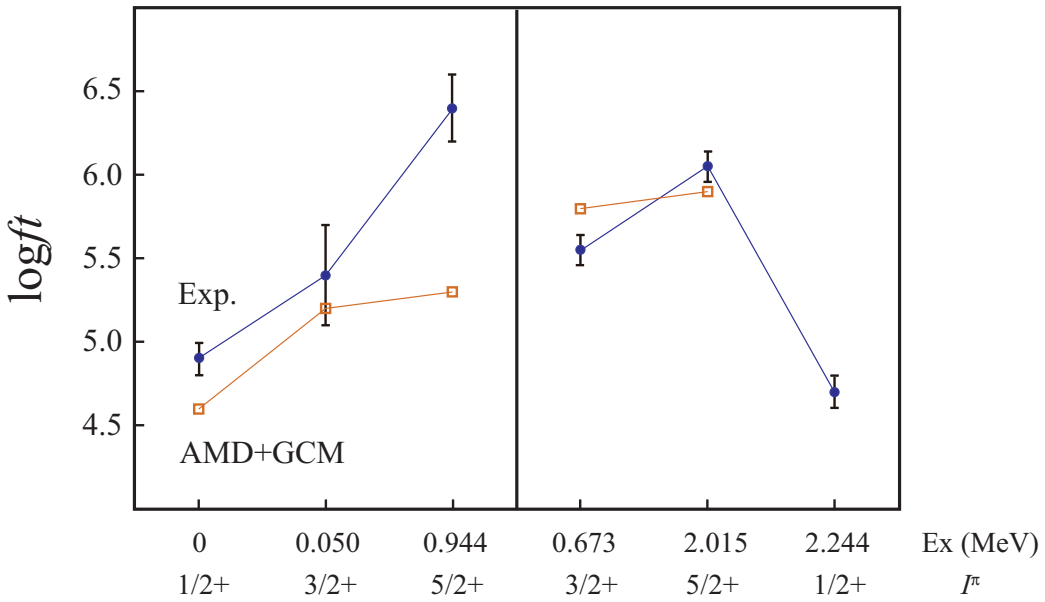

Figure 7.7: Comparison between experimental logft values (filled circles with error bars) and AMD+GCM calculations (open squares).

to the predicted levels, taking into account the level energy, the spin-parity, and the large $\log ft$ values of both the experiment and theory. These structure assignments are consistent with the large cross-sections of the proton knockout reactions of ^{32}Al, of which ground state has normal neutron 0p1h configuration, leading to these levels [MIL09].

The levels which have not been so far explained by the AMD+GCM calculations are those at 1.436 MeV [$(1/2^-, 3/2^-)$] and at 2.244 MeV ($1/2^+$). These levels must have nature neither of collective rotational band nor of spherical configurations. The AMD+GCM calculations predict a $1/2^+$ level at excitation energy region higher than 4 MeV, which is much above the neutron threshold at 2.310 MeV, and somehow the level energy does not come down, even by introducing the degree of freedom of γ deformations [KIM16]. It may be necessary to incorporate collectivity which is not taken into account in the AMD+GCM calculations. The detail of the 2.244-MeV level is discussed in the next section.

7.1.3 $1/2_2^+$ state at 2.244 MeV

The large β branching ratio $I_\beta = 19(4)$ % for the 2.244-MeV level strongly indicates the collective nature of this level. This is also investigated by the intensities of γ-rays depopulating the 2.244-MeV level. Table 7.2 shows the relative intensities of the 2244-, 2194-, and 1571-keV γ-rays leading to g.s. ($1/2^+$), 0.050- ($3/2^+$), and 0.673-MeV ($3/2^+$) levels, respectively, together with the Weisskopf estimates assuming pure $M1$ transitions. It is clearly seen that the transitions to the $1/2^+$ and $3/2^+$ rotational band levels are much more favored than the transition to the 0.673-MeV $3/2^+$ level which is characterized by the spherical configurations. These facts imply that the second $1/2^+$ level at 2.244 MeV has similar configurations to the $1/2_1^+$ and $3/2_1^+$ levels with largely deformed shape, or with dominant 2p3h configurations in other words. The large β branching ratio is consistent with the above picture. New theoretical approach to explain this $1/2^+$ level at 2.244 MeV characterized by collective nature is strongly awaited.

Table 7.2: Comparison between the γ-ray intensities and Weisskopf etimate.

E_γ (keV)	$E_i \rightarrow E_f$ (MeV)	$I_{\rm exp}$ (relative)	$I_{\rm W.e.}$ (relative)
2244	2.244 $\rightarrow$ g.s.	1	1
2194	2.244 $\rightarrow$ 0.050	0.25	0.96
1571	2.244 $\rightarrow$ 0.673	0.02	0.49

7.1.4 Summary: variety of structures in ^{31}Mg

Fig. 7.8 shows the summary of a variety of structures in ^{31}Mg, discussed so far. Various nuclear structures at low-lying states such as rotational bands associated with deformation and single particle-like states are observed in ^{31}Mg. The 0.050- ($3/2^+$) and 0.944-MeV ($5/2^+$) levels are understood as the members of the positive-parity $K^\pi = 1/2^+$ rotational band with the configuration of dominant 2p3h which corresponds to the $1/2^+[200]$ orbit. The 0.221- ($3/2^-$), 0.461- ($7/2^-$), and 1.029-MeV ($1/2^-$) levels are most likely the members of the $K^\pi = 1/2^-$ rotational band with the configuration of 1p2h corresponding to the $1/2^-[330]$ orbit. The 0.673- ($3/2^+$) and 2.015-MeV ($5/2^+$) levels are assigned to be single particle-like levels from the comparison with the AMD+GCM calculations. The 2.244-MeV level with large β branching ratio, which is not predicted at such a lower energy level in the AMD+GCM calculations, and some experimental results suggest that it has collectivity.

The idea of the "island of inversion" for ^{31}Mg has been discussed for many years based on the ground state or very limited number of low-lying levels. The present work gives comprehensive understanding for most of the levels below the neutron threshold for the first time. As a result it becomes possible to discuss the competition between the collective nature and the single-particle nature in such a neutron-rich region.

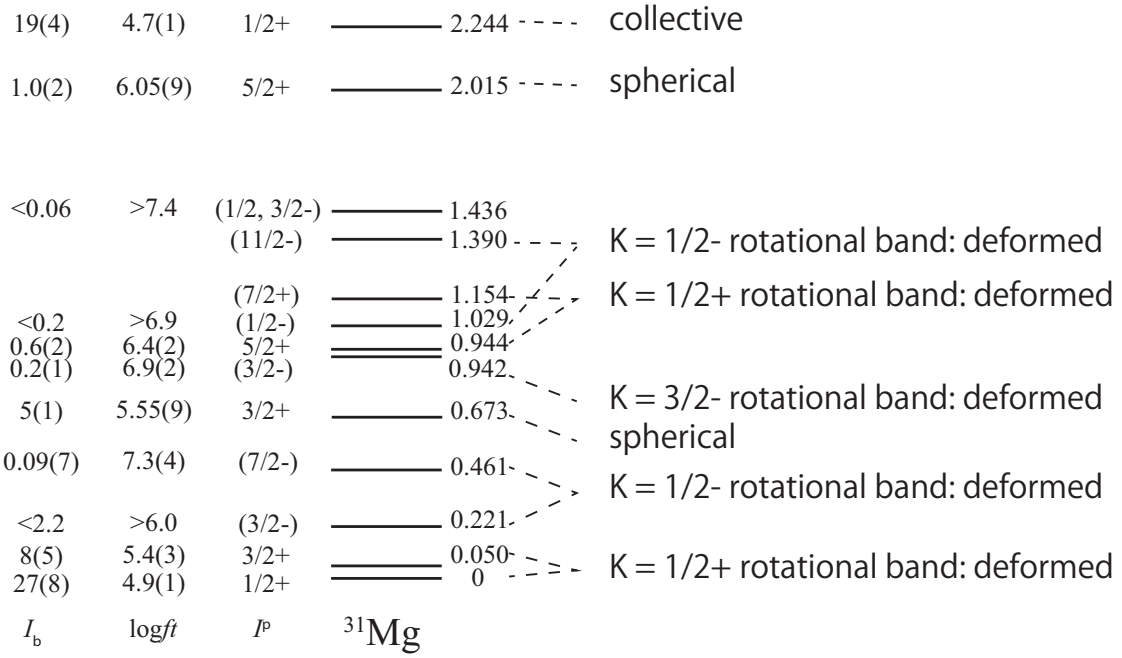

Figure 7.8: Summary of the observed structures in ^{31}Mg.

7.2 Structure of states in ^{30}Mg

The present work also aimed at getting more detailed information on the structures in ^{30}Mg than the preceding work [TAJ12] by the group, in which the author of the present thesis has been working. Because of the higher detection efficiency and higher ^{30}Na beam intensity in the present work than the previous work, the spin-parity assignments for the positive-parity levels in ^{30}Mg could be performed more precisely, enabling new assignments for three levels at 4.695 (3^+), 5.898 (1^+), and 6.066 MeV (3^+), and furthermore many weak intensity γ transitions have been found for the first time. As a result of the latter performance, six new levels were found and 4 levels with large logft values (> 7.0) in an excitation energy region of 3.3 - 4.8 MeV were proposed as the negative-parity states. Most of other results of ^{30}Mg in the previous work [TAJ12] were confirmed in the present work, except for the assignment renewals for the levels at 5.898 MeV [$(2^+) \rightarrow 1^+$] and 6.066 MeV ($2^+ \rightarrow 3^+$).

In the next section, the experimental results are compared with the AMD+GCM calculations and the shell model calculations which take into account the multi-particle-multi-hole excitations across the *sd-pf* shall gap. In Sec. 7.2.2 a unique nature of the 1^+ level at 4.967 MeV is discussed and a new type of collective motion, scissors mode [CAS05], is proposed for this level.

7.2.1 Levels understood in the frameworks of AMD+GCM and shell model

In Fig. 7.9, the experimental level scheme of ^{30}Mg is compared with the theoretical calculations of the AMD + GCM [KIM16] and of the shell model with a model space taking into account both the *sd*- and *pf*-shells (with SDPF-M Hamiltonian) [TAJ12]. Note the experimental 0^+_1, (2^+), and 4^+ levels at 0.0, 2.468, and 3.381 MeV are in good accord with the predicted 0p0h bands in both theories. The vibrational-like structure indicated by the experimental ratio of level energy $E(4^+)/E(2^+) = 2.28$ is reasonably reproduced both in the AMD+GCM calculations [$E(4^+)/E(2^+) = 2.68$] and in the shell model calculations [$E(4^+)/E(2^+) = 2.91$].

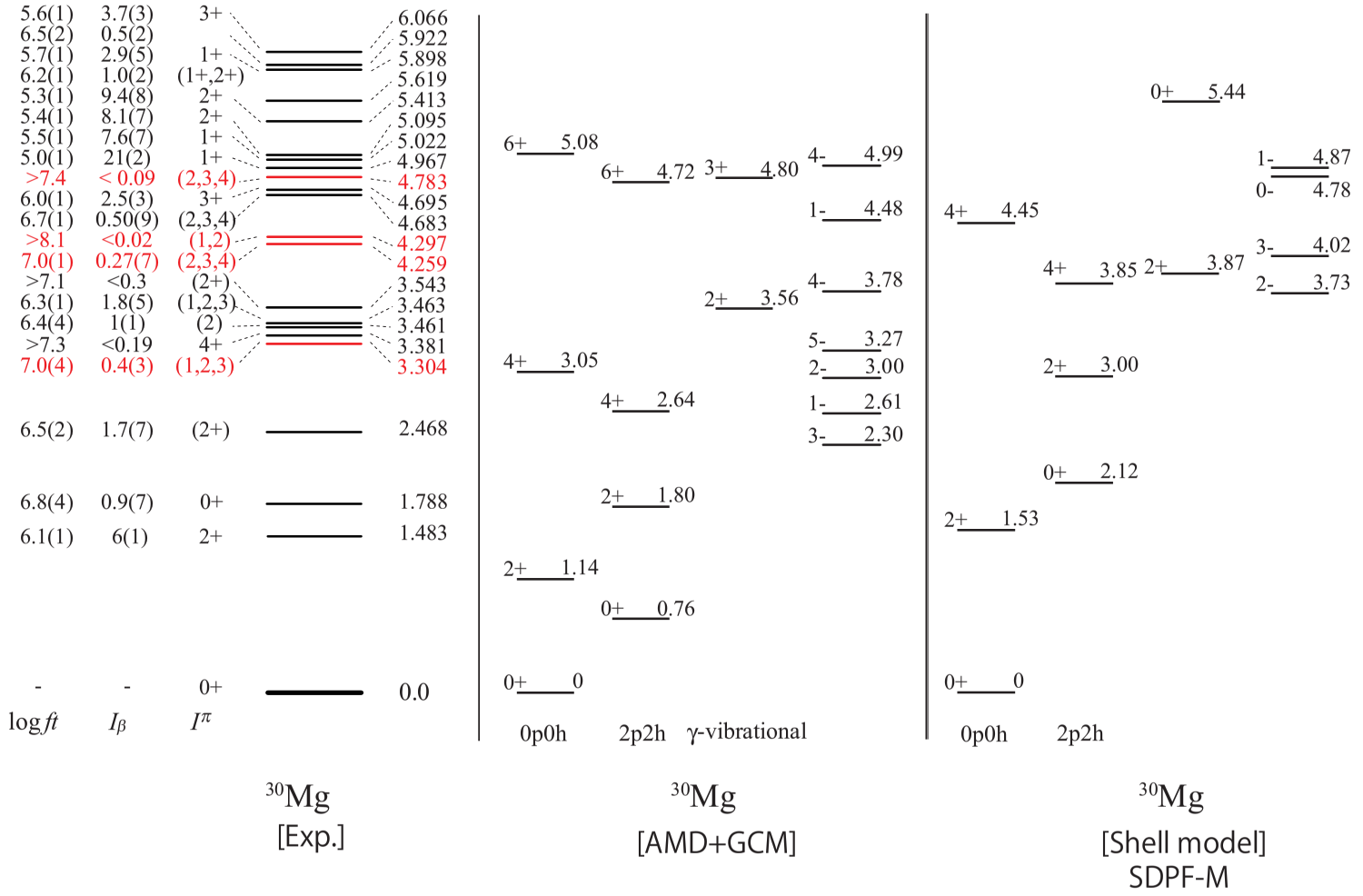

Figure 7.9: Comparison of the levels in ^{30}Mg with the AMD + GCM calculations [KIM16] and the shell model calculations [TAJ12]. Experimental levels in red color is the negative-parity levels proposed by the present work.

The second 0^+ level at 1.788 MeV, for which a large prolate deformation has been proposed by the conversion electron measurement of the $E0$ transition [0_2^+ (1.788 MeV) $\rightarrow$ 0_1^+ (g.s.)] [SCH09], is also predicted as the band head of the rotational band with 2p2h configurations in both the theories. The AMD+GCM calculations predict more collective nature ($\beta\sim+0.5$) than reality, as inferred from the predicted very low level energy (0.76 MeV). The experimental (2^+) level at 2.468 MeV does not correspond to the predicted 2^+ level of the 2p2h rotational band, since no γ-transition was observed from this level to the 0_1^+ level. It was proposed [TAJ12] that the 2.468-MeV level is the band head (2.95 MeV) of the γ-vibrational band predicted by the calculations of constrained Hartree-Fock-Bogoliubov plus local quasiparticle random phase approximation method (CHFB + LQRPA) [HIN11]. The AMD+GCM calculations also predict such 2^+ level, but due to restricted degree of freedom in γ-deformation, the predicted energy is rather high (3.56 MeV). The reason that the 2^+ level of the 2p2h rotational band built on the 0_2^+ level was not observed in the present work is probably that it is difficult to populate the levels with core excitation by the β decay.

As discussed before, 4 levels with large $\log ft$ values (> 7.0) were proposed in the present work as the negative-parity states (shown in red color in Fig. 7.9). It is understood that these levels correspond to the predicted negative-parity levels with 1p1h and 3p3h configurations in both theories.

7.2.2 Exotic structure of 1^+ level at 4.967 MeV

The 4.967-MeV level is characterized by the largest β-decay branching ratio of I_β = 21(2)%. This fact indicates that this 1^+ level has similar structure to the ground state of ^{30}Na, which was found to be deformed by the magnetic moment measurement [HUB78] and was recently confirmed in various reaction channels [PET15]. Therefore, the 1^+ level at 4.967 MeV must be deformed. It also should be noted that the γ-transitions to the 1.788-MeV second 0^+ level, which is largely deformed [SCH09], were observed only from the 4.967-MeV 1^+ and the 5.413-MeV 2^+ levels. Note that the latte level has the second largest I_β value of 9.48(2)%.

In order to get more insight into the 4.967-MeV level, the relative intensities of γ-ray transitions from this state are compared with the Weisskopf estimates, as shown in Fig. 7.10. It is seen that the 3179 keV transition [4.967 MeV (1^+) $\rightarrow$ 1.788 MeV (0^+)] is enhanced to a large extent relative to the 4967 keV transition [4.967 MeV (1^+) $\rightarrow$ g.s. (0^+)]. Such a strong enhancement in the $M1$ transition to the deformed 0^+ state is one of the features characteristic of a 1^+ state in scissors mode, which is a kind of vibrational mode where protons

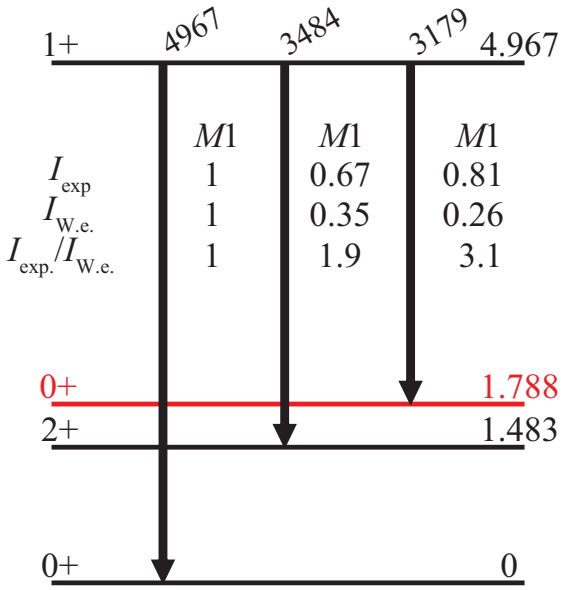

Figure 7.10: Relative intensities of γ-ray transitions from the 1^+ 4.967-MeVlevel. $I_{\mathrm{W.e}}$ is the Weisskopf estimate.

and neutrons are moving in anti-phase like a scissors [CAS05]. The energy difference of $\sim$ 3 MeV between the 1^+ and 0_2^+ levels is another indication for the scissors mode [CAS05]. Therefore, we propose here that the 1^+ state at 4.967 MeV is the 1^+ scissors mode state. The nucleus ^{30}Mg is the lightest one in which the scissors mode is observed. Detailed comparison with theoretical calculations for the scissors mode is anxiously awaited.

7.2.3 Summary: variety of structures in ^{30}Mg

Figure 7.11 shows the summary of the structures in ^{30}Mg. It is seen that various structures appear in the excited states of ^{30}Mg.

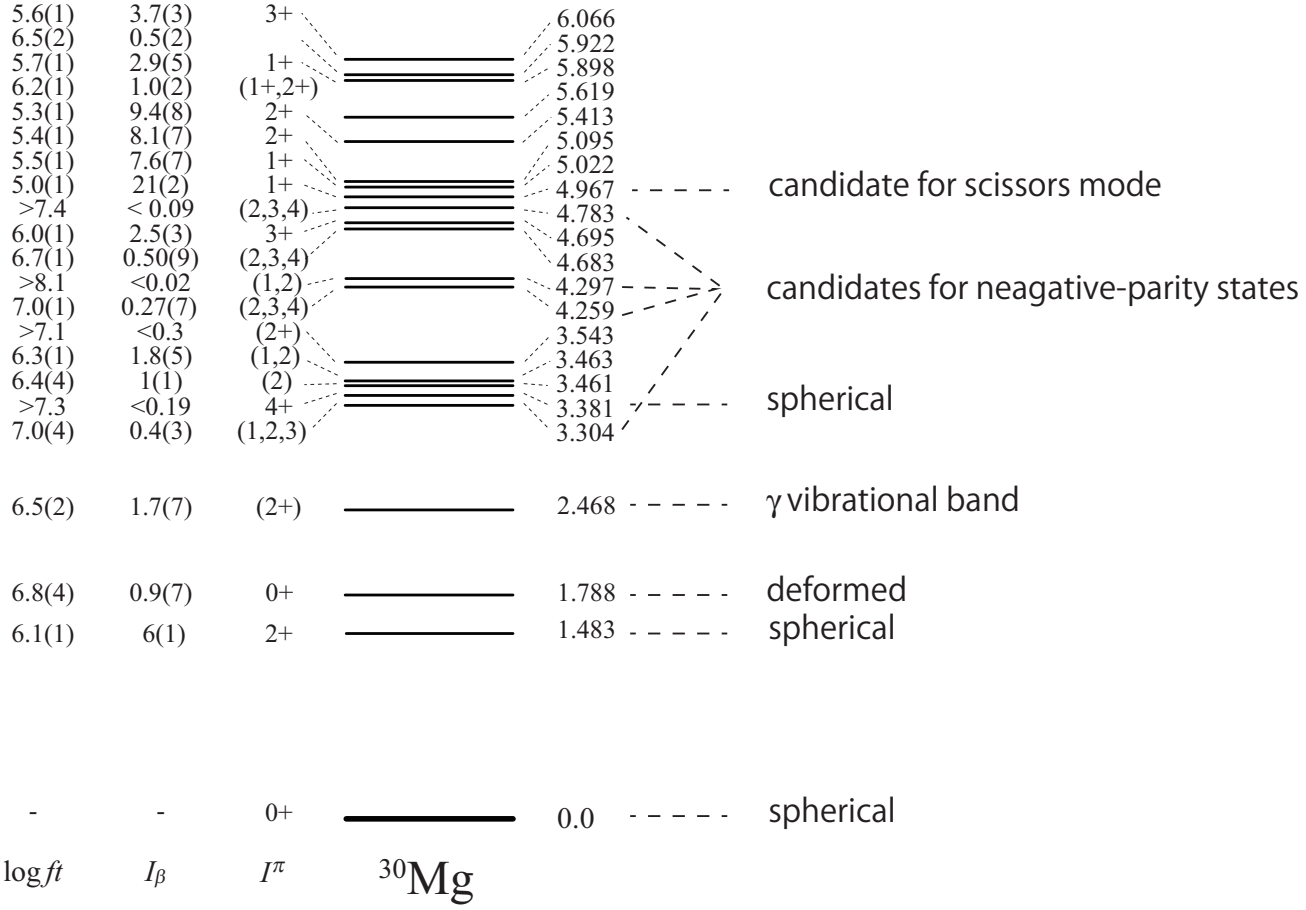

Figure 7.11: Summary: variety of structures in ^{30}Mg.

CHAPTER VIII

Summary

In the preset work, the excited states of the neutron-rich nucleus ^{31}Mg were studied aiming at comprehensive understanding of the structure of the nucleus which is located in the region of the N=20 "island of inversion". This nucleus has been investigated in various types of experiments for a long time, but none of the spins and parities, the important key quantities to understand the nuclear structure, has been assigned experimentally until the ground state magnetic moment was determined and the spin-parity was assigned as $1/2^+$ [NEY05]. Because of such a situation it has been difficult to systematically study how far the shell-model nature prevails and how the collective nature appears, when the neutron number N approaches to the magic number 20 around the region of island of inversion.

In the present work the excited states in ^{31}Mg were investigated in detail by the efficient method [KUR12; SHI14], which is able to unambiguously assign the spin-parity of the daughter states of the β-decay of ^{31}Na. Namely, the spatial asymmetry in the β decay of spin-polarized ^{31}Na was observed in coincidence with the γ-transitions in the daughter ^{31}Mg, and from the β-decay asymmetry, the spin values for the respective levels were determined. The experiment was successfully performed at TRIUMF by taking advantage of the unique highly spin-polarized ^{31}Na beam. The spin values of all the observed positive-parity levels in ^{31}Mg were precisely determined, and furthermore from the very detailed intensities of β-decays and γ-transitions, possible spin values for all the observed negative-parity levels in ^{31}Mg were restricted significantly.

The experimental results were compared with the theoretical predictions of collective rotational model and the AMD+GCM calculations. It was found that the levels in ^{31}Mg are categorized in four groups as follows.

(i) levels of the $K^\pi = 1/2^+$ and $1/2^-$ rotational band members:

The low-lying positive- and negative-parity levels in ^{31}Mg are well explained by the K^π

$= 1/2^+$ and $1/2^-$ rotational band schemes characterized by the single-particle orbits of $1/2^+[200]$ and $1/2^-[330]$, respectively, in a prolate-deformed potential. It is shown that these bands are similar to those of the rotational bands which have been observed in high excitation energy region of ^{25}Mg. This fact indicates that the ^{31}Mg is very deformed, although its neutron number is close to N=20. In fact the deformation parameters of the $K^\pi = 1/2^+$ and $1/2^-$ rotational bands of ^{31}Mg are predicted that $\beta \sim +0.4$ and $\sim +0.3$, respectively, by the AMD+GCM calculations [KIM07].

(ii) a level of the $K^\pi = 3/2^-$ rotational band member:
The $(1/2^-, 3/2^-)$ level at 0.942 MeV is most likely the band head of the $K^\pi = 3/2^-$ rotational band, which is predicted in the AMD+GCM calculations, with the single-particle orbit of $3/2^-[321]$ in a prolate-deformed potential. A larger deformation parameter for this band is predicted: $\beta \sim +0.5$. Other band members with higher spins are not populated in the β-decay of ^{31}Na.

(iii) levels with spherical nature:
The $3/2_2^+$ and $5/2_2^+$ levels at 0.673 and 2.015 MeV, respectively, are most likely the levels characterized by the spherical nature, predicted by the AMD+GCM calculations. It is interesting to note that the shell-model like structure still prevails at higher excitation energy region.

(iv) a level which is not understood by theoretical models:
The $1/2_2^+$ level at 2.224 MeV, characterized by the small $\log ft$ value, can not be explained by any theoretical models. Since the parent state, $^{31}\mathrm{Na}_{\mathrm{g.s.}}$ is very deformed, the small $\log ft$ value implies the collective nature of the $1/2_2^+$ level.

In the present work the measurement was also performed with the spin-polarized ^{30}Na to obtain more detailed information on the ^{30}Mg structure than the preceding work. The experimental results were compared with the theoretical predictions of the AMD+GCM calculations and the shell model calculations with the SDPF-M Hamiltonian. It was found that the levels in ^{30}Mg are categorized in five groups as follows.

(i) levels with spherical nature:
The low-lying three levels at 0.0 MeV (0_1^+), 1.483 MeV (2_1^+), and 3.381 MeV (4_1^+, assigned in another work) are in good accord with the predicted levels with 0p0h configurations.

(ii) a level of the largely deformed rotational band:
The second 0^+ level at 1.788 MeV is the band head of the rotational band with 2p2h configurations. The higher spin members of this band, such as 2^+, 4^+, and so on, were not observed in the present work. It may be due to that the levels with core excitation are difficult to populate in the β decay of ^{31}Na.

(iii) 1^+ scissors mode state where protons and neutrons are moving in anti-phase like a scissors:
The 1^+ level at 4.967 MeV has characteristic features of the 1^+ state in scissors mode. We propose that it is the scissors mode state in the lightest nucleus.

(iv) a level of γ-vibrational band:
The (2^+) level at 2.468 MeV shows good correspondence with the band head of the predicted γ-vibrational band. The 3^+ state as the higher member of this band was not observed in the present work.

(v) negative-parity states with 1p1h and 3p3h configurations:
By comparing with the theoretical predictions, it is proposed that the levels with large logft values (>7.0) in the excitation region of 3.3 - 4.8 MeV are the negative parity states.

In conclusion, the present work successfully showed that the competition between the single particle nature and the collective nature causes a variety of structures in ^{30}Mg and ^{31}Mg, which are located close to the region of N=20 island of inversion. It is important to investigate the structure changes in more neutron-rich nuclei such as ^{32}Mg, ^{33}Mg, and so on, in order to see the systematic change of the structure. It is to be noted that the neutron separation energy in ^{31}Mg is as low as 2.310 MeV. Therefore, it is also important to investigate the structures in the excitation energy region above the neutron threshold in the β-delayed neutron-γ spectroscopy.

ACKNOWLEDGEMENTS

I would like to express my appreciation to people who give me constructive comments and warm encouragement to make my research in the Ph.D courses at Osaka University.

My deepest appreciation goes to Prof. T. Shimoda who gave me the opportunity to engage in the great research project about the structure in Mg isotopes at TRIUMF and give me the critical advice on the present study. I am deeply grateful to Assoc. Prof. A. Odahara who gave me detail advices and comments on the data analysis and interpretation of the experimental results, and helps me carry out my study.

I would like to thank all the Osaka collaborators of the S1391 experiment at TRIUMF; to S. Morimoto for staying with me at TRIUMF for a long time and working on the preparations of the experiment especially for neutron detectors, to my colleagues in Shimoda laboratory: S. Kanaya, A. Yagi, H. Kanaoka, T. Kawamura, A. Nakahashi, T. Fujiwara, and T. Yoshizumi for supporting in various parts of the experiments. I would like to show my thanks to Dr. K. Tajiri and K. Kura who engaged the preceding experiment of the present work and built the foundation of the research project of the systematically study of Mg isotopes. They were kind to give me advices of the detectors setups and procedure of the experiment. I would like to express my appreciation to Dr. Y. Hirayama of High Energy Accelerator Research Organization (KEK) who gave me fruitful advice about the neutron detectors. My appreciation goes to M. Mihara, S. Yamaoka of Nuclear and Solid-State Physics Group in Osaka University, and T. Kobayashi of Tajima group in Osaka University for helping to anneal the Pt foil.

I would also like to thank to the researchers and staff members of TRIUMF for their collaborations. My appreciation goes to Dr. Matt Pearson for his technical support during our stay at TRIUMF, to Dr. C.D.P. Levy for operation of the laser system and providing the highly-polarized Na beams, and to other staffs for the providing the intense Na beams and various supports.

I would like to thank to staffs of Research Center for Nuclear Physics, Osaka University (RCNP), Osaka University Radioisotope Research Center, and Center for Nuclear study, the University of Tokyo (CNS) for lending us useful electronic circuits.

I am deeply grateful to the theoretical researchers for discussions of the structures in Mg isotopes. I would like to offer my special thanks to Assoc. Prof. M. Kimura of Hokkaido University for providing the results of AMD+GCM model calculations of ^{30}Mg and ^{31}Mg and discussions of the structures. I owe my gratitude to M. Yamagami who provided the calculation code of single-particle orbits in prolate-deformed potential. I would like to thank to Prof. Matsuyanagi for discussions in term of the collective model.

Finally, I wish express the deepest appreciation to my family for support and encouragement throughout my academic life.

APPENDIX A

Effectiveness of use of highly spin-polarized Na beam

The error of determination of AP value is expressed as

$$\Delta(AP) = \frac{\partial(AP)}{\partial R}\Delta R \ = \frac{\Delta R}{\sqrt{R}(\sqrt{R}+1)}, \tag{A.1}$$

where ΔR is given as

$$\begin{aligned}\Delta R &= \sqrt{\Big(\frac{\partial R}{\partial N_{R+}}\Delta N_{R+}\Big)^2 + \Big(\frac{\partial R}{\partial N_{L+}}\Delta N_{L+}\Big)^2 + \Big(\frac{\partial R}{\partial N_{R-}}\Delta N_{R-}\Big)^2 + \Big(\frac{\partial R}{\partial N_{L-}}\Delta N_{L-}\Big)^2} \\ &= R\sqrt{\Big(\frac{\Delta N_{R+}}{N_{R+}}\Big)^2 + \Big(\frac{\Delta N_{L+}}{N_{L+}}\Big)^2 + \Big(\frac{\Delta N_{R-}}{N_{R-}}\Big)^2 + \Big(\frac{\Delta N_{L-}}{N_{L-}}\Big)^2}.\end{aligned} \tag{A.2}$$

Assuming $N_{R+} = N_{L+} = N_{R-} = N_{L-} = N/4$ and $\Delta N = \sqrt{N}$, where N is total β-ray counts, ΔR is more simply expressed as

$$\Delta R = \frac{4R}{\sqrt{N}}. \tag{A.3}$$

By using Eqs. A.1 and A.3, the error of AP is calculated by using AP and total count N as

$$\begin{aligned}\left|\frac{\Delta(AP)}{AP}\right| &= \left| \ \frac{1}{AP} - AP \ \right| \frac{1}{\sqrt{N}} \\ &\sim \frac{1}{AP\sqrt{N}} \qquad (AP << 1).\end{aligned} \tag{A.4}$$

Eq. (A.4) indicates that the polarization P shows the larger contribution to the accuracy than the total β-ray counts N.

APPENDIX B

Relaxation time of the polarization in the Pt stopper

The relaxation time T_1 of the polarization of a nucleus implanted in a Pt stopper can be estimated by using Korringa's relation [KOR50] given as

$$T_1 \propto \frac{1}{g^2 T}, \tag{B.1}$$

where g and T are the g-factor of the incident parent nucleus and the temperature of the stopper, respectively. For ^{26}Na ($g = +0.9503$ [HUB78]), the relaxation time of 0.78(8) s have been measured at room temperature [MIN04]. The spin relaxation time for ^{30}Na and ^{31}Na are estimated by using the experimental relaxation time of ^{26}Na [$\tau(^{26}\mathrm{Na})$] as

$$T_1 = T_1(^{26}\mathrm{Na}) \times \frac{g(^{26}\mathrm{Na})^2}{g^2}. \tag{B.2}$$

The calculated T_1 for Na isotopes by Eq. (B.2) are listed in Table B.1.

Table B.1: Estimated spin relaxation time (τ) for Na isotopes implanted in Pt stopper at room temperature.The g-factors of Na isotopes were taken from Ref. [HUB78].

	g-factor	τ (s)	Half-life (ms)
^{26}Na	0.9503(6)	0.78(8)[a]	1.077(5)
^{30}Na	1.035(1)	0.7	48(2)
^{31}Na	1.532(1)	0.3	17.4(4)

[a]Taken from Ref. [MIN04]

APPENDIX C

Annealing of Pt foil

C.1 Procedure of annealing Pt foil

In order to avoid the possible perturbations and the relaxation of the polarization of Na beams due to the defect or distortion of the lattice of Pt foil, it is necessary to remove the local stress in the Pt foil by annealing. The foil was annealed by using the electric furnace. The picture and the illustration of the electrode of the electric furnace are shown in Fig. C.1 (a) and (b).

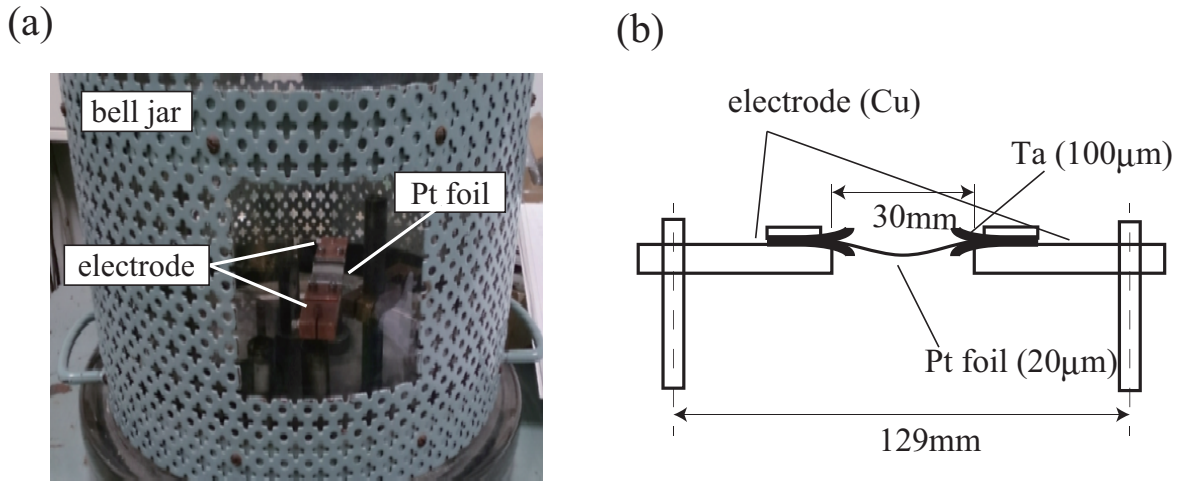

Figure C.1: (a) Picture of the electric furnace and (b) illustration of the electrode and the Pt foil.

The Pt foil washed with pure water, alcohol, and acetone was placed in vacuum ($\sim 10^6$ torr) at the center of the bell jar and was set on the electrode. The electric current was applied to the Pt foil and the current was gradually increased. In 2 hours, the Pt foil was heated from the room temperature to 1400°C around the melting point of Pt (1768°C) and the temperature was kept for 1 hour. The temperature was monitored by using the radiation

thermometer. Then, the temperature was lowered to 1200°C in 1 hour and kept for 8 hours. Again, the temperature was lowered to 800°C in 1 hour and kept constant for 10 hours. Finally, the Pt foil was lowered to room temperature in 2 hours.

C.2 X-ray diffraction analysis

In order to confirm the effectiveness of the annealing of the Pt foil, the X-ray diffraction analysis was performed for the Pt foil before and after annealing by using the characteristic X-rays of Cu ($K\alpha_1$ 8.048 keV and $K\alpha_2$ 8.028 keV). Figure C.2 (a) and (b) show the X-ray diffraction spectra of the Pt foil before and after annealing, respectively. The diffraction angles (2θ) were measured from 35° to 90°. In Fig. C.2 (a), there are five Bragg peaks for the planes of (111), (200), (220), (311), and (222). This facts indicate that the Pt foil before annealing consists of crystals oriented in various directions. On the other hand, there found only two Bragg peak for (111) and (222) planes in the spectrum for the annealed Pt foil, as shown in Fig. C.2 (b). It suggests that the crystal of Pt foil orients to the same direction. Figure C.3 shows the enlarged X-ray diffraction spectra focused on the Bragg peak for the (222) plane. It is found that there are two peaks in spectrum of the annealed Pt foil in Fig. C.3 (b). Each Bragg peak for a specific plane consists of two peaks which comes from the two X-rays of $K\alpha_1$ and $K\alpha_2$. In Fig. C.3 (a), the resonance peak are so broad that these peaks could not be separated. Such wide resonance peak comes from the local stress of the crystal such as lattice mismatch and/or lattice defect. The narrow peaks of the annealed Pt foil in Fig. C.3 (b) suggests that the distortion of the lattices of the Pt foil was removed by annealing.

The crystal structures of the Pt foils were also examined by the Laue method. Figure C.4 (a) and (b) show the Laue X-ray photographs of the Pt foil before and after annealing, respectively. In Fig C.4 (b), the Laue patterns are clearly found.

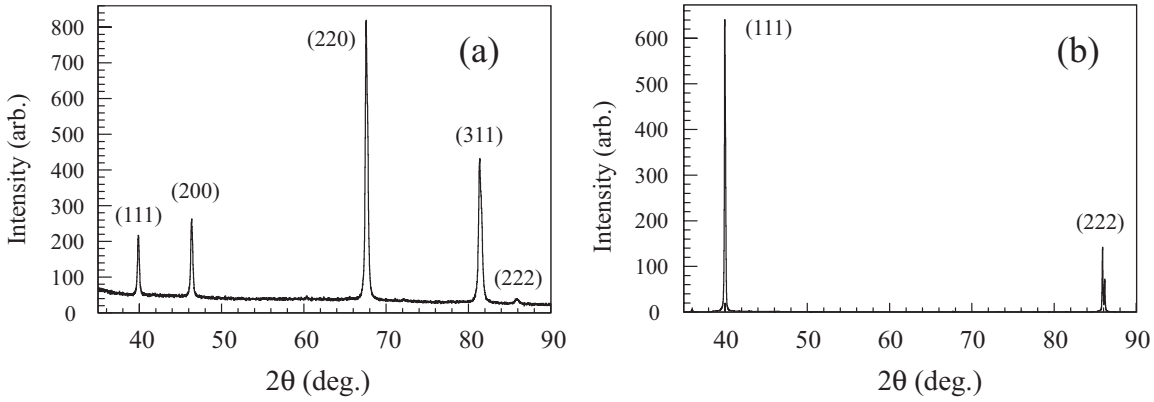

Figure C.2: X-ray diffraction spectra of the Pt foil (a) before and (b) after annealing for 2θ = 35° - 90°.

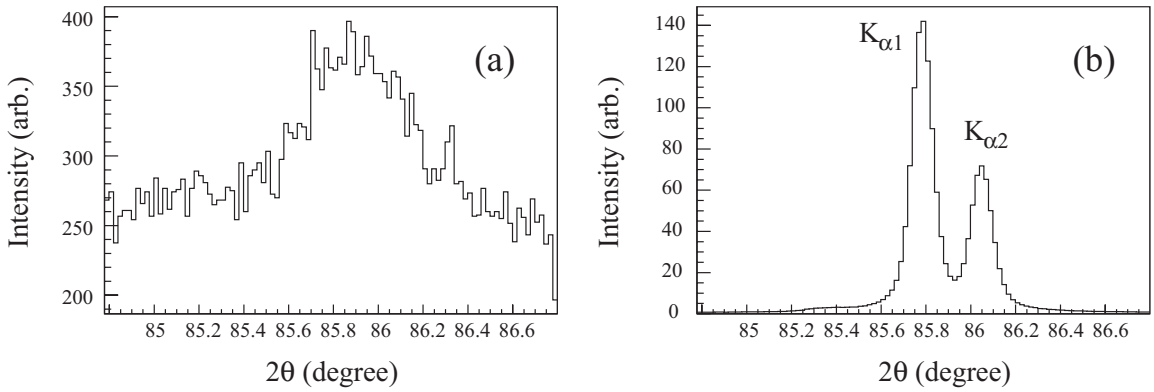

Figure C.3: X-ray diffraction spectra of the Pt foil (a) before and (b) after annealing for 2θ = 84.8° - 86.8°.

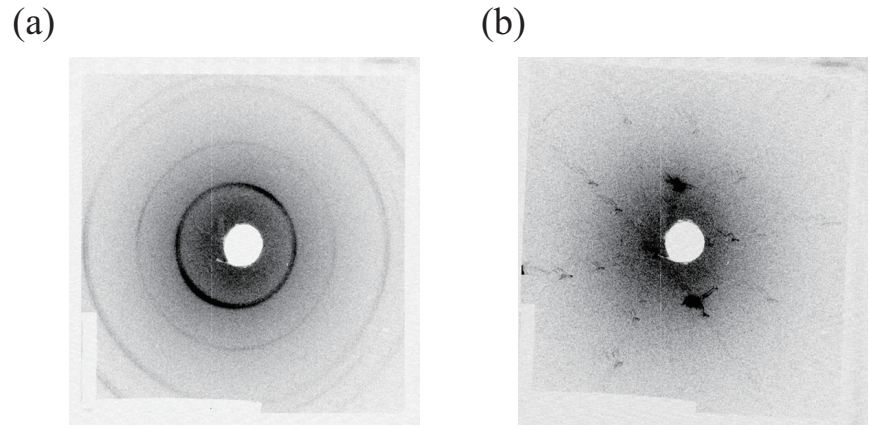

Figure C.4: Laue photographs of of the Pt foil (a) before and (b) after annealing.

APPENDIX D

Energy information of the plastic scintillators

Figure D.1 (a) shows a typical QDC spectrum of the plastic scintillator placed in front of Ge detectors. The peak of the energy loss of β rays was found around 300 ch, which is clearly separated from the pedestal. The threshold of the discriminators for the signals was adjusted to remove the pedestal at $\sim$ 200 ch. Figure D.1 (b) shows the QDC spectrum by using events which contain both QDC and TDC data of the plastic scintillator. It was clearly found that the pedestal was cut by the discriminator, and this assure the highly S/N measurement of β rays by the plastic scintillators.

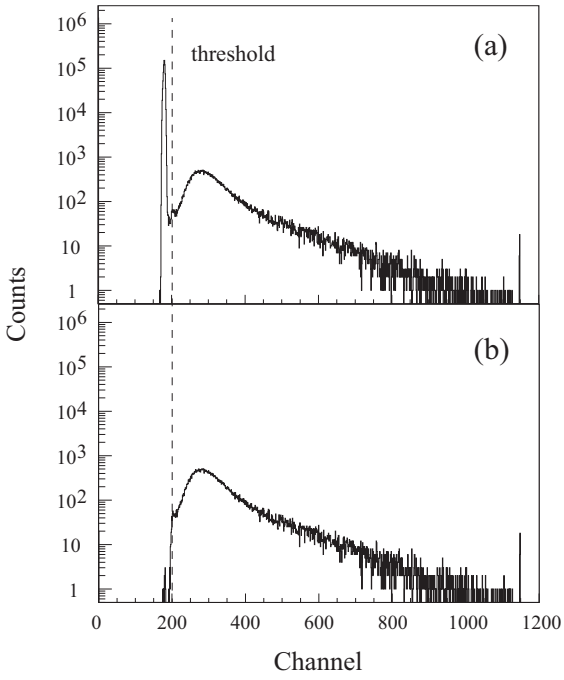

Figure D.1: QDC spectra of the plastic scintillator in front of Ge-2 (a) without and (b) with timing gate.

APPENDIX E

Gamma-ray angular distribution by residual polarization

In case that the polarization of the parent nucleus is very high, the β-delayed γ rays have angular dependence on the emission angle to the polarization direction. According to Ref. [MOR76], the angular distribution of γ rays associated with the polarized nucleus is given as

$$W(\theta) = \sum_k \rho_k(j_i) F_k(j_f \lambda j_i) P_k(\cos\theta), \tag{E.1}$$

where P_k, j_i, j_f, and λ are k-th Legendre polynomial, initial and final state spins, and multipolarity of the γ ray, respectively. ρ_k is statistical tensor defined as

$$\rho_k(j) = \sqrt{2j+1} \sum_m (-1)^{j-m} \langle jmj - m|k0\rangle a_m, \tag{E.2}$$

where m and a_m represent magnetic quantum number and the probabilities of the states specified by m. F_k is expressed by using Racah coefficient as

$$F_k(j_f \lambda j_i) = (-1)^{1+j_i-j_f} \sqrt{2j_i+1}(2\lambda+1)\langle \lambda 1 \lambda - 1|k0\rangle W(j_i j_i \lambda\lambda; k j_f). \tag{E.3}$$

The specific angular distribution of γ rays for the dipole radiation is given in Ref. [TOL53] as

$$W(\theta) = \begin{cases} 1 + \dfrac{3}{2} N_2 f_2 P_2(\cos\theta) & (\text{for } j_f = j_i - 1). \\ 1 - \dfrac{3}{2} K_2 f_2 P_2(\cos\theta) & (\text{for } j_f = j_i). \\ 1 + \dfrac{3}{2} M_2 f_2 P_2(\cos\theta) & (\text{for } j_f = j_i + 1). \end{cases} \tag{E.4}$$

N_2, K_2, and M_2 are given as

$$\begin{aligned} N_2 &= j_i/(2j_i - 1). \\ K_2 &= j_i/(j_i + 1). \\ M_2 &= j_i^2/(j_i + 1)(2j_i + 3). \end{aligned} \tag{E.5}$$

For the quadrupole transitions, the γ-ray angular distribution are given as

$$W(\theta) = \begin{cases} 1 - \dfrac{15}{7} N_2 f_2 P_2(\cos\theta) - 5 N_4 f_4 P_4(\cos\theta) & (\text{for } j_f = j_i - 2). \\ \\ 1 - \dfrac{15}{7} M_2 f_2 P_2(\cos\theta) - 5 M_4 f_4 P_4(\cos\theta) & (\text{for } j_f = j_i + 2). \end{cases} \tag{E.6}$$

N_4 and M_4 are given as

$$\begin{aligned} N_4 &= j_i^3/(j_i - 1)(2j_i - 1)(2j_i - 3). \\ M_4 &= j_i^4/(j_i + 1)(j_i + 2)(2j_i + 3)(2j_i + 5). \end{aligned} \tag{E.7}$$

f_2 and f_4 are defined as

$$\begin{aligned} f_2 &= \frac{1}{j^2}[\sum_m m^2 a_m - \frac{1}{3} j(j+1)]. \\ f_4 &= \frac{1}{j^4}[\sum_m m^4 a_m - \frac{1}{7} j(6j^2 + 6j - 5) \sum_m m^2 a_m + \frac{3}{35} j(j-1)(j+1)(j+2)]. \end{aligned} \tag{E.8}$$

Figure E.1 shows the angular distribution of γ rays emitted from the 100 % polarized nucleus for the half-integer spin states. In the practical case, the anisotropy of the γ rays are reduced due to the solid angle of the detectors and the reduction of the polarization in the process of the β decay.

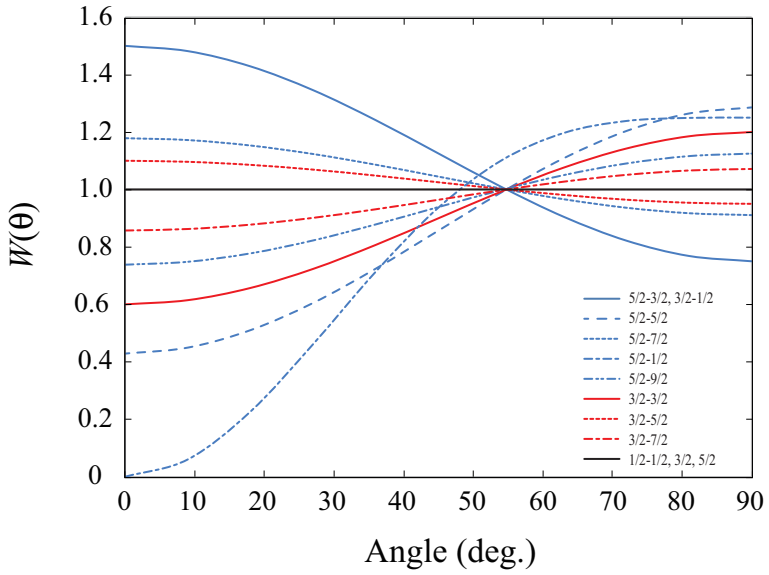

Figure E.1: Angular distribution of γ rays associated with spin-polarized nucleus.

APPENDIX F

Decoupling term

The wave function of the rotational motion (Ψ_{IMK}) is expressed as

$$\Psi_{IMK} = \sqrt{\frac{2I+1}{16\pi^2}}[\chi^j_K D^{(I)}_{M\ K} + (-1)^{I-j}\chi^j_{-K} D^{(I)}_{M\ -K}], \tag{F.1}$$

where I, j, M, and K represent total nuclear spin, the spin of the unpaired nucleon, the projection of the total angular momentum on the axis of the rotation, and the projection of the total angular momentum on the symmetry axis, respectively. $D^{(I)}_{M\ K}$ and χ^J_K are the Winger D-matrix, which represents eigenfunciton of rotating rigid body, and the wave function of the unpaired nucleon, respectively. The rotational Hamiltonian of the rotating system (H_{rot}) is simply given as

$$H_{rot} = \frac{2\hbar^2}{\mathcal{J}}\boldsymbol{R}^2 \tag{F.2}$$

The Hamiltonian is written by using $\boldsymbol{I}$ and $\boldsymbol{j}$ as

$$\begin{aligned} H_{rot} &= \frac{\hbar^2}{2\mathcal{J}}(\boldsymbol{I}-\boldsymbol{j})^2 \\ &= \frac{\hbar^2}{2\mathcal{J}}(\boldsymbol{I^2}+\boldsymbol{j^2}-2\boldsymbol{I}\cdot\boldsymbol{j}) \end{aligned} \tag{F.3}$$

where $\mathcal{J}$ is the moment of inertia. The rotational energy is given as

$$E_{rot} = \frac{\hbar^2}{2\mathcal{J}}I(I+1) + E_0 + E_{cor}. \tag{F.4}$$

E_0 represents internal energy and does not depend on the value of I, so that this term does not affect energy spectrum of the rotation. For $K \neq 1/2$, E_{cor}, which comes from the term of $\boldsymbol{I}\cdot\boldsymbol{j}$ in Eq. (F.3) and is called the Coriolis term, is ignored. For the $K = 1/2$ case, the symmetrization of the wave function in Eq. (F.1) allows a diagonal contribution to the

energy, therefore it could not be ignored. E_{cor} is expressed as

$$\begin{aligned} E_{cor} &= (\frac{\hbar^2}{\mathcal{J}})\langle\Psi_{IM1/2}|\boldsymbol{I}_+\boldsymbol{J}_- + \boldsymbol{I}_-\boldsymbol{J}_+ \ |\Psi_{IM1/2}\rangle \\ &= (\frac{\hbar^2}{\mathcal{J}})[a(-1)^{I+1/2}(I+1/2)] \end{aligned} \tag{F.5}$$

a is a decoupling parameter, and it is given as

$$a = \sum_j C_j^2(-1)^{j-\frac{1}{2}}(j+\frac{1}{2}), \tag{F.6}$$

C_j is configuration mixing coefficient defined as

$$\psi_{Nil} = \sum_j C_j\phi_j, \tag{F.7}$$

where ψ_{Nil} and ϕ_j are Nilsson wave function and wave function of the spherical single particle, respectively.

APPENDIX G

Deformation parameter

In order to express the magnitude of the quadrupole deformation, the deformation parameters of β or δ have been well-used. Assuming that the deformed nuclei have spheroid shapes, the radius of xy-plane and the length of z-axis (symmetry axis) are defined as a and c, respectively. In the case, the deformation parameter δ is defined as

$$\delta = \frac{c-a}{R_0}, \tag{G.1}$$

where R_0 is the radius of the sphere of the same volume. In other way, the spheroid shapes are also express by using the spherical harmonics $Y_{\lambda\mu}(\theta,\, \phi)$ as

$$\begin{aligned} R(\theta,\phi) &= R_0[1+\beta Y_{20}] \\ &= R_0[1+\beta\sqrt{\frac{5}{4\pi}}\frac{3\cos\theta-1}{2}]. \end{aligned} \tag{G.2}$$

where β is the deformation parameter. The relation of these deformation parameters of β and δ is

$$\delta = \frac{3}{2}\sqrt{\frac{5}{4\pi}}\beta. \tag{G.3}$$

BIBLIOGRAPHY

[ALB74] D.E. Alburger and D.R. Goosman, Phys. Rev. C **9**, 2236 (1974).

[ALB82] D.E. Alburger and E.K. Warburton, Nucl. Phys. A **385**, 474 (1982).

[ALF86-1] W.P. Alford, P. Craig, D.A. Lind, R.S. Raymond, J. Ullman, and B.H. Wildenthal, Nucl. Phys. A **457**, 317 (1986).

[ALF86-2] W.P. Alford, J.A. Cameron, E. Habib, and B.H. Wildenthal, Nucl. Phys. A **454**, 189 (1986).

[BAB16] H. Baba, http://rarfaxp.riken.go.jp/ baba/acquisition/system/nbbq.

[BAU87] P. Baumann, Ph. Dessagne, A. Huck, G. Klotz, A. Knipper, Ch. Miehe, M. Rmdane, G. Walter, G. Marguier, J. Giroux, and C. Richard-Serre, AIP Conf. Proc.:5th Int. Conf. on Nuclei Far from stability, Rosseau Lake, Canada (1987).

[BAU89] P. Baumann, Ph. Dessagne, A. Huck, G. Klotz, A. Knipper, Ch. Miehe, M. Ramdane, G. Walter, G. Marguier, H. Gabelmann, C. Richard-Serre, K. Schlösser, and A. Poves, Phys. Rev. C **39**, 626 (1989).

[BOH75] A. Bohr and B.R. Mottelson, *Nuclear Structure*, Vol. II, New York Benjamin, 1975.

[BRO06] B.A. Brown and W.A. Richter, Phys. Rev. C. **74**, 034351 (2006).

[CAS05] R.F. Casten, *Nuclear Structure from a Simple Perspective*, Second edition, Oxford University Press, 2005.

[CAU14] E. Caurier, F. Nowacki, and A. Poves, Phys. Rev. C **90**, 014302 (2014).

[CHU05] J.A. Church, C.M. Campbell, D.-C. Dinca, J. Enders, A. Gade, T. Glasmacher, Z. Hu, R.V.F. Janssens, W.F. Mueller, H. Olliver, B.C. Perry, L.A. Riley, and K.L. Yurkewicz, Phys. Rev. C **72**, 054320 (2005).

[DEA10] A.N. Deacon, J.F. Smith, S.J. Freeman, R.V. Janssens, M.P. Carpenter, B. Hadinia, C.R. Hoffman, B.P. Kay, T. Lauritsen, C. J. Lister, D. O ' Donnell, J. Ollier, T. Otsuka, D. Seweryniak, K.-M. Spohr, D. Steppenbeck, S.L. Tabor, V. Tripathi, Y. Utsuno, P.T. Wady, and S. Zhu, Phys. Rev. C **82**, 034305 (2010).

[DET79] C. Détraz, D. Guillemaud, G. Huber, R. Klapisch, M. Langevin, F. Naulin, C. Thibault, L.C. Carraz, and F. Touchard, Phys. Rev. C **19**, 164 (1979).

[DET83] C. Détraz, M. Langevin, M.C. Goffri-Kouassi, D. Guillemaud, M. Epherre, G. Audi, C. Thibault, and F. Touchard, Nucl. Phys. A **394**, 378 (1983).

[FOR11] H.T. Fortune, Phys. Rev. C **84**, 024327 (2011).

[FUK92] N. Fukunishi, T. Otsuka, and T. Sebe, Phys. Lett. B **296**, 279 (1992).

[GUI84] D. Guillemaud-Mueller, C. Detraz, M. Langevin, F. Naulin, M. De Saint-Simon, C. Thibault, F. Touchard, and M. Epherre, Nuclear Physics A **426**, 37 (1984).

[HAG97] E. Hagberg, I. Towner, T. Alexander, G. Ball, J. Forster, J. Hardy, J. Hykawy, V. Koslowsky, J. Leslie, H.-B. Mak, I. Neeson, and G. Savard, Phys. Rev. C **56**, 135 (1997).

[HAM10] I. Hamamoto, J. Phys. G **37**, 055102 (2010).

[HIN08] T.A. Hinners, V. Tripathi, S.L. Tabor, A. Volya, P.C. Bender, C.R. Hoffman, S. Lee, M. Perry, P.F. Mantica, A.D. Davies, S.N. Liddick, W.F. Mueller, A. Stolz, and B.E. Tomlin, Phys. Rev. C **77**, 034305 (2008).

[HIN11] N. Hinohara, K. Sato, K. Yoshida, T. Nakatsukasa, M. Matuo, and K. Matsuyanagi, Phys. Rev. C. **84**, 061302 (2011).

[HIR05] Y. Hirayama, T. Shimoda, H. Izumi, A. Hatakeyama, K.P. Jackson, C.D.P. Levy, H. Miyatake, M. Yagi, and H. Yano, Phys. Lett. B **611**, 239 (2005).

[HUB78] G. Huber, F. Touchard, S. Buttgenbach, C. Thibault, R. Klapisch, H.T. Duong, S. Liberman, J. Pinard, J.L. Vaille, P. Juncar, and P. Jacquinot, Phys. Rev. C **18**, 2342 (1978).

[IMA15] N. Imai, M. Mukai, J. Cederkäll, H. Aghai, P. Golubev, H.T. Johansson, D. Kahl, J. Kurcewics, T. Teranishi, and Y.X. Watanabe, Phys. Rev. C **90**, 011302(R) (2015).

[IWA01] H. Iwasaki, T. Motobayashi, H. Sakurai, K. Yoneda, T. Gomib, N. Aoi, N. Fukuda, Zs. Fülöp, U. Futakamib, Z. Gacsi, Y. Higurashi, N. Imai, N. Iwasa, T. Kubo, M. Kunibu, M. Kurokawa, Z. Liu, T. Minemura, A. Saito, M. Serata, S. Shimoura, S. Takeuchi, Y.X. Watanabe, K. Yamada, Y. Yanagisawa, and M. Ishihara, Phys. Lett. B **522**, 227 (2001).

[KAN16] S. Kanaya *et al.*, to be submitted.

[KIM07] M. Kimura, Phys. Rev. C **75**, 041302(R) (2007).

[KIM11] M. Kimura and H. Horiuchi, International Journal of Modern Physics E **20**, 893, 2011.

[KIM16] M. Kimura, private communication.

[KLO93] G. Klotz, P. Baumann, M. Bounajma, A. Huck, A. Knipper, G. Walter, G. Marguier, C. Richard-Serre, A. Poves, and J. Retamosa, Phys. Rev. C **47**, 2502 (1993).

[KOR50] J. Korringa, Physica **16**, 601 (1950).

[KUR12] K. Kura, K. Tajiri, T. Shimoda, A. Odahara, T. Hori, M. Kazato, T. Masue, M. Suga, A. Takashima, T. Suzuki, T. Fukuchi, Y. Hirayama, N. Imai, H. Miyatake, M. Pearson, C.D.P. Levy, and K.P. Jackson, Phys. Rev. C **85**, 034310 (2012).

[LEV03] C.D.P. Levy, A. Hatakeyama, Y. Hirayama, R.F. Kiefl, R. Baartman, J.A. Behr, H. Izumi, D. Melconian, G.D. Morris, R. Nussbaumer, M. Olivo, M. Pearson, R. Poutissou, and G.W. Wight, Nucl. Instrum. Methods B **204** 689 (2003).

[LEV04] C.D.P. Levy, R. Baartman, J.A. Behr, R.F. Kiefl, M. Pearson, R. Poutissou, A. Hatakeyama, and Y. Hirayama, Nucl. Phys. A **746**, 206 (2004).

[MAC05] H. Mach, L.M. Fraile, O. Tengblad, R. Boutami, C. Jollet, W.A. P*ló*ciennik, D.T. Yordanov, M. Stanoiu, M.J.G. Borge, P.A. Butler, J. Cederk*ä*ll, Ph. Dessagne, B. Fogelberg, H. Fynbo, P. Hoff, A. Jokinen,A. Korgul, U. K*ö*ster, W. Kurcewicz, F. Marechal, T. Motobayashi, J. Mrazek, G. Neyens, T. Nilsson, S. Pedersen, A. Poves, B. Rubio, E. Ruchowska, and the ISOLDE Collaboration, Eur. Phys. J. A **25**, 105 (2005).

[MAR05] F. Maréchal, D. Balabanski, D. Borremans, J.-M. Daugas, F. Santos, P. Dessagne, G. Georgiev, J. Giovinazzo, S. Grévy, P. Himpe, C. Jollet, I. Matea, G. Neyens, F. Perrot, E. Poirier, O. Roig, M. Stanoiu, C. Stodel, J.-C. Thomas, K. Turzó, D. Yordanov, E. Caurier, F. Nowacki, and A. Poves, Phys. Rev. C **72**, 044314 (2005).

[MAT93] M. Matoba, O. Iwamoto, Y. Uozumi, T. Sakae, N. Koori, T. Fujiki, H. Ohgaki, H. Ijiri, T. Maki, and M. Nakano, Phys. Rev. C **48**, 95 (1993).

[MAT07] C. Mattoon, F. Sarazin, G. Hackman, E. Cunningham, R. Austin, G. Ball, R. Chakrawarthy, P. Finlay, P. Garrett, G. Grinyer, B. Hyland, K.A. Koopmans, J.R. Leslie, A.A. Phillips, M.A. Schumaker, H.C. Scraggs, J. Schwarzenberg, M.B. Smith, C.E. Svensson, J.C. Waddington, P.M. Walker, B. Washbrook, and E. Zganjar, Phys. Rev. C **75**, 017302 (2007).

[MID64] R. Middleton and D.J. Pullen, Nucl. Phys. **51**, 77 (1964).

[MIL09] D. Miller, P. Adrich, B. Brown, V. Moeller, A. Ratkiewicz, W. Rother, K. Starosta, J. Tostevin, C. Vaman, and P. Voss, Phys. Rev. C **79**, 054306 (2009).

[MIN04] K. Minamisono, K. Matsuta, T. Minamisono, C.D.P. Levy, T. Nagatomo, M. Ogura, T. Sumikama, J.A. Behr, K.P. Jackson, H. Fujiwara, M. Mihara, and M. Fukuda, Hyperfine Interact. **159**, 261 (2004).

[MIY03] H. Miyatake, H. Ueno, Y. Yamamoto, N. Aoi, K. Asahi, E. Ideguchi, M. Ishihara, H. Izumi, T. Kishida,T. Kubo, S. Mitsuoka, Y. Mizoi, M. Notani, H. Ogawa, A. Ozawa, M. Sasaki, T. Shimoda, T. Shirakura, N. Takahashi, S. Tanimoto, and K. Yoneda, Phys. Rev. C **67**, 014316 (2003).

[MOR76] H. Morinaga and T. Yamazaki, *IN−BEAM GAMMA−RAY SPECTROSCOPY*, NORTH-HOLLAND PUBLISHING CAMPANY, 1976.

[MOT95] T. Motobayashi, Y. Ikedaa, Y. Ando, K. Ieki, M. Inoue, N. Iwasa, T. Kikuchi, M. Kurokawaa, S. Moriya, S. Ogawa, H. Murakami, S. Shimoura, Y. Yanagisawa, T. Nakamura, Y. Watanabe, M. Ishihara, T. Teranishi, H. Okuno, and R.F. Casten, Phys. Lett. B **346**, 9 (1995).

[NEY05] G. Neyens, M. Kowalska, D. Yordanov, K. Blaum, P. Himpe, P. Lievens, S. Mallion, R. Neugart, N. Vermeulen, Y. Utsuno, and T. Otsuka, Phys. Rev. Lett. **94**, 022501 (2005).

[NEY11] G. Neyens, Phys. Rev. C **84**, 064310 (2011).

[NIE05] O. Niedermaier, H. Scheit, V. Bildstein, H. Boie, J. Fitting, R. von Hahn, F. K*ö*ck, M. Lauer, U.K. Pal, H. Podlech, R. Repnow, D. Schwalm, C. Alvarez, F. Ames, G. Bollen, S. Emhofer, D. Habs, O. Kester, R. Lutter, K. Rudolph, M. Pasini, P. G. Thirolf, B.H. Wolf, J. Eberth, G. Gersch, H. Hess, P. Reiter, O. Thelen, N. Warr, D. Weisshaar, F. Aksouh, P. Van den Bergh, P. Van Duppen, M. Huyse, O. Ivanov, P. Mayet, J. Van de Walle, J. *Ä*yst*ö*5, P.A. Butler, J. Cederk*ä*ll, P. Delahaye, H.O.U. Fynbo, L.M. Fraile, O. Forstner, S. Franchoo, U. K*ö*ster, T. Nilsson, M. Oinonen, T. Sieber, F. Wenander, M. Pantea, A. Richter, G. Schrieder, H. Simon, T. Behrens, R. Gernh*ä*user, T. Kr*ö*ll, R. Kr*ü*cken, M. M*ü*nch, T. Davinson, J. Gerl, G. Huber, A. Hurst, J. Iwanicki, B. Jonson, P. Lieb, L. Liljeby, A. Schempp, A. Scherillo, P. Schmidt, and G. Walter, Phys. Rev. Lett. **94**, 172501 (2005).

[NNDC] National Nuclear Data Center, Brookhaven National Laboratory, http://www.nndc.bnl.gov.

[ORR91] N. Orr, W. Mittig, L.K. Fifield, M. Lewitowicz, E. Plagnol, Y. Schutz, Zhan Wen Long L. Bianchi, A. Gillibert, A.V. Belozyorov, S.M. Lukyanov, Yu.E. Penionzhkevich, A.C.C. Villari, A. Cunsolo, A. Foti, G. Audi, C. Stephan, and L. Tassan-Got, Phys. Lett. B **258**, 29 (1991).

[OUE13] C. Ouellet and B. Singh, Nuclear Data Sheets **114**, 209 (2013).

[PAS78] I. Paschopoulos, E. Muller, H.J. Korner, I.C. Oelrich, K.E. Rehm, and H.J. Scheerer, Phys. Rev. C **18**, 1277 (1978).

[PET15] M. Petri, P. Fallon, A.O. Macchiavelli, S. Heil, E. Rodriguez-Vieitez, D. Bazin, C.M. Campbell, R.M. Clark, M. Cromaz, A. Gade, T.Glasmacherd, I.Y.Lee, S.Malbrunot-Ettenauer, S.Paschalis, A.Ratkiewicz, J.R.Terry, D.Weisshaar, and M.Wiedeking, Phys. Lett. B **748**, 173 (2015).

[POV87] A. Poves and J.Retamosa, Phys. Lett. B **184**, 311 (1987).

[POV14] A. Poves, F. Nowacki, and E. Caurier, EPJ Web of Conferences **66**, 02084 (2014).

[PRI99] B.V. Pritychenko, T. Glasmacher, B.A. Brown, P.D. Cottle, R.W. Ibbotson, K.W. Kemper, L.A. Riley, and H. Scheit, Phys. Rev. C **63**, 011305 (2000).

[RAD11] D. Radford, RADWARE http://radware.phy.ornl.gov.

[SCH09] W. Schwerdtfeger, P. Thirolf, K. Wimmer, D. Habs, H. Mach, T. Rodriguez, V. Bildstein, J. Egido, L. Fraile, R. Gernhäuser, Hertenberger, K. Heyde, P. Hoff, H. H*ü*bel, U. K*ö*ster, T. Kr*ö*ll, R. Kr*ü*cken, R. Lutter, T. Morgan, and P. Ring, Phys. Rev. Lett. **103**, 012501 (2009).

[SEI11] M. Seidlitz,1,D.Mücher, P. Reiter, V. Bildstein, A. Blazhev,N.Bree, B. Bruyneel, J. Cederkäll,E. Clement, T. Davinson, P. Van Duppen, A. Ekstr*ö*me, F. Finke, L.M. Fraile, K. Geibel, R. Gernh*ä*user, H. Hess, A. Holler, M. Huyse, O. Ivanov, J. Jolie, M. Kalk*ü*hler, T. Kotthaus, R. Kr*ü*cken, R. Lutter, E. Piselli, H. Scheit, I. Stefanescu, J. Van de Walle, D. Voulot, N. Warr, F. Wenander, and A. Wiens, Phys. Lett. B **700**, 181 (2011).

[BAS10] M.S. Basunia, Nuclear Data Sheets **111**, 2331 (2010).

[SHI14] T. Shimoda, K. Tajiri, K. Kura, A. Odahara, M. Suga, Y. Hirayama, N. Imai, H. Miyatake, M. Pearson, C.D.P. Levy, K.P. Jackson, R. Legillon, C. Petrache, T. Fukuchi, N. Hamatani, T. Hori, M. Kazato, Y. Kenmoku, T. Masue, H. Nishibata, T. Suzuki, A. Takashima, and R. Yokoyama, Hyperfine Interact. **225**, 183 (2014).

[TAJ12] K. Tajiri, Doctoral Dissertation, Osaka University, 2012.

[TAK09] S. Takeuchi, N. Aoi, T. Motobayashi, S. Ota, E. Takeshita, H. Suzuki, H. Baba, T. Fukui, Y. Hashimoto, K. Ieki, N. Imai, H. Iwasaki, S. Kanno, Y. Kondo, T. Kubo, K. Kurita, T. Minemura, T. Nakabayashi, T. Nakamura, T. Okumura, T. K. Onishi, H. Sakurai, S. Shimoura, R. Sugou, D. Suzuki, M. K. Suzuki, M. Takashina, M. Tamaki, K. Tanaka, Y. Togano, and K. Yamada, Phys. Rev. C **79**, 054319 (2009).

[TER08] J. Terry, B. Brown, C. Campbell, J. Cook, A. Davies, D.-C. Dinca, A. Gade, T. Glasmacher, P. Hansen, B. Sherrill, H. Zwahlen, D. Bazin, K. Yoneda, J. A. Tostevin, T. Otsuka, Y. Utsuno, and B. Pritychenko, Phys. Rev. C **77**, 014316 (2008).

[THI75] C. Thibault, R. Klapisch, C. Rigaud, A.M. Poskanzer, R. Prieels, L. Lessard, and W. Reisdorf, Phys. Rev. C **12**, 644 (1975).

[TOI96] Richard B. Firestone, Verginia S. Shirley, Coral M. Baglin, S.Y. Frank Chu, and Jean Zipkin, Table of Isotpes, Eighth Edition, Volume I and II, A Wiley-Interscience publication, 1996.

[TOL53] H.A. Tolhoek and J.A.M. Cox, Physica **19**, 101 (1953).

[UTS04] Y. Utsuno, T. Otsuka, T. Glasmacher, T. Mizusaki, and M. Honma, Phys. Rev. C **70**, 044307 (2004).

[WAN10] Z.M. Wang, R. Chapman, X. Liang, F. Haas, M. Bouhelal, F. Azaiez, B.R. Behera, M. Burns, E. Caurier, L. Corradi, D. Curien, A. N. Deacon, Zs. Dombrádi, E. Farnea, E. Fioretto, A. Gadea, A. Hodsdon, F. Ibrahim, A. Jungclaus, K. Keyes, V. Kumar, A. Latina, N. Mărginean, G. Montagnoli, D. R. Napoli, F. Nowacki, J. Ollier, D. O'Donnell, A. Papenberg, G. Pollarolo, M.-D. Salsac, F. Scarlassara, J.F. Smith, K.M. Spohr, M. Stanoiu, A. M. Stefanini, S. Szilner, M. Trotta, and D. Verney, Phys. Rev. C **81**, 064301 (2010).

[WAR86] E. Warburton, D. Alburger, J. Becker, B. Brown, and S. Raman, Phys. Rev. C **34**, 1031 (1986).

[WAR90] E.K. Warburton, J.A. Becker, and B.A. Brown, Phys. Rev. C **41**, 1147 (1990).

[WAT81] A. Watt, R.P. Singhal, M.H. Storm, and R.R. Whitehead, J. Phys. G **7**, L145 (1981).

[WEA60] R.S. Weaver and R.E. Bell, Nucl. Instrum. Methods **9**, 149 (1960).

[WIL80] B. Wildenthal and W. Chung, Phys. Rev. C **22**, 2260(R) (1980).

[WIM10] K. Wimmer, T. Kröll, R. Krücken, V. Bildstein, R. Gernhäuser, B. Bastin, N. Bree, J. Diriken, P. Van Duppen, M. Huyse, N. Patronis, P. Vermaelen, D. Voulot, J. Van de Walle, F. Wenander, L.M. Fraile, R. Chapman, B. Hadinia, R. Orlandi, J.F. Smith, R. Lutter, P.G. Thirolf, M. Labiche, A. Blazhev, M. Kalkühler, P. Reiter, M. Seidlitz, N. Warr, A.O. Macchiavelli, H. B. Jeppesen, E. Fiori, G. Georgiev, G. Schrieder, S. Das Gupta, G. Lo Bianco, S. Nardelli, J. Butterworth, J. Johansen, and K. Riisager, Phys. Rev. Lett. **105**, 252501 (2010).

[YAM16] The calculation code was provided by M. Yamagami.

[YAN03] Y. Yanagisawa, M. Notani, H. Sakurai, M. Kunibud, H. Akiyoshi, N.Aoi,H. Baba, K. Demichi, N. Fukuda, H. Hasegawa, Y. Higurashi, M. Ishihara,N. Iwasa, H. Iwasaki, T. Gomi, S. Kanno, M. Kurokawa, Y.U. Matsuyama, S. Michimasa, T. Minemura, T. Mizoi, T. Nakamura, A. Saito, M. Serata, S. Shimoura, T. Sugimoto, E. Takeshita, S. Takeuchi, K. Ue, K. Yamada, K. Yoneda, and T. Motobayashi, Phys. Lett. B **566**, 84 (2003).

[ZWI78] B. Zwieglinski, G.M. Crawley, H. Nann, and J.A. Nolen, Jr., Phys. Rev. C **17**, 872 (1978).